

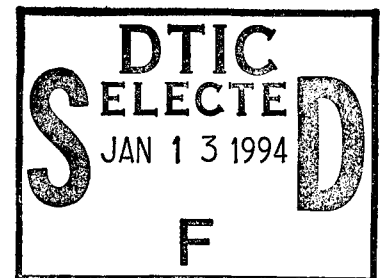
Final Report

Erbium-Laser-Based Infrared Sources

ARPA Solid State Laser and Nonlinear Materials Program

Prepared by:

Research Division
Schwartz Electro-Optics, Inc.
45 Winthrop Street
Concord, MA 01742



Principal Investigator: Dr. Peter F. Moulton

Contract Dates: October 1990 - June 1994

Contract Number: N00014-90-C-0235

Contract Agent: ONR

ARPA Program Manager: Dr. L.N. Durvasula

ONR Scientific Officer: Dr. Vern. L. Smiley

This document has been approved
for public release and sale; its
distribution is unlimited.

The views and conclusions obtained in this document are those of the authors and should not be interpreted as necessarily representing the official policies, either express or implied, of the Advanced Research Projects Agency of the U.S. Government

DTIC QUALITY INSPECTED &

19950110 019

Table of Contents

1. EXECUTIVE SUMMARY		1
2. BACKGROUND		3
3. MATERIALS GROWTH		5
4. CONVENTIONAL SPECTROSCOPY		7
4.1 Absorption		7
4.2 Fluorescence		30
4.3 Lifetimes		37
5. NONLINEAR SPECTROSCOPY		39
5.1 Excited-state Absorption, Upconversion and Cross Relaxation		39
5.2 Gain		45
6. LASERS AND NON-LASERS		61
6.1 Ti:sapphire-pumped, cw 3- μ m lasers		62
6.2 Diode-pumped, cw 3- μ m lasers		67
6.3 Diode-pumped, pulsed 3- μ m lasers		70
6.4 Pulsed 1.6- μ m laser operation from Er:YOS		73
6.5 Non-cw laser operation at 1.6 μ m		74
7. APPENDICES		76
7.1 Appendix A - Ph.D. Thesis		76
7.2 Appendix B - Optics Letters Paper		210
7.3 Appendix C - ASSL '92 Summary		214
7.4 Appendix D - LEOS '92 Abstract and Summary		219
7.5 Appendix E - ASSL '93 Summary		223
7.6 Appendix F - ASSL '94 Abstract and Summary		227

Accession For		1
NTIS	CRA&I	<input checked="" type="checkbox"/>
DTIC	TAB	<input type="checkbox"/>
Unannounced		<input type="checkbox"/>
Justification		
By		
Distribution /		
Availability Codes		
Dist	Avail and/or Special	
A-1		

1. Executive Summary

The Research Division of Schwartz Electro-Optics, as part of the ARPA Solid State Laser and Nonlinear Materials Program, conducted a three-year study "Erbium-Laser-Based Infrared Sources." The aim of the study was to improve the understanding of semiconductor-laser-pumped, infrared (IR) solid state lasers based on the trivalent rare-earth ion erbium (Er) doped into a variety of host crystals.

The initial program plan emphasized operation of erbium-doped materials on the 2.8-3.0- μm laser transition. Pulsed, Q-switched sources using that transition, when employed as a pump source for parametric oscillators, can provide tunable mid-IR energy. The dynamics of erbium lasers are more complex than conventional neodymium (Nd)-doped lasers and we intended to use pump-probe techniques to measure the level and temporal behavior of gain in various materials. To do so we constructed a number of different cw Er-doped lasers as probe sources and employed the Cr:LiSAF laser as a pulsed pump source that would simulate pulsed diode arrays. We identified the 970-nm wavelength pump band of Er as the most efficient and were able to make use of recently developed cw and pulsed InGaAs strained-quantum-well diode lasers in the effort. At the conclusion of the program we demonstrated the first pulsed diode bar pumping of the most promising materials for pulsed operation, the oxide garnets YSGG and GGG and the fluoride BaY_2F_8 .

As the program developed we identified a critical application of the cw erbium lasers in infrared sensor calibration and carried out a successful demonstration in collaboration with the Aerospace Corporation. As a result the study and development of cw lasers became a significant portion of the effort. In general, the oxide hosts such as the garnets YSGG, GGG and YAG operated more efficiently as cw sources than the fluorides YLF and BaY_2F_8 . We achieved a number of new milestones in cw-laser performance, including the first diode-pumped cw operation from several host crystals, a record power level of 0.5 W, obtained from Er:YSGG with diode pumping and the first cw, single-frequency, tunable Er:YAG laser.

Based on direction from potential customers, we added to the program the study of Er-doped lasers operating on the 1.5- μm -wavelength region laser transition. The application of these lasers is in eye-safe rangefinders, ladars and lidars. In general the type of host crystal with favorable properties for 1.5- μm lasers is one in which non-radiative decay of the 3- μm transition is rapid, the opposite of the criterion for low-threshold 3- μm laser hosts. We considered the oxides YVO_4 and YOS as candidate materials. Although we did observe the first pulsed operation from Er:YOS, our program provided further verification of the difficulty in operating Er-doped crystals as effective 1.5- μm lasers, even with diode pumping. The problem of the lower laser level being in the ground state is compounded by the presence of upconversion, which raises the pumping level needed to produce gain in the crystal. Our level of investigation of the fundamental properties of the candidate materials was not as extensive as for the 3- μm lasers, which suggests that further investigation is warranted.

Throughout the program we studied the conventional spectroscopic properties, absorption, fluorescence and level decay times of all the doped crystals, as well as some of the nonlinear properties such as upconversion. The spectroscopic measurements of two

materials, YSGG and GGG, formed the basis for a Ph.D. thesis that is included as Appendix A with this report. Also included as appendices in the report are abstracts and summaries of papers presented at conferences and a copy of an article that was published in Optics Letters.

As a result of this effort, we conclude that diode-pumped, cw Er-doped lasers can provide efficient (20-30% conversion of diode pump power), Watt-level operation in the 3- μm wavelength region. As higher-power, 970-nm cw diode sources become available we should be able to scale up the output power levels beyond the 0.5-W level achieved in the program. Pulsed-pumped, Er-doped lasers at 3 μm should also provide efficient operation, and should be investigated more fully if applications are found. One area of further study involves the Q-switching of both cw and pulse-pumped, Er-doped 3- μm lasers. For the cw-pumped systems this might be one approach to generating the 10-kHz-level pulse rates needed for some mid-IR applications. As far the as the use of Er-doped crystals for efficient, 1.5- μm sources, further investigation is required to determine whether host crystals exist that will operate as effective lasers.

The remainder of the Final Report covers materials growth, a discussion and graphical presentation of results of the conventional spectroscopic measurements, and consideration of our "nonlinear" spectroscopy, which includes upconversion and gain measurements. The report concludes with discussion of our laser and non-laser results. The bulk of the report is in Appendix A, a complete copy of the Ph.D. thesis done under the contract.

The Principal Investigator for the program was Peter Moulton. Most of the experimental effort was carried out by Bradley Dinerman, who completed his Ph.D. thesis at Boston College using data from the program. Others involved in the effort at the Research Division of SEO include David Rines and James Harrison. The program started in October of 1990 and was originally scheduled for completion in October of 1993, but was extended until June 15 of 1994 in order to assist the Aerospace Corporation in the application of 3- μm cw lasers to sensor calibration.

2. Background

There are numerous DoD and non-DoD applications for tunable sources in the mid-IR wavelength region. For systems based on solid state lasers, one approach to generation of tunable mid-IR is to use a fixed-wavelength, rare-earth-doped laser to pump a parametric oscillator (OPO). The latter can typically be tuned by changing the phase-match angle of the nonlinear crystal. Of all the rare-earth lasers, the most well developed are based on the Nd ion, operating around 1.06 μm . Other sources include Tm- and Ho-doped materials with output near 2 μm and Er-doped materials with 3- μm output.

While the Nd-doped lasers have been proven capable of generating high average powers and can be pumped by diode arrays, conservation of photons leads to Nd-pumped OPO conversion efficiencies of no better than 20% for a mid-IR output wavelength of 5 μm . Tm- and Ho-doped materials are now under investigation as OPO pump sources but suffer from either low-gain (Tm) and resultant damage problems or need cryogenic cooling (Ho) to obtain efficient operation. Er-doped 3- μm lasers present an interesting possibility as an OPO pump source. Not only is the photon loss reduced for 5- μm generation, but the Er transition is truly 4-level and does not require cryogenic cooling. On the other hand, the dynamics of Er-laser operation are complex due to ion-ion interactions and the long lifetime of the lower level may limit efficiency. In addition, there is concern that the gain of the Er transition may be too low to produce the high peak powers needed for OPO pumping. Finally, at the time this effort was started, there was limited data on the use of diodes as pump sources; nearly all of the prior work on Er lasers had involved lamp pumping. The aim of the effort was to improve the knowledge base on diode-pumped, Er-doped lasers.

Figure 1 shows a schematic of a possible tunable mid-IR source based on Er-doped lasers, an approach we discussed in the original proposal associated with the program. One of the issues in question then was the proper choice of pump wavelength, either in the 790-nm region to excite the $^4I_{9/2}$ Er state or the 970-nm region to excite the $^4I_{11/2}$ state. The Er-doped crystal would generate output at 2.8 μm to pump either an OPO based on CdSe or ZnGeP₂. In combination, the two materials could generate signal wavelengths spanning 3.3 to greater than 5 μm . (The idler outputs would cover from <6.4 to 18 μm). We considered the possibility of generating an alternate wavelength, 1.6 μm , from the Er-doped material as well, although the crystal would differ in doping and likely also in composition.

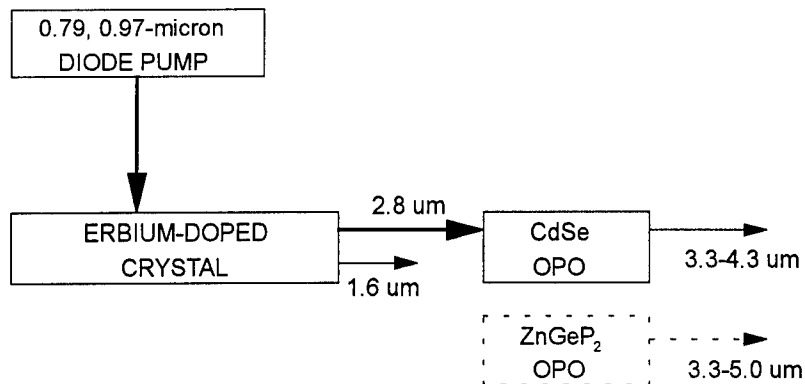


Figure 1. Schematic of possible IR source based on a diode-pumped Er laser.

Figures 2 and 3 show the signal wavelengths generated by CdSe and ZnGeP₂, respectively, for a 2.8- μm pump wavelength as the crystal phase-matching angle changes. The phase-matching calculations for CdSe show two possible signal wavelengths for a given angle, but the short-wavelength branch of Fig. 2 results for an idler wavelength far in the infrared; operation on that branch is impractical if not impossible.

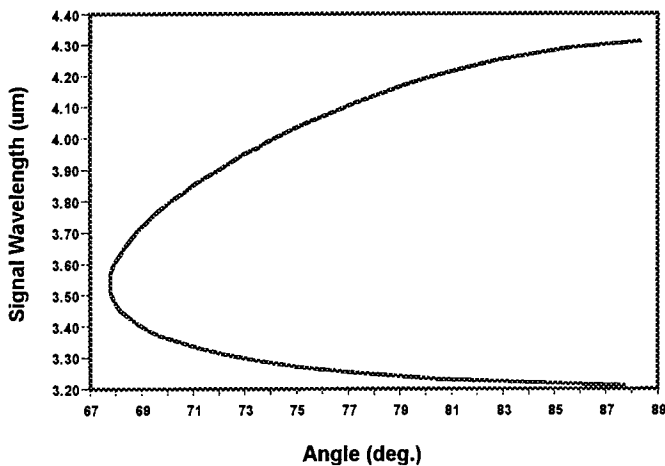


Figure 2.
Signal wavelength of CdSe OPO pumped by a 2.8- μm source, as a function of phase-match angle

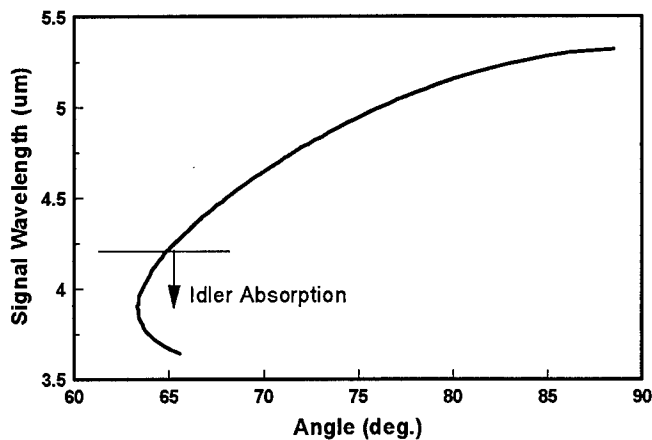


Figure 3.
Similar to Fig. 3 but for a ZnGeP₂ OPO. For signal wavelengths below 4.2 μm absorption of the idler by the nonlinear crystal may limit performance.

3. Materials Growth

Throughout the report we use common abbreviations for the various host crystals. Table 1 is a list of the abbreviations and corresponding full formulas for the materials.

Table 1. List of material abbreviations.

Abbreviation	Formula
BYF	BaY_2F_8
GGG	$Gd_3Ga_5O_{12}$
LiSAF	$LiSrAlF_6$
YAG	$Y_3Al_5O_{12}$
YLF	$LiYF_4$
YOS	Y_2SiO_5
YSGG	$Y_3Sc_2Ga_3O_{12}$
YVO	YVO_4

The following Table lists the crystals purchased for or provided to the program.

Table 2. List of materials from outside sources.

Material	Size	Source
Er:GGG (30%)	Ø 1in. x 2 in.	Airtron
Er:GGG (10%)	Ø 1in. x 2 in.	Airtron
Er:GGG (1%)	Ø 1in. x 2 in.	Airtron
Er:YSGG (30%)	Ø 1in. x 2 in.	Union Carbide
Er:YSGG (1%)	Ø 1in. x 2 in.	Airtron
Er:BYF (20%)	Ø 1in. x 2 in.	MIT
Er:YOS (1%)	Ø 0.5 in. x 0.25 in.	Bell Labs
Yb,Er:YOS (12%, 1%)	Ø 0.5 in. x 0.25 in.	Bell Labs
Yb,Er:YOS (6%, 0.5%)	Ø 1in. x 2 in.	ATE
Er:YVO (1%)	Ø 0.75 in. x 2 in.	Airtron
Yb,Er:YVO (6%, 0.5%)	Ø 0.6 in. x 2 in.	Airtron
Er:glass (QE-7)	1in. x 2 in. x 4 in.	Kigre
Cr:LiSAF	Ø 5 mm x 100 mm	Lightning

Key to sources for materials:

"Airtron" is Airtron - A Division of Litton Industries, Synoptics Group, 1201 Continental Blvd., Charlotte, NC 28273.

"Union Carbide" is Union Carbide, Crystal Products Group, 750 S. 32nd Street, Washougal, WA 98671.

"MIT" is the Crystal Physics Group at MIT. The growth effort was supervised by H.P. Jenssen, and was also funded by the DARPA Materials Program.

"Bell Labs" is AT&T Bell Laboratories. The material was grown there by C.D. Brandle and provided as samples to the program.

"ATE" is Applied Technology Enterprises, P.O. Box 1622, Irmo, SC 29063, an organization that provides a commercial outlet for AT&T Bell Laboratories. The material was grown at Bell Labs by C.D. Brandle.

"Kigre" is Kigre, Inc. Laser Components Div., 100 Marshland Rd., Hilton Head, SC 29926.

"Lightning" is Lightning Optical Corp., 431 E. Spruce St., Tarpon Springs, FL 34689.

Additional crystals of Er:YLF and Er:YAG were provided to the program from SEO inventory and small samples of Er:YOS and Yb:Er:YOS were provided by C.D. Brandle at Bell Labs.

4. Conventional Spectroscopy

Conventional spectroscopic measurements included absorption spectra, fluorescence spectra and fluorescence decay times for the different Er levels. Measurements of Er:GGG and Er:YSGG formed the basis for a Judd-Ofelt analysis, discussed in Appendix A, that predicts transition strengths amongst the levels. All of our spectroscopic data was read directly into IBM-PC-compatible computers, and is available in software for further analysis. Figure 4 shows a simplified energy-level diagram for the Er ion up to the $^4S_{3/2}$ state. Each state consists of a multiplicity of levels. The transitions indicated have been used to make lasers, with wavelengths in μm noted in the Figure. In this effort we considered just the 2.8-3- μm laser transitions from the $^4I_{11/2}$ to $^4I_{13/2}$ levels and 1.5-1.6- μm laser transitions from the $^4I_{13/2}$ to $^4I_{15/2}$ levels.

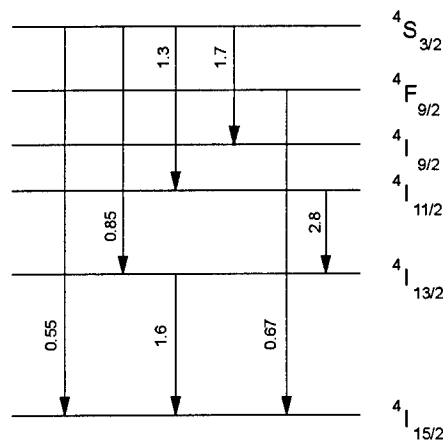


Figure 4. Lower-lying levels of Er ion, with observed laser transitions.

4.1 Absorption

We used a Perkin-Elmer Lambda 9 dual-beam spectrophotometer to measure the absorbance in samples, then divided the data by the path length in the crystal to obtain the absorption coefficient (in cm^{-1}) as a function of wavelength. Special emphasis was placed on absorption in the 790-nm, 970-nm and 1.6- μm regions from the $^4I_{15/2}$ ground state to the $^4I_{9/2}$, $^4I_{11/2}$, and $^4I_{13/2}$ states, respectively. The 790 and 970-nm bands are candidates for diode pumping while data from the 1.6- μm band can be used to predict the performance of the 1.6- μm laser transition. In order to better understand the energy levels within the manifolds, we measured the absorption of several samples cooled to liquid nitrogen temperatures.

Data on absorption in Er:YSGG and GGG is found on pages 31-35 of Appendix A.

We include in this section of the Report data on Er:YAG, Er:BYF, Er:YOS and Er:YVO. In addition, we show data on Yb,Er:YOS and Yb,Er:YVO.

Figures 5-8 present absorption spectra of Er:YAG (16%) while Figure 9-12 are similar spectra for Er:BYF (20%). The orientation and polarization properties of the measuring light were random for Er:BYF, which has a monoclinic crystal structure and resultant complicated dependence of absorption intensity on crystal orientation and polarization. In general rare-earth-doped YAG crystals have the narrowest linewidths of

all hosts, because of a high average optical phonon energy. Fluorides such as BYF with lower phonon energies have broader linewidths, and this is apparent in comparing spectra for YAG and BYF. The broader linewidths lead to relatively featureless pump bands, an advantage with diode pumping in that temperature control of the diode is not as critical.

Absorption spectra from the 1.6- μm -laser candidate Er:YOS appears in Figures 13-16. The doping level was estimated by the grower to be 1%. As with BYF, YOS is monoclinic, and our data is randomly polarized.

At the low doping levels needed to maintain low laser thresholds for the 1.6- μm transition, the absorption in the pump bands is weak. In an attempt to improve pump absorption, one can co-dope Er-doped material with Yb^{3+} ions, which provide strong absorption in the 900-1000-nm range and can sensitize Er via transfer from the excited $^2\text{F}_{5/2}$ state of Yb to the $^4\text{I}_{11/2}$ state of Er. Figures 17-19 show spectra for 0.5% Er:YOS doped with 6% Yb. The absorption in the 800-nm region (Fig. 17) is essentially the same as with Er:YOS, except beyond 820 nm, where the tail of the strong Yb transition is evident. Fig. 18 shows that the Yb absorption is broad and intense, ideal for diode pumping, and totally obscures any absorption from the Er ions. As expected, Fig. 19 shows only Er-related absorption. The intensity of Er absorption is higher in the co-doped sample than that of the Er:YOS crystal, even though the nominal Er doping is supposed to be half as great. This discrepancy may be related to polarization effects, but may also indicate a large uncertainty in the actual Er doping levels.

We measured absorption spectra for Er:YVO (1%), another 1.6- μm -laser candidate. YVO is uniaxial and we took data for sigma and pi polarizations. In the visible wavelength range the YVO material showed a steady increase in background absorption as the wavelength reduced below 600 nm, reaching $> 10 \text{ cm}^{-1}$ at 350 nm. This may be connected with color centers in the material, as well as absorption from the YVO_4 complex. Figures 20a and 20b present pi- and sigma-polarization data in the 980-nm region. As with YOS, we also considered the use of Yb as a sensitizer. Figs 21a and 21b show absorption for Yb,Er:YVO with 6% Yb and 0.5% Er. The Yb absorption dominates and is intense, reaching a peak absorption of $> 24 \text{ cm}^{-1}$. We took additional data in the 800- and 1500-nm regions, which when examined later showed that the spectral resolution is likely too low to resolve some of the line structure and accurately represent all of the peak absorption coefficients. We present it here for use in line-position determination, with Figures 22a and 22b showing 800-nm data and 23a and 23b showing 1500-nm data.

Because of the unique crystal-field environment in YVO, rare-earth-doped YVO crystals tend to exhibit a higher cross section and reduced Stark splitting of the energy levels compared to other materials. This leads to more intense absorption lines. If we compare data for the garnet materials YSGG, GGG and YAG, after correcting for differences in doping levels, we find that the 970- and 1500-nm absorption transitions are 3-6x more intense in YVO, assuming that the YVO crystal is indeed doped at the 1% level.

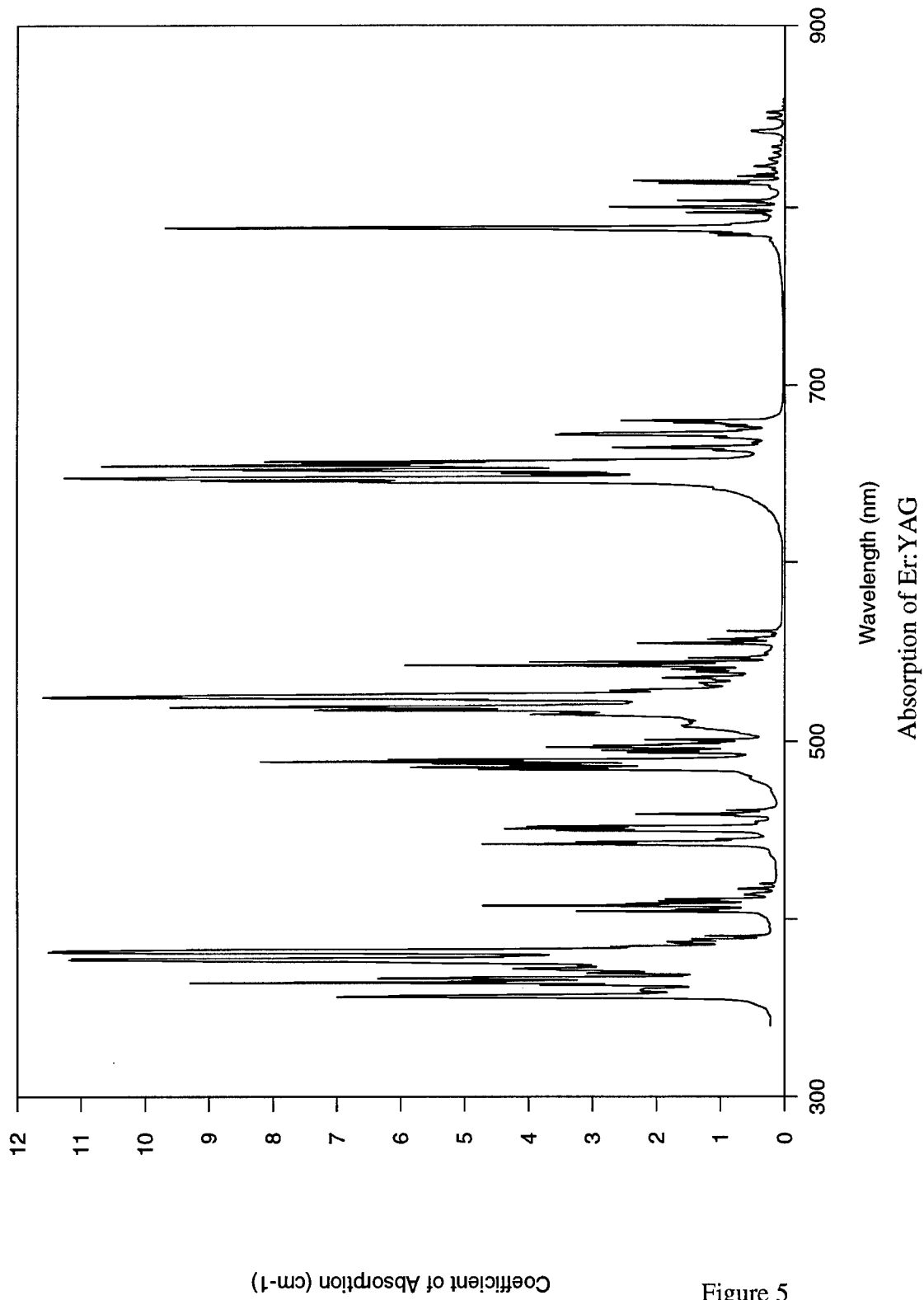


Figure 5

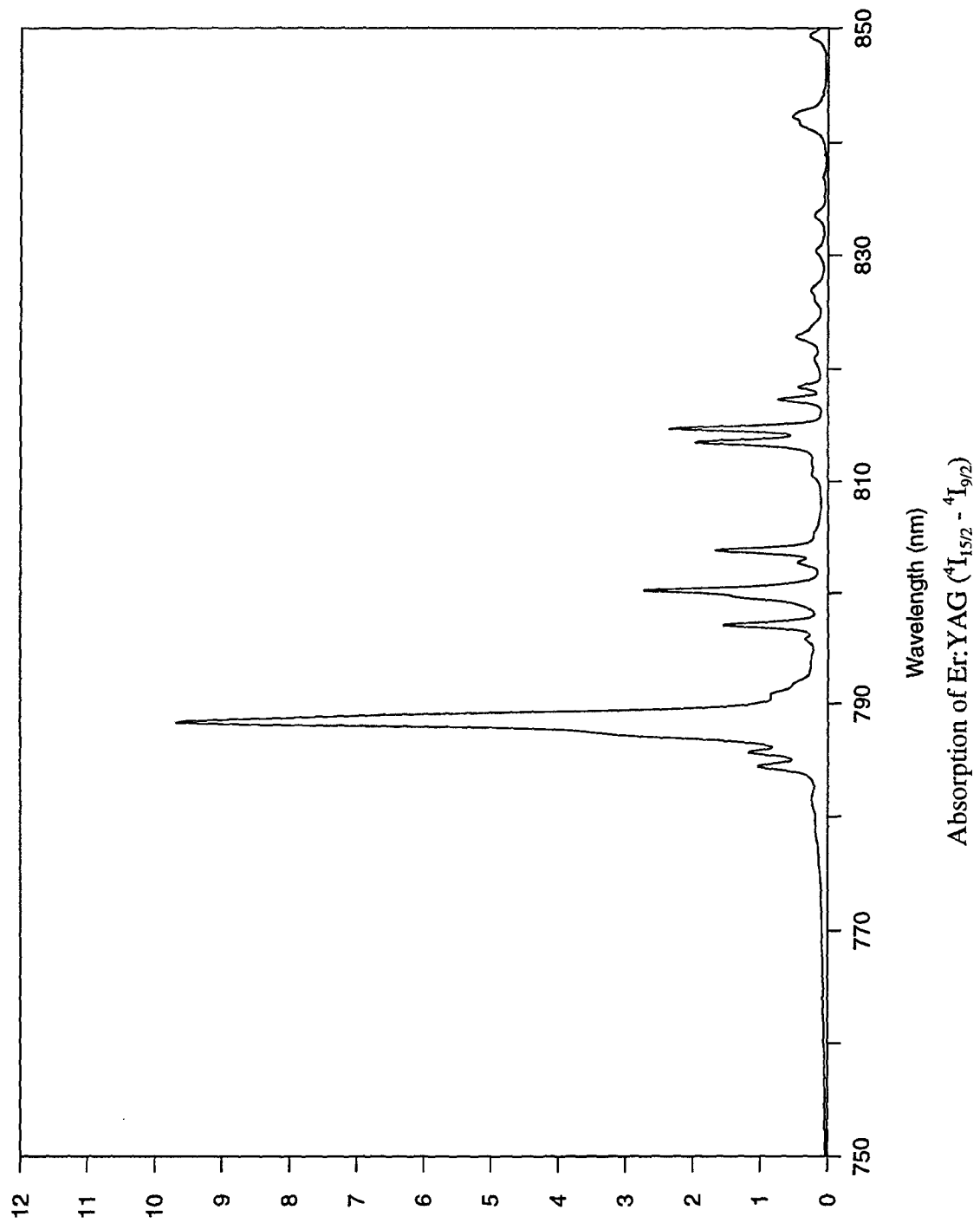


Figure 9

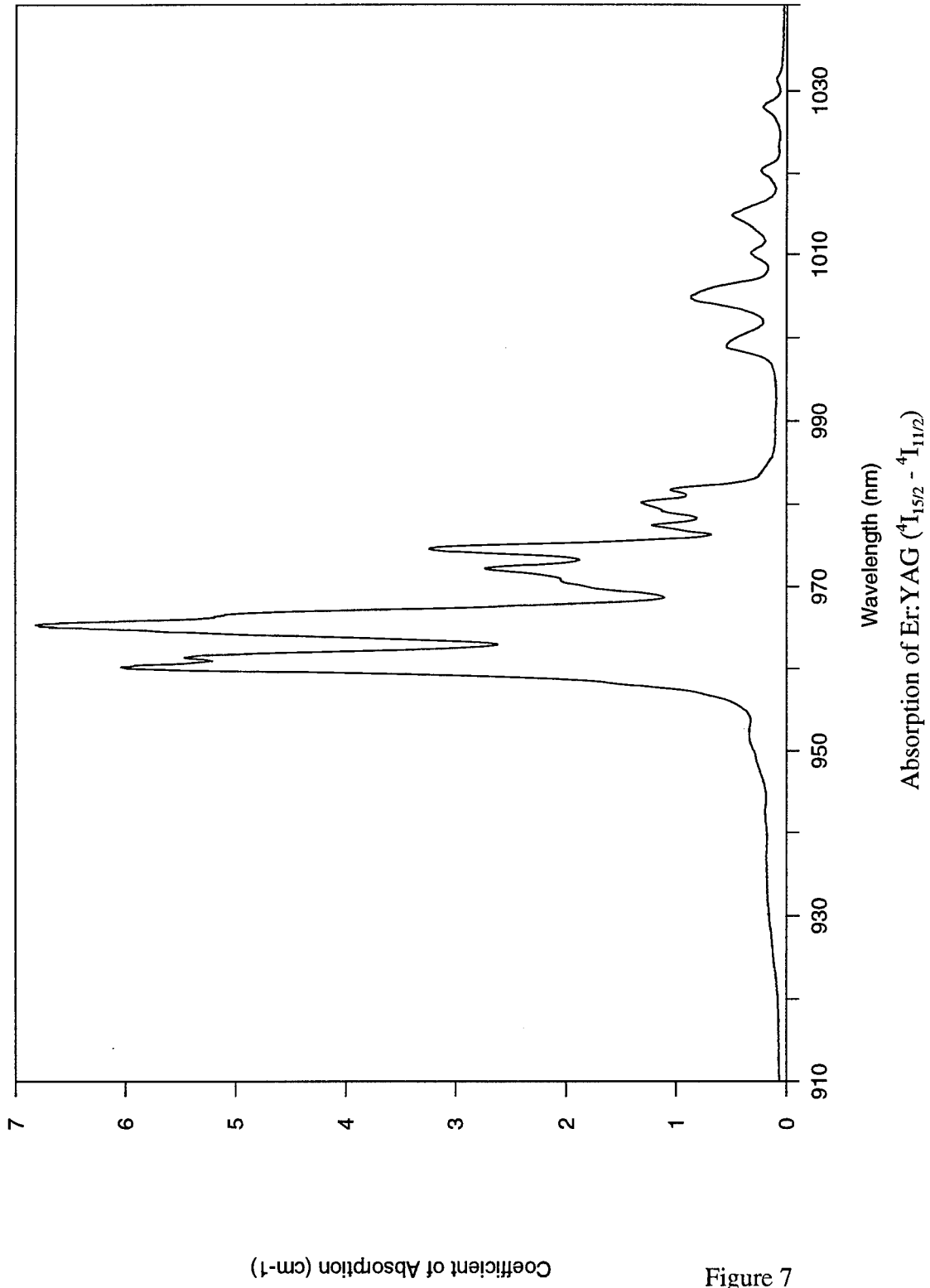


Figure 7

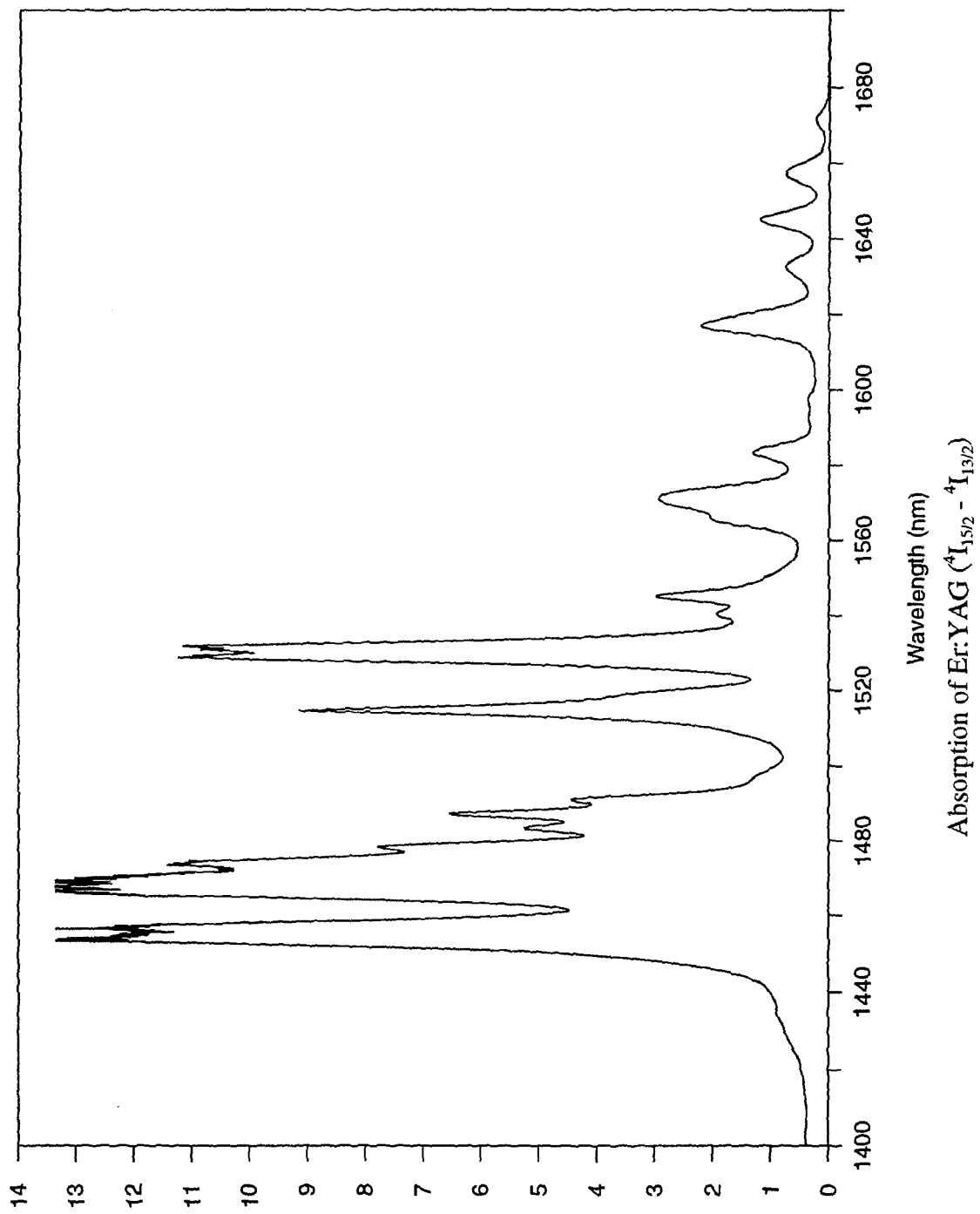


Figure 8

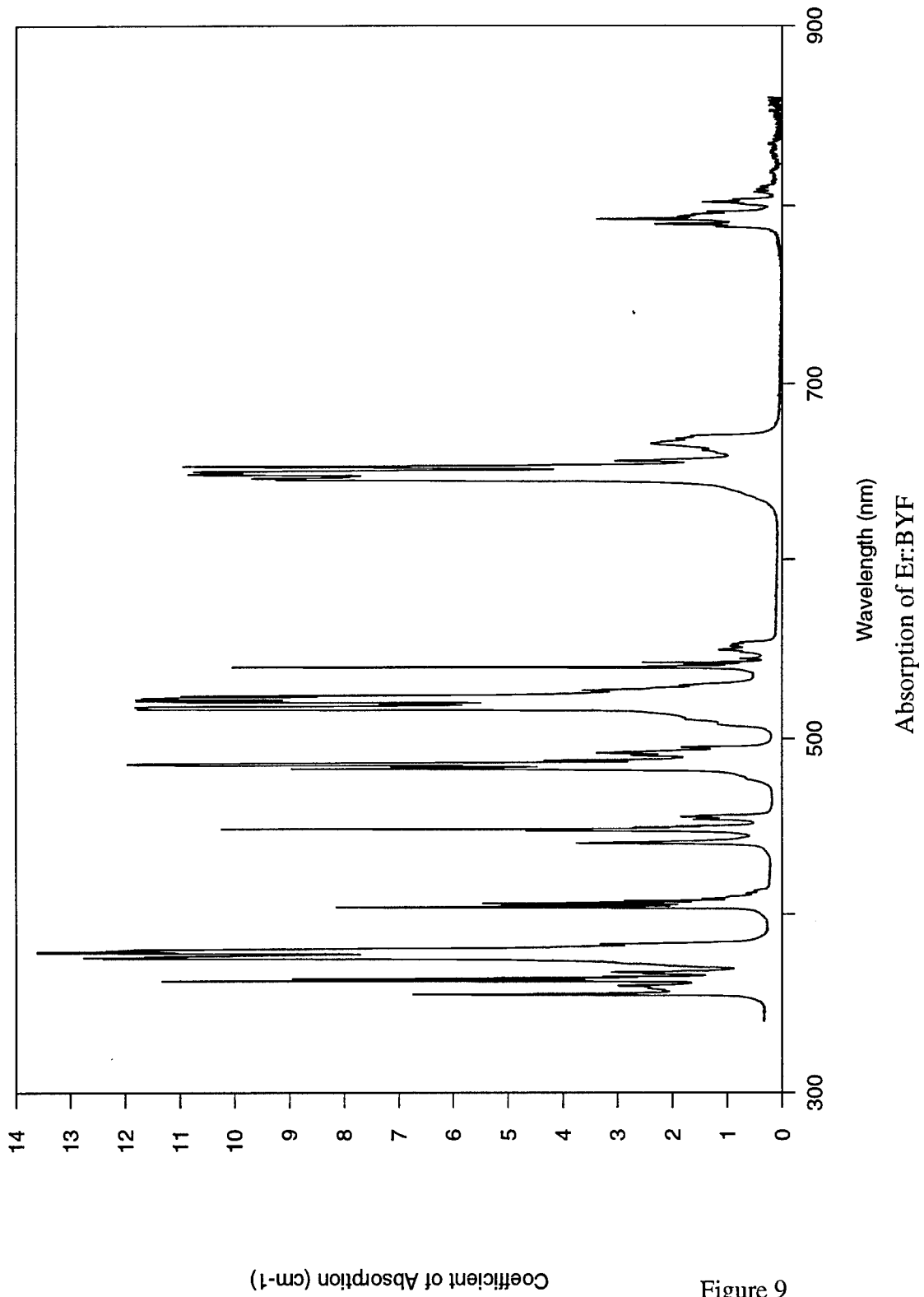


Figure 9
Coefficient of Absorption (cm⁻¹)

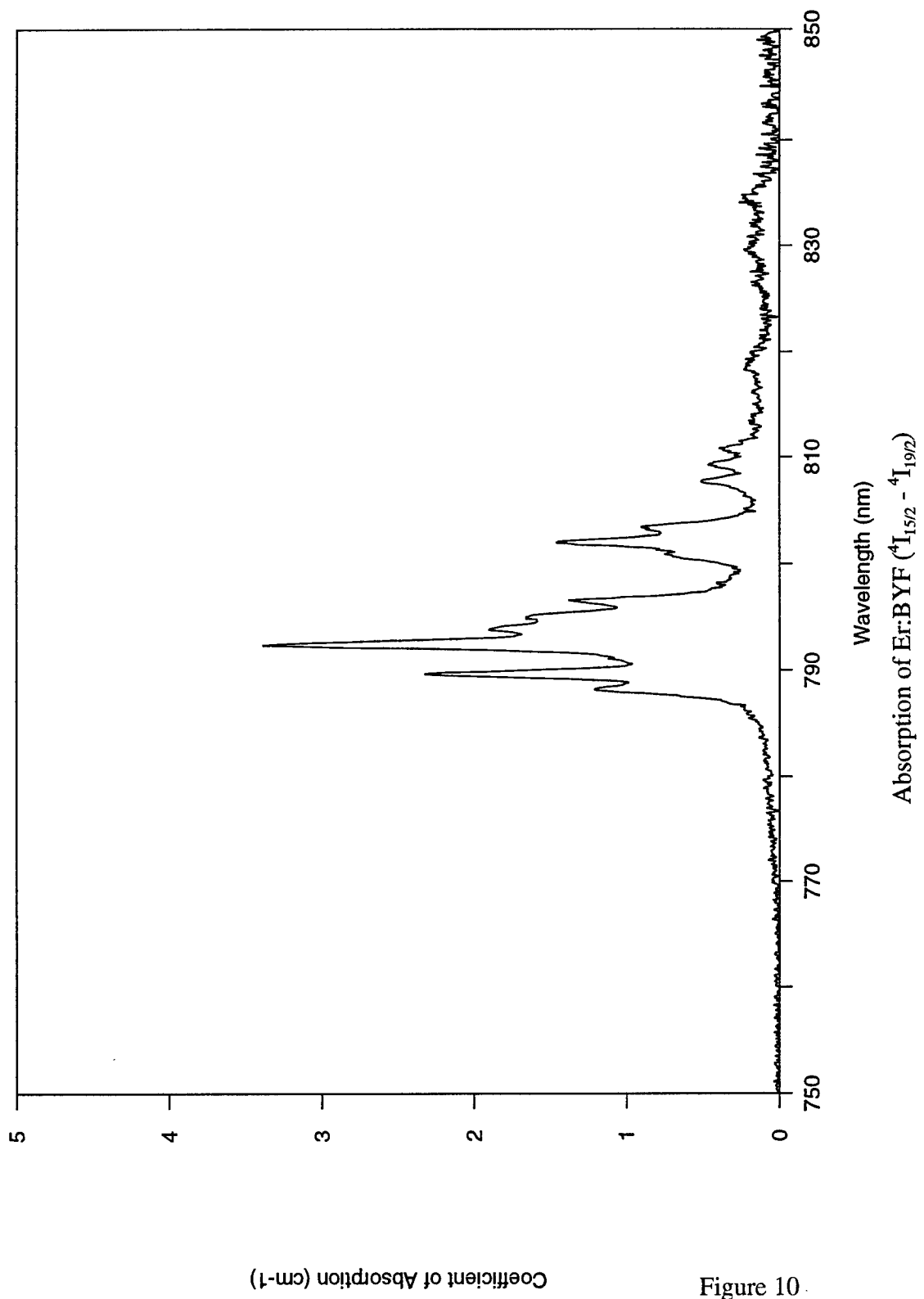


Figure 10

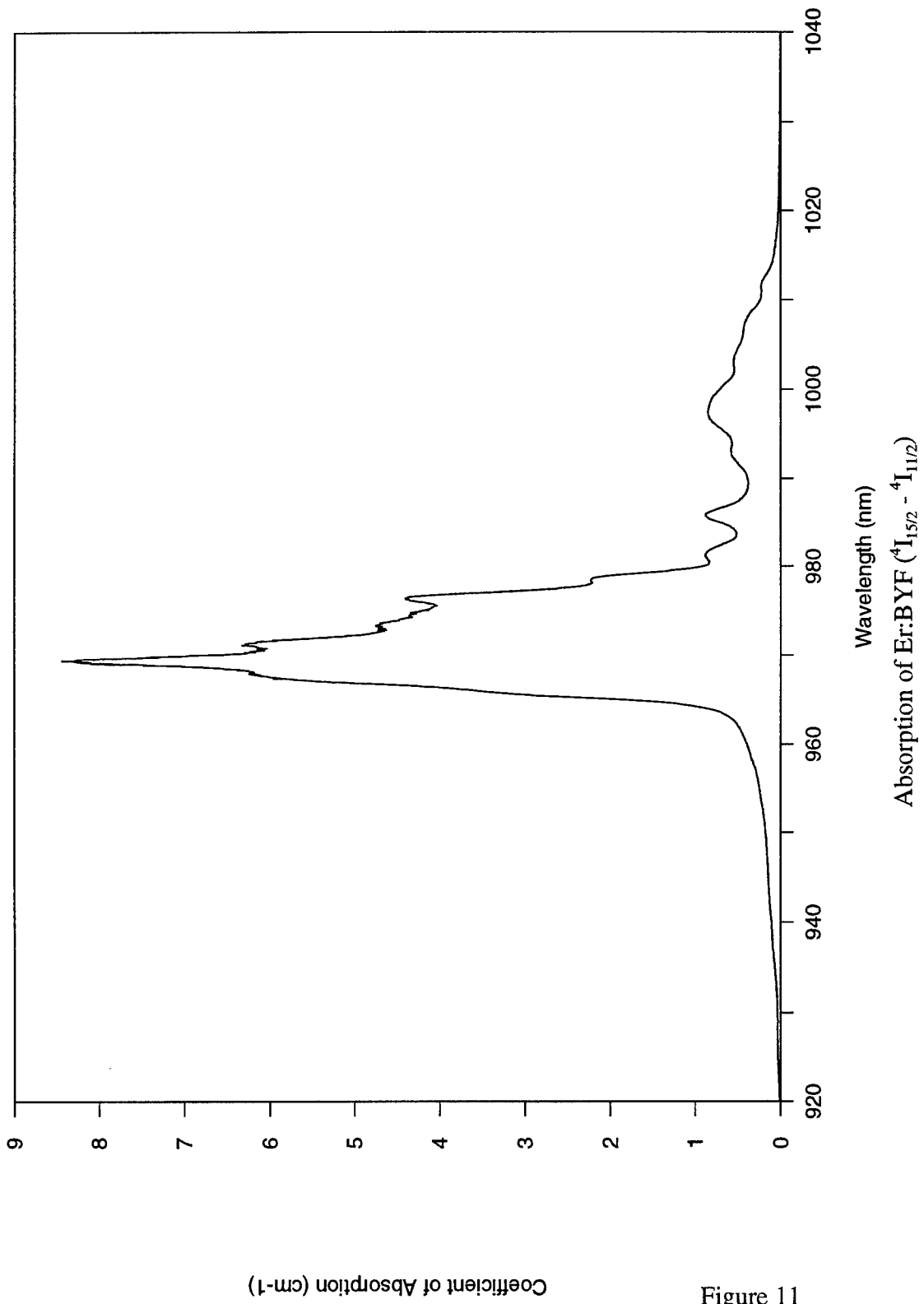


Figure 11

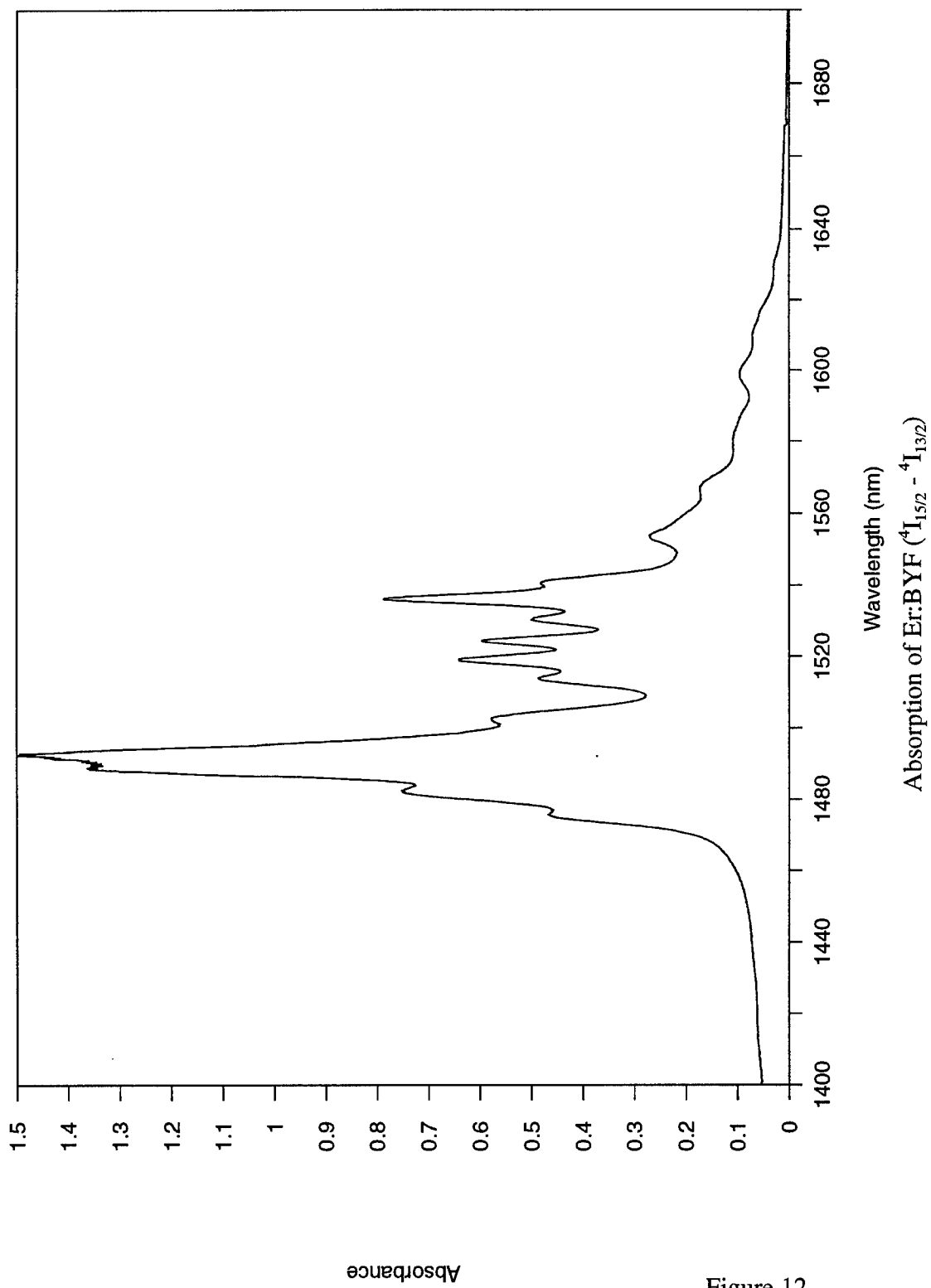


Figure 12

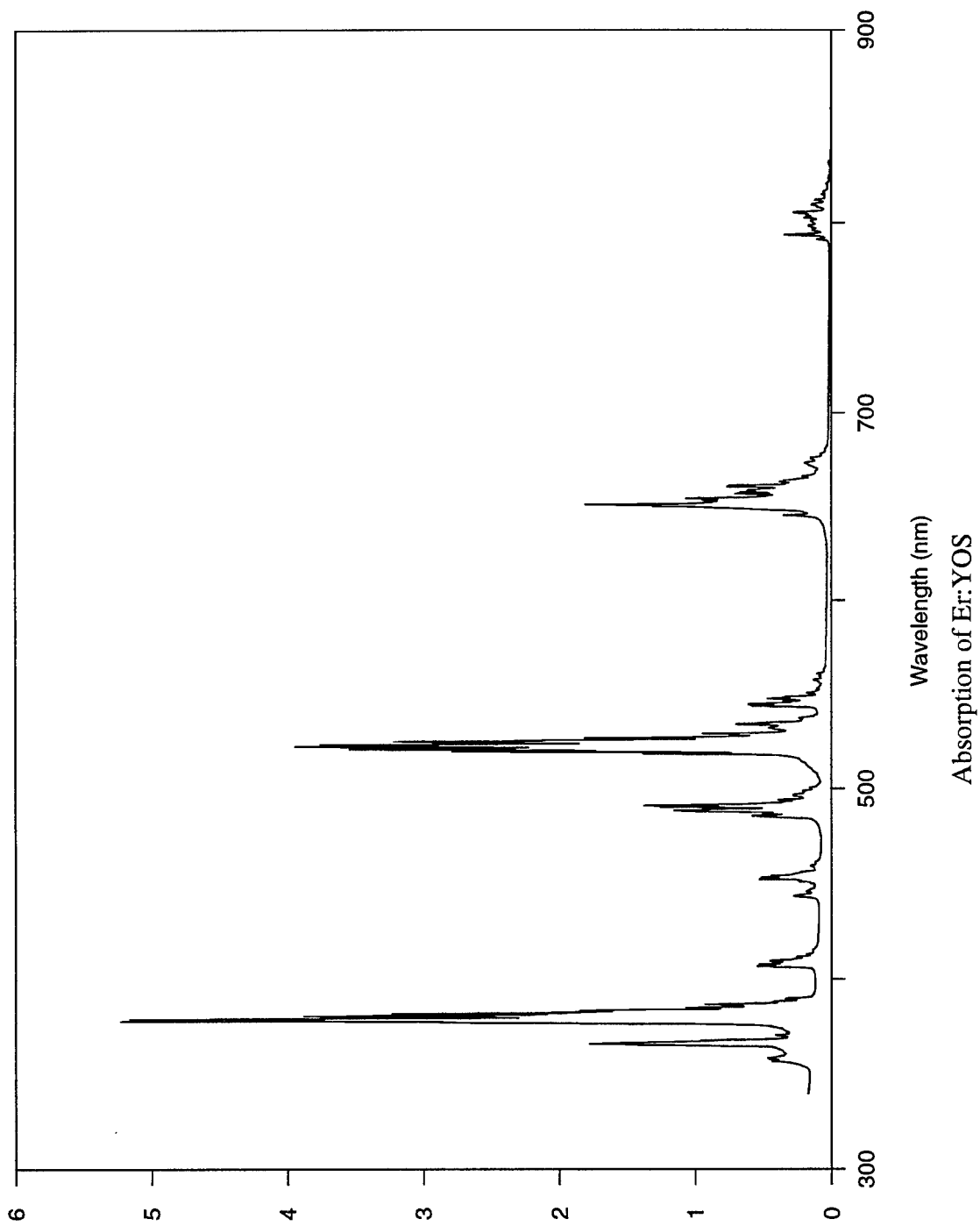


Figure 13

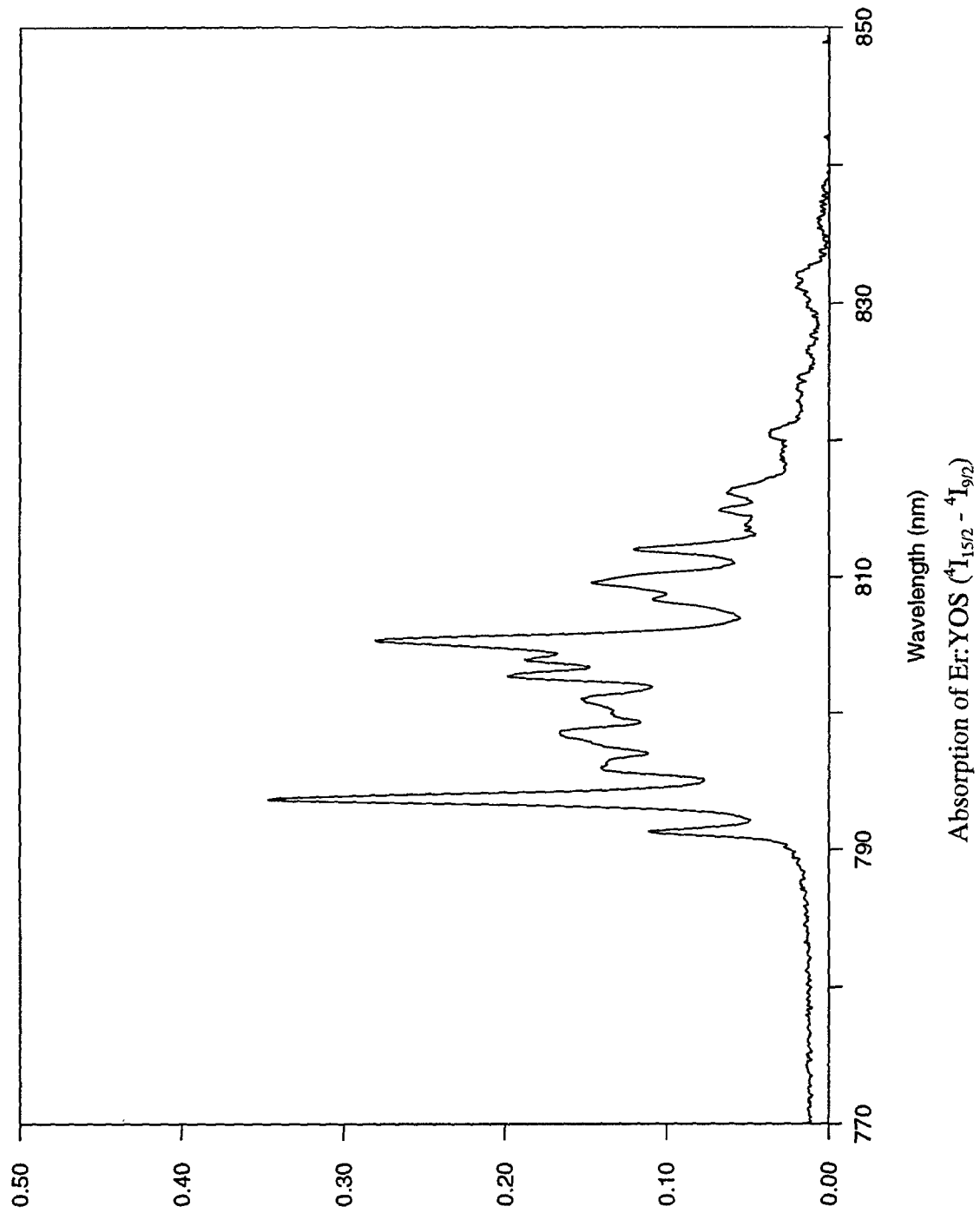


Figure 14

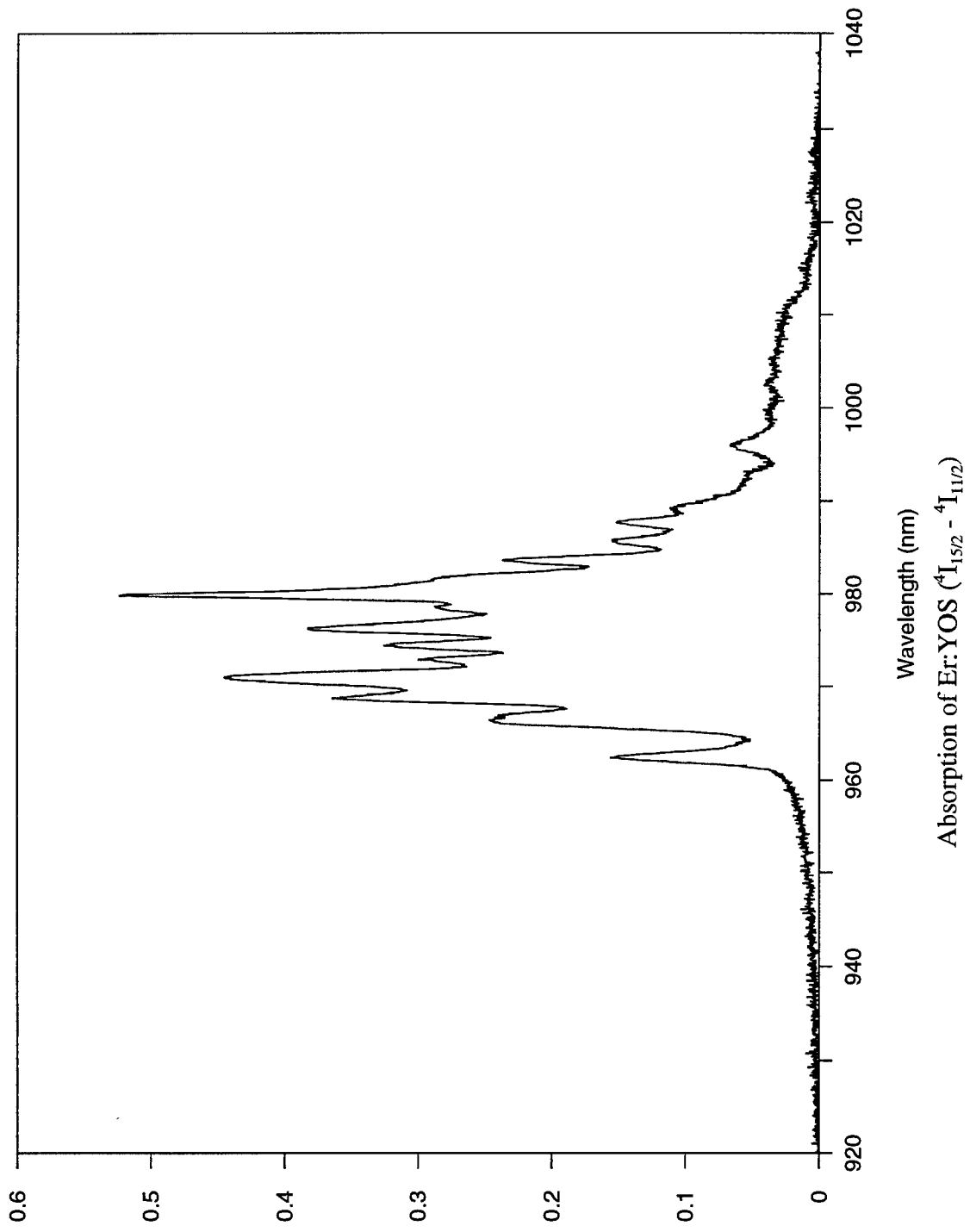


Figure 15

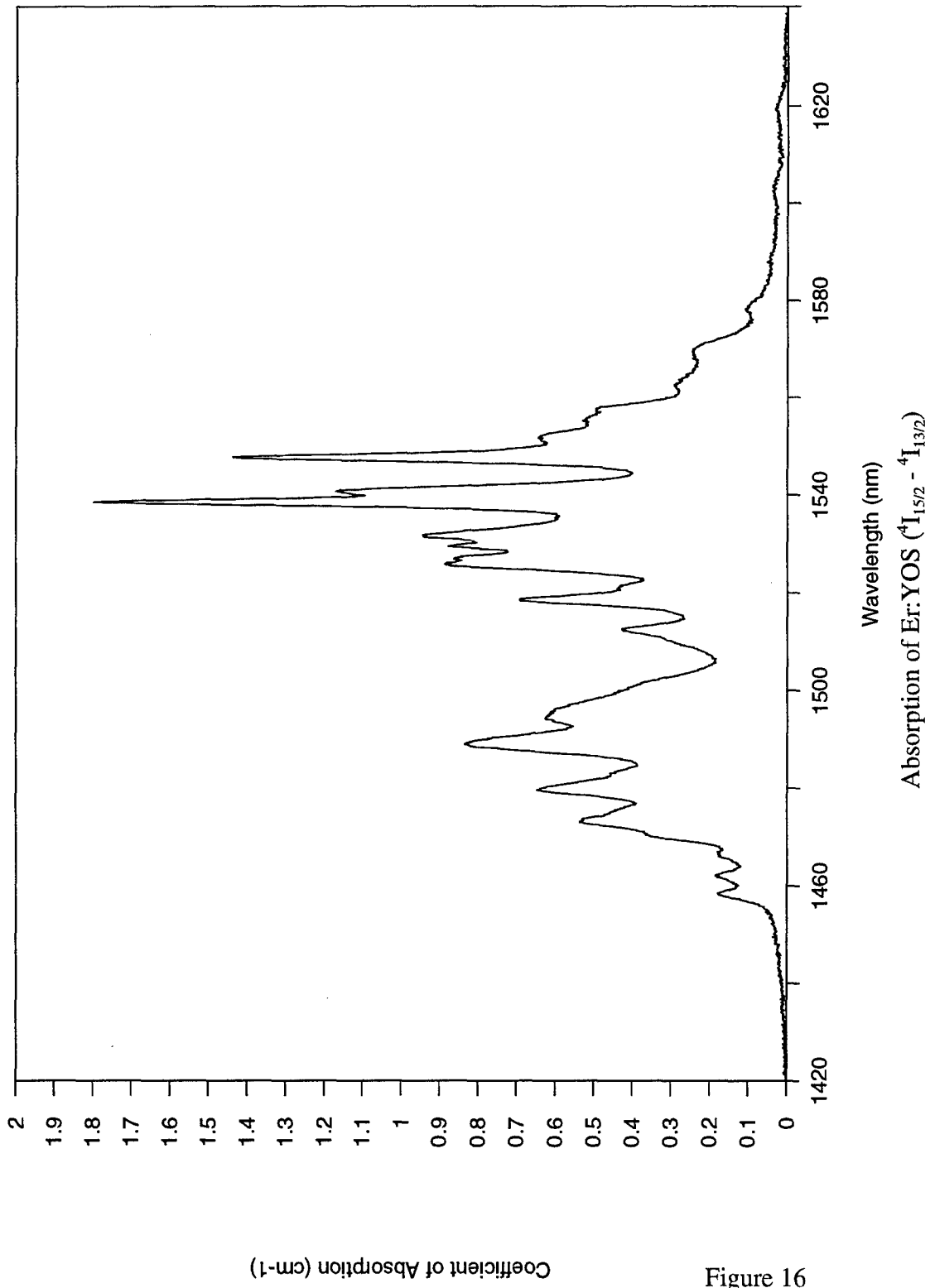


Figure 16

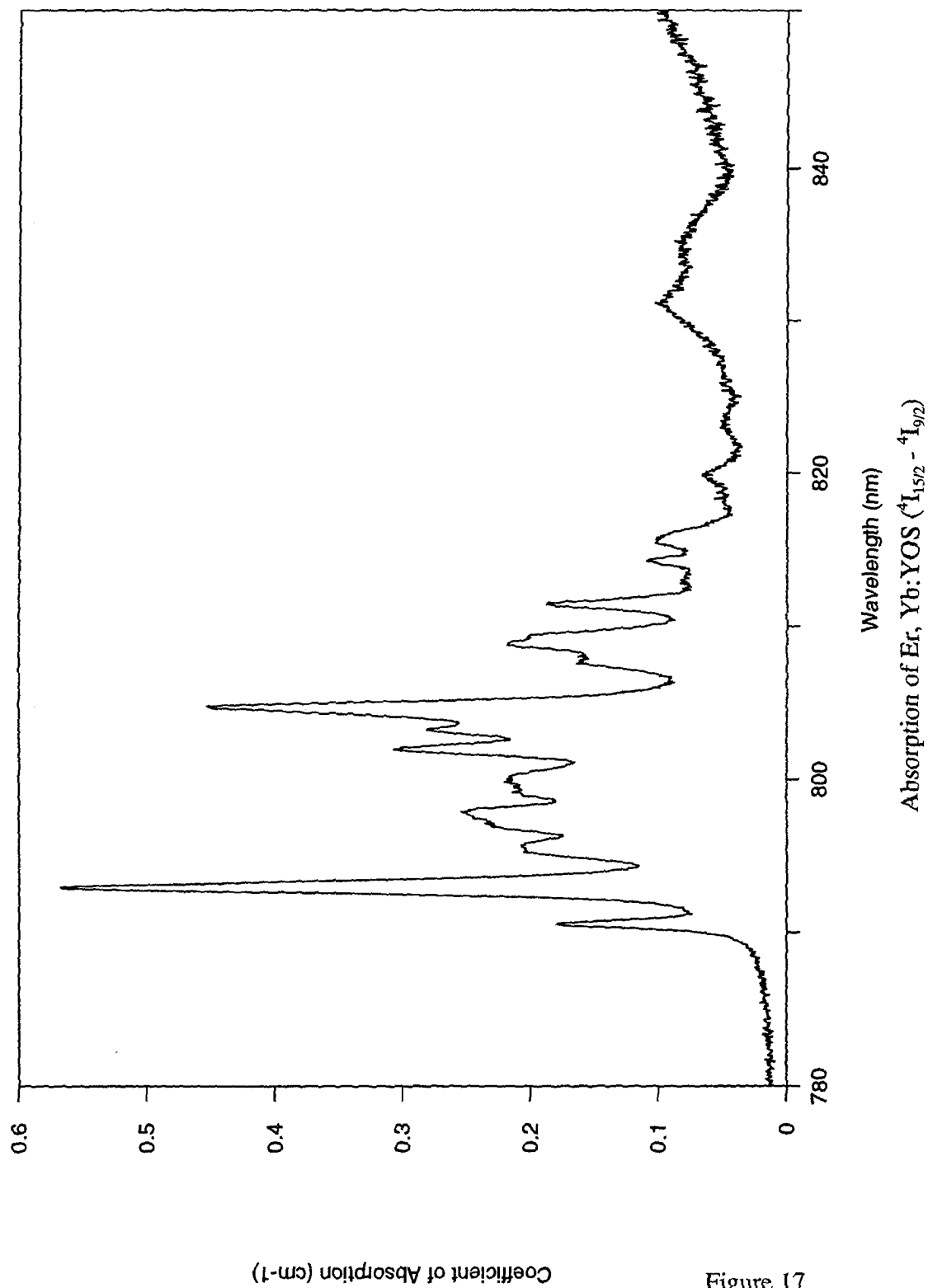
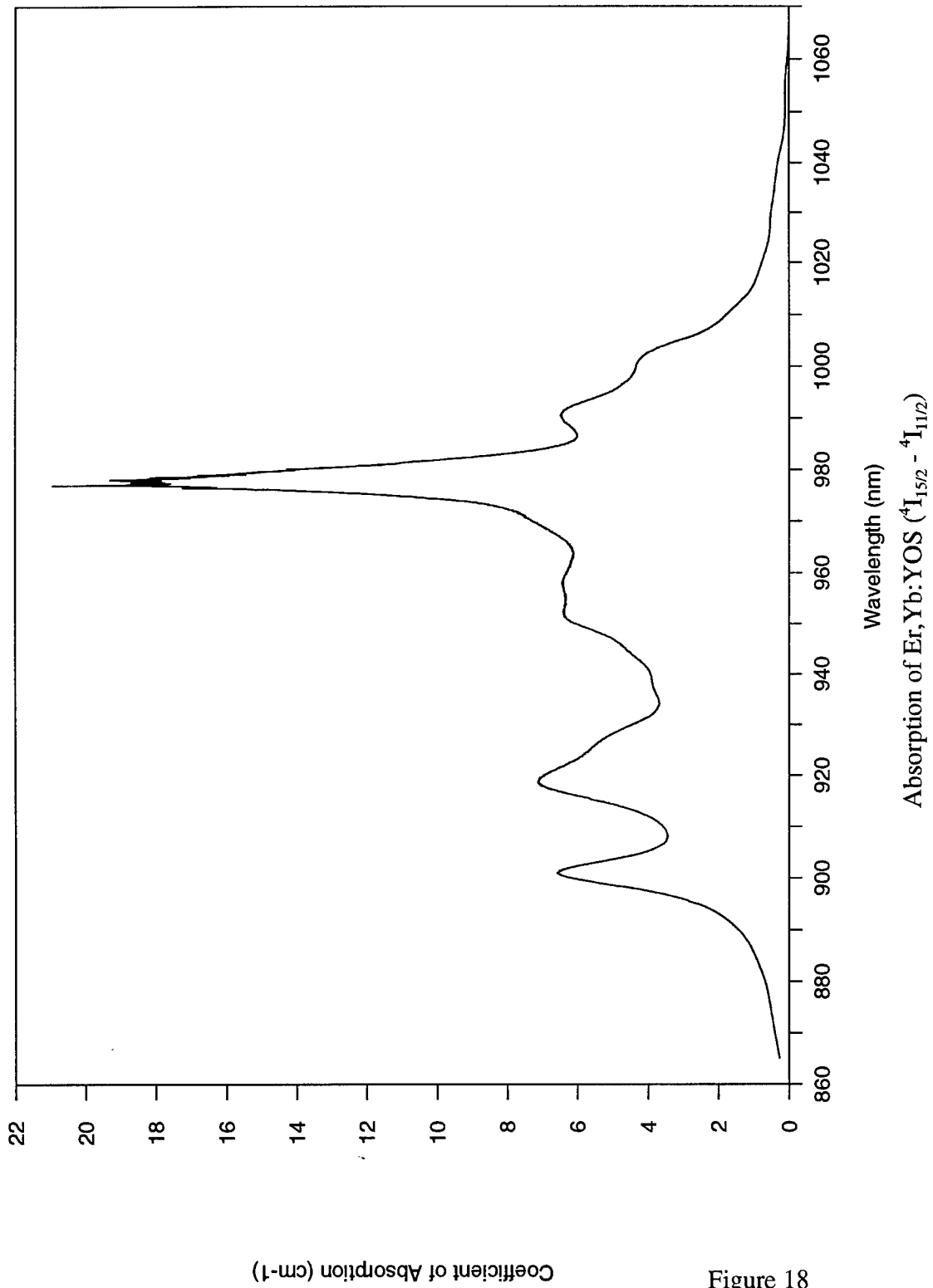


Figure 17



Coefficient of Absorption (cm⁻¹)

Figure 18

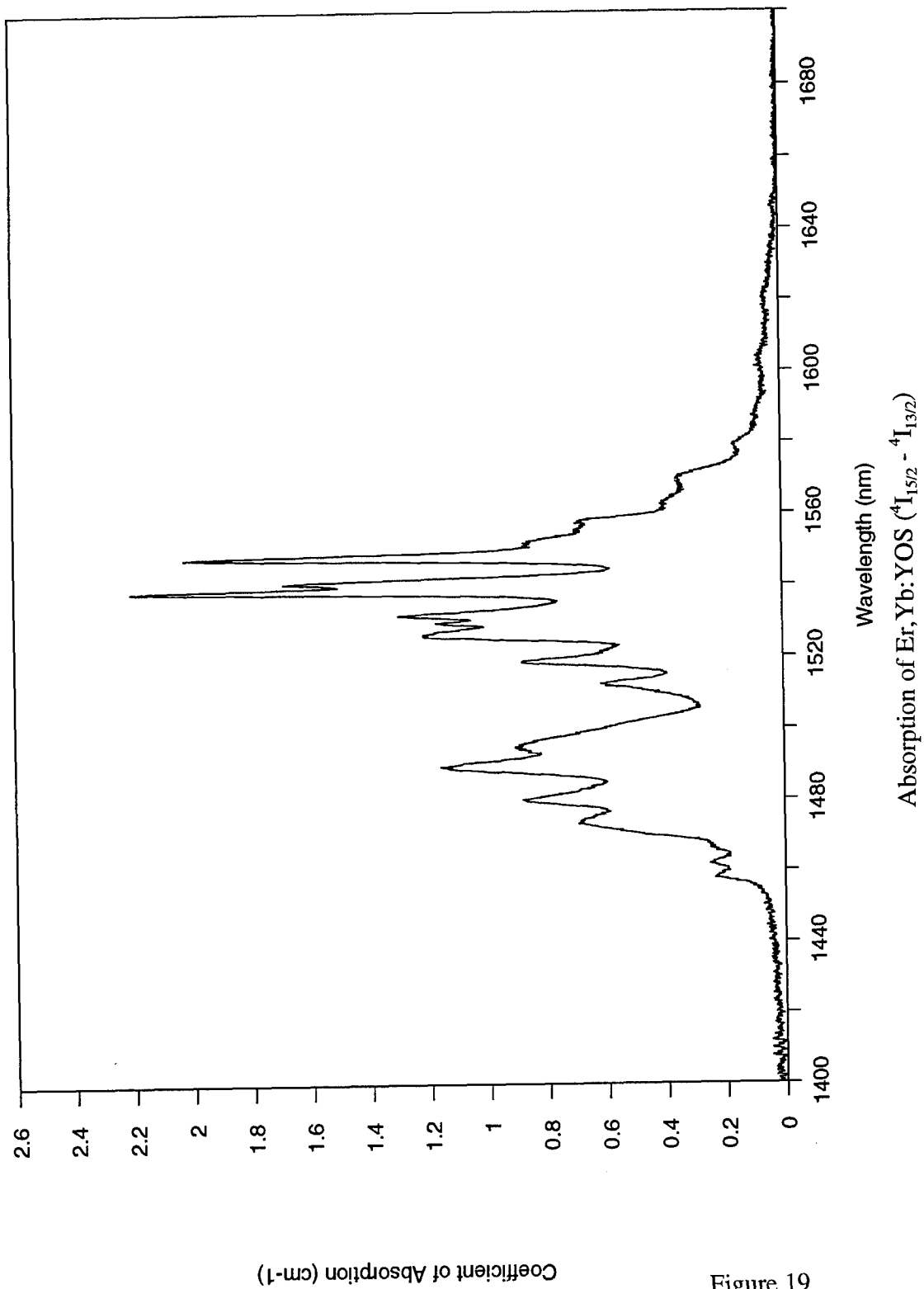


Figure 19

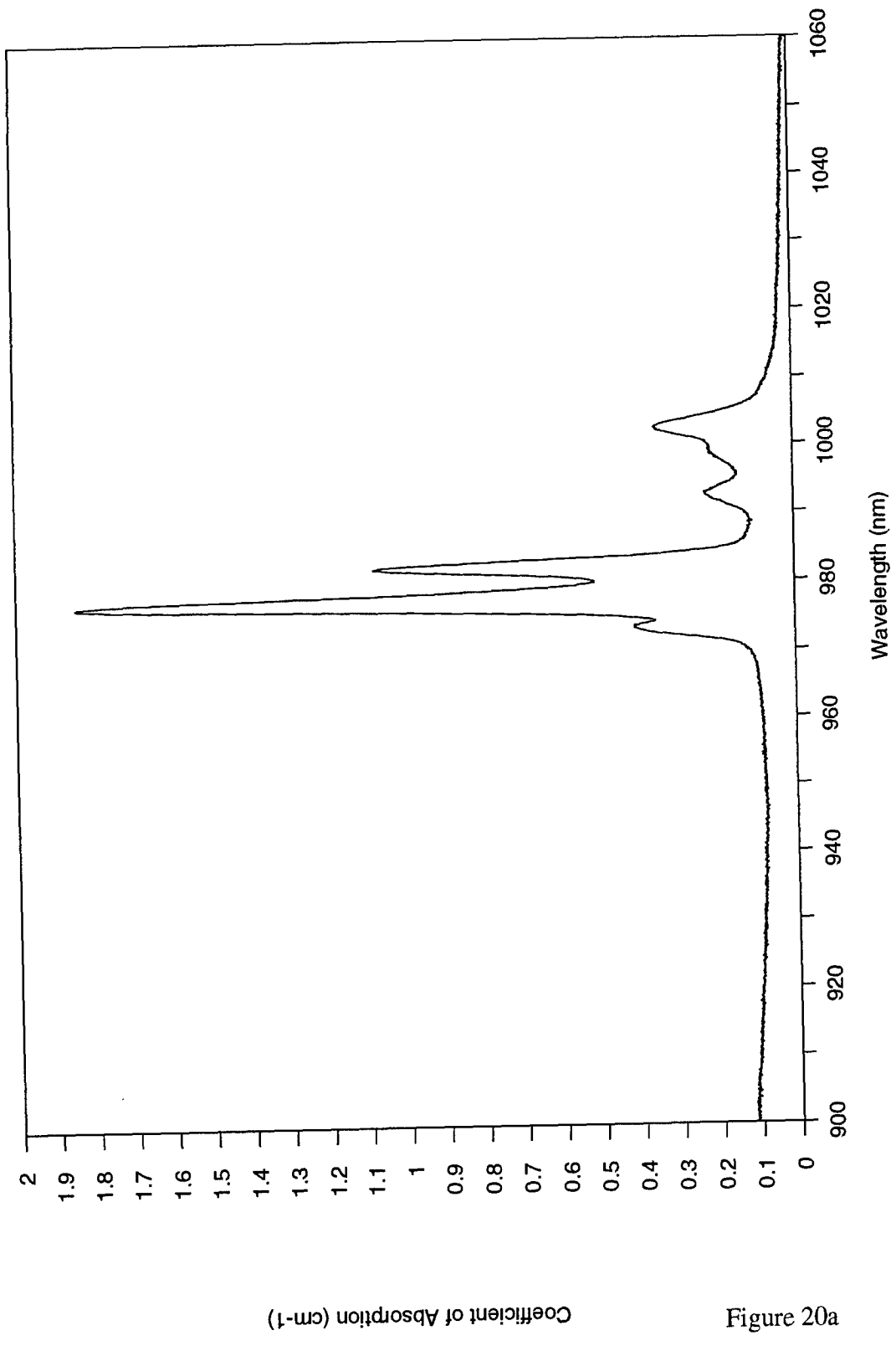


Figure 20a

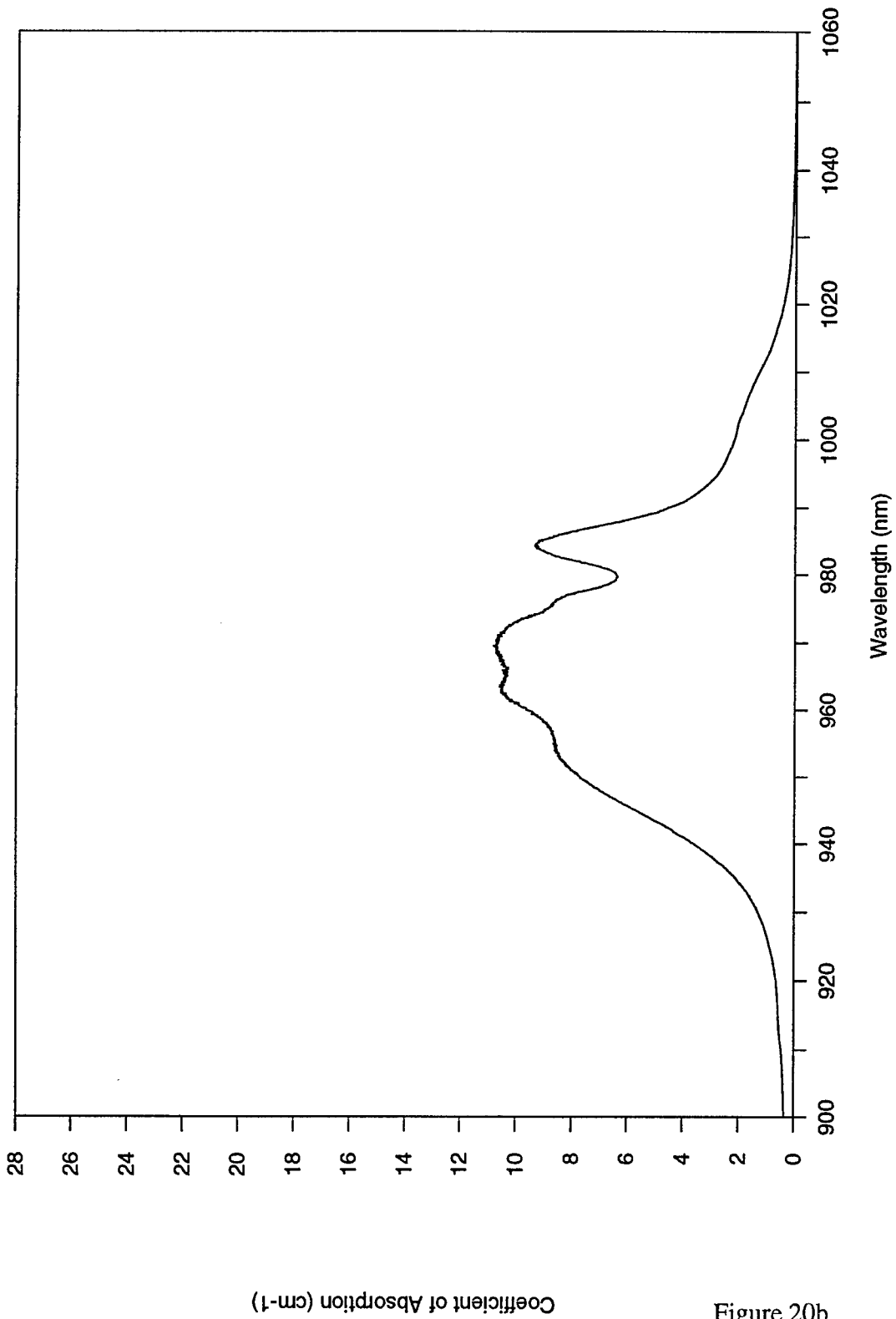
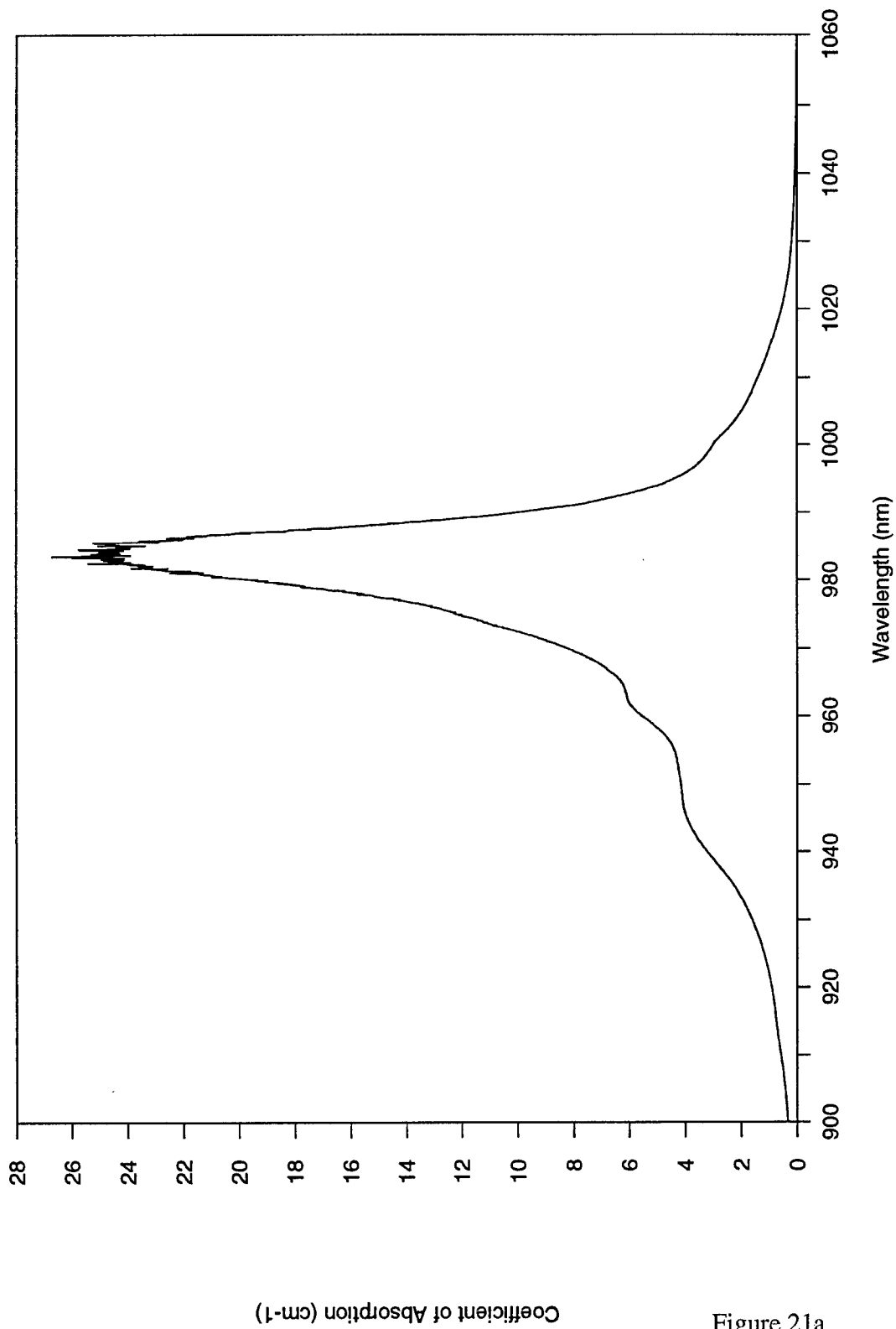


Figure 20



Pi-Polarized Absorption Spectrum of Er,Yb:YVO (0.5%, 6%)

Figure 21a

Coefficient of Absorption (cm⁻¹)

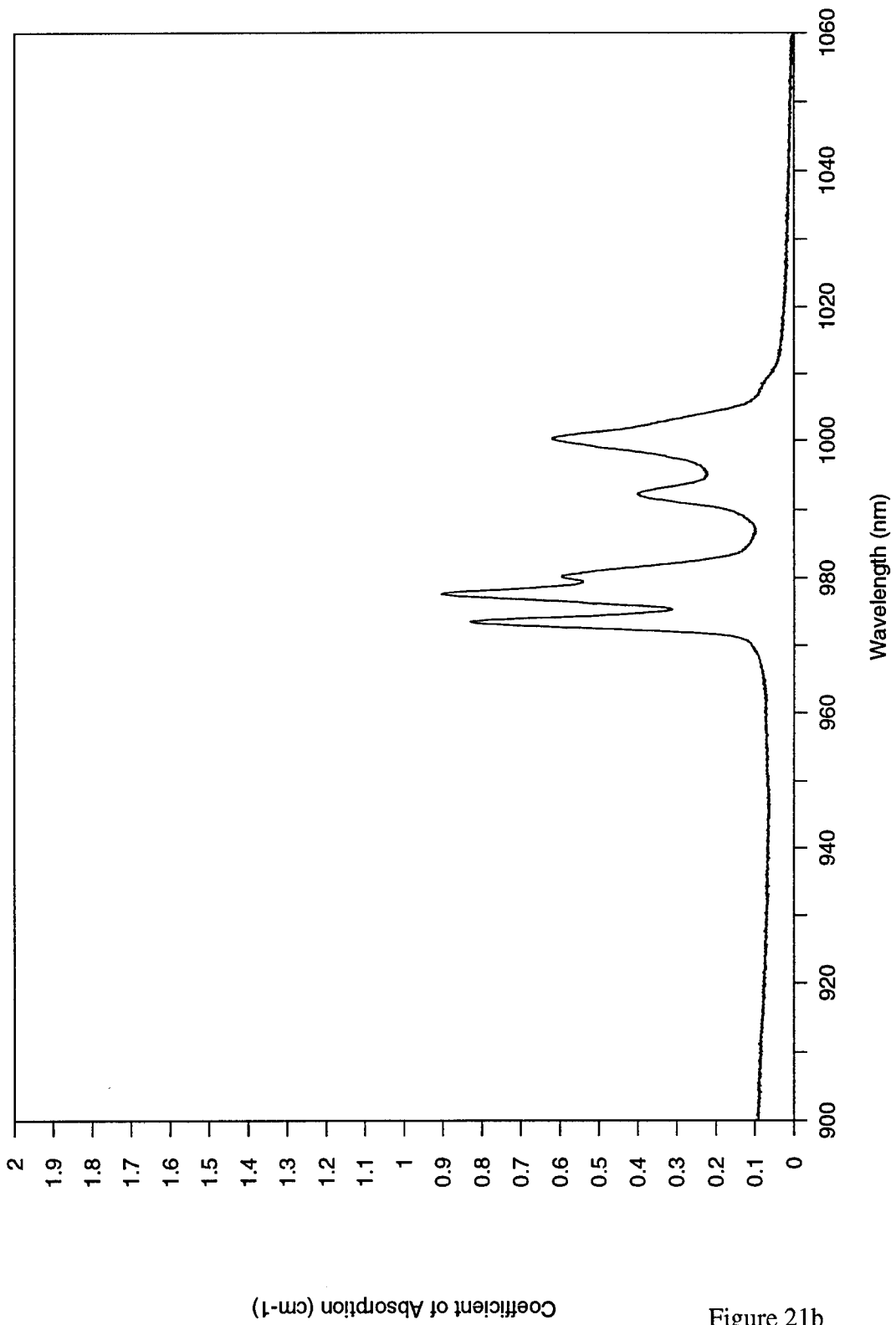


Figure 21b

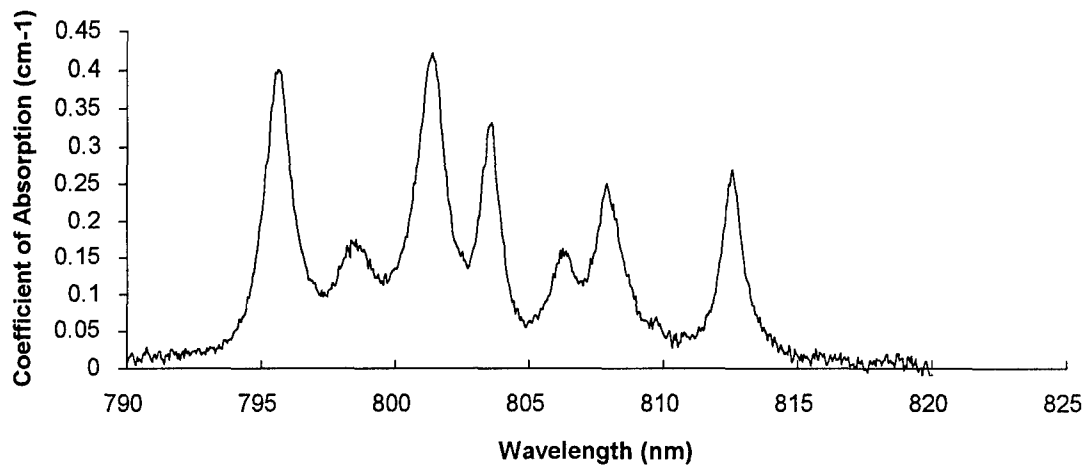


Figure 22a. Pi-polarized absorption of Er:YVO, not fully spectrally resolved

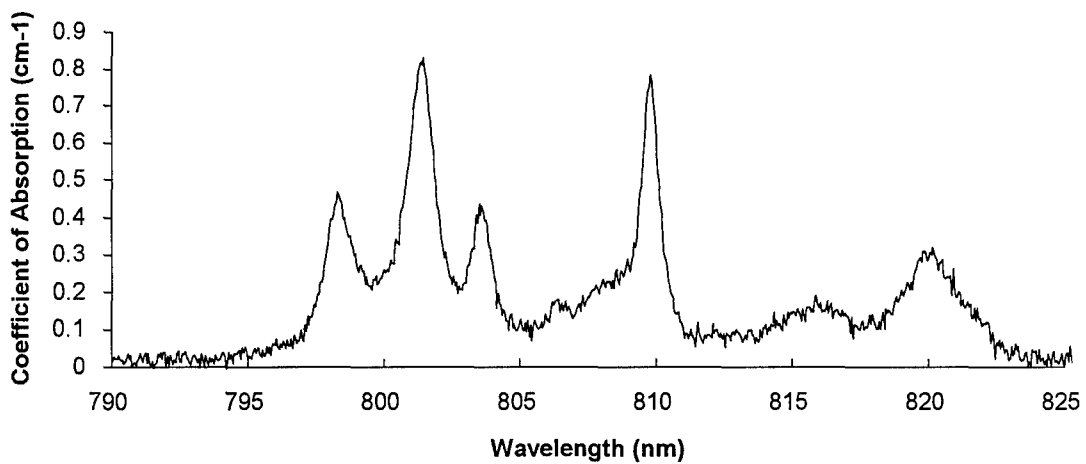


Figure 22b. Sigma-polarized absorption of Er:YVO, not fully spectrally resolved

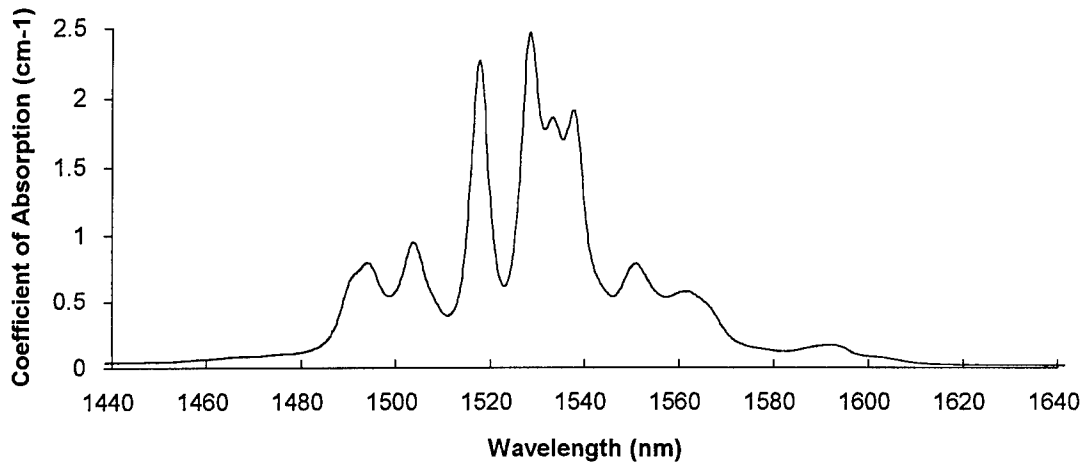


Figure 23a. Pi-polarized absorption of Er:YVO, not fully spectrally resolved

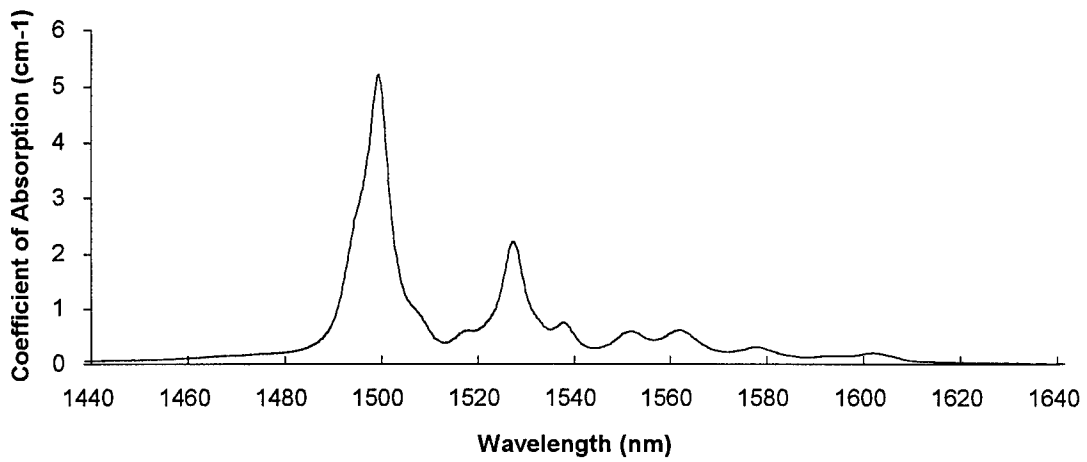


Figure 23b. Sigma-polarized absorption of Er:YVO, not fully spectrally resolved

4.2 Fluorescence

We used a ISA HR-640 grating spectrometer with appropriate gratings (1200, 600 and 300 g/mm, blazed at 1, 1.5 and 2 μm , respectively) and a dry-ice-cooled PbS detector to measure the fluorescence spectra from our samples. The samples were excited by an argon-ion laser. We calibrated the spectral response of the system with a tungsten standard lamp. For measurements in the 2.8- μm region we took care to purge the spectrometer with dry nitrogen.

In general, we observed fluorescence spectra in the 1- μm region from ${}^4\text{I}_{11/2} \rightarrow {}^4\text{I}_{15/2}$ transitions, in the 1.5- μm region from ${}^4\text{I}_{13/2} \rightarrow {}^4\text{I}_{15/2}$ transitions and in the 2.8- μm region from ${}^4\text{I}_{11/2} \rightarrow {}^4\text{I}_{13/2}$ transitions. Data on fluorescence in Er:YSGG and GGG is found on pages 36-39 of Appendix A. Figures 24, 25 and 26 show emission from Er:YAG (16%) in the three wavelength regions. Finally, in Figures 27 and 28a,b we present 1.5- μm emission from Er:YOS (1%) and Er:YVO(1%), with the latter material shown in two polarizations.

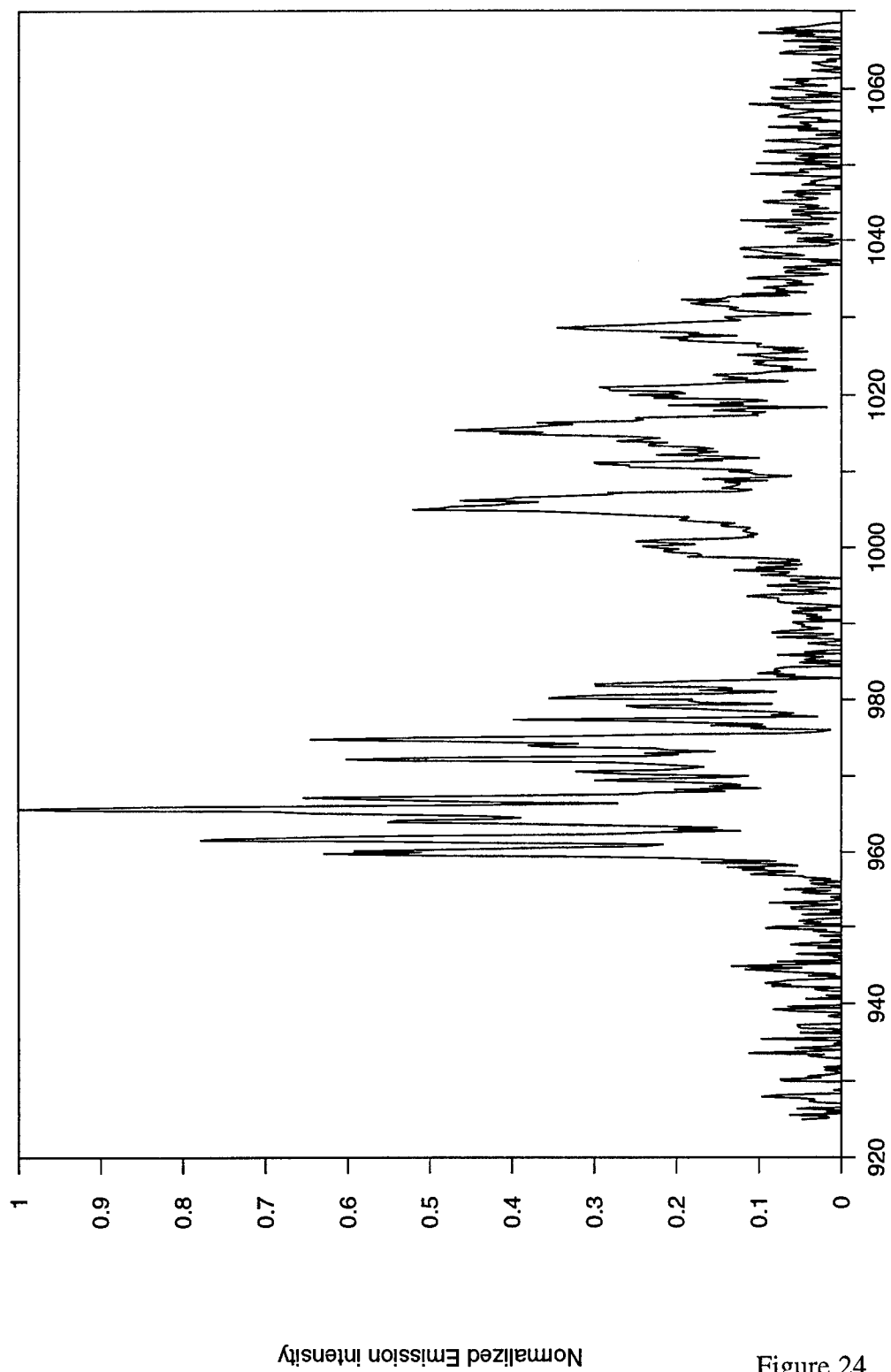
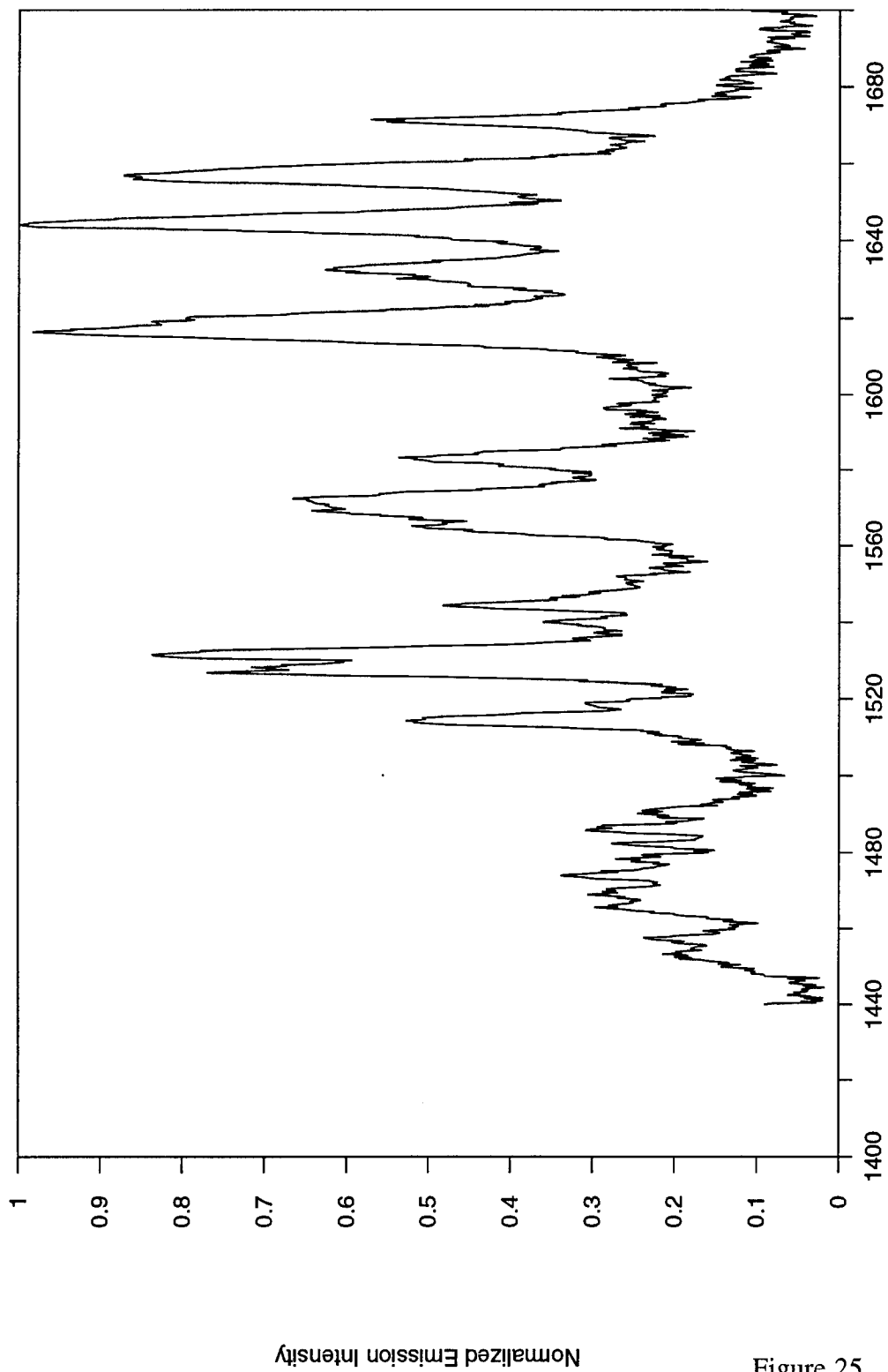
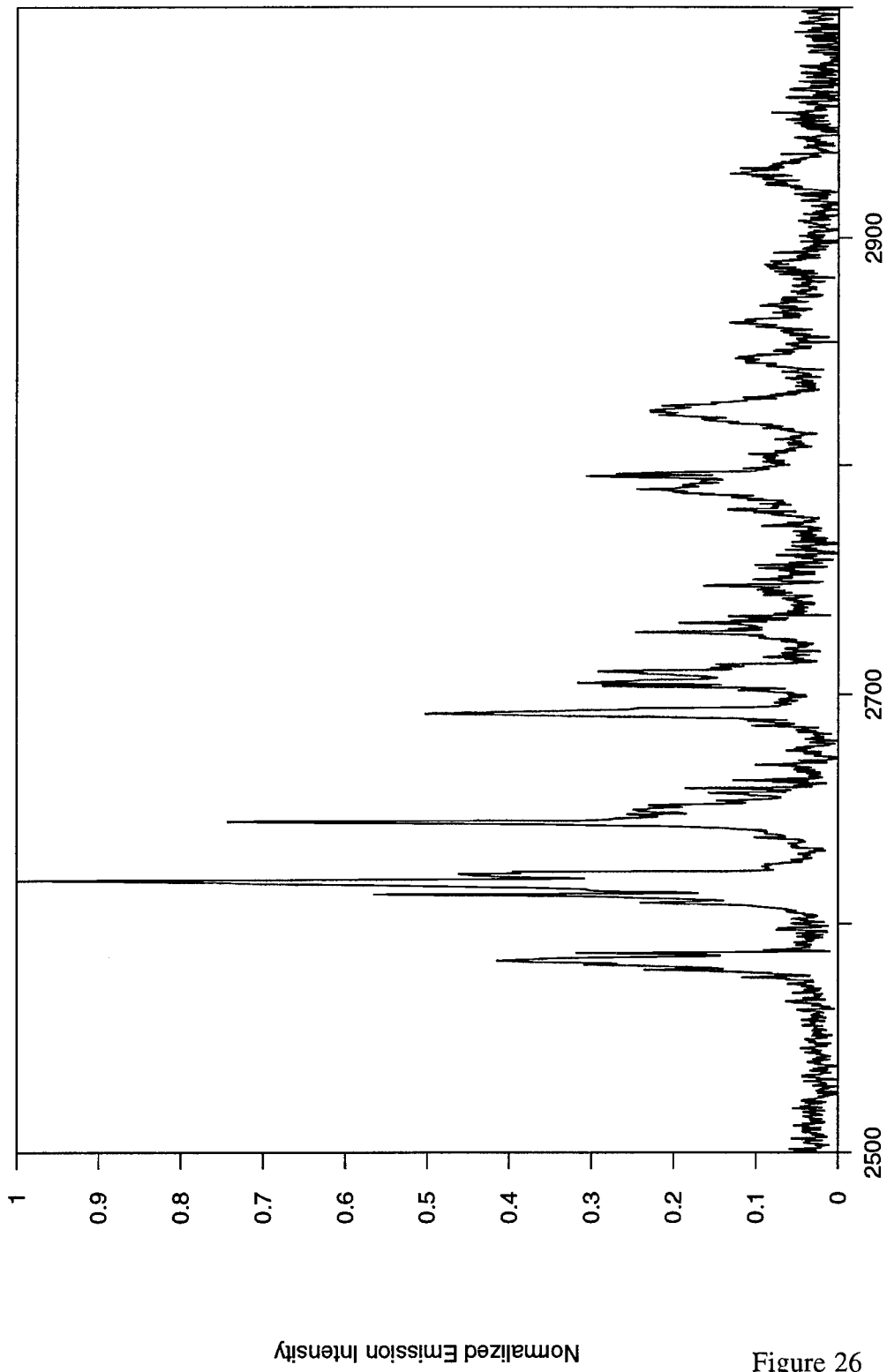


Figure 24



Normalized Emission Intensity

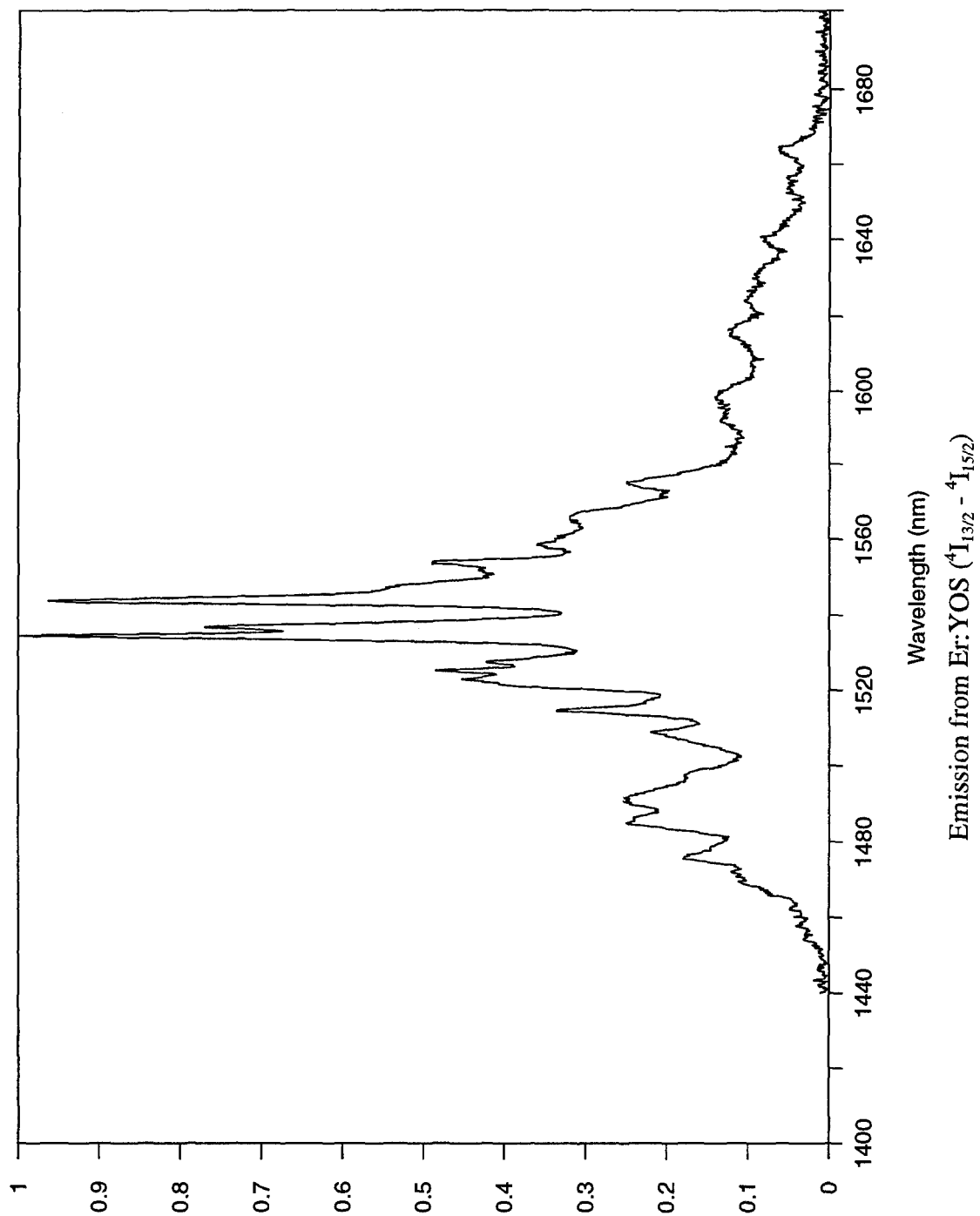
Figure 25.



Emission from Er:YAG (${}^4I_{11/2} - {}^4I_{13/2}$)

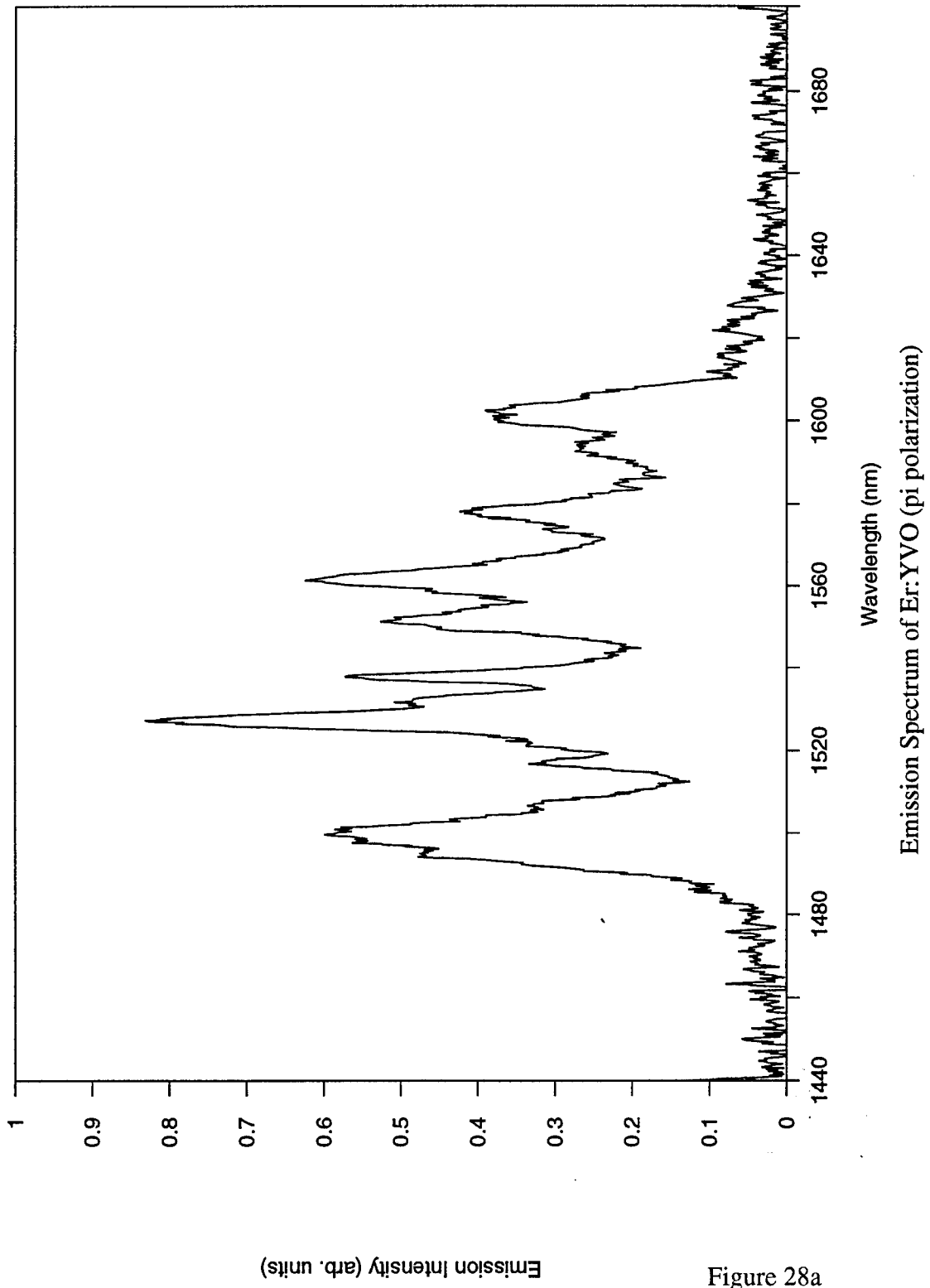
Normalized Emission Intensity

Figure 26



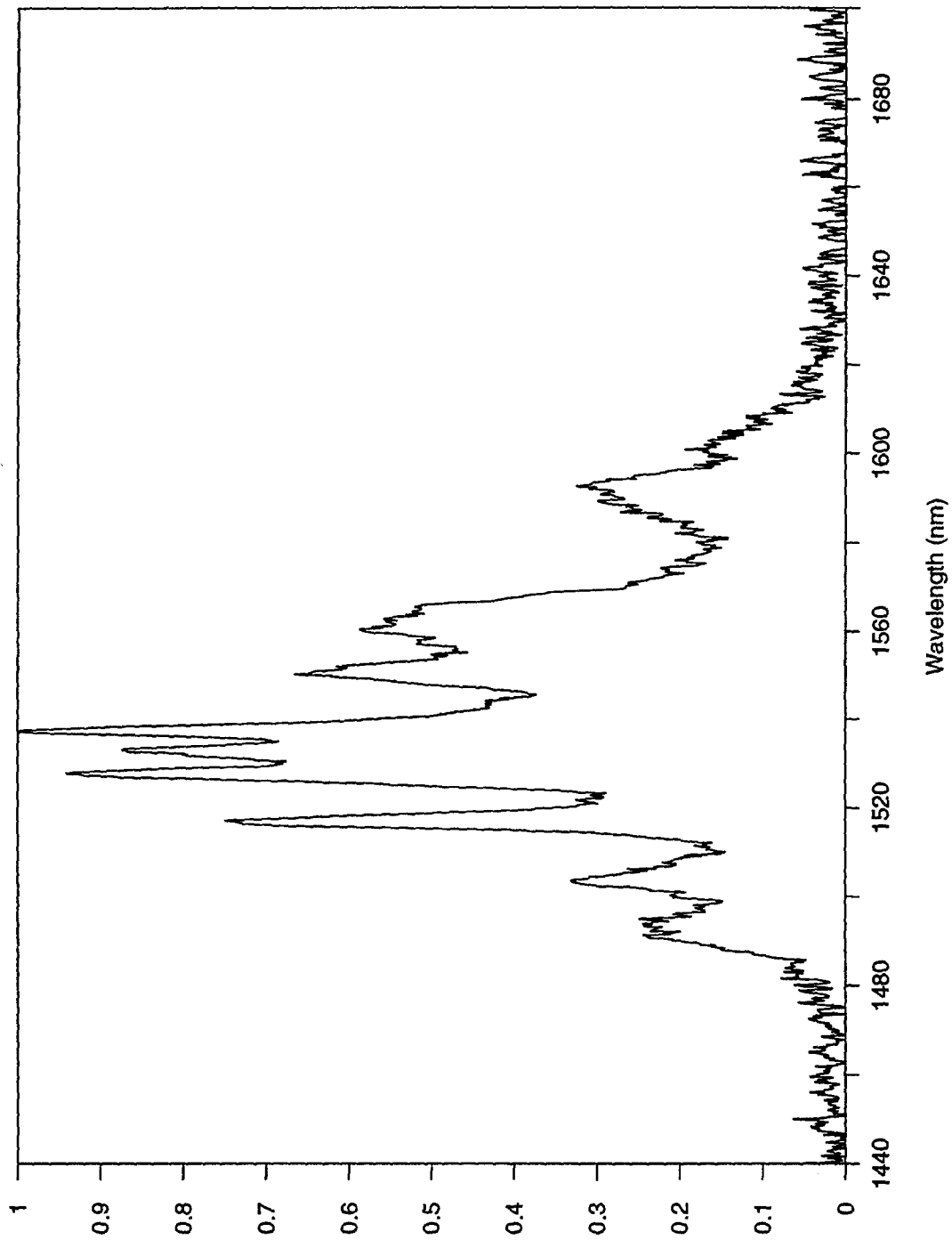
Normalized Emission Intensity

Figure 27.



Emission Intensity (arb. units)

Figure 28a



Emission Spectrum of Er:YVO (sigma polarization)

Emission Intensity (arb. units)

Figure 28b

4.3 Lifetimes

We determined the decay times of different Er states in a number of host crystals by pulsed excitation and subsequent detection and analysis of the time-varying fluorescence emission. We used a variety of laser excitation sources, including a pulsed diode laser at 970 nm, a chopped cw Ti:sapphire laser at 970 nm, a pulsed Ti:sapphire laser at 790 nm and a Q-switched, frequency doubled Nd:YAG laser at 532 nm. Decay signals near 2.8 μm , 1.5 μm , 835 nm and 557 nm provided data on lifetimes of the $^4I_{11/2}$, $^4I_{13/2}$, $^4I_{9/2}$ and $^4S_{3/2}$ states. Figure 29 shows the typical geometry and instrumentation used for the decay-measurement experiments, while Figure 30 is an example of the actual decay signal and Figure 31 shows the signal analyzed on a semi-log plot.

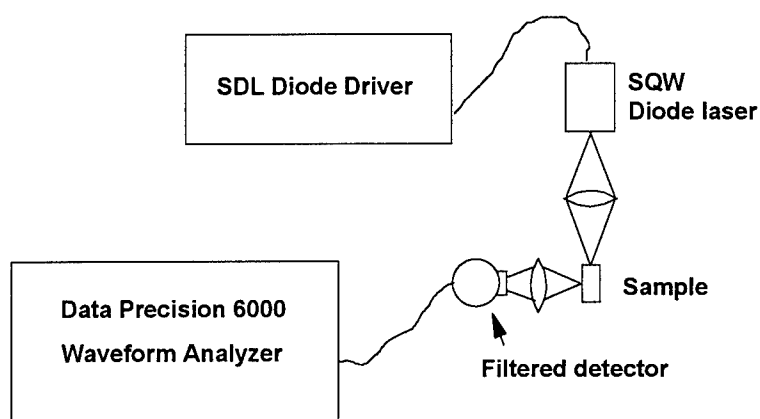


Figure 29. Experimental setup for some decay measurements. Others employed different excitation sources.

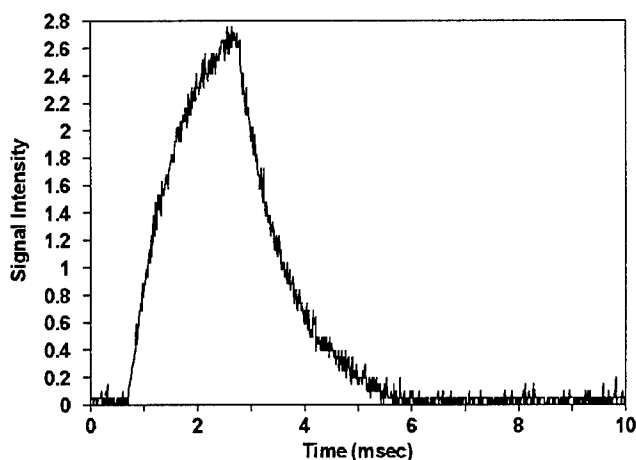


Figure 30. Sample decay signal from Er:GGG fluorescence at 2.8 μm , excited by 970-nm pulsed diode laser.

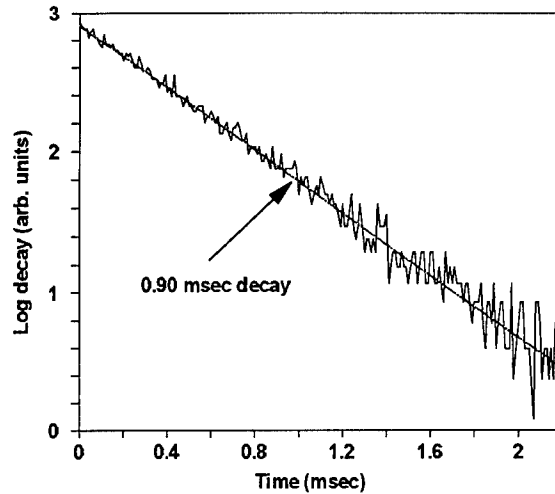


Figure 31. Log plot of decay signal in Figure 30, with preliminary fit.

The Table below summarizes our decay time measurements for the different Er states, as a function of host crystal and, in some cases, doping level. We suspect that the reduction in Er:GGG and Er:YSGG lifetimes for the $^4I_{11/2}$ and $^4I_{13/2}$ levels may be due to other rare-earth impurities, but that issue requires further study. The last column is the ratio of lifetimes for the lower and upper levels for the 2.8- μm laser transition. In the absence of other processes, the larger the ratio, the more difficulty one might experience in getting efficient, low-threshold laser operation in the 2.8- μm transition. As we show later, the ratio is in fact a poor criterion for choosing a good 2.8- μm laser, since processes such as cross relaxation and upconversion play a significant role in the laser process.

Additional discussion of the decay-time measurements appears in pages 25 and following in Appendix A.

Table 3. Summary of decay times for different materials.

Material	$^4S_{3/2}$ (μsec)	$^4I_{9/2}$ (μsec)	$^4I_{11/2}$ (msec)	$^4I_{13/2}$ (msec)	$^4I_{13/2} /$ $^4I_{11/2}$
Er:GGG (30%)	0.68	1.90	0.96	4.86	5.1
Er:GGG (10%)	5.12	3.98	0.99	10.2	10.3
Er:GGG (1%)	118.7	4.57	1.10	13.6	12.3
Er:YSGG (30%)	1.16	1.32	1.3	3.4	2.6
Er:YSGG (1%)	120.2	2.78	1.43	9.52	6.7
Er:BYF (20%)	8.20	9.1	3.74	6.67	1.78
Er:YLF (20%)	6.21	5.94	3.8	10.8	2.8
Er:YAG (33%)	0.5	0.63	0.12	7.25	60.4
Er:YOS (1%)	--	--	0.043	12.7	295
Er:YVO(1%)	--	--	0.057	6.2	109

5. Nonlinear Spectroscopy

5.1 Excited-state Absorption, Upconversion and Cross Relaxation

One of our major initial concerns in the effort was the choice of pump wavelength to use with the diode-laser source. Figure 32 shows the energy levels of the Er ion along with upward arrows, the length of which correspond to pump energy at either 790 or 970 nm. (The downward arrow shows the 2.8- μm laser transition.) Both pump wavelengths can clearly induce transitions (excited-state absorption, or ESA) from the two states, $^4I_{11/2}$ and $^4I_{13/2}$, involved in Er laser operation. These transitions serve to rob useful pump energy away by promoting the Er ions to higher-lying states. Some of the excitation falls back to the initial state, but there are inevitable losses involved in the process. The only excited-state transition that looks improbable involves a 970-nm pump originating on the $^4I_{13/2}$ level.

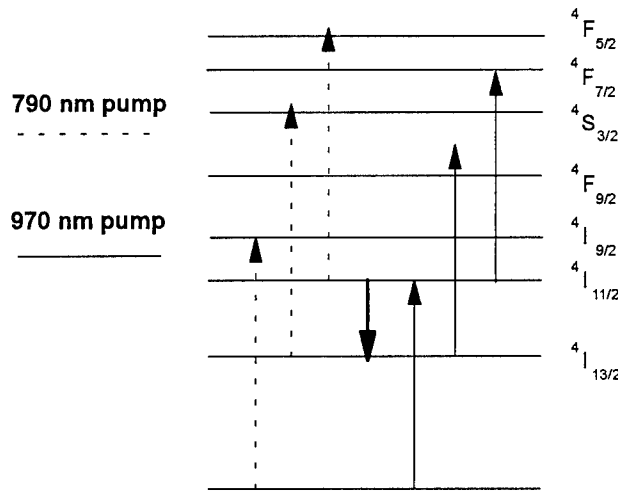


Figure 32. Possible transitions for excited-state absorption of the pump

Another process that affects the operation of Er lasers is upconversion, which results from the interaction of a pair of Er ions. In upconversion, three examples of which are shown schematically in Figure 33, two ions in an excited state exchange energy, dropping one ion down to a lower state and promoting the other ion to a higher-lying state. For the Er ion upconversion is energetically possible from the laser-active states. Upconversion from the $^4I_{13/2}$ state, which results in one ion in the ground state and the other in the $^4I_{9/2}$ state, is a potential detriment to 1.6- μm laser operation, but can assist 2.8- μm laser action by depleting the lower laser level, while at the same time providing re-pumping of the upper level.

A related process, also shown in Fig. 33 for two examples, is cross relaxation, another ion-ion interaction in which one ion in an excited state drops to a lower state and another ion goes into a higher state. In principal, upconversion and cross relaxation can cancel each other, so that there is no significant effect on laser operation except for a small energy loss during the processes. For example, cross-relaxation involving an ion in

the ground state and one in the $4I_{9/2}$ state results in two ions in the $4I_{13/2}$ state, the inverse of the cross relaxation process cited above.

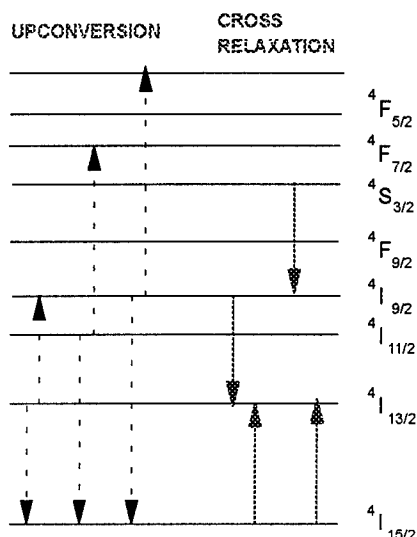


Figure 33. Examples of upconversion and cross relaxation between Er ions

In the program we attempted to improve the understanding of excited-state absorption, upconversion and cross relaxation in Er-doped materials, particularly as they affect laser operation. The first two processes lead to excitation of Er levels higher than energetically possible with a single pump photon. We can test for the presence of either by looking for fluorescence from the high-lying Er levels, particularly green emission from the $4S_{3/2}$ state. Figure 34 shows the experimental apparatus we used in an early set of experiments. We employed a cw Ti:sapphire laser to pump a sample of Er-doped material, and observed the green emission intensity as a function of pump wavelength. The pump power varied from 0.66 W at 800 nm to 0.11 W at 970 nm. We used a 2.5-cm-focal-length lens to focus the mm-size pump beam and a 700-nm short-pass filter in front of the emission detector.

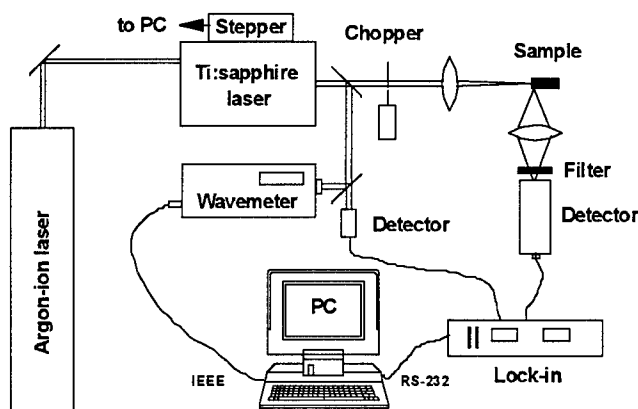


Figure 34. Experimental apparatus used to examine nonlinear pumping

We show in Figure 35 the green emission intensity vs. wavelength for a 30-% doped sample of Er:GGG, pumped into the $^4I_{9/2}$ state; also plotted is the absorption spectra. If the green emission resulted only from upconversion we would expect to see peaks in the excitation and absorption spectra track, but this is clearly not the case. In fact, there are emission peaks where no absorption peaks are apparent. The process of ESA depends on the coincidence of two sets of transitions, and the ESA excitation spectra is not likely to coincide with the conventional absorption spectra. Figure 36 shows similar data for $^4I_{11/2}$ pumping, where, again, the green excitation spectrum has a different shape from the absorption spectrum.

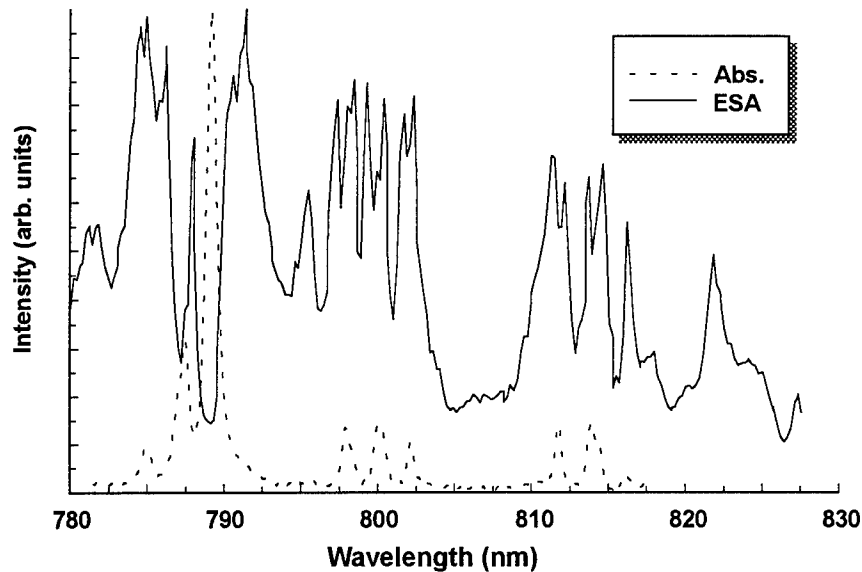


Figure 35. Green emission vs. excitation wavelength (ESA) along with absorption spectra in the 800-nm region for Er:GGG.

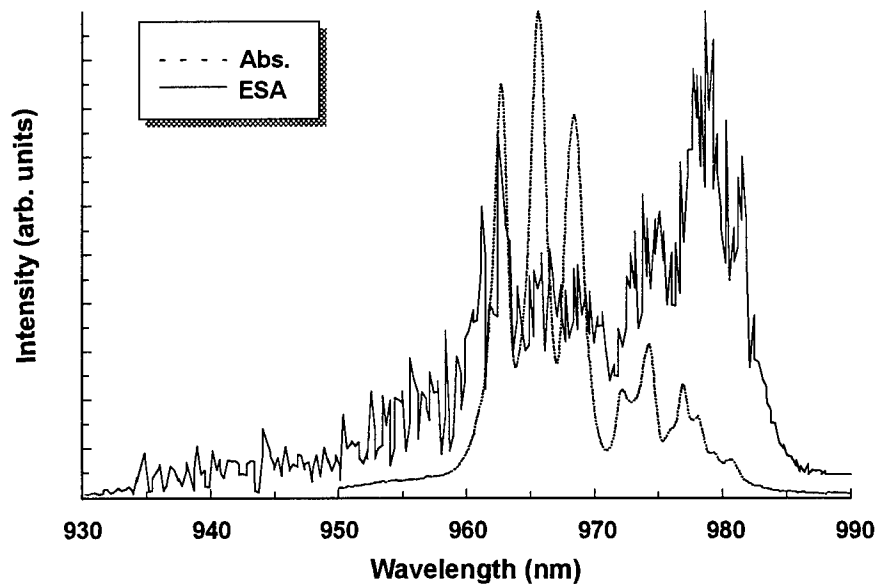


Figure 36. Similar to Figure 35 but for the 970-nm wavelength region

We fixed the Ti:sapphire source at one wavelength and measured the variation of the Er:GGG green signal intensity with pump power. Figure 37 plots signal level vs. pump power, and Figure 38 plots the logarithmic signal level vs. the logarithm of the pump power. We would expect for ESA that the signal would depend on the square of power. This would also be true for an upconversion signal at low pump powers, but at higher powers, when the upconversion process became the dominant route for decay, the signal would be linear in power. As Fig. 38 shows, the signal follows a square-law behavior at low powers but transitions to a linear dependence at high powers. Thus, although the spectral data tends to show that ESA creates the green signal, the power dependence shows that upconversion must be a factor as well.

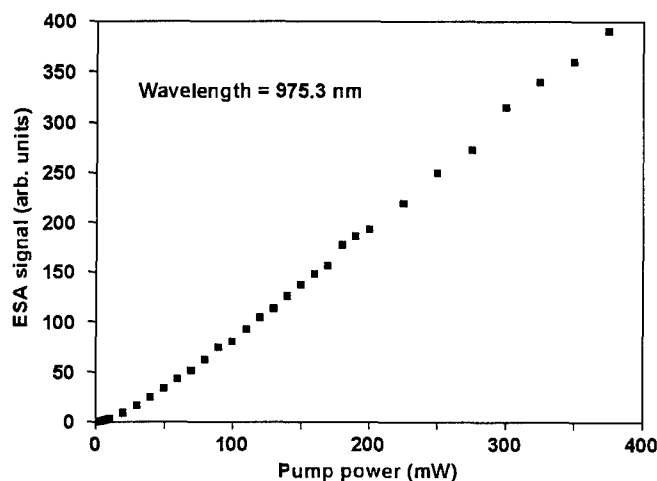


Figure 37. Er:GGG green signal level as a function of pump power at 975.3 nm

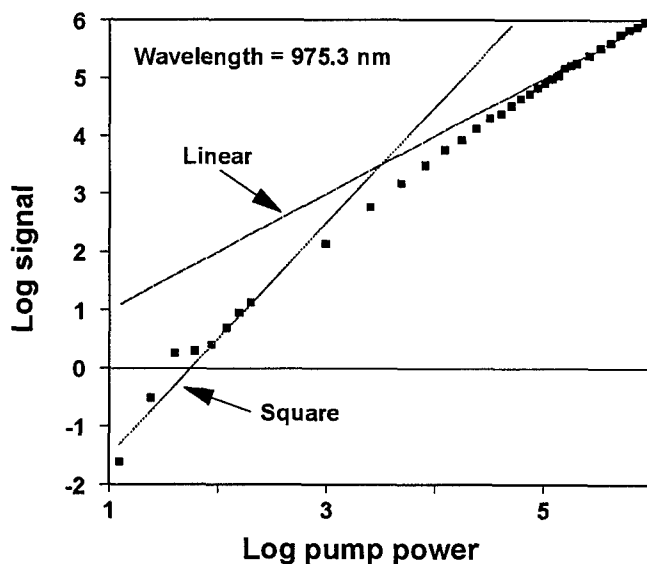


Figure 38. Log-log plot of data (points) in Figure 37. Lines showing linear and square-law dependence are plotted for reference.

The difference in pump-power levels in the 790 and 970-nm regions added uncertainty to the relative level of ESA for the two pump regions. Under the assumption of a linear dependence of signal on pump power we conclude that the green signal produced by 970-nm pumping is about half as intense at the peak compared to the signal created by 790-nm pumping. This suggests the use of the longer wavelength region for laser excitation.

We also observed the green excitation spectra for Er:YLF (20%) at the two wavelength regions and found that 970-nm pumping into the $^4I_{11/2}$ state produced a green fluorescence more than an order-of-magnitude weaker than that for 790-nm pumping. In addition, we found good match between excitation and absorption spectra.

The rate of upconversion out of a state is proportional to the square of the population density in the state times (twice, in our formalism) the upconversion coefficient. In later experiments we attempted to obtain a more quantitative understanding of the effects of upconversion by determining the upconversion coefficients for GGG and YSGG. This was based on prior work by Hans Jenssen and his students at MIT, who studied the crystals YLF and BYF and developed a methodology for upconversion-coefficient measurements. A complete discussion of our work appears in Appendix A, Chapter 3 (pages 55-87.)

For reference, we repeat the summary Table of upconversion coefficients from Chapter 3 (page 79) of Appendix A. Data marked with a # is from others, and the third set of values for BYF is the result of our analysis of the raw data of others. The second set of values for GGG resulted from an alternative fit to the data.

Table 4. Upconversion coefficients for different materials

	α_1	σ_1	α_2	σ_2
Material	(x 10 ¹⁷ cm ³ /sec)			
GGG (10%)	2.2	5.2	1.3	1.1
GGG (30%)	0.5	0.2	5.2	1.3
GGG (30%)	2.5	na	2.0	na
YSGG (30%)	6.7	3.3	4.3	1.1
YAG (33%)#	4.0	na	3.0	na
BYF (20%)	16.0	26.6	0.7	0.8
BYF (20%)#	3.5	na	0.8	na
BYF (20%)#	12.0	0.4	0.7	0.2
YLF (20%)	2.1	0.5	0.5	0.3
YLF (30%)#	3.0	na	1.8	na

In the Table above, α_1 and α_2 are the upconversion coefficients from the $^4I_{13/2}$ and $^4I_{13/2}$ states, respectively and σ_1 and σ_2 are the associated standard deviations for the measurement. The measurement technique we and others have used is subject to considerable errors, suggesting that development of more precise techniques is in order. In general, the coefficients for both levels are similar, which means that for 2.8- μ m laser

operation we must consider the effect of upconversion from both upper and lower laser levels.

Besides ESA and upconversion, we also need to consider the effects of cross relaxation in Er laser systems. Figure 33 shows examples of cross relaxation from the $^4I_{9/2}$ and $^4S_{3/2}$ states, both involving one ion in the ground state. For this type of cross relaxation the rate depends on the product of the ground-state and excited-state populations. In the low-pumping limit, where we do not deplete a large fraction of the ground state the cross relaxation rate depends only on the excited-state density, and thus cross relaxation is a linear, rather than nonlinear process.

To determine the rate we must measure the decay rate from the excited level involved, and then subtract out the rate due to photon and phonon emission. In practice, we know neither of these rates *a priori* and we must try to determine the rate by other approaches. The most straightforward is to measure the level decay rate for low Er concentrations, where we assume that the cross-relaxation rate is nil, and then measure the rates at higher concentrations. Provided that no additional rare-earth or other impurities are added to the material at higher doping levels, if the decay rate from the level drops with increasing concentrations, we can assume that the difference in rates from the low-concentration limit are the cross relaxation rates.

An examination, in Table 3, of the decay times for the $^4S_{3/2}$ state shows a drastic lifetime reduction with increased Er concentration, and we can assume that the decay times (and rates) at concentrations above 10% are essentially all due to cross relaxation. The $^4I_{9/2}$ state shows a more gradual reduction; the effect of cross relaxation is masked by the high rate of decay from phonon emission. Table 5 presents our calculations of the decay rates from the $^4I_{9/2}$ state for different materials, and our estimate of the cross relaxation rate determined by subtracting the rate for low concentrations from rates at higher concentrations.

Table 5. Calculated cross relaxation (CR) rates for the $^4I_{9/2}$ state

Material	Lifetime (μ sec)	Decay rate ($\times 10^5$ sec.)	CR rate ($\times 10^5$ sec.)	β_{32}
GGG (1%)	4.57	2.19	-	1
GGG (10%)	3.98	2.51	0.32	0.87
GGG (30%)	1.9	5.27	2.41	0.42
YSGG (1%)	2.78	3.60	-	1
YSGG (30%)	1.32	7.58	3.98	0.47
BYF (1%)*	9.6	1.04	-	1
BYF (10%)*	9.6	1.04	0	1
BYF (20%)	8.2	1.22	0.18	0.85
BYF (50%)*	4.2	2.38	1.34	0.44
BYF (100%)*	2.3	4.35	3.32	0.24
YLF (3.5%)*	6.7	1.49	-	1
YLF (8.5%)*	6.6	1.52	0.03	0.98
YLF (20%)	6.2	1.61	0.12	0.93
YLF (30%)*	5.3	1.89	0.4	0.79

The data on material marked with * is from D.S. Knowles Ph.D. Thesis at MIT, reference 4 on page 87 of Appendix A. The accuracy of our CR rate calculations is low in many cases, given that the rate may be a small difference between large numbers. The rate is monotonic in Er concentration and is lower for the fluoride crystals, an indication that phonons may be needed in the CR process. The quantity β_{32} is the ratio of the low-concentration decay rate to the total decay rate, and represents the fraction of excitation that leaves the $^4I_{9/2}$ state via photon/phonon emission.

We will discuss below how the upconversion coefficients and cross relaxation data figure into calculations of laser performance from Er-doped materials.

5.2 Gain

Given the complex nature of Er laser action, especially in the 2.8- μm region, and uncertainties about the key spectroscopic parameters, we decided to carry out direct measurements of pulsed-pumped gain in various crystals, using a pump-probe setup. Two critical elements to the gain measurements were a cw probe source and a pump source. We built cw Er-doped lasers as probes, a project that took on more resources than originally anticipated when important applications for the cw sources themselves developed. The properties of the cw lasers are discussed in Section 6. For a pump source, after we decided to concentrate on the 970-nm region, we chose a lamp-pumped Cr:LiSAF laser as a relatively inexpensive substitute for high-energy semiconductor laser arrays. We built the Cr:LiSAF laser, with a 5x100 mm rod, on our commercial *Laser 1-2-3* platform, and used our transistor-switched flashlamp driver to smoothly vary the lamp pulse duration over a wide range, since we wanted to observe the effect of pump pulsewidth on Er-laser gain.

Figure 39 shows early data on the threshold of the Cr:LiSAF laser on flashlamp pulsewidth. The upper-state lifetime of Cr:LiSAF is 67 μsec , and for pump pulses much longer than this we expect, to first order, that the threshold will be constant in power. Thus the threshold energy should increase linearly with pulsewidth, and we observe that in the data of Fig. 39, which shows the first operation of a Cr:LiSAF with pump pulsewidths in the msec range.

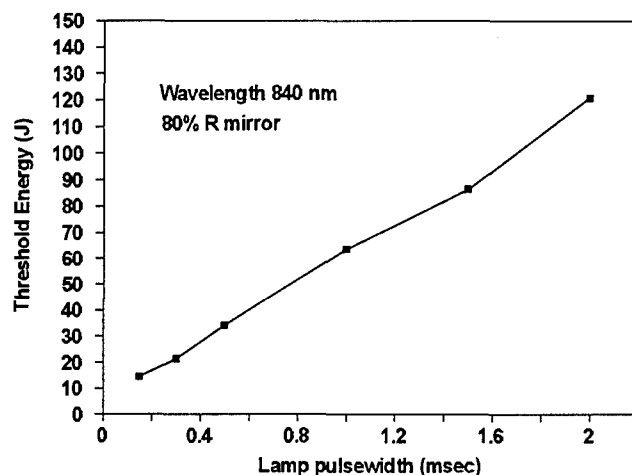


Figure 39. Variation of Cr:LiSAF laser threshold with flashlamp pulsewidth

The input-output curves for two lamp pulsewidths are plotted in Figure 40. The lower slope efficiency for the longer pulsewidth is likely the result of the lower peak current in the lamp. The lower current shifts more of the lamp emission to the red and leads to a poorer overlap of lamp emission and Cr:LiSAF absorption.

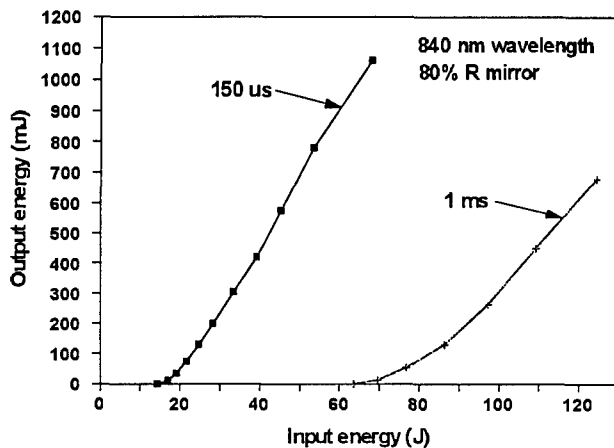


Figure 40. Cr:LiSAF laser input-output curves for two lamp pulsewidths

We added two prisms to the Cr:LiSAF laser cavity and tuned the laser to 970 nm. The output energy was considerably reduced, as expected. Fortunately, the quality of commercial Cr:LiSAF had improved from the rod we initially used, partly as the result of the efforts of B. Chai at CREOL, and we obtained a new rod for our system. The improvement in performance was substantial, as the input-output curves of Figure 41 show. The new rod operated with lower thresholds and higher efficiency at 970 nm than the old rod did at the gain peak of 840 nm.

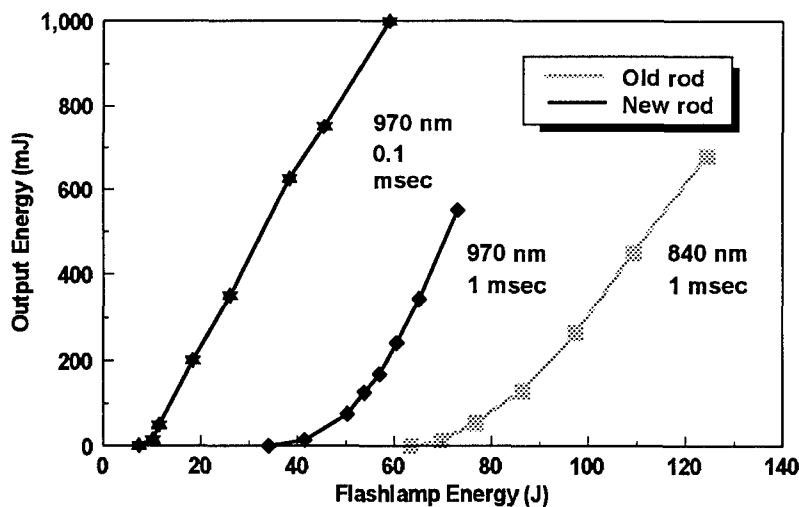


Figure 41. Input-output curves comparing performance of old and new Cr:LiSAF rods.

Figure 42 is a schematic representation of the pump-probe system we used for pulsed gain measurements. We passed the output of the variable-pulsewidth Cr:LiSAF laser through anamorphic optics to create a line focus and side-pumped the Er-doped material under test. The diode-pumped, cw Er laser provided a probe beam that we passed through the excited region of the side-pumped crystal, in a direction perpendicular to the pump beam. The detector ((InAs) measured the transient signal induced in the probe beam by the action of optical gain. We recorded the transient data on a Data Precision 6000 digitizer and also noted the peak absolute gain using an oscilloscope to determine the DC and peak levels of the probe signal.

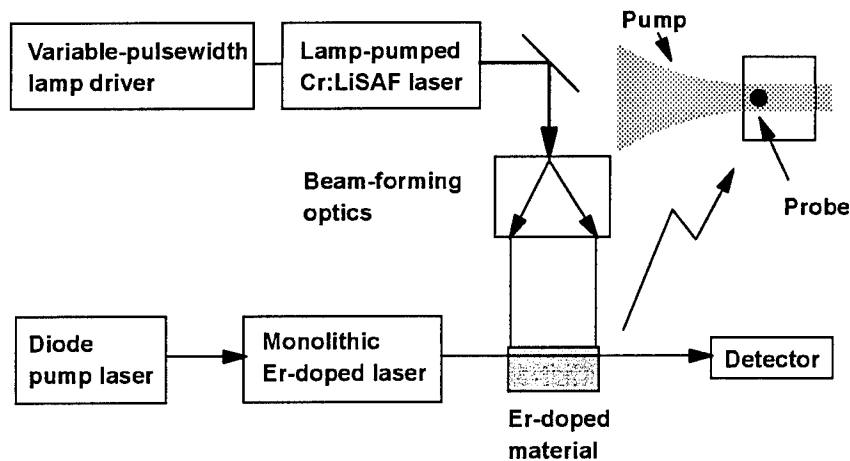


Figure 42. Schematic of pump-probe experiment

The Cr:LiSAF laser output passed through a 3.5x beam expander and then through a pair of cylinder lenses arranged to produce an effective focal length of 80 cm. We used a pinhole on a translation stage to determine the beam height of the focused Cr:LiSAF laser; the height (FWHM) was 0.36 mm, in good agreement with the value estimated based on a measured Cr:LiSAF divergence of 1.3 mrad in the vertical plane. The beam width was 1 cm, with a nearly uniform distribution of energy. The output of the probe laser was focused by a 20-cm lens through the sample and the measured spot diameter at the sample location was 0.24 mm. Thus the probe beam size fell within the height of the pumped region. We wedged the uncoated probe entrance and exit faces of the samples by 15 degrees to avoid the possibility of parasitic oscillations.

To avoid changes in pump-beam divergence with lamp average power we operated the Cr:LiSAF laser at a constant pump energy and pulse rate (2 Hz), and attenuated the beam through the use of a rotatable waveplate and a polarizer. We took gain over a 1-month period and returned after three months to measure the variation in gain signal with probe-beam height. At that point the Cr:LiSAF rod shattered and we discovered that the rod diameter had been reduced approximately 25% by the solvent action of the cooling water. We subsequently learned that the pH of the cooling water must be maintained in a narrow region around 7 to avoid dissolving the Cr:LiSAF rods, and that our de-ionized cooling water was too acidic. We do not know how much the rod diameter changed over the course of the gain experiments and how our pump focus size

changed. Thus we have some uncertainty about comparing gain amongst the different materials, but we believe the effect of the slowly reducing rod diameter is minor.

We took gain data (in the order listed) on crystals of Er:YSGG (30%), Er:GGG (30 and 10%), Er:BYF (20%) and Er:YLF (20%). Table 6 presents the pump wavelengths we employed for the different materials along with the peak absorption coefficient for the wavelength and, for reference, the upper-state lifetime.

Table 6. Pump wavelengths used in gain measurements

Material	Wavelength (nm)	Absorption coefficient (cm ⁻¹)	Lifetime (msec)
Er:YSGG (30%)	965.5	15	1.3
Er:GGG (10%)	968.5	6	0.96
Er:GGG (30%)	968.5	18	0.99
Er:BYF (20%)	971.0	6	3.7
Er:YLF (20%)	911.0	15	3.8

We measured peak gain vs. pump energy for pump pulsewidths of 125, 250, 500, 750 and 1000 μ sec and employed pump energies of 50, 100, 200, 300, 400 and 500 mJ. The following Figures plot data for each of the materials, first showing gain as a function of pulse energy for different pulsewidths and then as function of pulsewidth for different energies.

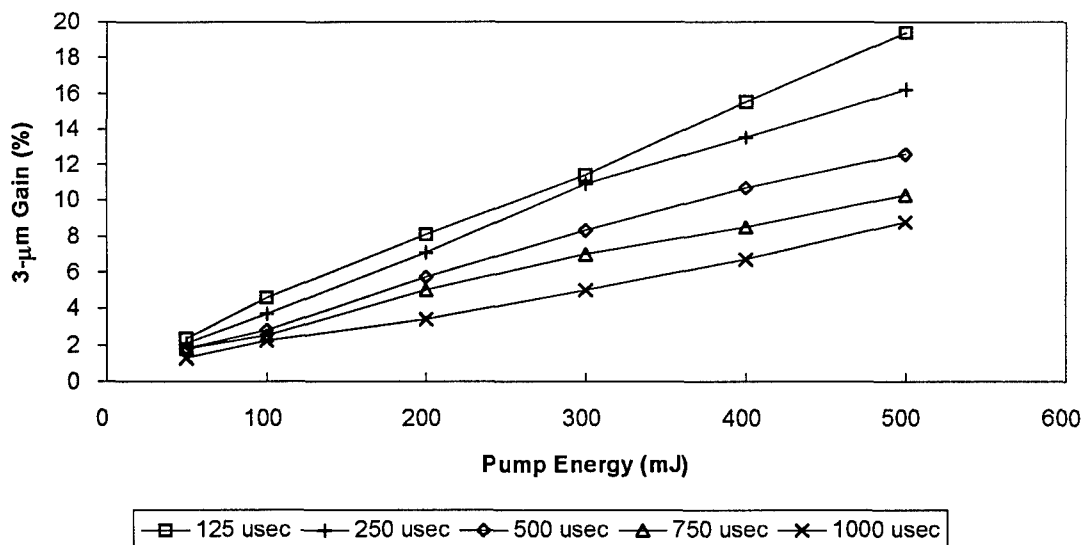


Figure 43. Gain vs. pump energy for YSGG

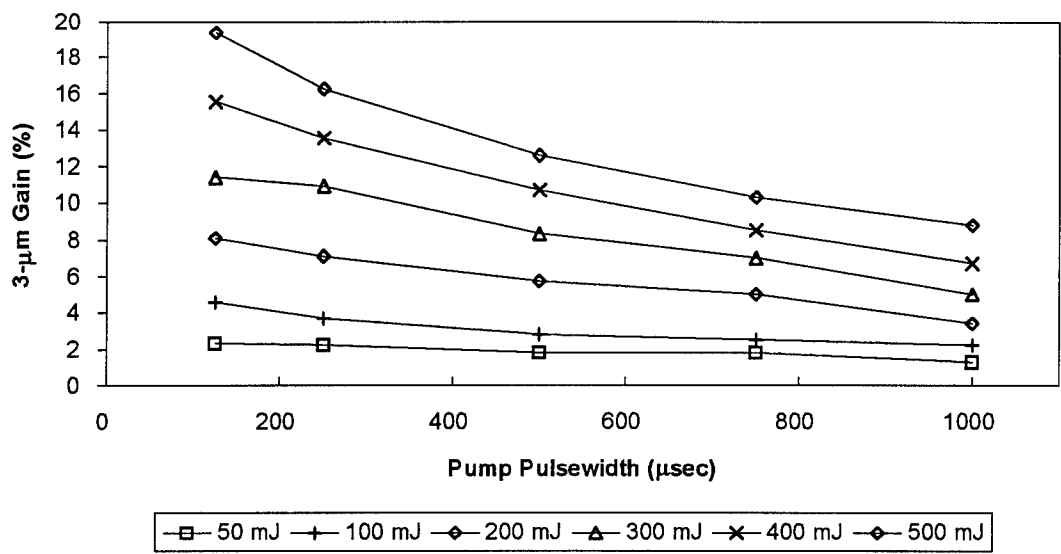


Figure 44. Gain vs. pump pulsewidth for YSGG

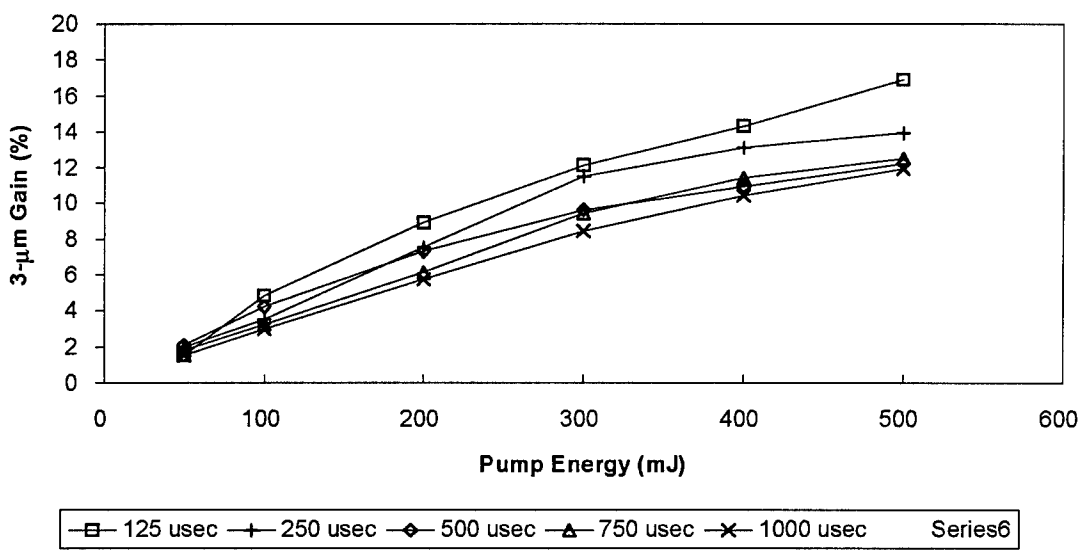


Figure 45. Gain vs. pump energy for GGG (30%)

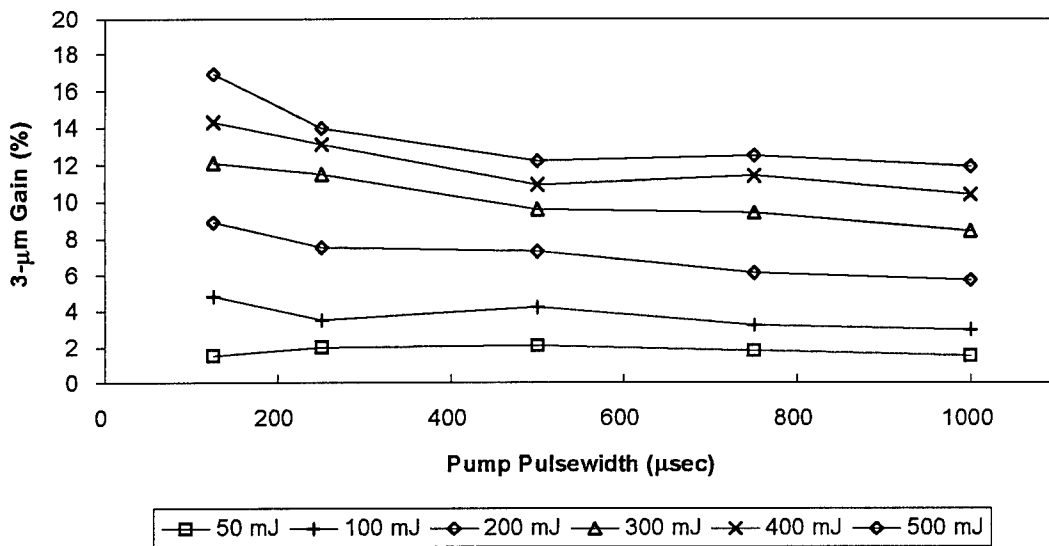


Figure 46. Gain vs. pump pulsewidth for GGG (30%)

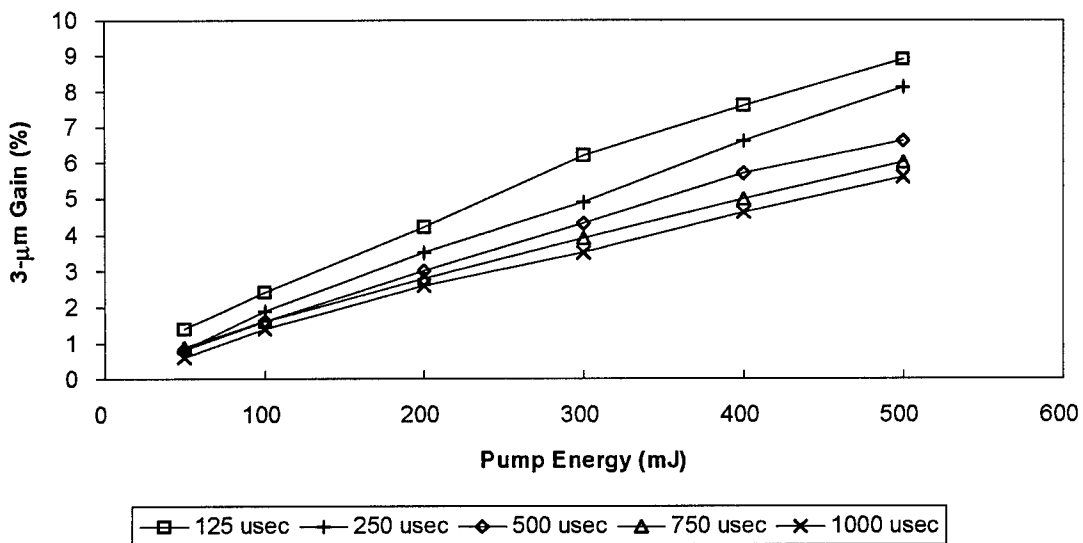


Figure 47. Gain vs. pump energy for GGG (10%)

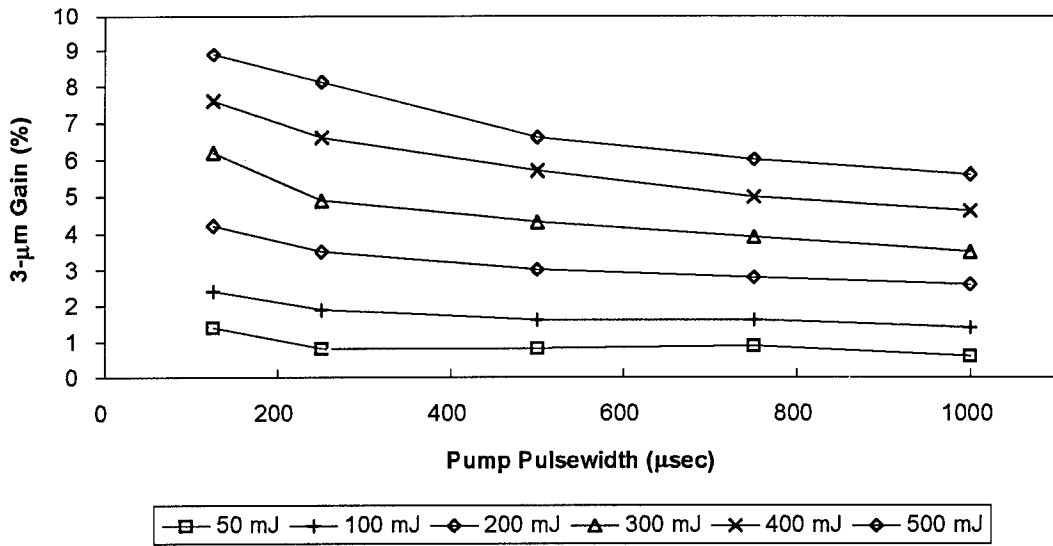


Figure 48. Gain vs. pump pulsewidth for GGG (10%)

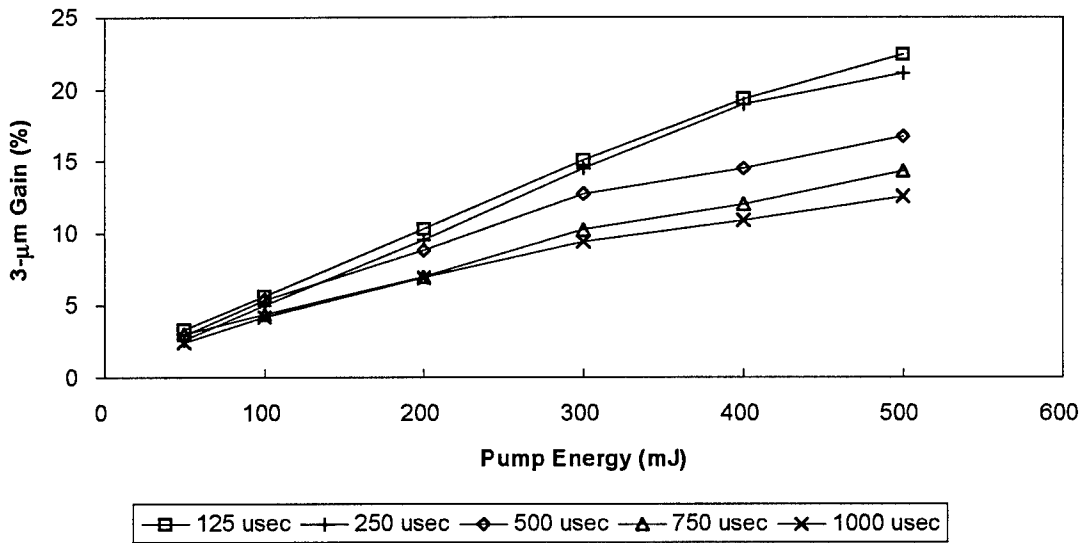


Figure 49. Gain vs. pump energy for BYF

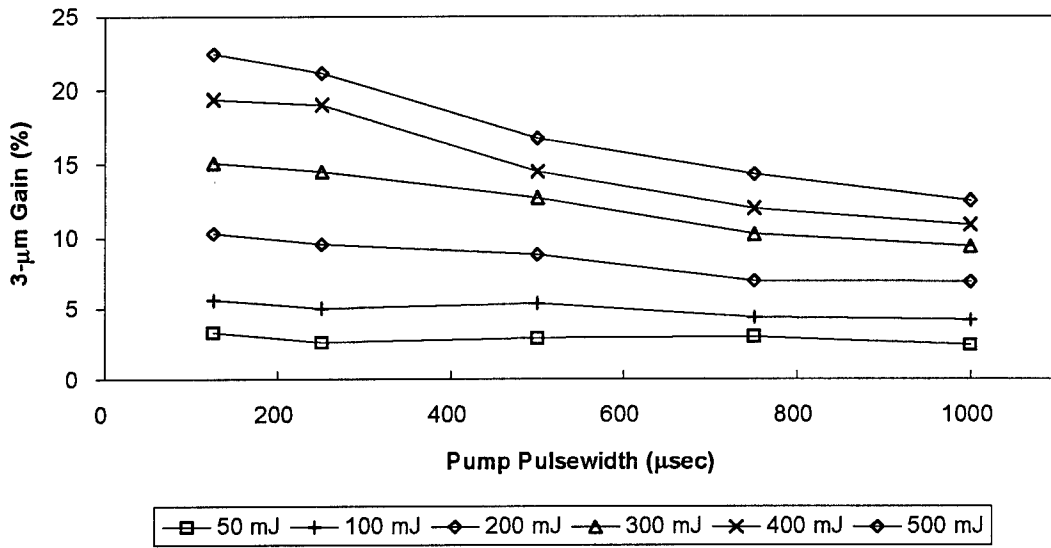


Figure 50. Gain vs. pump pulsewidth for BYF

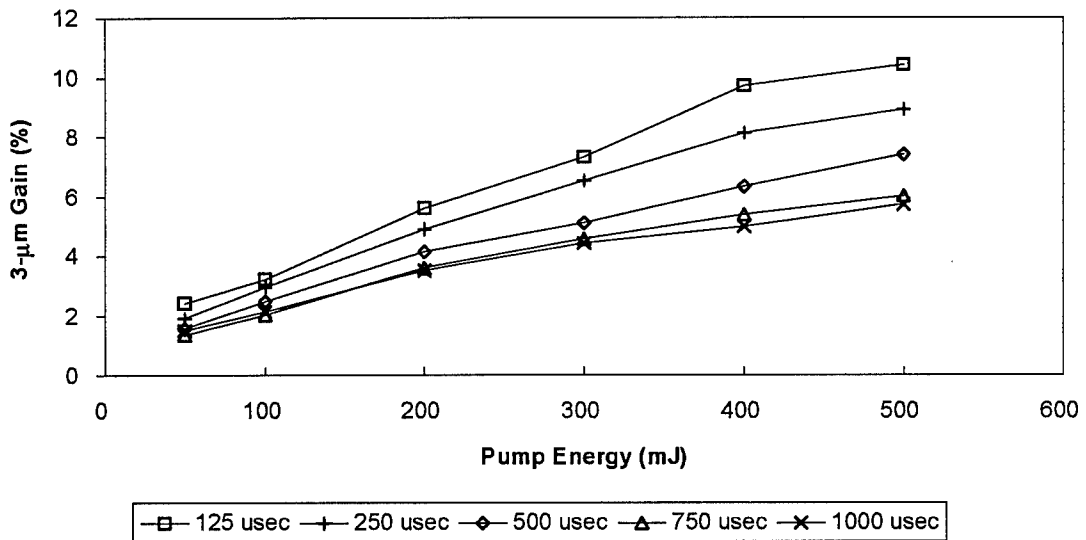


Figure 51. Gain vs. pump energy for YLF

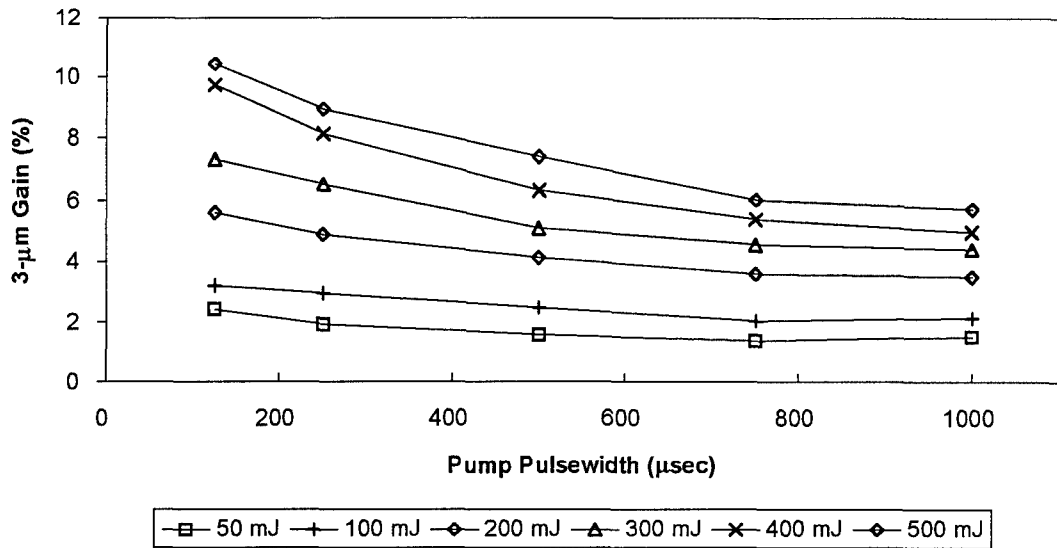


Figure 52. Gain vs. pump pulsewidth for YLF

The following Figures compare the materials for selected operating conditions. Figures 53 and 54 present gain vs. pump energy at pulsewidths of 125 and 1000 μsec, respectively. Figures 55 and 56 show gain as a function of pump pulsewidth for pump energies of 100 and 500 mJ, respectively. Finally, Figure 57 plots gain as a function of pulsewidth for constant pump power (50 mJ at 125 μsec, 100 mJ at 250 μsec, etc.) simulating conditions that would be appropriate for a diode-array pump source.

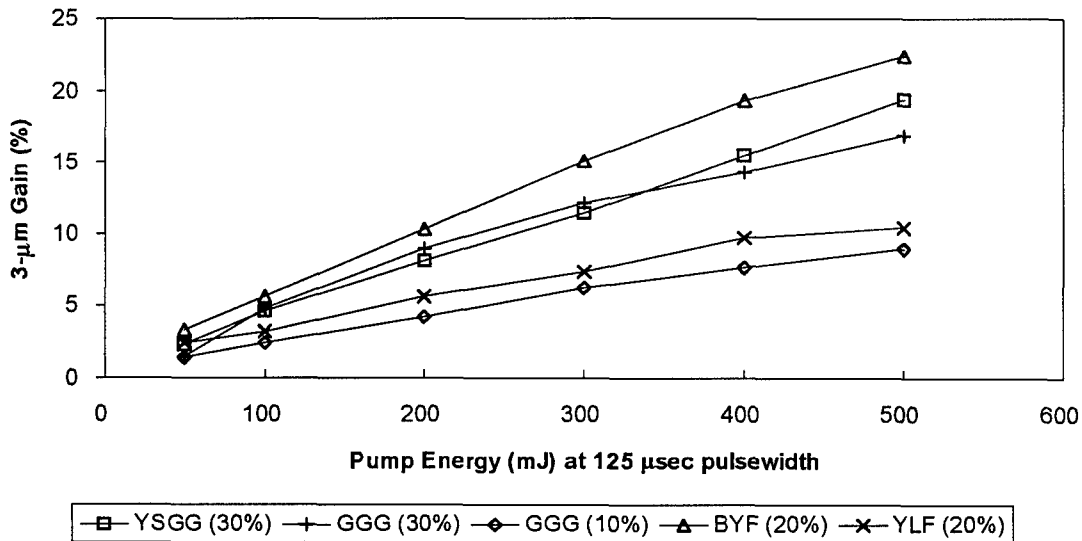


Figure 53. Gain for different materials vs. pump energy, 125-μsec pulsewidth

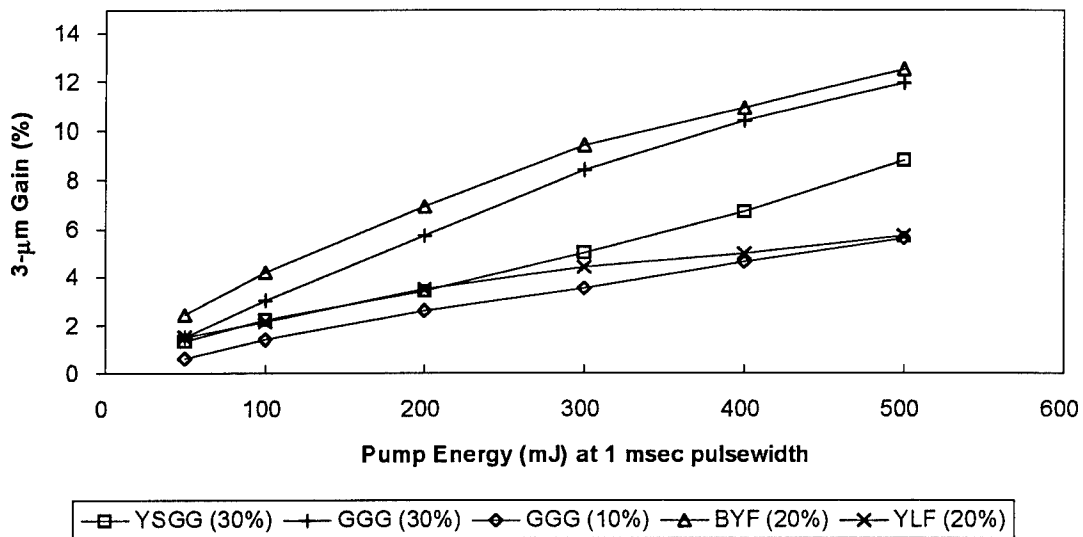


Figure 54. Gain for different materials vs. pump energy, 1-msec pulsewidth

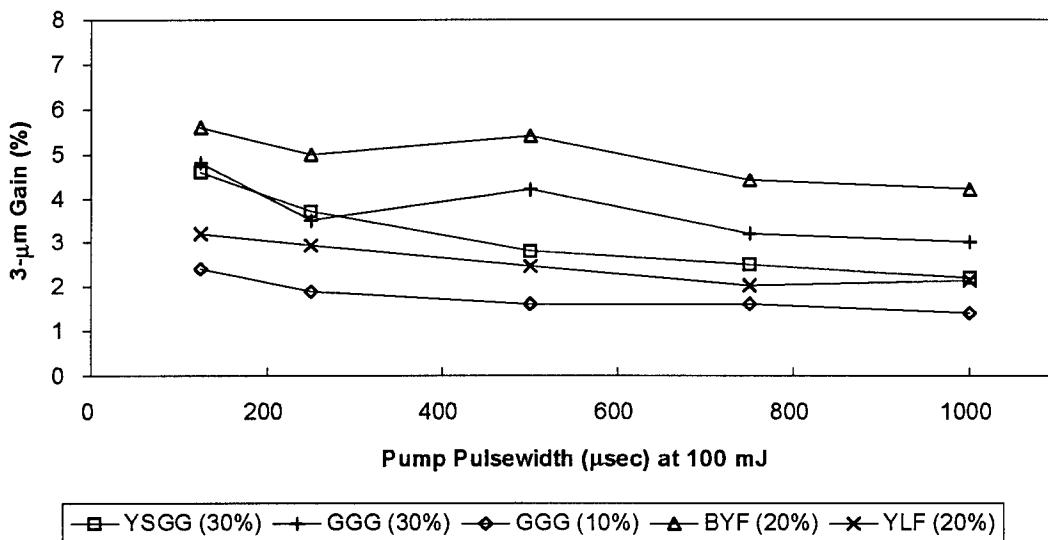


Figure 55. Gain vs. pump pulsewidth for different materials, 100-mJ pump energy

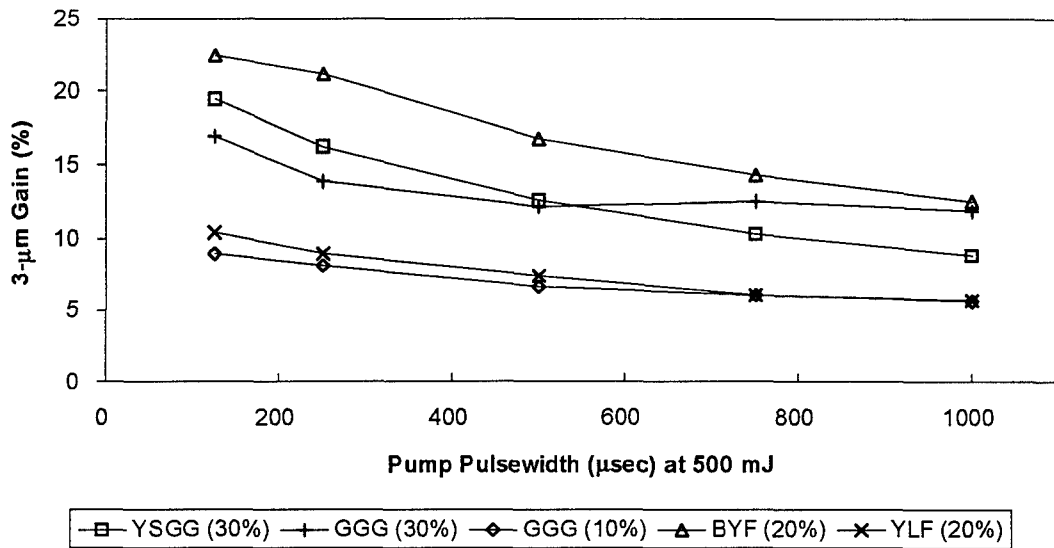


Figure 56. Gain vs. pump pulsewidth for different materials, 500-mJ pump energy

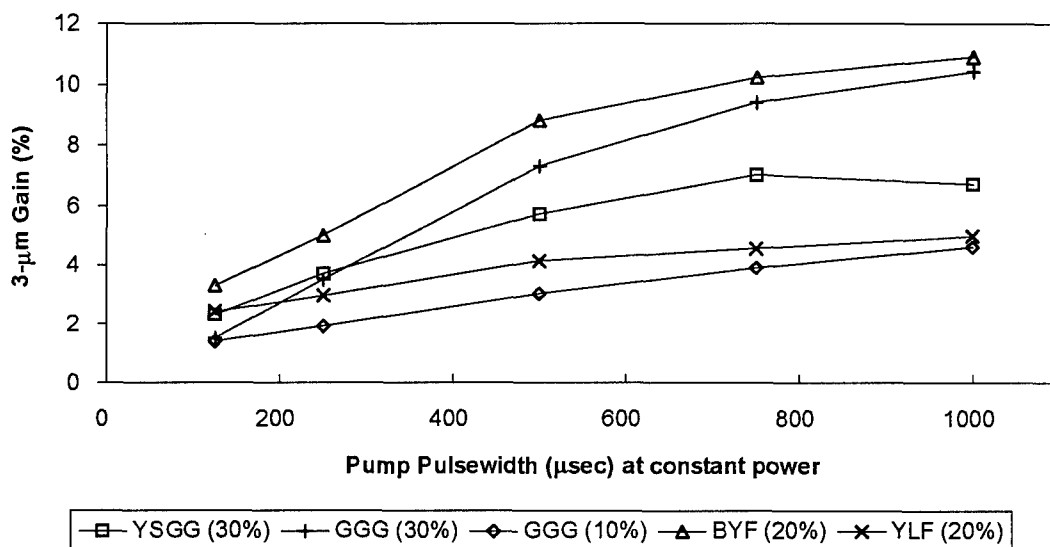


Figure 57. Gain vs. pulsewidth at constant power

The data on peak gain is useful in comparing the suitability of materials for pulsed diode-pumped operation, especially with Q-switching. The clear winner in terms of maximum available gain is Er:BYF. We note that the crystal under test was randomly oriented, and further studies with other samples are needed to determine how far, if at all, our sample was from optimum orientation. Considering that the absorption coefficient for BYF (from Table 9) is small compared to all materials but 10%-doped GGG, the gain per volume excitation rate is even higher than the graphs indicate.

The gain in all materials showed a monotonic decrease with increasing pulsewidth, with, in general, the amount of decrease becoming more significant as the pump energy increased. For short pump pulses the gain vs. pump-energy relation was

closest to linear, but the relation became more sublinear as the pump duration increased, except for YSGG, which showed a super-linear relation. This is, in general, an indication that nonlinear processes such as upconversion play a role in the depleting the upper laser level. Both BYF and GGG showed the least reduction in gain with pulse duration.

Our interest in the effect of pump-pulse duration on gain is motivated by the realization that diode array pump sources are essentially constant-power devices, and the longer the pump pulse the greater the energy available from the array. Figure 57 provides an indication of the performance of different materials under diode-pumping conditions, since the gain is shown as a function of pump duration for constant-power conditions. We conclude from the Figure that BYF and GGG would be best suited for array pumping, other considerations such as thermo-mechanical properties neglected. The most efficient pump duration for Q-switched operation appears to be 0.5 msec, as longer durations yield sublinear increases in gain and, hence, energy storage. Normal-mode laser operation, where the inversion density is clamped, might be able to operate with longer pulses. We note in Fig. 57 that the gain for all materials does not appear to extrapolate to zero, an indication that systematic as well as general estimation errors may have influenced our measurements.

The amount of data we took on the temporal behavior of the gain is large and we will not attempt to reproduce all of it here. For each of the materials YSGG, GGG(30%) and BYF we show two plots of gain vs. time. The first is with a constant pump pulsewidth of 125 μ sec and shows normalized gain at pump energies of 200 and 500 mJ, in order to show how the shape of the curve changes with energy. The second plot is gain at a constant 400 mJ pump energy, but with pulsewidths of 125, 250, 500, 750 and 1000 μ m, and shows how the peak gain and gain decay is affected by pulsewidth.

For YSGG, Figures 58 and 59, we see that the decay shape is relatively unaffected by pump energy (Fig. 58) and that gain is present at times much longer than that expected from the upper-state lifetime. For a laser with a long lower-level lifetime, the case for 3- μ m Er lasers, we expect in the limit of infinite lower lifetime that the gain decays at twice the decay rate of the upper level. This comes about because gain is proportional to the difference in upper- and lower-level populations, and every decrease in upper-level population is accompanied by an increase in that of the lower level. At long times we would expect the gain to go negative, as the population of the lower state builds up. For YSGG, with an upper-state lifetime of 1.3 msec, we would expect to see a gain decay-time from peak to 1/e of 0.65 msec. This is in fact what we observe at low pump energies, from 50-200 mJ. At higher energies the 1/e time reduces slightly, reaching 0.55 msec at 500 mJ of pump. However, at times beyond the 1/e point we see the gain decay much more slowly and stay positive for a long period of time. We believe this results from upconversion from the lower laser state, which feeds the upper state and maintains enough upper-level population to achieve net gain for an extended period. The slight decrease in initial gain decay time is likely the result of upconversion from the upper level. In Figure 59 we see the peak gain in YSGG begin to reduce as the pump pulsewidth becomes comparable to and then greater than the gain decay time.

The temporal behavior of gain in GGG (30%), Figures 60 and 61, shows a slight reduction in 1/e time with pump energy. The data for GGG is noisier, and leads to greater errors in estimating the actual 1/e time, but the value falls in the range 0.4-0.6 msec, roughly half the upper-level lifetime. Gain at long times is much less than for YSGG and

for the 500 mJ pump has fallen to zero 8 msec from the peak. Our data on GGG upconversion coefficients shows that the value for the lower laser state is significantly smaller, for some estimations, than for other materials, which may explain the lack of gain at long times.

For the material BYF, the data in Figures 62 and 63 show a more pronounced reduction in $1/e$ time with pump energy, but the $1/e$ value is longer than the other two materials in all cases. This is apparent in Figure 63, which shows the least reduction in peak gain with increasing pulsewidth of the three materials. In examining all the gain decay data we find that the $1/e$ time at 100 mJ of pump is about 1.9 msec, or half the upper level lifetime, but the $1/e$ time drops steadily with increasing energy, reaching 0.75 msec for a 500-mJ pump.

Figure 64 shows gain decay data for YSGG, GGG (30%), GGG (10%) and BYF, all at a 125 μ sec pulsewidth and 500 mJ of pump energy, with the peak gain of all materials normalized to unity and the time-scale extended out to 25 msec from start in all cases. We have offset the GGG data from the other two for clarity. Both BYF and YSGG show gain extending all the way to the end, while for the two GGG samples the gain decays to zero at long times.

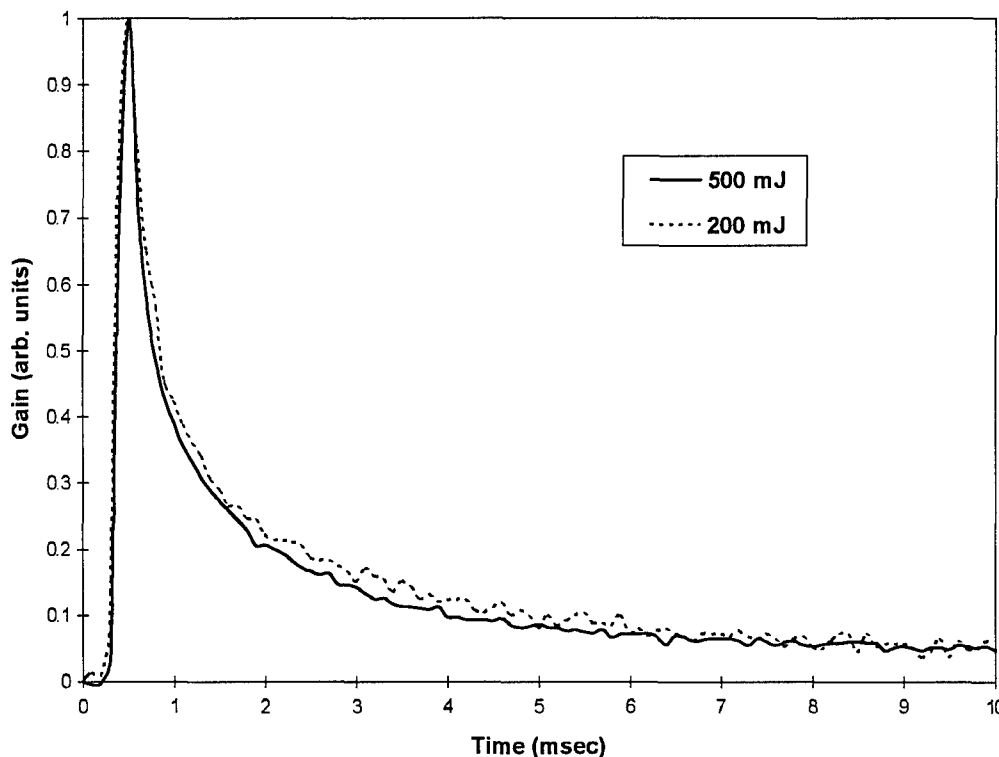


Figure 58. YSGG gain signals with 125 μ sec pump pulsewidth, two pump energies

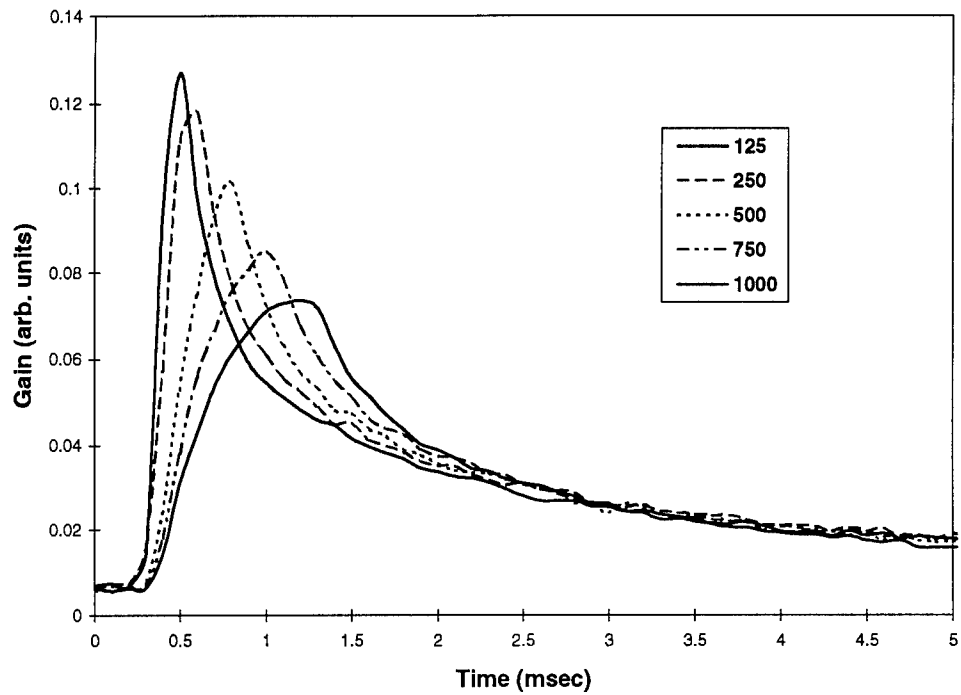


Figure 59. YSGG gain signals for different pump pulsewidths, 400 mJ pump energy

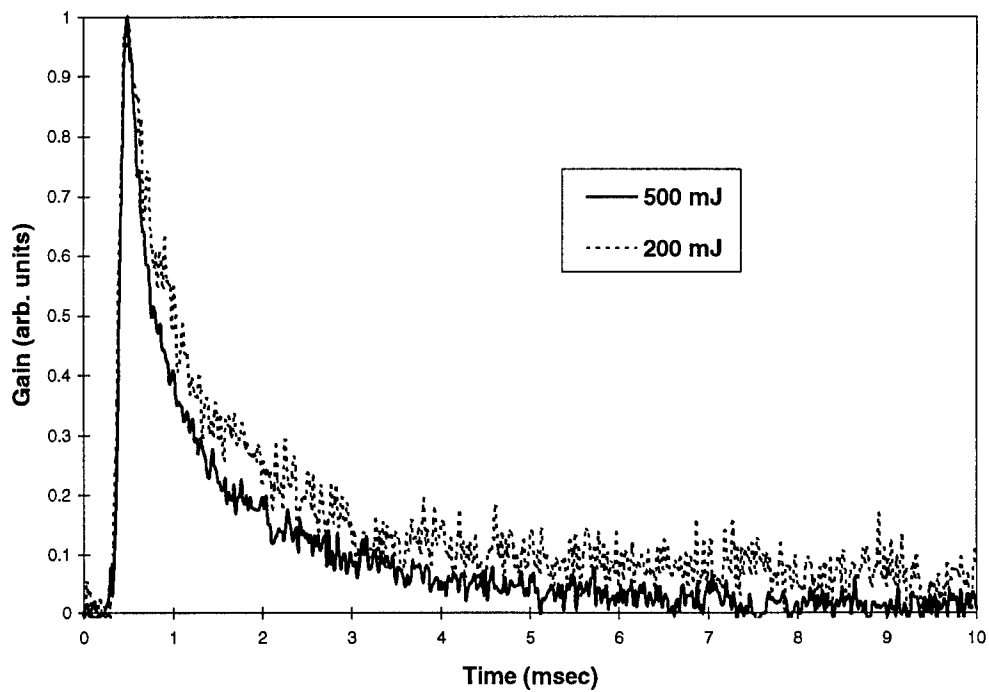


Figure 60. GGG gain signals for 125 μ sec pump pulsewidth, two pump energies

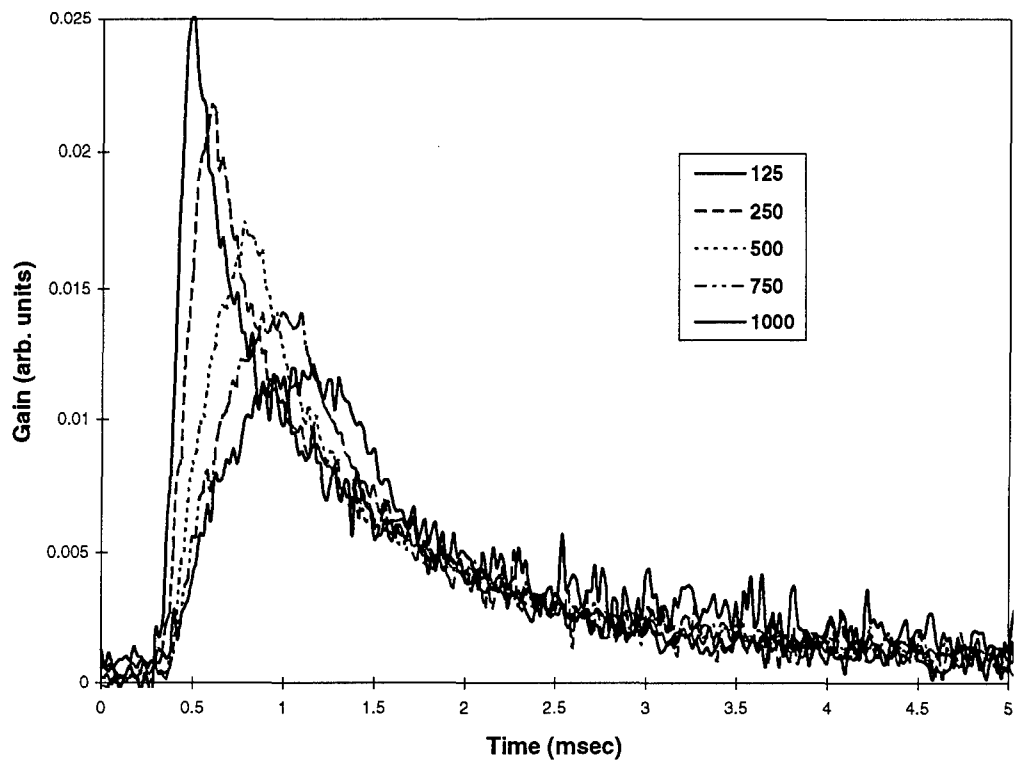


Figure 61. GGG gain signals for different pump pulsewidths, 400 mJ energy

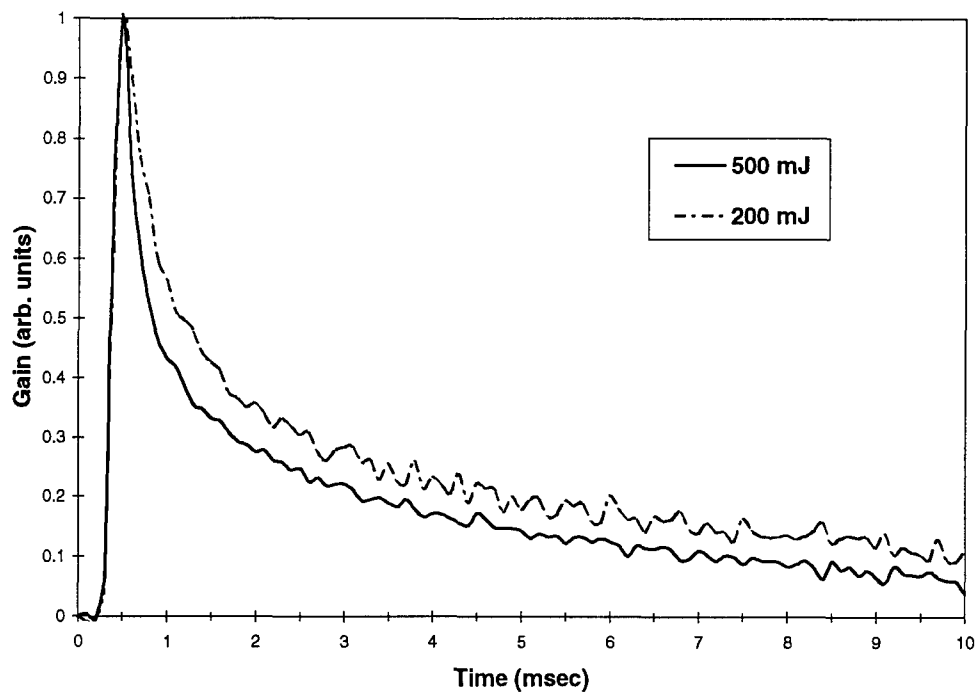


Figure 62. BYF gain signals for 125 μsec pump pulsewidth, two pump energies

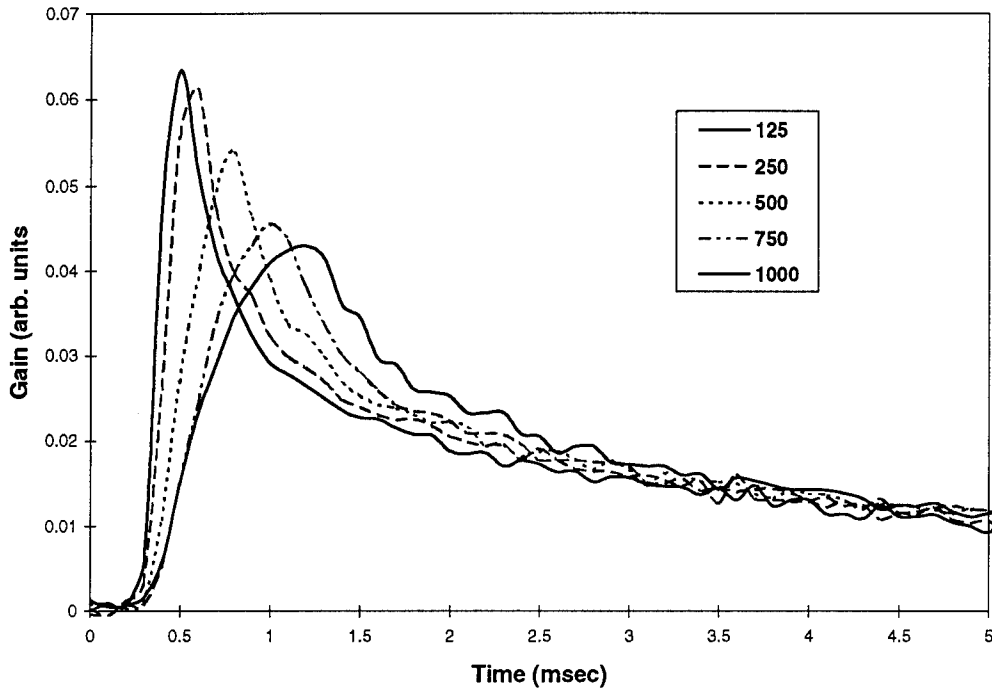


Figure 63. BYF gain signals for different pump pulsewidths, 400 mJ energy

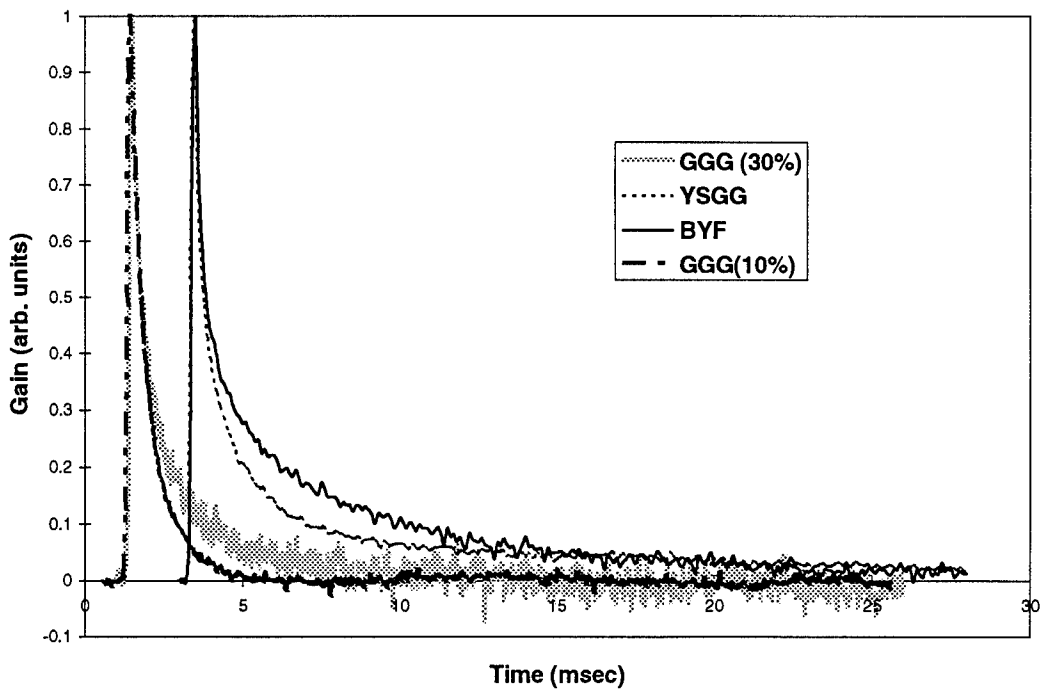


Figure 64. Comparison of gain signal shapes for different materials, 500 mJ pump

In principle, we could use the linear and nonlinear spectroscopic data we obtained on the different materials to calculate the expected temporal behavior of the gain. The program resources, in the end, did not permit this, but we present here a discussion of how to proceed in follow-on work.

In heavily Er-doped crystals the pumping process is strongly affected, if not dominated by upconversion and cross-relaxation involving pairs of Er ions. As we noted, upconversion from two ions in the upper level leads to excitation of the $^4S_{3/2}$ state. Nearly all the decay from this state is by a cross relaxation process that leaves one ion in the lower laser state and another in the $^4I_{9/2}$ state. Relaxation from the $^4I_{9/2}$ state is almost entirely the result of either phonon decay to the upper laser state or a cross relaxation that places two ions in the lower laser state. The ratio of phonon decay to total decay is β_{32} , as we noted before. Upconversion from two ions in the lower laser state leads to an ion in the $^4I_{9/2}$ state, where either one upper-state or two lower-state excitations may result. Based on these processes, we can write the rate equations for the upper- and lower-state populations, N_2 and N_1 , respectively, as

$$\begin{aligned} dN_2/dt &= W_p - N_2/\tau_2 - (2 - \beta_{32}) \alpha_2 N_2^2 + \beta_{32} \alpha_1 N_1^2 \\ dN_1/dt &= N_2/\tau_2 - N_1/\tau_1 - 2 \beta_{32} \alpha_1 N_1^2 + (3 - 2 \beta_{32}) \alpha_2 N_2^2, \end{aligned}$$

where W_p is the external pump rate, τ_2 and τ_1 are the upper- and lower-level lifetimes and α_2 and α_1 are the upper- and lower-level upconversion coefficients. We make the approximation here that all of the excitation decaying from the upper state by single-ion processes ends up in the lower state, although the equations can be modified to account to allow for the partial decay of the upper state directly to ground.

With the differential equations shown one can proceed to use standard numerical approaches to solutions for the populations and find the difference, which represents the gain within a scale factor, the gain cross section.

6. Lasers and Non-lasers

Data on some of our experiments with 3- μ m-wavelength Er-doped lasers appears in Chapter 4 (p.88ff) of Appendix A, for Er:GGG and Er:YSGG. In addition, we enclose as Appendix B, a reprint of an Optics Letters article discussing cw-laser operation from YSGG, GGG and YAG. In Appendices C, D, E and F we include abstracts and summaries from papers on 3- μ m laser operation presented at the OSA Advanced Solid State Lasers Conferences in 1992, 1993 and 1994 and at the LEOS Annual Meeting in 1992. In this Section we will provide additional data on our studies on 3- μ m lasers as well as our attempts to obtain laser action in the 1.6- μ m wavelength region from Er:YVO and Er:YOS.

The development of Er-doped cw lasers in the 3- μ m wavelength region began as a component of the gain measurement effort, and later became an end in itself when an important DoD application for cw laser emerged. Our studies of cw lasers employed monolithic resonator designs, an example of which appears in Figure 65. We obtained the first laser operation from the monoliths through the use of a Ti:sapphire pump laser, and later employed diode lasers as pump sources.

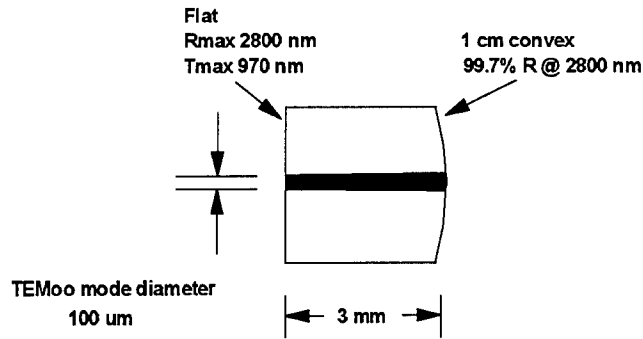


Figure 65. Side-view of 3- μm monolithic laser

The first two Subsections following deal with Ti:sapphire and diode-pumped cw lasers. The next Subsection covers our work on pulsed 3- μm lasers end-pumped by a pulsed diode array, and the final Subsection describes our attempts at obtaining 1.6- μm laser action.

6.1 Ti:sapphire-pumped, cw 3- μm lasers

The Ti:sapphire laser provided a convenient, tunable pump source that allowed us to carry out some parametric characterization of the monoliths. We focused the diffraction-limited output of the laser onto the flat dichroic-coating surface with a simple single-element lens. Figure 66 shows the variation in threshold we observed for the Er:GGG monolith with lens focal length; the input beam diameter was approximately 1 mm. Using calibrated pinholes, we measured the focused beam spot sizes (radii) for the 5- and 10-cm lenses to be 19 and 40 μm , respectively. The slope efficiencies for different lenses were comparable.

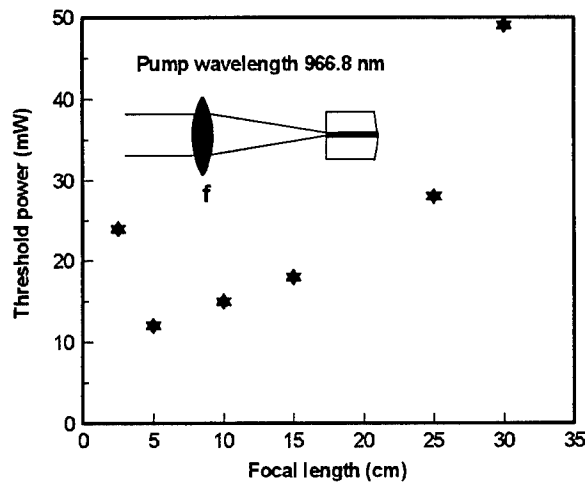


Figure 66. Variation of Er:GGG laser threshold with pump-lens focal length

Input/output curves and thresholds for cw lasers fabricated from GGG (30%), YSGG, YAG, BYF appear in Appendices B-F, with a good summary of room-temperature data in Appendix D. In addition, we observed cw operation from YLF (20%). Figure 67 is a summary plot of the input-output data for all the materials.

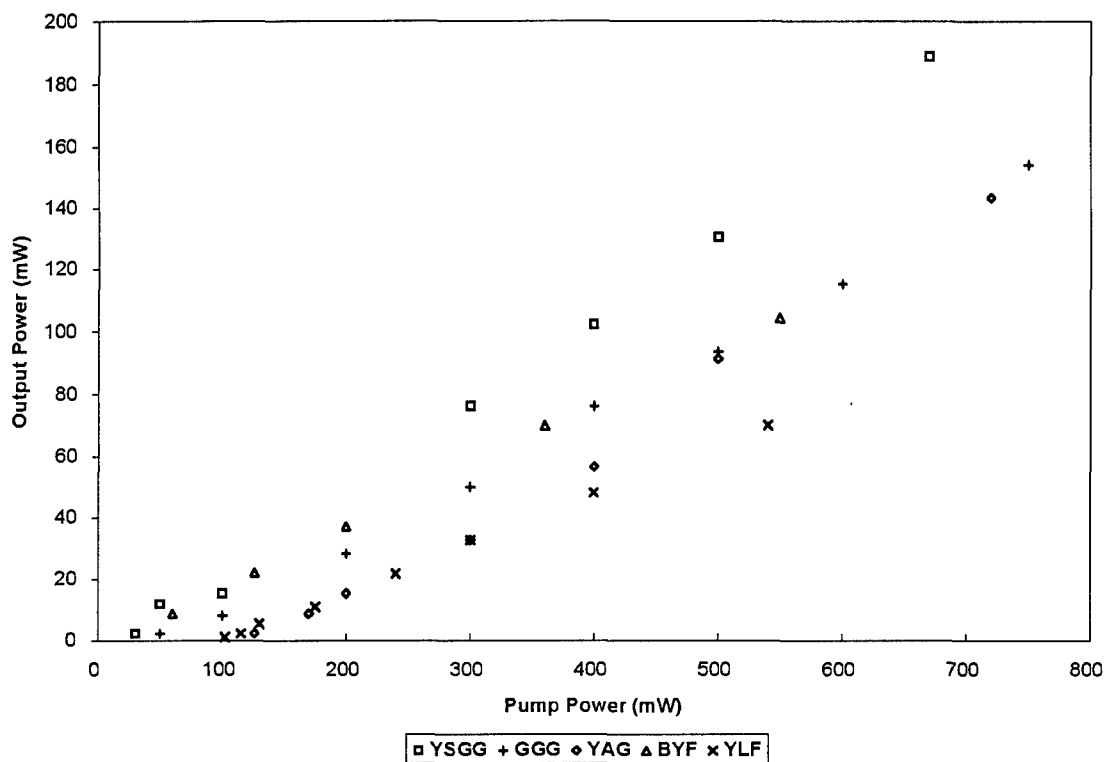


Figure 67. Input-output data for Ti:sapphire-pumped, 3- μ m lasers

In addition to the standard monoliths, we operated a Ti:sapphire-pumped, 1-mm-thick monolith of Er:YAG to obtain single-line output, as discussed in Appendices B and F. We show the input-output data for this laser in Figure 68.

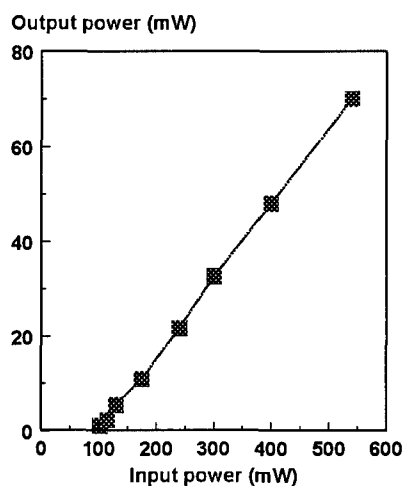


Figure 68. Er:YAG single frequency input-output data

The monoliths could be easily mounted in a liquid-nitrogen-cooled Dewar to examine operation at cryogenic temperatures. We did this for crystals of GGG, YSGG and YAG. Table 7 lists the pump wavelengths, observed thresholds and output wavelengths from the three materials at nominal liquid-nitrogen temperature. Both GGG and YAG exhibited multi-line operation and the spectral features were broad, with widths of 8 and 15 nm, respectively.

Table 7. Data on cryogenic 3- μ m lasers

Material	Pump wavelength (nm)	Laser wavelength(s) (nm)	Threshold power (mW)
GGG	969.5	2873.5 2867.4	7
YSGG	969.5	2869.5	6
YAG	969.4	2898.5 2858.4	14

Figure 69 shows the input-output power curves. One notable change from room temperature is the low threshold for YAG, which may be the result of an increased upper-state lifetime at cryogenic temperatures.

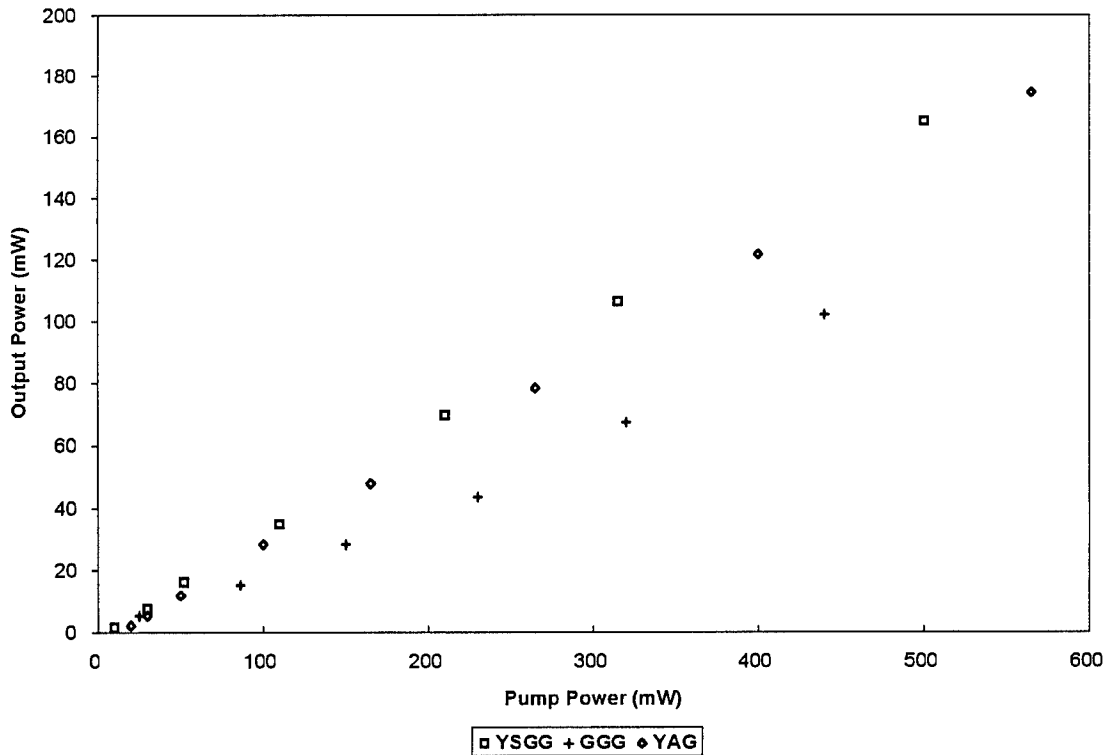


Figure 69. Input-output power data for Ti:sapphire-pumped, cryogenic 3- μ m lasers

One of the most significant uses for the Ti:sapphire pump laser was in determining the affect of pump wavelength on laser output power. We scanned the pump laser wavelength in a system similar to that shown in Figure 34, and measured the output power of the monoliths, in most cases at two average pump-power levels, one near threshold and the other well over threshold. Data for YSGG also appears in Figure 1 of Appendix B, where we have superimposed the absorption spectra for the material. In general, we did not find a major discrepancy between the absorption and laser excitation spectra. Any discrepancy would have been the result of excited-state absorption of the pump, as discussed in Section 5.1. We note that the cw lasers operated with fairly low inversion densities, and our results do not rule out the potential for excited-state absorption at the inversion densities used in pulsed, Q-switched Er-doped lasers.

Figures 70-73 show laser excitation data for GGG, YSGG, YAG and BYF, respectively. Except for YAG, where the threshold power was high, we took data at two pump levels, and the ratios over threshold are calculated at the most optimal pump wavelength. The long short-wavelength tails in the YSGG and GGG data do correspond to real absorption regions in the crystal, and are not a nonlinear effect.

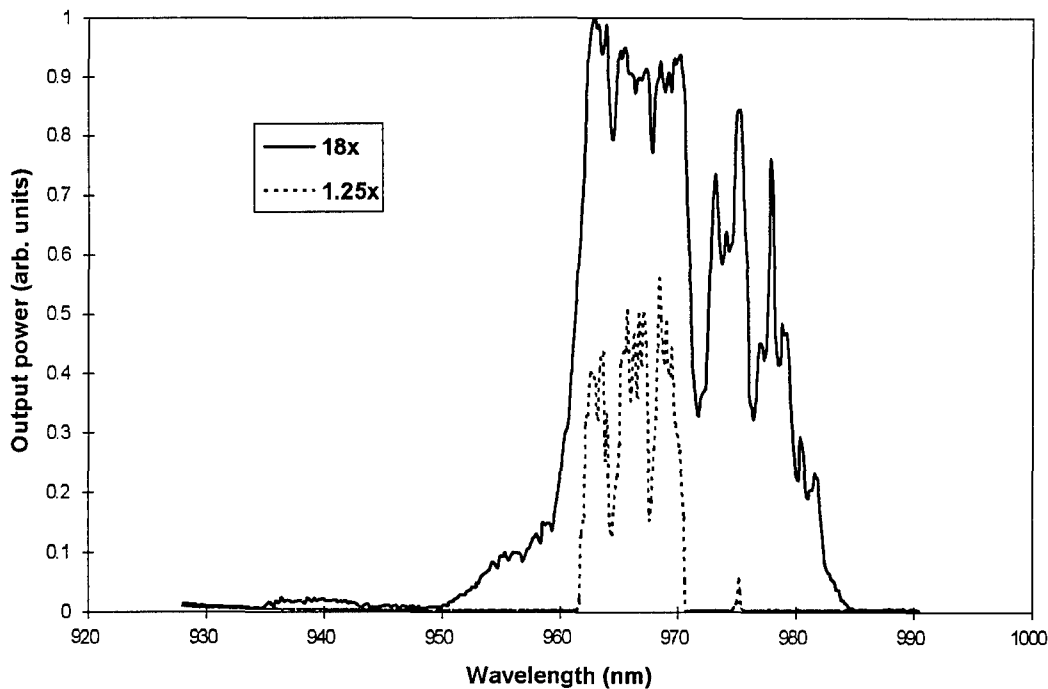


Figure 70. Laser excitation spectra for GGG, at two ratios over threshold.

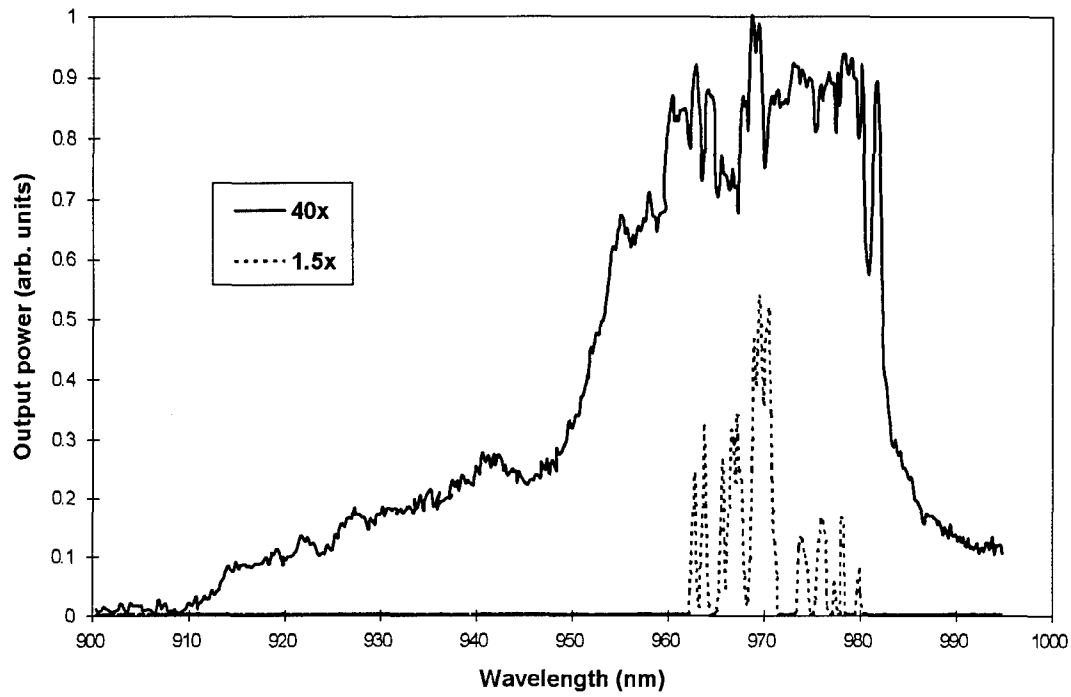


Figure 71. Laser excitation spectra for YSGG, at two ratios over threshold

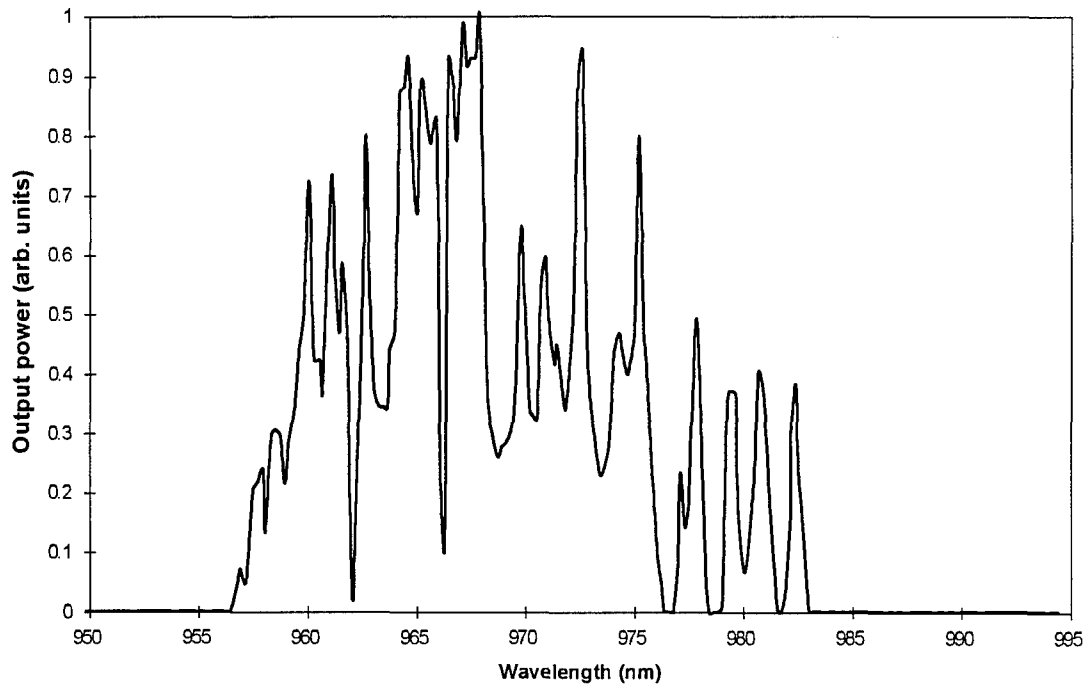


Figure 72. Laser excitation spectrum for YAG

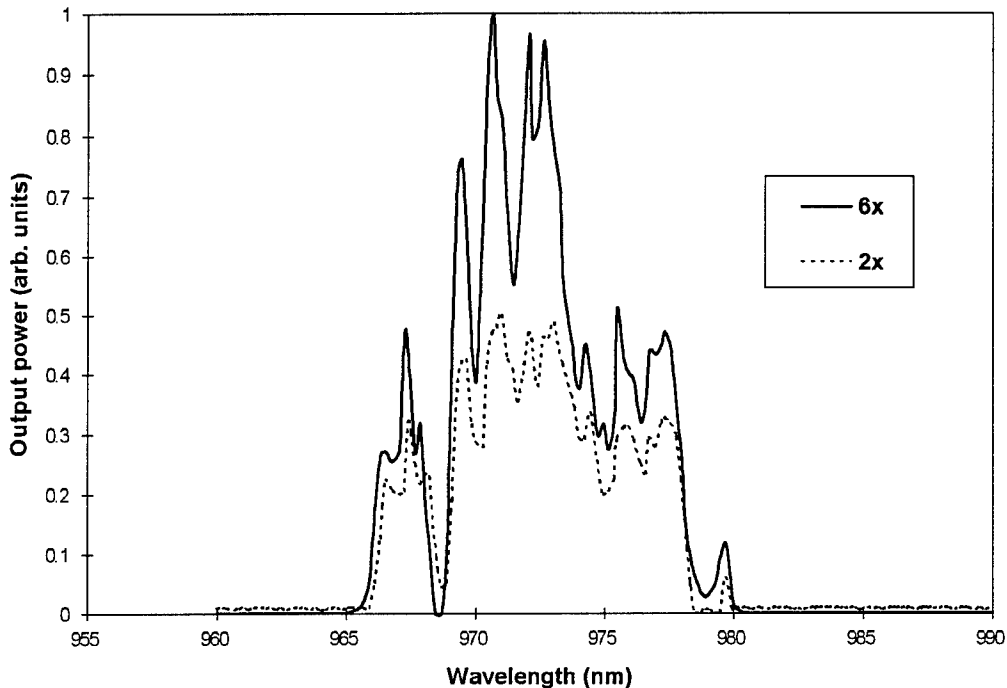


Figure 73. Laser excitation spectra for BYF, at two ratios over threshold

6.2 Diode-pumped, cw 3- μm lasers

At the outset of the program, semiconductor lasers operating in the 970-nm wavelength region were still laboratory devices. Shortly after the program began, SDL, Inc. commercialized strained-quantum-well InGaAs lasers and we could obtain devices suitable for pumping Er-doped materials directly into the 3- μm laser upper state. Details discussion of our work with the diodes as pump sources appears in Chapter 4 of Appendix A, as well as in Appendices B-E.

The first device we obtained was a single-transverse-mode, 50-mW laser (SDL-6302-H1) and we characterized its input-output and temperature-tuning characteristics. Figure 74 shows the temperature tuning data, which indicates that the device tunes at a rate of 0.27 nm/C. and was capable of accessing the Er absorption region. We used the 50-mW device as a pump source for the YSGG, GGG and BYF monoliths, and input-output data appears in Figures 75 and 76. The low-power, diode-pumped monoliths served as the probe sources for our gain-measurement experiments.

SDL introduced higher-power, multimode devices (SDL-6552-P1), with power outputs at the 1-W level from a 100- μm -wide stripe. These devices allowed us to obtain higher power levels from GGG, YSGG and BYF and also allowed us to overcome the high threshold power of YAG and obtain diode-pumped operation. We subsequently used the diode-pumped YAG laser as a source for experiments done at the Aerospace Corporation. The sensitive nature of this work precludes more detailed discussion in this unclassified document. To obtain the highest power levels from the monoliths we polarization-combined two of the 1-W devices in an arrangement shown schematically in

Figure 77. Input-output data for monoliths pumped by the two-diode system appear in Figure 78. We were not able to tune the 1-W devices to an optimum pump wavelength for BYF, which was longer than that for the other hosts, and thus we do not believe the high-pump-power data represents the best obtainable for that material.

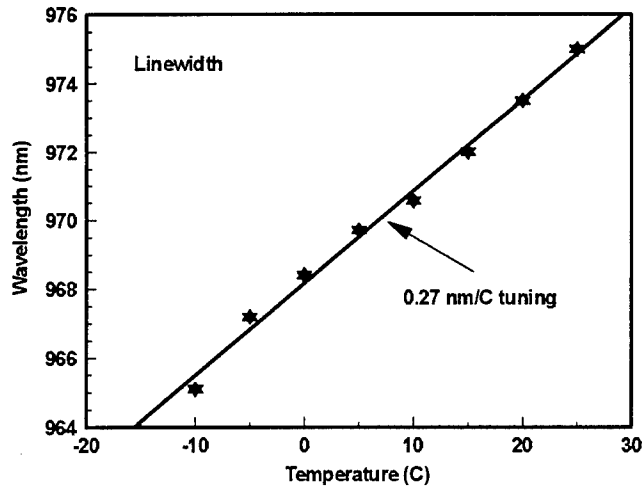


Figure 74. Temperature-tuning data for SDL-6302-H1 diode laser

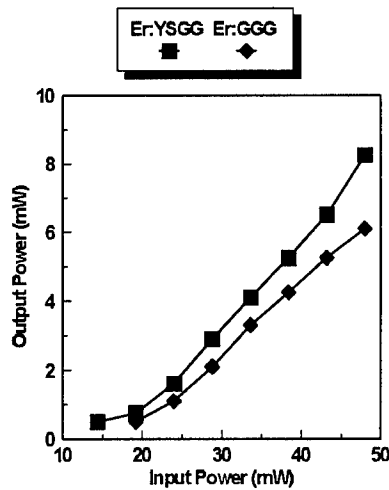


Figure 75. Input-output data for diode-pumped YSGG and GGG monoliths

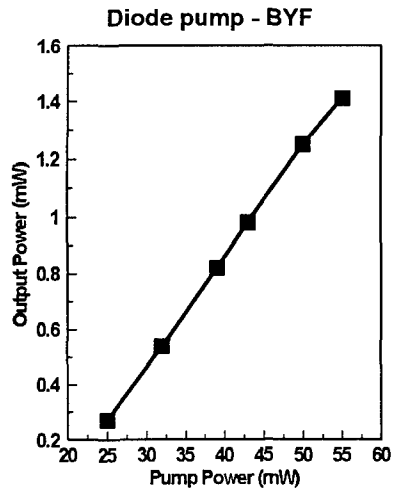


Figure 76. Input-output data for diode-pumped BYF monolith

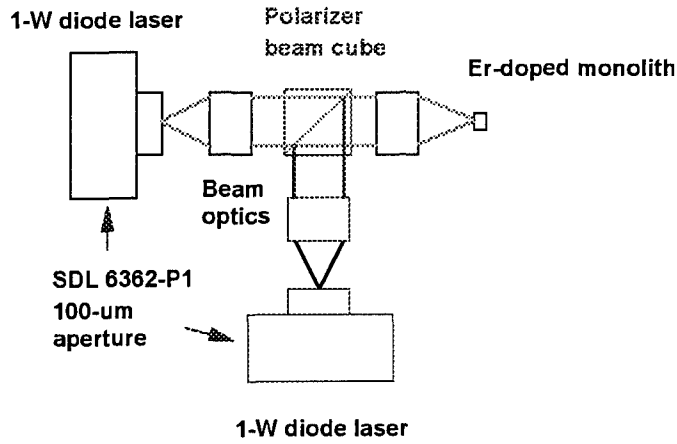


Figure 77. Schematic of double-diode pumping system

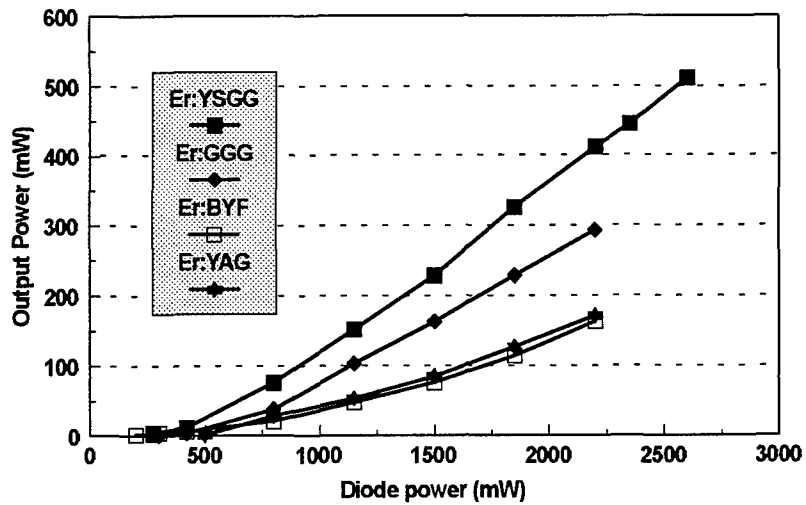


Figure 78. Input-output data for double-diode pumped monoliths

6.3 Diode-pumped, pulsed 3- μm lasers

We were able to obtain the loan of a SDL, 970-nm pulsed diode array from Dr. J. Andrew Hutchinson at the Army NVESD for use as a pump source with 3- μm , Er-doped lasers.

Our experiments, which must be considered of a preliminary nature, employed the array in an end-pumped configuration, similar to that described by Shannon and Wallace to excite oscillation in Nd:YAG [Opt. Lett. **16**, 5 (1991)]. Figure 79 is a schematic of the laser design. The Er-laser resonator consisted of a plano/Brewster gain element and a concave high reflector. The flat, pump surface of the laser crystals we used were dichroically coated for high transmission (HT) at 0.97 μm and high reflection (HR) at 2.8 μm . The internal Brewster's angle facet of the crystals eliminated the need for 3- μm anti-reflection (AR) coatings, which typically suffer from water adsorption, and are very lossy, sometimes more so than an uncoated surface. The laser crystals were 7-mm, along the propagation axis. The high-reflector had a 10 cm radius-of-curvature, and we placed CaF_2 window within the cavity, rotatable about Brewster's angle, to provide variable output coupling. The physical length of the resonator was 8.5 cm, for which the calculated mode dimensions (diameters) are 396 μm x 812 μm at the coated crystal surface, and 1231 μm x 1336 μm at the external mirror.

Our pump laser was a 1-cm-long, single diode-laser bar (SDL 3230-TS), capable of operation at 970 nm with a 2.5% duty factor. We drove the device with an Analog Modules 770-34 driver, which had an adjustable pulsewidth and rate. The maximum peak power out of the bar was 80 W. We coupled the pump emission into the laser crystal with a 3-element optical lens system and placed an uncoated rod lens ($f=1.2$ mm) in near-contact with the diode laser to collect the emission in the highly divergent plane (perpendicular to the plane of the diode junction). An aspheric lens ($f=8.5$ mm, AR @ 0.97 μm) placed ~ 9 mm from the rod lens and ~ 5 mm from the laser crystal collected and focused the emission onto the pump surface of the crystal. We included a cylindrical lens ($f=12.7$ mm, AR @ 0.97 μm) to reduce astigmatism and placed it between the rod lens and the sphere at a distance of ~ 6 mm from the rod lens. Based on Shannon and Wallace, we estimate the focused spot at the crystal to be 1.1 mm x 150 μm . Note that these dimensions do not favor TEM_{00} -mode operation since the pump volume significantly overfills the mode volume.

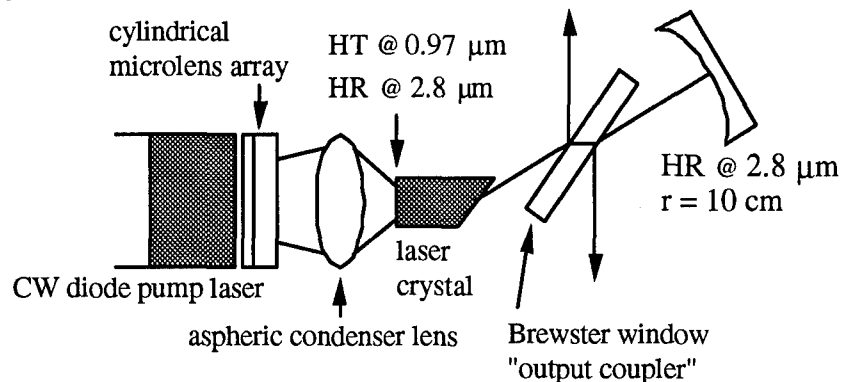


Figure 79 Schematic of pulsed-laser system

We fabricated laser crystals from YSGG, GGG (30%) and BYF, and bonded them to water-cooled, copper heatsinks. The BYF sample developed a small fracture during the coating procedure and showed significant scattering when probed with a visible helium-neon laser, thus the data may not fairly reflect the relative performance of BYF with the other crystals. Input/output data for YSGG, GGG and BYF are shown in Figures 80, 81 and 82, respectively, for pulsewidths ranging from 0.2 msec to 1.0 msec at a 10 Hz repetition rate. Figure 83 compares data for the three materials at the 1-msec pulsewidth level. The measured output pulse energies reflect the sum of the output from both the front and back surfaces of the intracavity Brewster window. The pump energies are those incident on the laser crystal. Maximum pulse energies obtained at 1.0 msec, 20 Hz were 3.8 mJ from YSGG, 2.0 mJ from GGG, and 3.8 mJ from BYF.

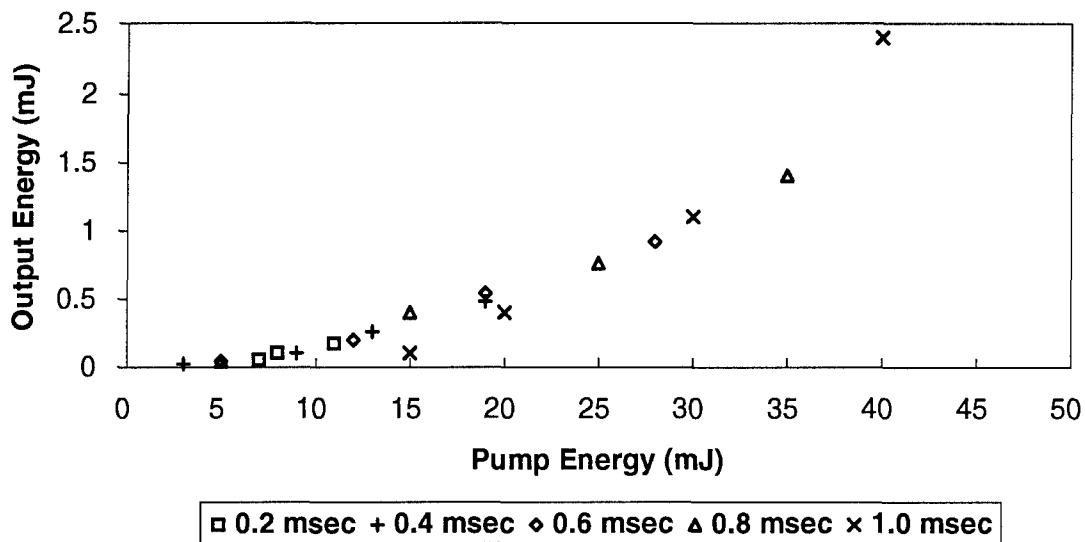


Figure 80. Input-output data for pulsed YSGG laser

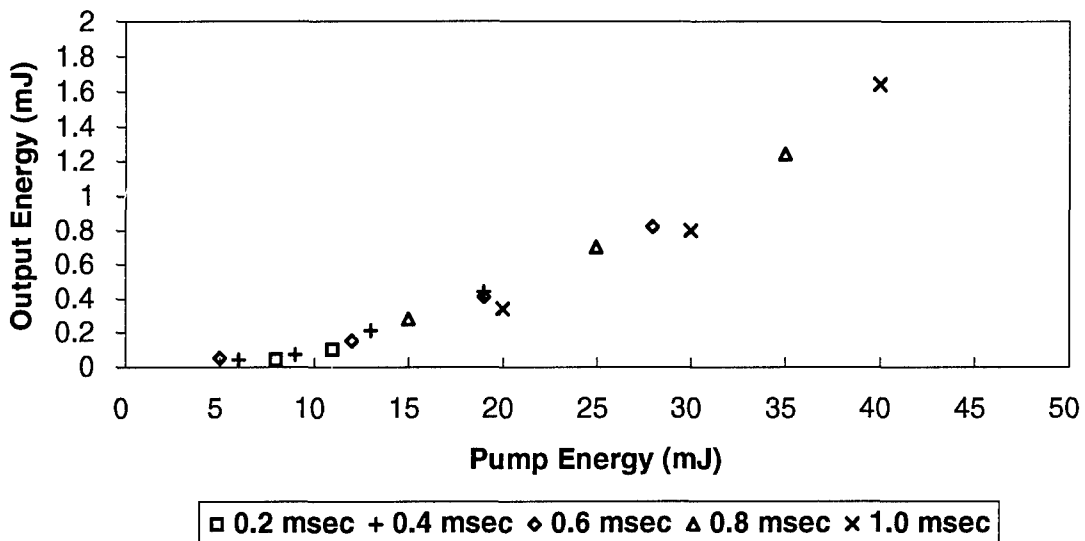


Figure 81. Input-output data for pulsed GGG laser

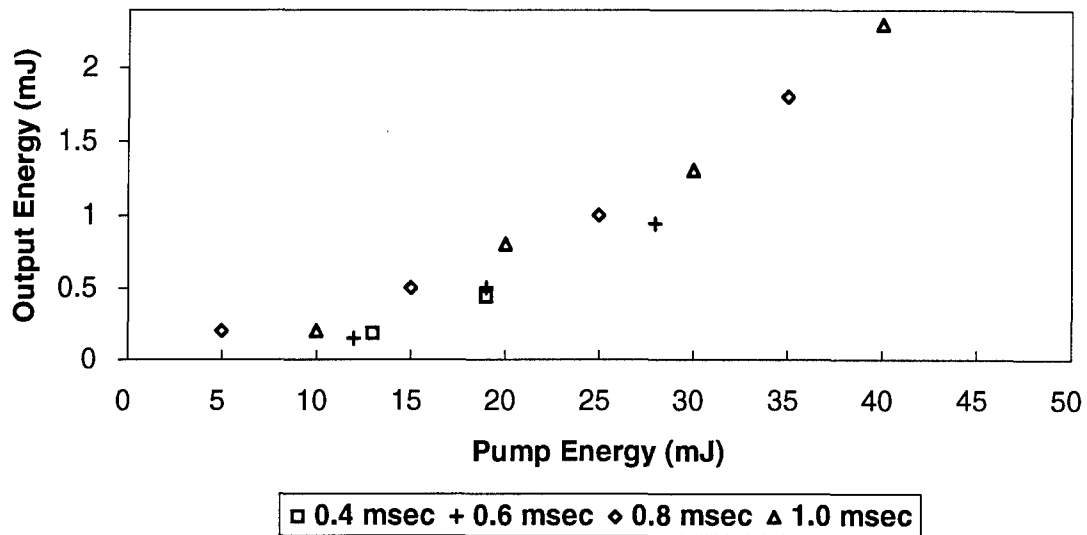


Figure 82. Input-output data for pulsed BYF laser

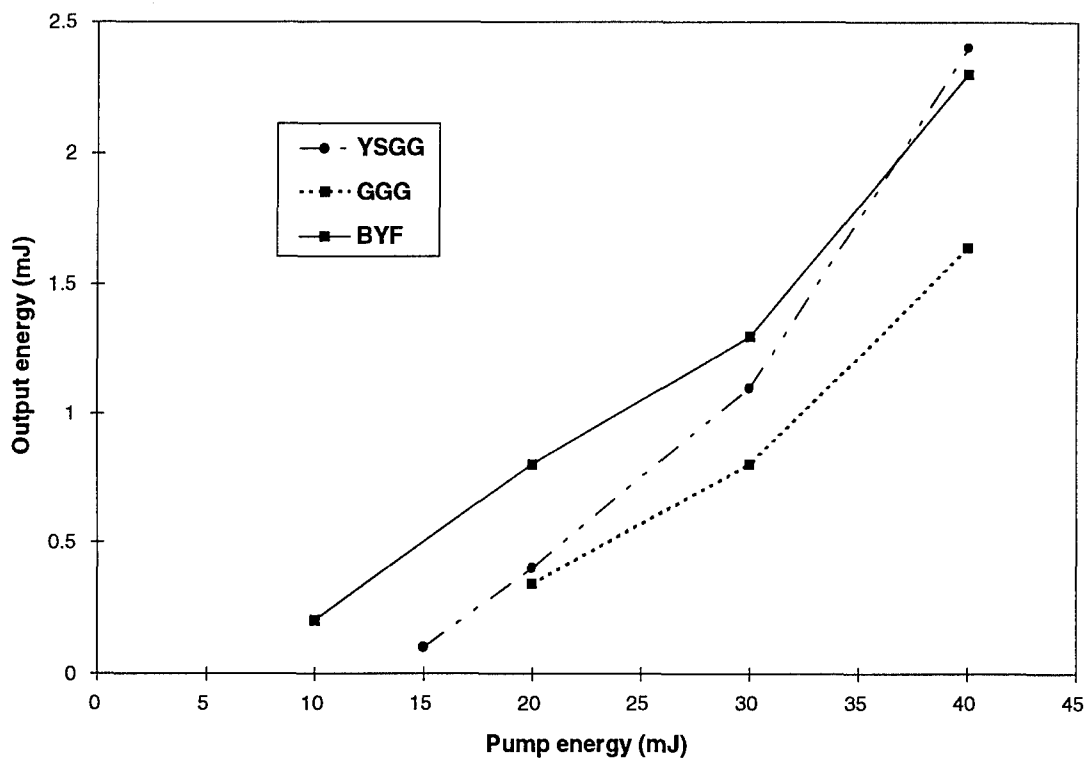


Figure 83 Comparison of pulsed-laser performance for 1-msec pulsewidths

Examination of the input-output data indicates that the slope efficiency of the system increases superlinearly as the pump pulsewidth broadens. The cause of this effect is unclear, but might become evident when we can model the dynamic behavior of the lasers. The lower energy threshold of BYF compared to the other crystals is consistent with the gain experiments described in Section 5.2. The general lower efficiency of the

pulsed lasers compared to the cw devices is undoubtedly due to the poor overlap between the pumped volume and resonator mode.

The open resonators in our pulsed lasers are an important step in the development of more advanced laser systems employing Q-switches and/or tuning elements. The results presented here were obtained with non-optimized systems. Current and future investigations should include more efficient coupling of the pump emission into the resonator mode in order to obtain TEM₀₀ operation and higher output powers, the use of standard output couplers to produce a single output beam, and the use of higher-power, cw diode-laser bars as pump sources.

6.4 Pulsed 1.6- μm laser operation from Er:YOS

For 3- μm Er-doped lasers the first-order choices of host crystals are materials where the $^4I_{11/2}$ -state lifetime is long and preferably comparable to or greater than that of the $^4I_{13/2}$ state. Second-order choices include consideration of upconversion and cross relaxation coefficients. For 1.6- μm Er-doped lasers the criteria are different; we want materials where the $^4I_{11/2}$ -state lifetime is short and decay is non-radiative into the $^4I_{13/2}$ state. A short lifetime prevents a large population buildup in the $^4I_{11/2}$ state, which can lead to losses through upconversion. In addition, if we sensitize the material with Yb ions, the short lifetime reduces the rate of back-transfer from Er to Yb. Figure 84 shows the Er energy levels and presents our data on lifetimes of candidate materials for 1.6- μm lasers. From the Figure, both YOS and YVO have shorter lifetimes than YAG, and we chose them for investigation.

A major problem with obtaining operation on the 1.6- μm laser transition is the need to overcome ground-state absorption. The transition is not strictly 3-level, as we can operate on transitions that terminate on higher-lying levels of the ground $^4I_{15/2}$ manifold. Figure 85 presents a calculation of the gain in Er:YOS as a function of relative inversion, the ratio of upper-level population to total population. The calculation, based on the standard McCumber approach was done with knowledge of the absorption spectrum and of the "zero-phonon" line energy. As is clear from the Figure, we need large inversions (<0.3) to obtain even small levels of gain.

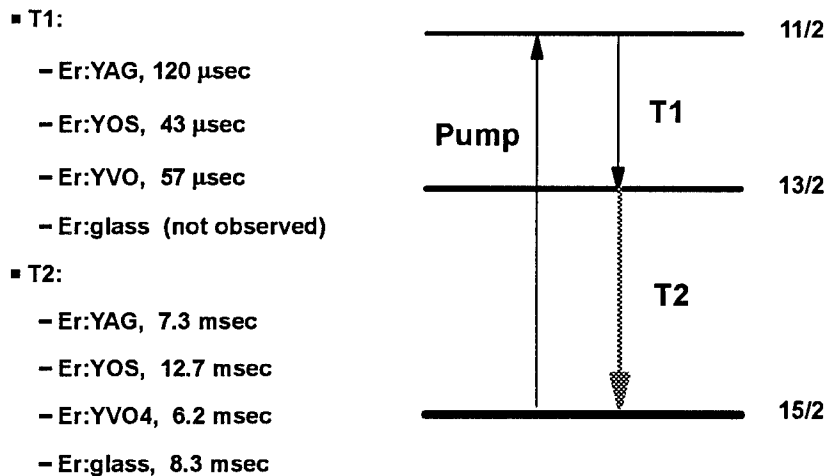


Figure 84. Properties of candidate Er-doped materials for 1.6- μm laser operation

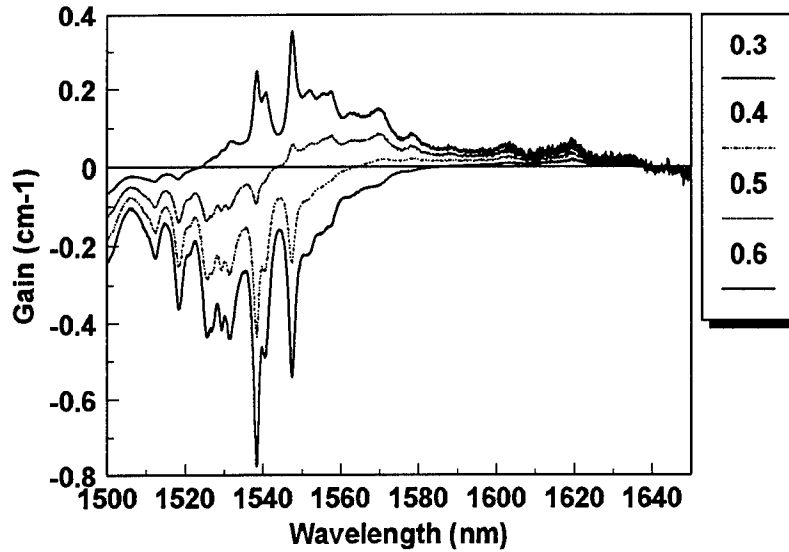


Figure 85. Gain in Er:YOS

In order to keep the threshold pump energies low, the Er doping must be low, which leads to difficulty in obtaining good coupling to the optical pump source, given that the absorption coefficient for the pump will be small. Our first and only success in obtaining pulsed operation from Er:YOS involved end-pumping with the pulsed Cr:LiSAF laser. The laser experiment is diagrammed in Figure 86. The laser operated at a wavelength of 1.547 μm , but the crystal fractured after a short period of operation. The threshold energy of 300 mJ was substantial, and not encouraging for the prospect of diode pumping.

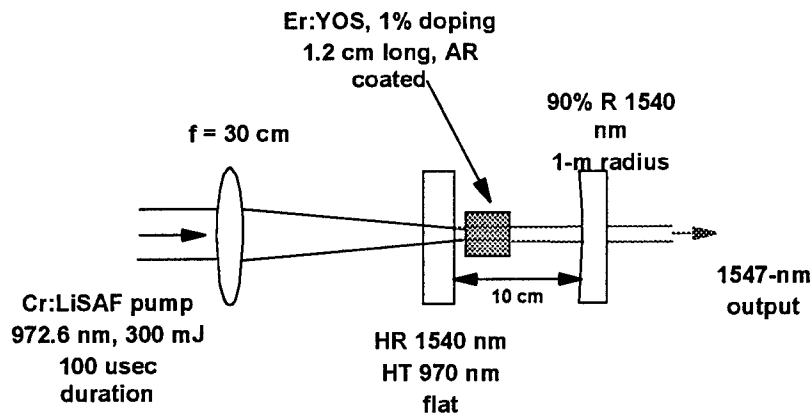


Figure 86. Configuration for 1.5- μm Er:YOS laser

6.5 Non-cw laser operation at 1.6 μm

With the rapid development of high-power parametric oscillators, which provide efficient conversion of Nd:YAG Q-switched lasers into 1.5-1.6- μm , eyesafe sources, we concluded that the need for development of pulsed Er-doped lasers at 1.6 μm was no

longer important. There might be some application for cw sources, in areas such as coherent lidar or fiber communications, and we directed our efforts at attempts to obtain cw laser action from YOS and YVO. In this case we used Yb-sensitized crystals, which had more intense absorption at the pump wavelength due to the high concentration of Yb ions. Figure 87 shows the experimental configuration we used for both materials. At power levels ranging from 400 mW at 900 nm to 240 mW at 970 nm, and with a 10-cm focusing lens, we were not able to obtain any indication of laser action from either material.

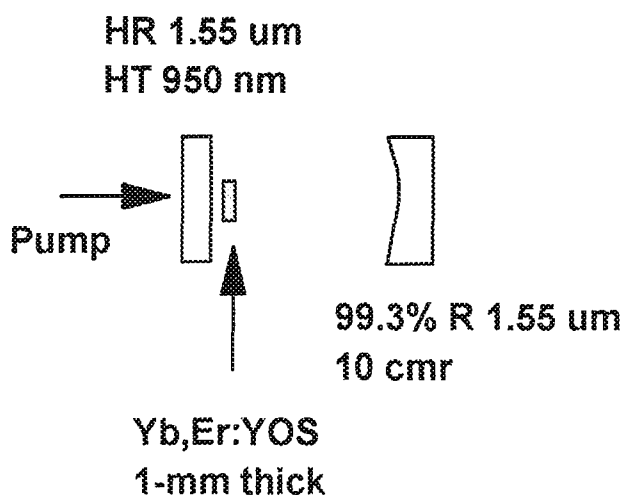


Figure 87. Schematic of cw non-laser configuration

It should be clear from this report that the effort put into the study of 1.6- μm Er-doped lasers was not as extensive as that for 3- μm lasers. Thus we have fewer fundamental spectroscopic measurements to help explain our inability to obtain cw laser action from the candidate YVO and YOS materials. The effect of upconversion from the upper laser state would likely raise the threshold pumping rate, but the extent of this effect is unknown. Crucial data missing include upconversion coefficients and the level of cross relaxation for Er ions in the two materials, and the effectiveness of sensitization of Er by Yb ions. Future work should emphasize these and other measurements and may lead to a more optimal choice of doping levels as well as the attainment of laser operation.

7. Appendices

7.1 Appendix A - Ph.D. Thesis

Spectroscopic Characterization and 3- μm CW laser Operation of $\text{Er}^{3+}:\text{Gd}_3\text{Ga}_5\text{O}_{12}$ and $\text{Er}^{3+}:\text{Y}_3\text{Sc}_2\text{Ga}_5\text{O}_{12}$

Ph.D. Thesis submitted by Bradley J. Dinerman to Boston College

BOSTON COLLEGE
GRADUATE SCHOOL OF ARTS AND SCIENCES
Department of Physics

SPECTROSCOPIC CHARACTERIZATION AND 3- μ m CW LASER OPERATION
OF $\text{Er}^{3+}:\text{Gd}_3\text{Ga}_5\text{O}_{12}$ AND $\text{Er}^{3+}:\text{Y}_3\text{Sc}_2\text{Ga}_3\text{O}_{12}$

a dissertation
by
Bradley J. Dinerman

Submitted in partial fulfillment of the requirements
for the degree of Doctor of Philosophy

May, 1994

© copyright by BRADLEY JAY DINERMAN

1993

Abstract

Trivalent erbium (Er^{3+}), when doped into the insulating crystals $\text{Gd}_3\text{Ga}_5\text{O}_{12}$ and $\text{Y}_3\text{Sc}_2\text{Ga}_3\text{O}_{12}$ (GGG and YSGG, respectively), displays numerous channels for energy transfer and radiative decay. The spectroscopic and 3- μm laser properties of these ion-host combinations are studied and modelled in a series of experiments.

GGG and YSGG belong to the gallium-garnet class of crystalline materials, in which rare-earth impurities substitute into the non-centrosymmetric sites of Gd^{3+} and Y^{3+} , respectively. These hosts characteristically exhibit lower phonon energies than aluminum garnets, such as YAG, and therefore have potential to display relatively high radiative quantum efficiencies of luminescent transitions. Ease of growth and mechanical durability also influence the decision to use these materials.

Spectroscopic analyses, which include absorption, emission, and lifetime measurements, are made for each material in Chapter 2. The Judd-Ofelt Theory is applied to the integrated, room-temperature absorption spectra of ground-state transitions in the visible and near-infrared. The three Judd-Ofelt Parameters are determined and used to further calculate electric-dipole transition probabilities, radiative lifetimes, branching ratios, and radiative quantum efficiencies of many of the 4f excited states. The results reveal radiative lifetimes significantly longer than those actually observed for the $^4\text{I}_{11/2}$, $^4\text{I}_{9/2}$, and $^4\text{S}_{3/2}$ states, which indicate that strong quenching processes operate in these media. Radiative quantum efficiencies of 24% and 32% are observed from the $^4\text{I}_{11/2}$ state for GGG and YSGG, respectively.

The role of upconversion energy-transfer from the $^4\text{I}_{11/2}$ and $^4\text{I}_{13/2}$ states of Er:GGG and Er:YSGG is examined in Chapter 3. These are the upper and lower states, respectively, of the 3- μm laser transition. Different upconversion mechanisms affect both states by removing population from them and redistributing the excitation to other electronic

states. A knowledge of the effect of upconversion on the populations of these states therefore indicates the potential of these materials as cw-laser gain media. An experiment is conducted in which the luminescence which occurs from the $^4S_{3/2}$ and $^4I_{9/2}$ states following chopped, cw pumping is analyzed in two time domains: that resulting from direct excitation and that resulting following upconversion-induced excitation.

The ratio of upconversion-induced luminescence to pump-induced luminescence is quantified and applied to a simplified four-equation rate model, from which values of the $^4I_{13/2}$ and $^4I_{11/2}$ upconversion coefficients, α_1 and α_2 , are calculated. The calculated α_1 is typically larger than the calculated α_2 , which partially explains the mechanism by which cw laser oscillation occurs. The result is that upconversion removes population from the lower laser state, some of which is 'recycled' into the upper laser state.

The values calculated for α_1 and α_2 are compared to those predicted from a direct rate-equation model by inserting the calculated values into the equations with appropriate spectroscopic parameters and observing the predicted rate of change of the upconversion ratios. The observed and the calculated ratios are in most cases in excellent agreement. 30%-erbium-doped YSGG shows higher rates of upconversion from the $^4I_{13/2}$ state and lower rates from the $^4I_{11/2}$ state than 30%-erbium-doped GGG, indicating that YSGG may perform more efficiently than GGG as a cw 3- μ m laser..

The 3- μ m laser properties of Er:GGG and Er:YSGG are investigated in Chapter 4. Monolithic laser resonators are used to avoid losses typically associated with atmospheric water-vapor absorption and poor anti-reflection coatings of conventional, external resonators in the 3- μ m spectral region. The lasers are pumped directly into the $^4I_{11/2}$ upper state near 0.97 μ m by either a Ti:sapphire or InGaAs diode laser. Excitation spectra are obtained by tuning the Ti:sapphire laser over the absorption bands and observing the 3- μ m output as a function of pump wavelength. Pump wavelengths near 965 nm typically result in the most intense emission, and are therefore selected as the standard pump wavelength.

Slope efficiencies approaching the theoretical quantum limit are obtained, and high output powers are observed. Greater than 0.5-W of 2.79- μm laser emission and nearly 0.3-W of 2.82- μm emission are observed from diode-pumped Er:YSGG and Er:GGG, respectively. The efficiencies and properties of the two host materials are typically very similar, yet YSGG categorically operates better than GGG. This may be attributed to the rates of upconversion calculated in Chapter 3.

The spectral and spatial characteristics of the emission are also observed. The lasers typically operate on four or five longitudinal modes. Tunable, single-frequency emission is demonstrated from Er:YAG at 2.94- μm . TEM_{00} -mode operation from GGG and YSGG is observed under Ti:sapphire-pumped conditions; multimode operation is observed from the diode-pumped system.

Acknowledgements

I gratefully acknowledge the assistance and support of many people without whom this dissertation would not have been possible:

Dr. Baldassare (Rino) Di Bartolo: thesis advisor and philosopher extraordinaire. My studies were guided from beginning to end by your many years of experience as both a spectroscopist and a professor. I especially appreciate the opportunities that you gave to me in Erice and Hampton, and will not forget them.

Dr. Peter Moulton: physicist, boss, and maker of horrible puns. I thank you for giving me the opportunity to conduct my research at Schwartz Electro-Optics and for having faith in my work over the past three years. You correctly pointed out that all clouds have an erbium lining, and I hope that the results that have come from this research will be of benefit now and in the future. So, Peter, now that the Ph.D. is official, maybe we can discuss some salary upconversion?

I thank Drs. Michael Graf and George Goldsmith for assisting on my thesis committee. I sincerely hope the material was not too uninteresting (you may lie if it was), and I appreciate your critiques of the work.

I also acknowledge the help of everyone at Schwartz Electro-Optics, who showed me the workings of lasers, lasers, and more lasers. These include, in no special order: Henry Zenzie, Andrew Finch, Glen Rines, James Harrison, David Welford, John Flint, Gail Scott, David Rines, Fred Roebuck, James Bushee, Richard Schwarz, Yelena Isyanova, Marilyn Lubenau, and Robert Martinsen (of Lightwave Atmospheric).

I thank Brian Walsh of Boston College for developing and supplying the computer software to calculate the Judd-Ofelt Parameters. This program proved to be an invaluable tool to ease the horrors of multiple-equation solving. I recommend that anyone involved in calculations of this sort contact Brian for assistance.

There are probably others whom I neglected to acknowledge. If you are one of these, whoever you are and for whatever you did, I thank you.

This research was supported by the Advanced Research Projects Agency (ARPA) under the ARPA Solid State Laser and Nonlinear Materials Program, contract number N00014-90-C-0235.

I would like to conclude my acknowledgements with a quote from Henry Zenzie of Schwartz Electro-Optics, who, after having seen my equations on the computer screen shortly before thesis completion, optimistically told me, "Anything this complicated can't possibly predict reality." Ouch.

Dedication

This thesis is gratefully and lovingly dedicated to my parents, Gerald and Phyllis Dinerman. I am reminded of the day of my first graduate-level class at Boston College, after which I came home and announced, “This isn’t for me. I think I should forget about school and open a health club, or something like that”.

Despite my reservations, and after deciding that I really was their child and not just switched with another in the hospital, they gave me the encouragement and motivation to continue. I thank them for their constant ‘shove and love’ which helped me to continue to where I am today. I would also like to ask them for a raise in my allowance.

Table of Contents

Acknowledgements.....	i
Dedication.....	iii
Table of Contents.....	iv
List of Tables.....	vi
List of Figures.....	viii
Chapter 1: Introduction.....	1
1.1 General Goals of the Research.....	1
1.2 Specific Goals of the Research.....	3
1.3 Lasers Today.....	4
1.4 General Background.....	6
References for Chapter 1.....	9
Chapter 2: Spectroscopy of Er ³⁺ :GGG and Er ³⁺ :YSGG.....	10
2.1 Introduction to Chapter 2.....	10
2.2 Physical Properties of GGG and YSGG.....	11
2.3 Electronic States and the Crystal Field.....	14
2.4 Electronic States and Transition Probabilities: The Judd-Ofelt Theory.....	17
2.5 Spectral Characteristics of Er:GGG and Er:YSGG.....	22
2.6 Calculation of the Judd-Ofelt Parameters.....	42
2.7 Discussion of the Judd-Ofelt Results.....	51
References for Chapter 2.....	53
Chapter 3: Energy Transfer in Er:GGG and Er:YSGG.....	55
3.1 Introduction to Chapter 3.....	55
3.2 Energy Transfer within Rare-Earth-Doped Solids.....	56
3.3 Energy Transfer: The Förster-Dexter Theory.....	59

3.4 Energy Transfer in Er ³⁺	62
3.5 Rate Equations.....	66
3.6 Determination of the Upconversion Coefficients.....	69
3.7 Discussion of Experimental Results	80
References for Chapter 3.....	87
Chapter 4: Laser Operation of Er:GGG and Er:YSGG.....	88
4.1 Introduction to Chapter 4.....	88
4.2 Three-, Four-, and Quasi-Three-Level Lasers.....	89
4.3 The Laser Oscillator.....	91
4.4 CW Laser Measurements.....	95
A. Excitation Data.....	95
B. Power, Temperature, Spectral, and Spatial Data	99
References for Chapter 4.....	107
Chapter 5: Summary and Conclusions	108
5.1 Introduction to Chapter 5.....	108
5.2 Summary of the Results.....	109
5.3 Suggestions for Future Work.....	113
Appendix: Relevant Publications.....	118

List of Tables

- Table 2-1: Some mechanical and optical properties of undoped GGG, YSGG, and YAG.
- Table 2-2: Calculated values of the squares of the reduced matrix elements for Er^{3+} transitions from the $^4\text{I}_{15/2}$ ground state.
- Table 2-3: Calculated values of the squares of the reduced matrix elements for Er^{3+} transitions of the given state.
- Table 2-4: Energies (in cm^{-1}) of the levels in the four lowest states of Er^{3+} in GGG, YSGG, and YLF.
- Table 2-5: Measured values of the $^4\text{S}_{3/2}$, $^4\text{I}_{9/2}$, $^4\text{I}_{11/2}$ and $^4\text{I}_{13/2}$ radiative lifetimes of Er^{3+} in GGG and YSGG for different concentrations; as well as the ratio of the $^4\text{I}_{13/2}$ and $^4\text{I}_{11/2}$ lifetimes.
- Table 2-6: Calculated values of feeding efficiencies and cross-relaxation efficiencies for the $^4\text{I}_{9/2} \rightarrow ^4\text{I}_{11/2}$ and $^4\text{I}_{13/2} \rightarrow ^4\text{I}_{15/2}$ transitions as functions of material and ion concentration.
- Table 2-7: Data extracted from absorption spectra of Er:GGG (30%) used to calculate the Judd-Ofelt Parameters.
- Table 2-8: Data extracted from absorption spectra of Er:YSGG (30%) used to calculate the Judd-Ofelt Parameters.
- Table 2-9a: Values of branching ratios, electric- and magnetic-dipole transition probabilities, and lifetimes for excited-state transitions in Er:GGG (30%), as calculated from the Judd-Ofelt Theory.
- Table 2-9b: Values of branching ratios, electric- and magnetic-dipole transition probabilities, and lifetimes for excited-state transitions in Er:GGG (30%), as calculated from the Judd-Ofelt Theory.

- Table 2-10a: Values of branching ratios, electric- and magnetic-dipole transition probabilities, and lifetimes for excited-state transitions in Er:YSGG (30%), as calculated from the Judd-Ofelt Theory.
- Table 2-10b: Values of branching ratios, electric- and magnetic-dipole transition probabilities, and lifetimes for excited-state transitions in Er:YSGG (30%), as calculated from the Judd-Ofelt Theory.
- Table 3-1: Upconversion data for Er:YSGG (30%).
- Table 3-2: Upconversion data for Er:GGG (30%).
- Table 3-3: Upconversion data for Er:GGG (10%).
- Table 3-4: Parameters used and results obtained for selected example of upconversion data.
- Table 4-1: Values of laser thresholds and slope efficiencies for different erbium lasers as functions of crystal temperature and pump source.
- Table 4-2: Erbium-laser wavelengths as functions of host and temperature.

List of Figures

- Figure 2-1: Absorption spectra of undoped (a) GGG and (b) YSGG.
- Figure 2-2: Electronic energy states of erbium.
- Figure 2-3: Visible absorption spectrum of Er:YSGG (30%) at 300 K.
- Figure 2-4: Visible absorption spectrum of Er:GGG (30%) at 300 K.
- Figure 2-5: $^4I_{15/2} \rightarrow ^4I_{11/2}$ absorption spectrum of Er:YSGG (30%) at 300 K.
- Figure 2-6: $^4I_{15/2} \rightarrow ^4I_{11/2}$ absorption spectrum of Er:GGG (30%) at 300 K.
- Figure 2-7: $^4I_{15/2} \rightarrow ^4I_{13/2}$ absorption spectrum of Er:YSGG (30%) at 300 K.
- Figure 2-8: $^4I_{15/2} \rightarrow ^4I_{13/2}$ absorption spectrum of Er:GGG (30%) at 300 K.
- Figure 2-9: Visible absorption spectrum of Er:GGG (30%) at 77 K.
- Figure 2-10: $^4I_{15/2} \rightarrow ^4I_{11/2}$ absorption spectrum of Er:GGG (30%) at 77 K.
- Figure 2-11: $^4I_{15/2} \rightarrow ^4I_{13/2}$ absorption spectrum of Er:GGG (30%) at 77 K.
- Figure 2-12: $^4I_{11/2} \rightarrow ^4I_{15/2}$ emission spectrum for Er:YSGG (30%) at 300 K.
- Figure 2-13: $^4I_{11/2} \rightarrow ^4I_{15/2}$ emission spectrum for Er:GGG (30%) at 300 K.
- Figure 2-14: $^4I_{13/2} \rightarrow ^4I_{15/2}$ emission spectrum for Er:YSGG (30%) at 300 K.
- Figure 2-15: $^4I_{13/2} \rightarrow ^4I_{15/2}$ emission spectrum for Er:GGG (30%) at 300 K.
- Figure 2-16: $^4I_{11/2} \rightarrow ^4I_{13/2}$ emission spectrum for Er:YSGG (30%) at 300 K.
- Figure 2-17: $^4I_{11/2} \rightarrow ^4I_{13/2}$ emission spectrum for Er:GGG (30%) at 300 K.
- Figure 2-18: $^4I_{13/2} \rightarrow ^4I_{15/2}$ emission spectrum for Er:GGG (30%) at 77 K.
- Figure 2-19: $^4I_{11/2} \rightarrow ^4I_{13/2}$ emission spectrum for Er:GGG (30%) at 77 K.
- Figure 2-20: $^4I_{11/2}$ emission from (a) Er:GGG and (b) Er:YSGG for indicated concentrations at 300 K.
- Figure 2-21: $^4I_{13/2}$ emission from (a) Er:GGG and (b) Er:YSGG for indicated concentrations at 300 K.

- Figure 3-1: Basic Energy Transfer.
- Figure 3-2: Upconversion pathways within the erbium-doped system.
- Figure 3-3: Cross-relaxation pathways within the erbium-doped system.
- Figure 3-4: Experimental arrangement used to measure upconversion luminescence.
- Figure 3-5: Upconversion luminescence from Er:YSGG (30%).
- Figure 3-6: Comparison of upconversion ratios derived from data to values calculated from model for Er:YSGG (30%).
- Figure 3-7: Comparison of upconversion ratios derived from data to values calculated from model for Er:GGG (30%).
- Figure 3-8: Comparison of upconversion ratios derived from data to values calculated from model for Er:GGG (10%).
- Figure 3-10: Dependence of upconversion coefficients on upconversion ratio Y .
- Figure 3-11: Dependence of upconversion coefficients on upconversion ratio Z .
- Figure 3-12: Dependence of upconversion coefficients on $^4I_{9/2}$ radiative lifetime τ_3 .
- Figure 3-13: Dependence of upconversion coefficients on spot radius r .
- Figure 4-1: Partial energy-level diagram of a typical (a) three-level and (b) four-level laser .
- Figure 4-2: Dimensions and coatings of erbium laser monolith, and calculated TEM₀₀ resonator mode.
- Figure 4-3: Experimental arrangement used for excitation measurements.
- Figure 4-4: Laser excitation spectra for Er:GGG and Er:YSGG.
- Figure 4-5: Absorption spectra of Er:GGG (30%) and Er:YSGG (30%).
- Figure 4-6: Ti:sapphire-pumped erbium-laser power data for (a) 300 K and (b) 77 K.
- Figure 4-7: Diode-pumped erbium-laser power data for 77 K.
- Figure 4-8: Laser spectra of Ti:sapphire-pumped Er:GGG and Er:YSGG.

Figure 5-1: Experimental arrangement of diode-pumped erbium laser using external-mirror resonator.

Figure 5-2: Energy data as a function of pulsewidth at 10 Hz for pulsed-pumped Er:GGG.

Figure 5-3: Energy data as a function of pulsewidth at 10 Hz for pulsed-pumped Er:GGG.

Chapter 1: Introduction

1.1 General Goals of the Research

The development of coherent near-infrared light sources has motivated significant research in the past years. There are two general reasons for this interest. First, the strong absorption bands of water molecules in this region (especially near 3 μm) suggest that a laser emitting in the near-infrared could be used as an investigative or manipulatory tool in systems which contain water. For instance, the presence of water (in all three thermodynamic phases) in the Earth's atmosphere indicates that a laser could be used as a probe to investigate the structure and dynamics of different levels of the atmosphere, while the presence of liquid water in people (a person consists of ~70% water) suggests that a laser would be useful as a medical device.

Second, the near-infrared emission can be manipulated in such a manner that the light can be wavelength-shifted to the mid-infrared, generating tunable emission near 3 or 4 microns. This is accomplished through a technique known as optical parametric oscillation, in which an optically nonlinear crystal (such as CdSe) provides the shifting effect. The materials currently used in optical parametric oscillators (OPOs) generally have high pump power thresholds, which are typically overcome using pulsed pump sources or high-power cw sources.

Research at various institutions is now centered on developing efficient diode-laser-pumped systems near 3 μm that employ the rare-earth ion erbium as the active species. Factors which are considered in the development of this laser include the desired spectral and spatial characteristics of the output, and the method of excitation (continuous or pulsed). Semiconductor diode lasers are of interest as excitation sources due to their small size, long lifetimes, and low power requirements.

The overall goal of the research, in view of the above considerations, is to develop an efficient diode-laser-pumped cw 2.8- μm erbium laser, taking into account all variables and considerations.

1.2 Specific Goals of the Research

The nature of the energy transfer acting within rare-earth-doped solids plays a crucial role in the operation of the material as a laser. Energy transfer processes occur following excitation of the medium which may eventually lead to laser emission. It is also possible, however, that the emission will be quenched as a result of these processes. It becomes necessary, therefore, to study and understand the basic physical processes in order to determine if the system may be operated as a laser, and then to determine and optimize the conditions necessary to operate the laser in the most efficient and practical manner that is possible.

The mechanisms of energy transfer which operate within the material can very often be identified and understood by conducting basic spectroscopic measurements of the material under different excitation conditions. The direction of energy flow within the system and the identification of various loss channels may be determined and quantified with these measurements.

The specific goal of this research is to conduct basic spectroscopic measurements on trivalent erbium doped into the crystals gadolinium gallium garnet, $\text{Gd}_3\text{Ga}_5\text{O}_{12}$, and yttrium scandium gallium garnet, $\text{Y}_3\text{Sc}_2\text{Ga}_3\text{O}_{12}$ (GGG and YSGG, respectively). These measurements will then be used to obtain parameters which may be used to create a working model of the system. These parameters include the Judd-Ofelt Parameters and the upconversion coefficients (definitions and descriptions of which will be given in later sections of this work). A comparison will be made between the model and the actual system using these terms and additional experimental data to test the validity of the procedures used.

1.3 Lasers Today

Since the invention of the ruby laser in the 1960's [1], the development of solid-state laser light sources has motivated great research efforts. The laser (an acronym for Light Amplification by the Stimulated Emission of Radiation) is a highly versatile tool, one which until the latter half of this century was not available. The laser has found uses both in the laboratory (as high-energy or high-power monochromatic, directional light sources) and in the marketplace (for applications as diverse as supermarket bar-code scanners, atmospheric probes, information retrieval systems, and surgical tools).

The three most common forms of lasers employ either a gas, liquid, or solid as the active medium. Gas lasers (such as carbon dioxide and argon) have active media that are highly pure and free from defect, but are very inefficient (~1%) since they require dangerously high voltages and currents to operate. In addition, the tubes containing the gases are often subject to leakage or breakage. Liquid (organic dye) lasers offer a broad tuning spectrum and deliver high energy pulses. The dyes, which are degradable, however, are highly toxic, rendering them difficult to handle. Solid-state lasers have recently attracted much interest due to their rugged construction, relatively small size, and long operating lifetimes. In addition, semiconductor-diode lasers (a sub-class of solid-state lasers) operate efficiently (~60% optical-to-optical) with low power requirements, a condition desired when high-power sources are not readily available.

One current limitation of solid-state lasers is the relatively limited spectral coverage afforded by the gain media. Most materials lase at discrete wavelengths or are tunable within a narrow band. As new ion-host combinations are developed, however, a greater spectral range is covered. Non-linear solid-state materials used in conjunction with the lasers also generate new emission wavelengths. Frequency-doubling crystals, for instance,

generate emission at harmonic wavelengths shorter than the fundamental; and OPOs generate tunable emission at wavelengths longer than the fundamental.

Two general categories of solid-state lasers employ either transition-metal-doped or rare-earth-doped hosts. The transition metal ions Cr^{3+} and Ti^{3+} , for instance, are frequently used for their broadband absorption of visible radiation, conducive to efficient flashlamp excitation, which is followed by a broad emission in the near-infrared, generating a wide tuning spectrum. Examples of Cr^{3+} and Ti^{3+} doped lasers include Chromium-LiSAF ($\text{Cr}^{3+}:\text{LiSrAlF}_6$), Alexandrite ($\text{Cr}^{3+}:\text{BeAl}_2\text{O}_4$), and Titanium-Sapphire ($\text{Ti}^{3+}:\text{Al}_2\text{O}_3$); which are tunable from 790 \rightarrow 980 nm, 720 \rightarrow 790 nm, and 680 \rightarrow 1020 nm, respectively.

Rare-earth-doped solid-state lasers are not as tunable as the chromium-doped lasers, yet rare-earth-doped hosts present a multitude of sharp, intense absorption and emission lines in both the visible and near-infrared. They may be pumped efficiently with diode lasers, resulting in compact laser systems. Furthermore, if diode lasers or other laser sources are not readily available in the spectral band necessary to excite the ion, flashlamps may frequently be substituted, provided that the crystal is sensitized with chromium or another broadband absorber (which will then transfer the excitation energy to, or activate, the rare-earth ion). Rare-earth ions frequently used as laser sources include Nd^{3+} , Tm^{3+} , Ho^{3+} and Er^{3+} ; doped into hosts such as YLF (LiYF_4) and YAG ($\text{Y}_3\text{Al}_5\text{O}_{12}$). They may be operated in cw, long-pulse, or Q-switched modes; and may often be operated at room temperature.

1.4 General Background

The use of rare-earth ions as laser sources first attracted general interest in the 1960s. Investigations of the spectroscopic properties of these systems showed that complex energy transfer mechanisms may operate within them. This led to the notion that perhaps specific transitions in these systems, if properly influenced, would generate coherent light in an efficient manner.

The study of the properties of erbium as a laser ion has shown many interesting channels for energy transfer. These energy transfer processes include upconversion and cross-relaxation, and are highly dependent on system parameters such as temperature, dopant concentration, and excitation density.

Much research has been conducted in an attempt to understand this ion and the influence of different host lattices upon its spectral properties. As early as the 1960's, the energy states were mapped out and compared to those of other rare-earth ions doped into LaCl_3 [2].

Early interest in the use of erbium as a laser ion concentrated on the transition between the two lowest electronic states at 1.5 μm . This wavelength is considered to be 'eyesafe'. The human eye absorbs throughout its volume, rather than on a surface, such as the retina, in this spectral region. Therefore, the probability for acute damage is less, making this laser useful in such applications as eyesafe rangefinders. In addition, this wavelength is easily transmitted through silicon-based fibers, making it extremely useful in optical communication systems and medical delivery systems.

Interest in the transition near 2.8 μm has developed more recently. The strong absorption of 2.8- μm radiation by water has motivated research for an erbium-based medical laser, and the development of OPOs has motivated a search for new, high-cw-power pump

lasers for these devices. Early research into this transition resulted in pulsed laser sources¹, due to the nature of available pump sources (generally flashlamps) as well as a lower laser level lifetime that may be significantly longer than that of the upper laser level (this property of erbium, which results in a population bottleneck and therefore a self-terminating laser, will be discussed in a later chapter). YAG has been a common host for the erbium ion due to its hardness, high thermal conductivity, favorable emission wavelength (2.94 μm , the peak of liquid-water absorption), and ease of fabrication. An unfavorable combination of upper- and lower-laser-state lifetimes in conjunction with a strong competition between radiative and non-radiative processes between the states, however, results in high cw laser thresholds for this material. New crystalline hosts are therefore being sought which result in efficient and practical laser emission.

The first research into the possibility of using GGG as a host showed discouraging results. [3] It was found that the flashlamps used, which already limited any laser to pulsed operation (or, at best, quasi-cw operation), induced the formation of stable color-centers in the material, limiting the material to a very finite 'shelf lifetime'. Research into Er,Cr:YSGG showed more promising results. [4] This material, in which the chromium ions sensitized the erbium ions, generated relatively efficient emission in the pulsed mode. Commercial products based on this material have been developed. [5]

Upconversion and excited-state absorption (ESA) effectively redistribute the population of both the upper and lower laser states. These mechanisms, in conjunction with the use of newly-developed Ti:sapphire and semiconductor-diode lasers whose emission

¹ For medical purposes, pulsed sources are generally desirable. Surgical techniques such as sclerostomy (the opening of fistulas, or drainage holes, in the eyeball's sclera to relieve glaucoma-induced intra-ocular pressure) require precise tissue ablation. Thermal damage to the tissue in the vicinity of the cut must be minimized. This is most easily accomplished with microsecond laser pulses. One current problem with this technique is the difficulty of laser transmission through the fiber. Hydroxyl bonds, which are responsible for the high absorption of 2.8- μm radiation by water, are also present in silica-based fibers. New sapphire- or fluoride-based fibers, which contain significantly less hydroxyls, show promise for delivery systems.

wavelengths were able to selectively excite the erbium energy-levels, overcame the population bottleneck to generate cw laser emission. In 1987, the first diode-pumped 2.8- μm cw erbium laser was demonstrated in Er:LiYF₄. [6]

References for Chapter 1

- [1] Maiman, T.H. "Stimulated Optical Radiation in Ruby". *Nature*. **187**, 493. (1960).
- [2] G.H. Dieke and H.M. Crosswhite. "The Spectra of the Doubly Ionized and Triply Ionized Rare Earths". *Applied Optics*. **2**, 675. 1963.
- [3] A.A. Kaminskii. "Stimulated Emission of Ho^{3+} and Er^{3+} Ions in $\text{Gd}_3\text{Ga}_5\text{O}_{12}$ Crystals and Cascade Laser Action of Ho^{3+} Ions Over the $^5\text{S}_2 \rightarrow ^5\text{I}_5 \rightarrow ^5\text{I}_6 \rightarrow ^5\text{I}_8$ Scheme". *Physica Status Solidi (a)*. **53**, K219. (1979).
- [4] P.F. Moulton, J.G. Manni, and G.A. Rines. "Spectroscopic and Laser Characteristics of Er,Cr:YSGG". *IEEE Journal of Quantum Electronics*. **24**, 6. (1988).
- [5] Schwartz Electro-Optics, Orlando, Florida. Laser 1-2-3 (Modular Flashlamp-Pumped Laser System).
- [6] G.J. Kintz, R. Allen, and L. Esterowitz. "CW and Pulsed 2.8 μm Laser Emission From Diode-Pumped $\text{Er}^{3+}:\text{LiYF}_4$ at Room Temperature". *Applied Physics Letters*. **50**, 22. (1987).

Chapter 2: Spectroscopy of Er³⁺:GGG and Er³⁺:YSGG

2.1 Introduction to Chapter 2

This chapter presents the results of measurements of the basic spectroscopic properties of Er-doped GGG and YSGG, which include absorption, emission, and radiative lifetime. These materials were chosen in anticipation that they would be easy to grow, durable, present strong absorption peaks, and show high radiative quantum efficiencies at the 3- μm laser transition.

The measurements, in addition to revealing the energy-level structure of the ion, may also be used to obtain basic spectroscopic parameters, including direct-feeding efficiencies and cross-relaxation efficiencies. These parameters will have significant influence on the results of Chapter 3, which analyzes the effects of energy transfer within the system.

The measurements may also be used to gain insight into the rates of decay of excited states, and the influence of non-radiative processes on these rates. The intensity and rate of radiative decay from an electronic state is always influenced by thermal relaxation of the lattice. Phonon decay may in fact dominate over radiative decay at sufficiently high temperatures. The effects of non-radiative decay on the emission properties may be quantified using the Judd-Ofelt Theory, which derives decay rates by demanding a knowledge of the energy-level structure of the ion and integrating its absorption spectra. The analysis also calculates the branching coefficients of excited states, which have application to the energy-transfer analysis of Chapter 3.

2.2 Physical Properties of GGG and YSGG

Gadolinium gallium garnet, $Gd_3Ga_5O_{12}$, called GGG, and yttrium scandium gallium garnet, $Y_3Sc_2Ga_3O_{12}$, called YSGG, are the crystals under consideration as hosts for the erbium ion. Other crystals, such as $Y_3Al_5O_{12}$ [1], $Gd_3Sc_2Ga_3O_{12}$ [2], BaY_2F_8 [3], and $LiYF_4$ [4] (YAG, GSGG, BYF, and YLF, respectively), have all been used with varying degrees of success as hosts. Multi-phonon non-radiative relaxation tends to dominate the decay from the upper laser state in aluminum-garnets due to the high phonon frequencies associated with the presence of aluminum ions, which results in a short upper-state lifetime and high laser thresholds. Fluorides, on the other hand, have lower phonon energies due to the weaker lattice bonds, but for the same reason, are much less durable than the garnets. GGG and YSGG were chosen as potential host materials for three significant reasons: 1) the gallium-garnets have reduced multi-phonon decay rates compared to the aluminum-garnets due to the lower phonon frequencies associated with the gallium-garnets, which should result in higher laser efficiencies. 2) These materials are sufficiently hard to withstand the high temperatures and electric fields that are encountered in high-power laser sources. 3) Large single-crystal boules of gallium garnets are easy to grow. [YSGG is, unfortunately, expensive to grow due to the scarcity of scandium. GGG, on the other hand, is relatively inexpensive.] Some of the material and optical properties of GGG and YSGG are listed in Table 2-1. Those of YAG are also shown for purposes of comparison.

Upon visual inspection, undoped garnets appear optically transparent. The absorption spectra of these materials confirm this feature. This is an important quality in a laser host, as it is generally desirable that the laser ion, and not the host lattice itself, be responsible for absorption of the excitation. Figure 2-1a shows the absorption spectrum of un-

doped GGG in the visible region. Absorption lines in the near ultraviolet are the only features present. These correspond to electronic transitions within the Gd^{3+} ions, and do not play a role in this study of erbium. The absorption spectrum of YSGG (Figure 2-1b) shows a similar transparency to GGG, minus the gadolinium absorption features.

PROPERTY	$Gd_3Ga_5O_{12}$	$Y_3Sc_2Ga_3O_{12}$	$Y_3Al_5O_{12}$
lattice structure	cubic [9]	cubic [9]	cubic [9]
space group	$O_h^{10}-Ia3d$ [9]	$O_h^{10}-Ia3d$ [9]	$O_h^{10}-Ia3d$ [9]
melting point ($^{\circ}C$)	1735 [5]	1877 [5]	1940 [5]
Debye temperature (K)	512 [6]	unavailable	725 [9]
thermal conductivity (W/cm $^{\circ}C$)	0.09 [7]	0.079 [11]	0.13 [9]
specific heat (J/g $^{\circ}C$)	0.415 [8]	~0.4 [12]	0.145 [9]
density (g/cm 3)	6.1 [5]	4.59 [5]	4.55 [9]
hardness (Moh's)	7.5 [6]	unavailable	8.4 [9]
optical transparency region (nm)	400-6000	400-6000	240-6000 [9]
refractive index (at ~3 μm)	1.9341 [10]	1.9171 [13]	1.8113 [14]

Table 2-1: Some mechanical and optical properties of undoped GGG, YSGG, and YAG. Letters in brackets indicate reference as source of information. Values with no reference were experimentally obtained.

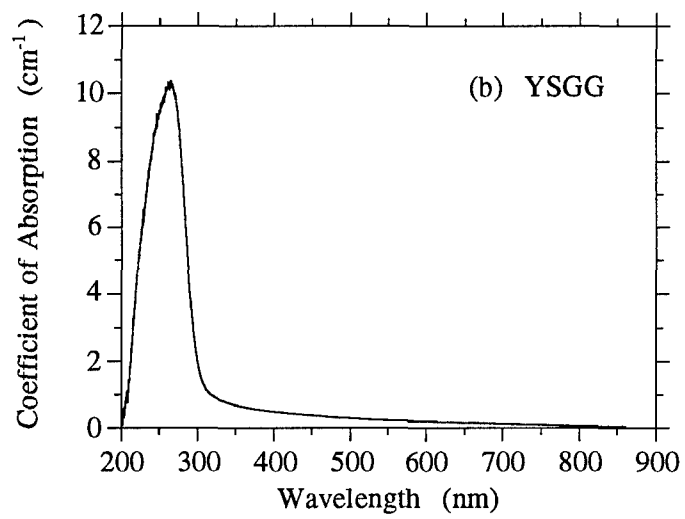
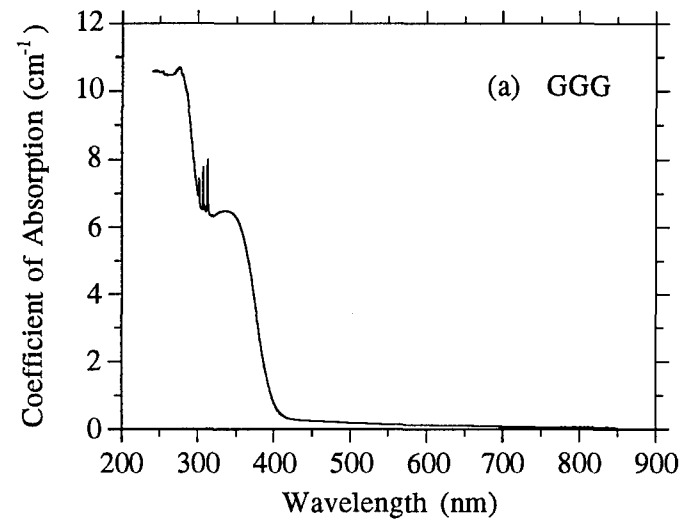


Figure 2-1: Absorption spectra of undoped (a) GGG and (b) YSGG.

2.3 Electronic States and the Crystal Field

GGG and YSGG belong to a class of crystalline hosts whose constituent ions are grouped as $A_3(B)_2[B]_3O_{12}$, or $A_3B_5O_{12}$, if $(B)=[B]$. The unit cell of this structure contains eight formula units. The 24 A ions occupy dodecahedral (D_2) "c" sites, into which rare-earth impurities typically substitute. The B ions may occupy two types of sites with different oxygen coordination: 16 octahedral "a" positions (C_{3i}) and 24 tetrahedral "d" positions (S_4). The "a" sites form a body-centered-cubic lattice. The oxygen atoms enter 96 general "h" positions. [9]

The rare-earth ions, which typically reside in non-centrosymmetric sites, replace Gd^{3+} in $Gd_3Ga_5O_{12}$ and Y^{3+} in $Y_3Sc_2Ga_3O_{12}$. No charge compensation is necessary since the displaced ion is also trivalent. YSGG is generally considered to be a more disordered material than GGG because a fraction of the rare-earth dopant may occasionally also enter into the octahedral sites of scandium within the garnet sublattice. The bulk of the dopants will be found in the dodecahedral "c" sites. Despite this difference, the overall spectroscopic and laser properties of erbium-doped GGG and YSGG remain similar. Differences in properties within YSGG resulting from the different lattice sites will not be analyzed in this work.

Rare-earth ions belong to the Lanthanide series of elements, and have atomic numbers that vary from $Z=58$ to 71. Their electronic configuration is given by

$$1s^22s^22p^63s^23p^63d^{10}4s^24p^64d^{10}5s^25p^64f^m5d^n6s^2 \quad [2.3.1],$$

where $m=2,3,\dots,14$, and $n=0$ or 1. A screening effect, which arises from filled shells outside of the partially filled 4f shell, shields the inner orbits from the electric field of other neighboring ions. This allows the use of the weak crystal-field scheme to calculate the

splitting of the energy levels of the rare earth ions in the crystal. The crystal field is the overall field that the electron feels due to the attraction and repulsion of other ions' nuclei and electrons. The energies of the states closely resemble those of the free ion since the 4f electrons are not strongly influenced or perturbed by the crystal field. This feature is valid in most crystals commonly used as rare-earth laser hosts. The relative positions of the levels within the states, or manifolds, however, vary significantly from host to host due to the different field strengths.

A complete description of the calculation of the energy levels in the weak crystal-field scheme is presented by Di Bartolo. [15] Essentially, one generally begins by calculating the energy eigenvalues of the isolated ions. The crystal field may be treated as a perturbation of the free ion states, because the crystal field interaction is small in comparison to the spin-orbit interaction. The spin-orbit splitting of energy levels is generally on the order of 1000 cm^{-1} , while the crystal field splitting (Stark splitting) is on the order of 100 cm^{-1} . The full Hamiltonian of one ion becomes

$$H = \sum_{i=1}^n \left\{ \frac{p_i^2}{2m} - \frac{Ze^2}{r_i} + e^2 \sum_{j>i} \frac{1}{r_{ij}} + eV(r_i, \theta_i, \phi_i) \right\} + \lambda \mathbf{L} \cdot \mathbf{S} \quad [2.3.2]$$

where the first term represents the kinetic energy of the electrons, the second term is the interaction between the electrons and the nucleus, the third term is the interaction between different electrons, the fourth term is the perturbation due to the crystal field, and the fifth term is the spin-orbit interaction of the electrons. The outer summation is carried from $i=1$ to n , where n is the number of electrons in the ion, and the inner summation for all values $j>i$. The perturbing potential takes the form

$$V(r_i, \theta_i, \phi_i) = \sum_{lm} A_{lm} r_i^l Y_l^m(\theta_i, \phi_i) \quad [2.3.3]$$

where A_{lm} is a parameter which describes the strength and symmetry of the crystal field and is given by the positions of the neighbors around the dopant ion, r_i is the radius of the 4f electronic orbit, and $l \leq 6$ for 4f electrons [16]. Terms of [2.3.3] for l -even contribute to the centers of gravity and splittings of the energy states in accordance with the site-symmetry. Odd- l terms may not necessarily contribute to the energy, but will be responsible for admixing the 4f states with higher-lying states of opposite parity.

The energy levels of rare-earth ions may be uncovered experimentally by studying the absorption spectra of the materials. The absorption spectrum of a rare-earth ion generally consists of a series of sharp spectral lines, which may broaden at higher temperatures due to the excitation or de-excitation of phonons in the crystal.

Absorption transitions may or may not be seen, however, in emission spectra. Whereas a strong emission line comes from a transition from a long-lived upper state, absorption transitions, on the other hand, may end on short-lived states which then decay to the longer-lived metastable state.

2.4 Electronic States and Transition Probabilities: The Judd-Ofelt Theory

The centers of gravity of the electronic states of rare-earth ions vary little from host to host. The notation $^{2S+1}L_J$ is generally employed to distinguish one state, or manifold, from another. Here S is the vector sum of the spins of the electrons of the ion; L is the vector sum of the orbital angular momenta, where $L=0, 1, 2, 3, 4, 5\dots$, then designated by the letters S, P, D, F, G, H..., respectively; and J is the vector sum $S+L$. For example, a state represented as $^4I_{9/2}$ indicates $S=3/2$, $L=6$, and $J=9/2$. Furthermore, there is exactly a $(2J+1)$ -fold degeneracy for any state within the 4f shell. Whether or not this degeneracy is lifted depends on the number of 4f electrons in the ion and on the symmetry of the crystal field around the ion. The degeneracy is frequently entirely removed for ions with an even number of 4f electrons, leaving $2J+1$ Stark levels. The degeneracy is half removed for ions with an odd number of 4f electrons, leaving $J+1/2$ Stark levels. Erbium, which has an odd number of 4f electrons, has, for example, 5 distinct levels within the $^4I_{9/2}$ state.

In 1962, B.R. Judd and G.S. Ofelt worked independently to explain and quantify the nature of transitions occurring within the 4f configuration of a rare-earth ion in a solid [17,18]. The result, known as the Judd-Ofelt Theory, is a method which allows an approximate calculation of transition line strengths and radiative lifetimes between or of any state of a rare-earth ion in a crystal based solely on a series of reduced matrix elements for the ion and the measured absorption spectra of the ion in the crystal.

Strong luminescent transitions occur from excited states of the rare-earth ions. Transitions may be electric dipole, magnetic dipole, or electric quadrupole in nature. Magnetic-dipole transitions are allowed between states of identical parity, but do not explain the intense spectral lines that are observed. The probability of magnetic-dipole transitions is weak in comparison to that of electric-dipole transitions, and electric-quadrupole

pole transitions are rarely observed. Electric dipole transitions, however, are forbidden between two states with the same parity, i.e.,

$$\langle \Psi | D_1^q | \Psi' \rangle = 0$$

No violation of the parity selection rule will occur if a state with opposite parity admixes with one or both of the states involved in the transition, resulting in a 'forced' electric dipole transition. The odd order terms of the static crystal field potential expansion may admix 4f states with those of opposite parity from a higher electronic configuration of the ion, such as 5d, if the ion is located at a site with no inversion symmetry.²

For electric dipole transitions, Judd and Ofelt defined the transition strength as

$$S(J \rightarrow J') = \sum_{t=2,4,6} \Omega_t \left| \langle \Psi J \| U^{(t)} \| \Psi' J' \rangle \right|^2, \quad [2.4.1]$$

where $\langle \Psi J \| U^{(t)} \| \Psi' J' \rangle$ are unit tensor operators, or reduced matrix elements (for which $t=2, 4, 6$) which connect states involved in transitions, and Ω_t are parameters to be determined which connect the crystal field to the ion's energy levels. [The splitting of the 4f states is assumed to be small relative to the energies of the admixed states, typically from the 5d configuration. This assumption simplified the calculations which ultimately resulted in Equation [2.4.1]] The reduced matrix elements are summed over the relevant states when two or more excited states overlap, and an average energy value is used to describe them. The three reduced matrix elements for each 4f transition of a rare-earth element are almost independent of the host lattice, and their calculation involves a knowledge of the free-ion wave functions. Since the introduction of the Judd-Ofelt Theory, the matrix elements have been calculated and presented in tabular form for most transitions of all the

² Transitions involving a change in vibrational state can also circumvent the parity selection rule. However, the Judd-Ofelt Theory deals typically with electronic transitions; it is a static, not dynamic, model. Vibronic transitions are less frequently considered.

rare-earth ions. Table 2-2 lists some of the matrix elements for electric-dipole transitions in erbium from the ground state; and Table 2-3 lists those from excited states. [9]

Judd and Ofelt summed over the intensities of each Stark level for a given transition in their calculations of transition probabilities, assuming that the population of the manifolds was equally distributed amongst each Stark level. This approximation implies that the model is valid for temperatures at or above which the levels are thermally populated. This is a reasonable approximation, since kT at 300 K $\approx 208 \text{ cm}^{-1}$, which is on the order of the splittings of the states.

It is only necessary to determine the three parameters Ω_2 , Ω_4 , and Ω_6 , known as the Judd-Ofelt Parameters, to connect the transition strength with the reduced matrix elements. These parameters, which are deduced from the absorption spectra of the material, incorporate the effect of the host lattice upon the free ion.

The Judd-Ofelt Theory may be quantitatively summarized as follows:

$$S(J \rightarrow J') = \frac{3hc}{8\pi^3 e^2} \cdot \frac{2J+1}{\rho} \cdot \frac{9n}{(n^2+2)^2} \cdot \frac{1}{\bar{\lambda}} \cdot \int_{J \rightarrow J'} \alpha(\lambda) d\lambda = \sum_{t=2,4,6} \Omega_t \left| \langle \Psi_J \| U^{(t)} \| \Psi'_{J'} \rangle \right|^2 \quad [2.4.2]$$

where $S(J \rightarrow J')$ is the line strength of an electric dipole transition between states J and J' , h is Planck's constant, c is the speed of light, e is the charge on an electron, J is the angular momentum quantum number of the state from which the transition occurs, ρ is the number density of the dopant ion, n is the refractive index of the material, $\bar{\lambda}$ is the mean wavelength of the transition, and $\int \alpha(\lambda) d\lambda$ is the integrated absorption intensity of the transition.

The degeneracy factor $(2J+1)$ is included since the matrix elements of the electric-dipole operator are summed over all components of the initial state. [19] The factor $9n/(n^2+2)^2$ appears as a correction to the refractive index due to the local crystalline field. [20] An overly-constrained series of equations, each containing the three unknowns, Ω_2 , Ω_4 , and Ω_6 , will result from using Equation [2.4.2] with as many transitions that are

experimentally feasible. The three parameters may then be determined using a least-squares fit.

J'	Energy (cm ⁻¹)	t=2	t=4	t=6
⁴ I _{13/2}	6610	0.0195	0.1173	1.4316
⁴ I _{11/2}	10219	0.0282	0.0003	0.3953
⁴ I _{9/2}	12378	0	0.1733	0.0099
⁴ F _{9/2}	15245	0	0.5354	0.4618
⁴ S _{3/2}	18462	0	0	0.2211
² H _{11/2}	19256	0.7125	0.4125	0.0925
⁴ F _{7/2}	20422	0	0.1469	0.6266
⁴ F _{5/2}	22074	0	0	0.2232

Table 2-2: Calculated values of the squares of the reduced matrix elements for Er³⁺ transitions from the ⁴I_{15/2} ground state. [9]

J	J'	Energy (cm ⁻¹)	t=2	t=4	t=6
⁴ I _{13/2}	⁴ I _{15/2}	6480	0.0188	0.1176	1.4617
⁴ I _{11/2}	⁴ I _{13/2}	3640	0.0210	0.1100	1.0400
	⁴ I _{15/2}	10120	0.0259	0.0001	0.3994
⁴ F _{9/2}	⁴ I _{9/2}	2880	0.0960	0.0061	0.0120
	⁴ I _{11/2}	5110	0.0671	0.0088	1.2611
	⁴ I _{13/2}	8750	0.0096	0.1576	0.0870
	⁴ I _{15/2}	15240	0	0.5655	0.4651
⁴ S _{3/2}	⁴ I _{9/2}	6080	0	0.0729	0.2285
	⁴ I _{11/2}	8240	0	0.0037	0.3481
	⁴ I _{13/2}	11870	0	0	0.0789
	⁴ I _{15/2}	18350	0	0	0.2560

Table 2-3: Calculated values of the squares of the reduced matrix elements for Er³⁺ transitions of the given state. [9]

Once the three Judd-Ofelt Parameters have been identified, it is possible to go back and calculate, using Equation 2.3.1, the radiative decay probability, using

$$A(J \rightarrow J') = \frac{64\pi^4 e^2}{3h(2J+1)} \cdot \frac{n(n^2+2)^2}{9} \cdot \frac{S(J \rightarrow J')}{\lambda^3} \quad [2.4.3];$$

radiative lifetimes, using

$$\tau_{\text{rad}} = \left[\sum_{J'} A(J \rightarrow J') \right]^{-1} \quad [2.4.4];$$

or branching ratios, using

$$\beta_{JJ'} = A(J \rightarrow J') \tau_{\text{rad}} \quad [2.4.5].$$

To obtain a true measure of the state lifetime, it is also necessary to include a contribution due to magnetic dipole transitions. In most cases, this contribution is small; even negligible. There is a significant contribution, however, for the ${}^4I_{13/2} \rightarrow {}^4I_{15/2}$ and for the ${}^4I_{11/2} \rightarrow {}^4I_{13/2}$ transitions in Er^{3+} . The magnetic-dipole oscillator strength is determined from a reduced matrix element dependent on the values L and S in combination with fundamental constants. These elements are difficult to locate in the literature; although the magnetic-dipole probabilities have been calculated by Weber for $\text{Er}:\text{LaF}_3$. [21]

The rare earth ion Er^{3+} has the electronic configuration with $m=12$ and $n=0$, referring to Expression 2.3.1. This is equivalent to the closed configuration of the xenon atom with additional shells given by $[\text{Xe}]4f^{12}5d^06s^2$. Its atomic number is 68, and its mass is 167.26 amu. The electronic states of trivalent erbium are shown in Figure 2-2. The splitting of the states may be calculated using the perturbation approach, or may be experimentally deduced by comparing the absorption spectra with the luminescence spectra of the ion, at room temperature and at liquid-nitrogen temperatures, at which point the lines are very distinct and easy to identify. Table 2-4 lists the energy levels for the lowest four states of erbium in the crystals GGG, YSGG [22], and YLF [9], for comparison.

Absorption measurements were obtained using a Perkin Elmer λ -9 Dual Beam UV/VIS/NIR Spectrophotometer. This device computes and displays values of absorbance $[A(\lambda)]$ by comparing the intensity of radiation (T) of wavelength λ transmitted through a sample of length ℓ to that which was incident on the crystal (T_0). A value for the coefficient of absorption $[\alpha(\lambda)]$ may be calculated from this by using the expressions

$$T = T_0 e^{-\alpha(\lambda)\ell} \quad \text{and} \quad T = T_0 10^{-A(\lambda)},$$

to get

$$\alpha(\lambda) = 2.3026 \cdot A(\lambda) / \ell \quad [2.5.1].$$

The absorption spectra for Er:YSGG and Er:GGG with nominal 30% dopant concentrations are shown in Figures 2-3 through 2-8 for transitions from the $^4I_{15/2}$ ground state at room temperature (~ 300 K). [Note: 30%-doped GGG and YSGG correspond to concentrations of 3.80×10^{21} ions/cm³ and 3.70×10^{21} ions/cm³, respectively.] All absorption spectra are corrected for Fresnel losses at the crystal surface. The absence of absorption near 600 nm is responsible for the pinkish color of erbium-doped garnets. Features key to this study present in the spectra are the absorption bands near 520 nm, 790

nm, 970 nm, and 1500 nm; corresponding to transitions to the $^4S_{3/2}$, $^4I_{9/2}$, $^4I_{11/2}$, and $^4I_{13/2}$ states, respectively.

State	GGG	YSGG	YLF
$^4I_{9/2}$	12739	12742	xxxxx
	12695	12698	12660
	12564	12574	12565
	12526	12527	12466
	12313	12312	12360
$^4I_{11/2}$	10404	10400	xxxxx
	10395	10397	10315
	10360	10360	10289
	10353	10352	10283
	10284	10285	10235
	10271	10269	10222
$^4I_{13/2}$	6848	6848	6738
	6793	6786	6724
	6721	6726	6697
	6703	6706	6674
	6596	6597	6579
	6581	6581	6539
	6567	6566	6535
$^4I_{15/2}$	495	496	347
	481	476	320
	403	405	291
	369	380	252
	73	72	56
	39	41	29
	30	35	17
	0	0	0

Table 2-4: Energies (in cm^{-1}) of the levels in the four lowest states of Er^{3+} in GGG, YSGG, and YLF. (Values for GGG were determined experimentally. Values for YSGG and YLF are reproduced from [22] and [9], respectively. The highest levels of the $^4I_{11/2}$ and $^4I_{9/2}$ states in YLF have not been accurately determined.)

Spectra are also shown (Figures 2-9 through 2-11) for Er:GGG cooled to 77 K by liquid nitrogen. The spectra still show the same transitions, though the individual lines are much narrower due to decreased thermal broadening. In addition, many of the lines corresponding to longer wavelength absorption within the same transitions have vanished since the higher levels of the ground state are less likely to be occupied at low temperatures (the probability of occupancy is given by a Boltzmann distribution).

Luminescence spectra were obtained at both room temperature and liquid-nitrogen temperature by exciting the samples into the $^4S_{3/2}$ and $^4F_{7/2}$ states with the focused emission of a Coherent Argon laser. Luminescence was monitored along the direction of excitation using an Instruments SA 0.64-m Scanning Monochromator. Gratings used include a 1200-groove/mm grating blazed at 1 μm , a 600-groove/mm grating blazed at 1.5 μm , and a 300-groove/mm grating blazed at 2 μm . The luminescence was detected with a dry-ice-cooled Hamamatsu PbS detector and Stanford Research Systems SR510 Lock-In Amplifier. OCA Microcoatings bandpass or cutoff filters were placed over the exit slit of the monochromator to ensure detection of emission from only a specific transition. The system was purged of atmospheric water vapor by blowing nitrogen gas through the monochromator. This was necessary due to the strong absorption of the emission near 2800 nm by the water vapor. Figures 2-12 through 2-17 show the luminescence for both Er:GGG and Er:YSGG near 970 nm, 1500 nm, and 2800 nm; which correspond to the $^4I_{11/2} \rightarrow ^4I_{15/2}$, $^4I_{13/2} \rightarrow ^4I_{15/2}$, and $^4I_{11/2} \rightarrow ^4I_{13/2}$ transitions, respectively. The spectra for Er:GGG cooled to 77 K by liquid nitrogen are shown for the latter two transitions (Figures 2-18 and 2-19). All emission spectra are corrected for detector and grating sensitivity.

To determine the lifetime of the relevant states, temporal analyses of the emission were conducted. A state's radiative lifetime is characteristic of that state, and in the absence of energy transfer, represents the time required for the population of the state to fall to $1/e$

of its initial value via spontaneous emission. The lifetime is independent of the terminal state. It is a function only of the initial state. In its most basic form (pure radiative decay), the population in the excited state decays exponentially as

$$I(t) = I_0 e^{-\frac{t}{\tau}} \quad [2.5.2],$$

where $I(t)$ represents the emission intensity at some time t after the initial excitation pulse, and τ represents the radiative lifetime. The decay still occurs exponentially in the presence of thermal relaxation, though the effective upper state lifetime is reduced as

$$\tau^{-1} = \tau_{\text{rad}}^{-1} + \tau_{\text{non-rad}}^{-1} \quad [2.5.3].$$

Values of state lifetimes are usually rewritten in the more convenient form

$$\tau = -t / \ln(I / I_0) \quad [2.5.4].$$

Radiative lifetimes may increase due to energy migration (fluorescence trapping), decrease due to impurity quenching, or either increase or decrease due to upconversion and/or cross-relaxation processes, dependent on which transition is being monitored. The latter two processes involve the nonradiative exchange of energy between two neighboring ions, during which one ion is promoted to a higher state and the other ion is demoted to a lower state. These processes are non-linear with respect to excited-state population, and manifest themselves as non-exponential luminescence time decays. It is impossible in this case to assign one true lifetime for the decay, since the slope of Eq. [2.5.4] will no longer be constant. For small deviations from true exponential decay, lifetimes were assigned which corresponded to the exponential portion of the curve. This approximation is reasonable, as the deviations, indicative of energy transfer, generally occur at times short compared to the overall decay (energy transfer occurs most significantly for large excited-

state populations). For much larger deviations, when it may be possible to assign two or more possible lifetime values due to enhanced energy-transfer processes, average values of lifetime are used which correspond to neither the earliest portion of the decay nor the noisy, long tail of the decay.

Lifetime measurements of Er:GGG and Er:YSGG were conducted by exciting the ions directly into the state to be monitored (with the exception of the $^4I_{13/2}$ state, for which a resonant excitation source was not readily available). The pump beam was defocused in all cases in order to minimize emission quenching or enhancement due to energy transfer. A cw Ti:sapphire laser (Schwartz Electro-Optics Titan-CW) operating near 970 nm, a pulsed Ti:sapphire laser (Schwartz Electro-Optics Titan-P) near 790 nm, and a frequency-doubled, Q-switched Nd:YAG laser at 532 nm were used as sources to excite the erbium ions into the $^4I_{11/2}$, $^4I_{9/2}$, $^4S_{3/2}$, and states, respectively. The pulsed Ti:sapphire laser was pumped with the output of the frequency-doubled Nd:YAG laser and operated at 10 Hz in a 10-nsec pulse.

The emission, monitored at 90° to the direction of excitation, was analyzed near 2800 nm, 1500 nm, 835 nm, and 557 nm to derive the radiative lifetimes for the $^4I_{11/2}$, $^4I_{13/2}$, $^4I_{9/2}$ and $^4S_{3/2}$ states, respectively. An EG&G Judson InAs detector in conjunction with a high-gain amplifier and appropriate bandpass filters was used to detect the emission near 1500 nm and 2800 nm. A photomultiplier tube placed at the exit slit of an Acton Research 0.25-m monochromator was used to detect the luminescence near 835 nm and 557 nm.

A single-exponential decay was observed under low-power, defocused pumping only for emission from the $^4I_{13/2}$ state. Decay from the $^4I_{11/2}$, $^4I_{9/2}$, and $^4S_{3/2}$ states were exponential, except at early times, during which diffusion and energy transfer mechanisms typically contribute to lifetime quenching. These decay curves are shown as a function of erbium concentration for emission from the $^4I_{11/2}$ and $^4I_{13/2}$ states of erbium-doped GGG

and YSGG in Figures 2-20 and 2-21, respectively. Results which correspond to true exponential decay are summarized numerically in Table 2-5. These results are not shown graphically due to the noisy nature of the signal. Future calculations which require the use of lifetime values will use the results of Table 2-5, however, and not those of Figures 2-20 and 2-21.

It is possible to extract the feeding efficiency of the ${}^4I_{9/2} \rightarrow {}^4I_{11/2}$ transition from the lifetime data. Garnets typically have high phonon energies, and therefore the probability for multiphonon decay is relatively high, for example, when compared to such materials as fluorides, which possess lower phonon energies. It is expected that in lightly-doped garnets, the nonradiative decay from ${}^4I_{9/2} \rightarrow {}^4I_{11/2}$ will dominate over the cross-relaxation decay (${}^4I_{9/2}, {}^4I_{15/2} \rightarrow ({}^4I_{13/2}, {}^4I_{13/2})$), which is not highly probable at low-doping concentrations; and over the relatively slow radiative decay. The feeding efficiency in low concentration samples may then be assumed to be 100%. If this is the case, then a comparison of the lifetimes of low-doped samples to high-doped samples should reveal the feeding efficiency as a function of the concentration. The feeding efficiency may therefore be defined as

$$\beta_{xy} = \frac{\tau_{\text{high-concentration}}}{\tau_{\text{low-concentration}}},$$

and the efficiency of cross-relaxation for this transition may be defined as

$$\beta_{c-r} = 1 - \frac{\tau_{\text{high-concentration}}}{\tau_{\text{low-concentration}}} = 1 - \beta_{xy}.$$

[The feeding-efficiency-subscripts x and y are an arbitrary designation for the transitions' initial and final states; and will be explained in greater detail in Section 3.5] Feeding

efficiencies for Er:GGG and Er:YSGG for the ${}^4I_{9/2} \rightarrow {}^4I_{11/2}$ transition are shown in Table 2-6.

This method may not, however, be so easily applied to the ${}^4I_{11/2} \rightarrow {}^4I_{13/2}$ transition due to the greater energy difference between the states. The probability for multiphonon decay is high, but reduced compared to the ${}^4I_{9/2} \rightarrow {}^4I_{11/2}$ transition. This will result in competition between the nonradiative path (${}^4I_{11/2} \rightarrow {}^4I_{13/2}$) and the two radiative pathways (${}^4I_{11/2} \rightarrow {}^4I_{13/2}$ and ${}^4I_{11/2} \rightarrow {}^4I_{15/2}$), and it will not be possible to say with certainty that the feeding efficiency, even at low concentrations, is equal to unity.

It is expected, however, that at low concentrations, the feeding efficiency of the ${}^4I_{13/2} \rightarrow {}^4I_{15/2}$ transition will be unity, due to only one possible radiative and non-radiative decay path (excluding cross-relaxation pathways). Feeding and cross-relaxation efficiencies may therefore be calculated in an identical manner as that for the ${}^4I_{9/2} \rightarrow {}^4I_{11/2}$ transition. Results are shown in Table 2-6.

Material	$^4S_{3/2}$ (μsec)	$^4I_{9/2}$ (μsec)	$^4I_{11/2}$ (msec)	$^4I_{13/2}$ (msec)	$^4I_{13/2} / ^4I_{11/2}$
Er:GGG (30%)	0.68	1.90	0.96	4.86	5.1
Er:GGG (10%)	5.12	3.98	0.99	10.22	10.3
Er:GGG (1%)	118.65	4.57	1.10	13.57	12.3
Er:YSGG (30%)	1.16	1.32	1.3	3.4	2.6
Er:YSGG (1%)	120.20	2.78	1.43	9.52	6.7

Table 2-5: Measured values of the $^4S_{3/2}$, $^4I_{9/2}$, $^4I_{11/2}$ and $^4I_{13/2}$ radiative lifetimes of Er^{3+} in GGG and YSGG for different concentrations; as well as the ratio of the $^4I_{13/2}$ and $^4I_{11/2}$ lifetimes.

Material	$^4I_{9/2} \rightarrow ^4I_{11/2}$		$^4I_{13/2} \rightarrow ^4I_{15/2}$	
	β_{32}	β_{c-r}	β_{20}	β_{c-r}
Er:GGG (30%)	0.42	0.58	0.36	0.64
Er:GGG (10%)	0.87	0.13	0.75	0.25
Er:GGG (1%)	1.0	0.0	1.0	0.0
Er:YSGG (30%)	0.48	0.52	0.36	0.64
Er:YSGG (1%)	1.0	0.0	1.0	0.0

Table 2-6: Calculated values of feeding efficiencies and cross-relaxation efficiencies for the $^4I_{9/2} \rightarrow ^4I_{11/2}$ and $^4I_{13/2} \rightarrow ^4I_{15/2}$ transitions as functions of material and ion concentration.

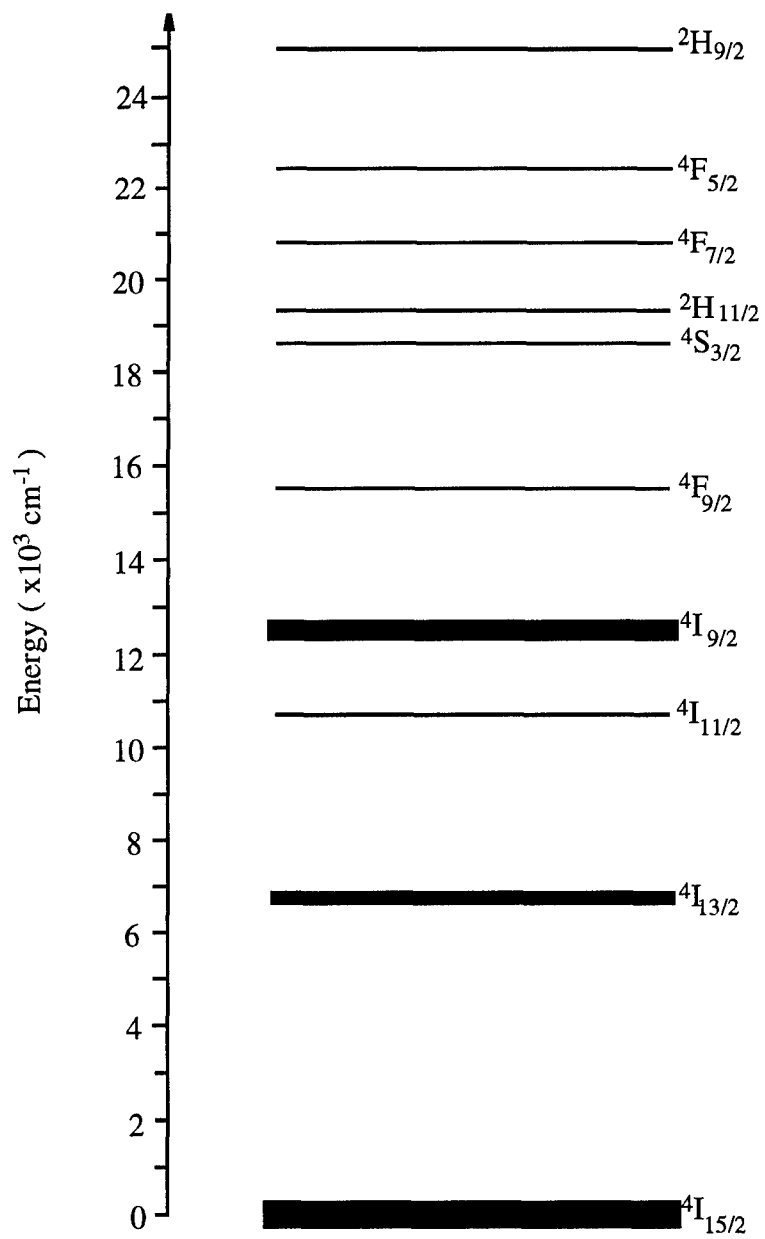


Figure 2-2: Electronic energy states of erbium.

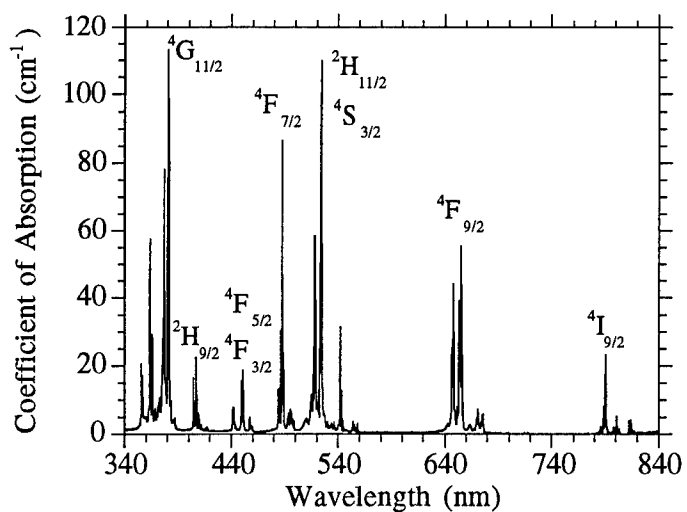


Figure 2-3: Visible absorption spectrum of Er:YSGG (30%) at 300 K.

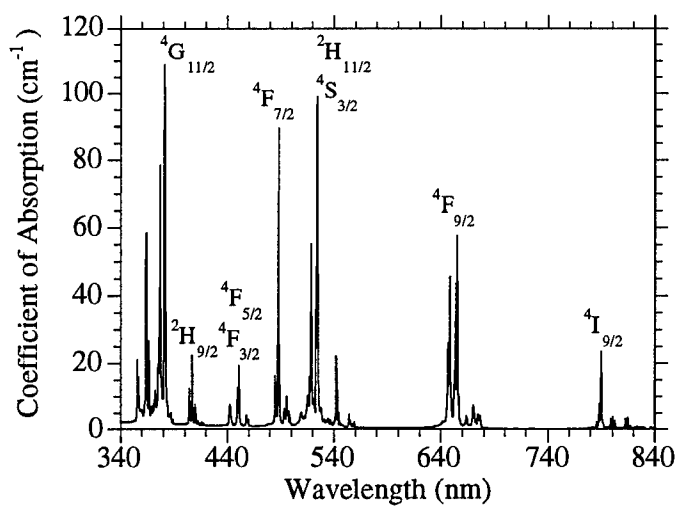


Figure 2-4: Visible absorption spectrum of Er:GGG (30%) at 300 K.

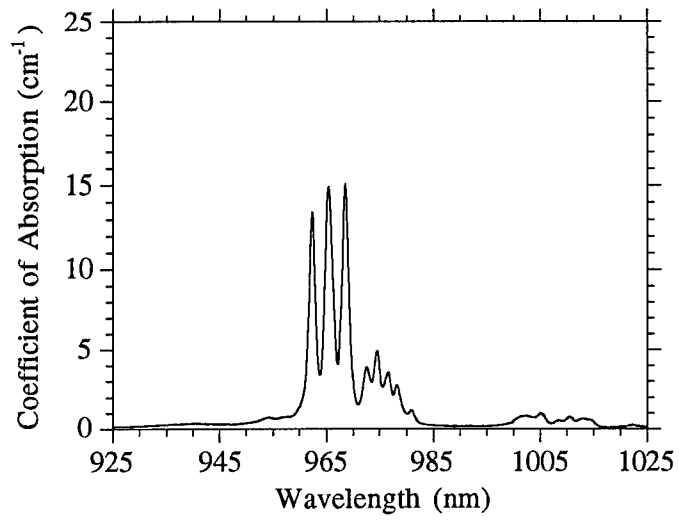


Figure 2-5: ${}^4I_{15/2} \rightarrow {}^4I_{11/2}$ absorption spectrum of Er:YSGG (30%) at 300 K.

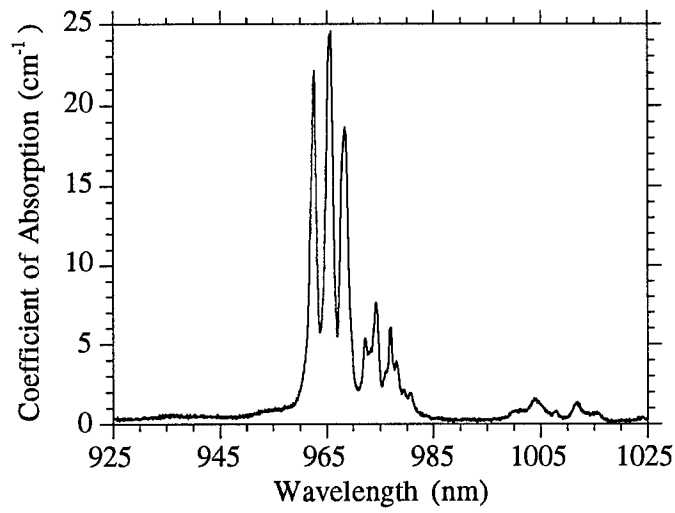


Figure 2-6: ${}^4I_{15/2} \rightarrow {}^4I_{11/2}$ absorption spectrum of Er:GGG (30%) at 300 K.

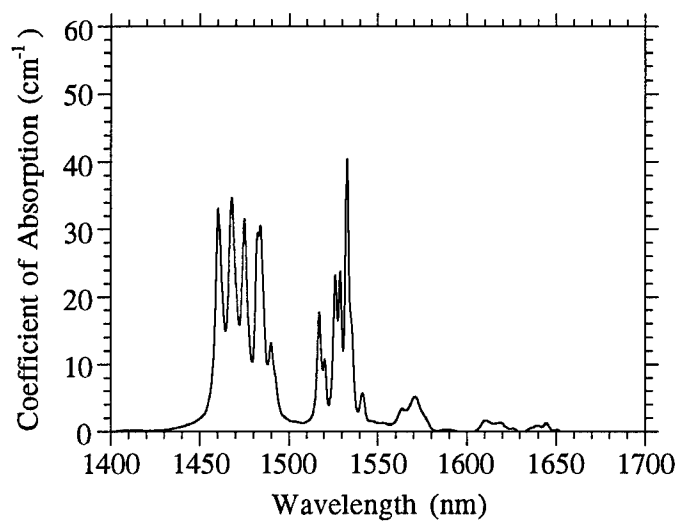


Figure 2-7: ${}^4I_{15/2} \rightarrow {}^4I_{13/2}$ absorption spectrum of Er:YSGG (30%) at 300 K.

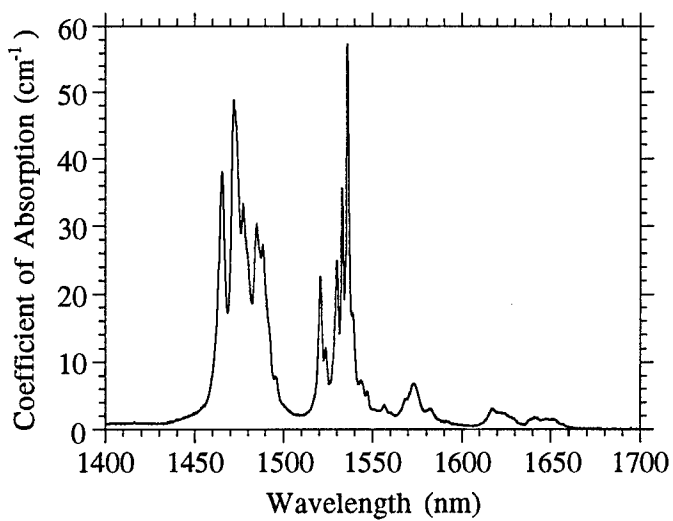


Figure 2-8: ${}^4I_{15/2} \rightarrow {}^4I_{13/2}$ absorption spectrum of Er:GGG (30%) at 300 K.

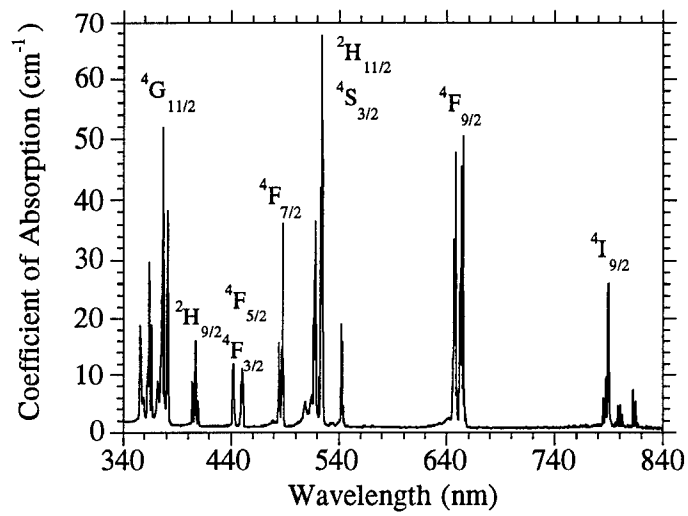


Figure 2-9: Visible absorption spectrum of Er:GGG (30%) at 77 K.

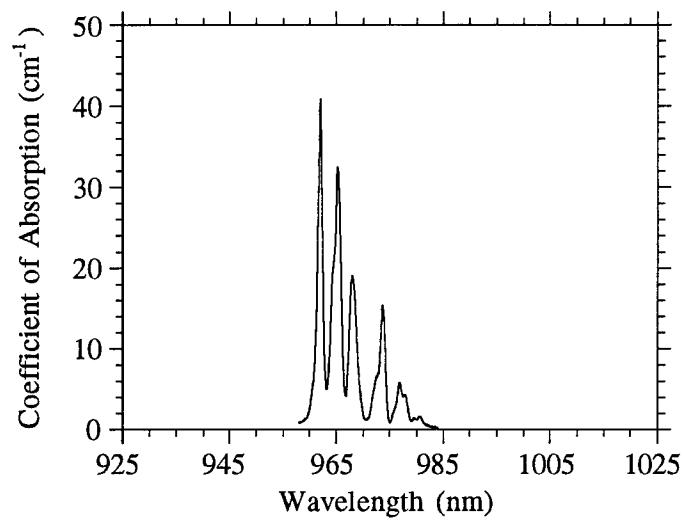


Figure 2-10: $^4I_{15/2} \rightarrow ^4I_{11/2}$ absorption spectrum of Er:GGG (30%) at 77 K.

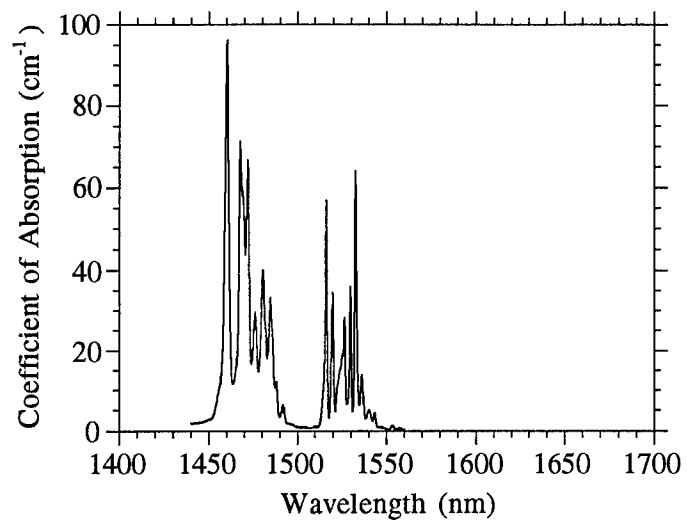


Figure 2-11: ${}^4I_{15/2} \rightarrow {}^4I_{13/2}$ absorption spectrum of Er:GGG (30%) at 77 K.

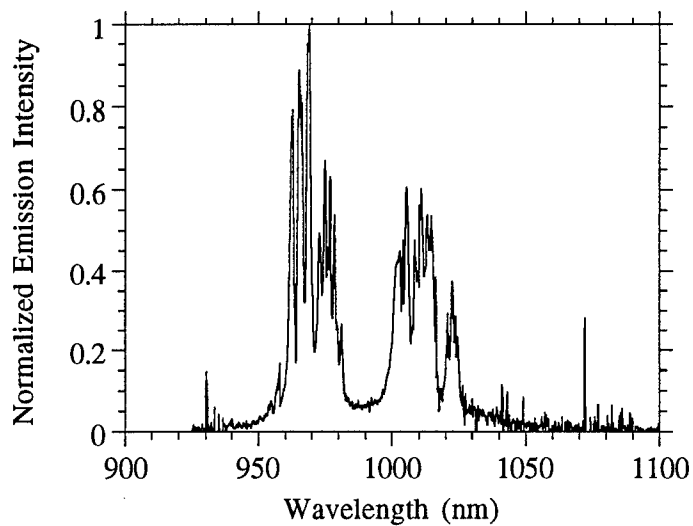


Figure 2-12: ${}^4I_{11/2} \rightarrow {}^4I_{15/2}$ emission spectrum for Er:YSGG (30%) at 300 K.

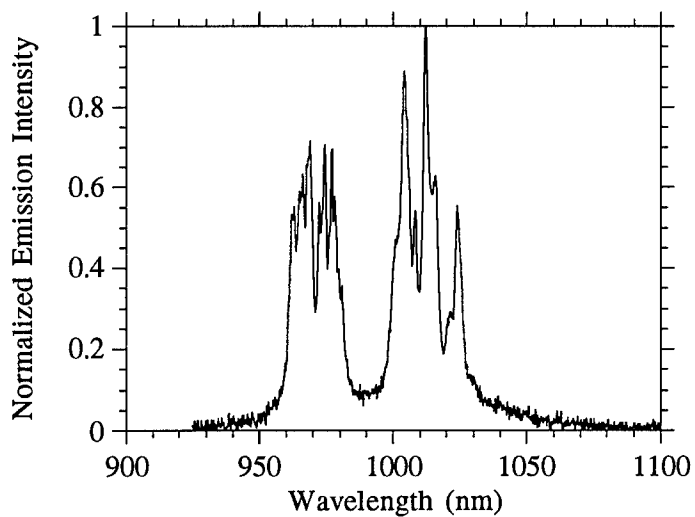


Figure 2-13: ${}^4I_{11/2} \rightarrow {}^4I_{15/2}$ emission spectrum for Er:GGG (30%) at 300 K.

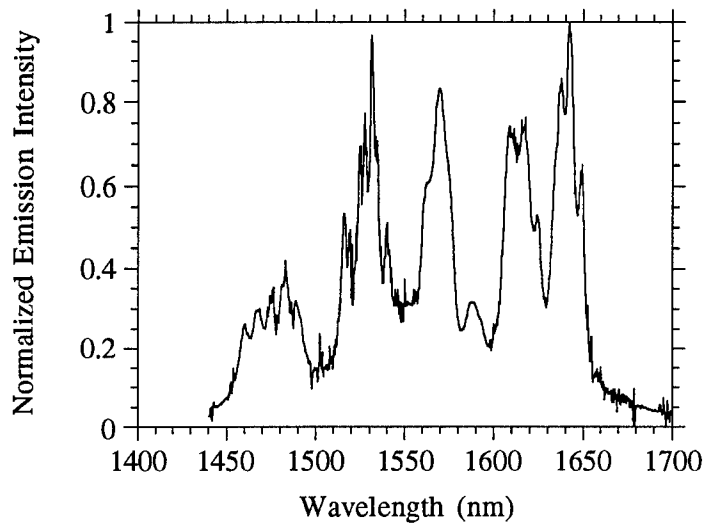


Figure 2-14: ${}^4I_{13/2} \rightarrow {}^4I_{15/2}$ emission spectrum for Er:YSGG (30%) at 300 K.

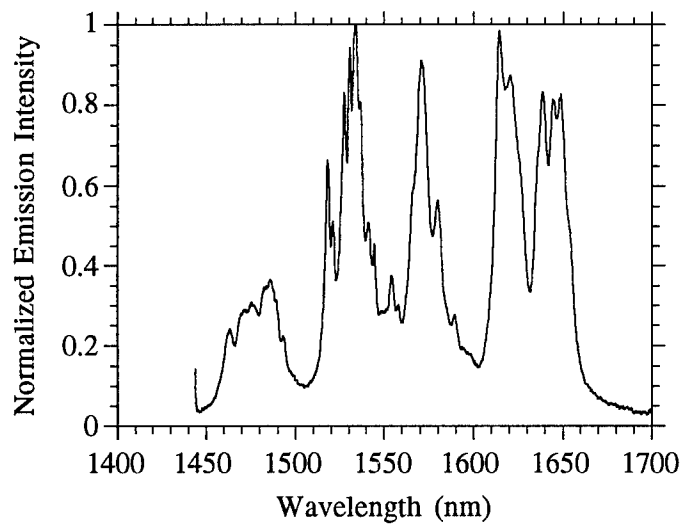


Figure 2-15: ${}^4I_{13/2} \rightarrow {}^4I_{15/2}$ emission spectrum for Er:GGG (30%) at 300 K.

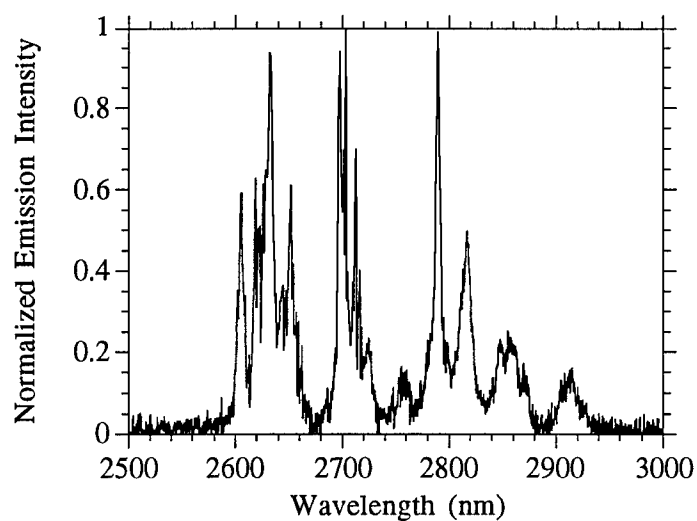


Figure 2-16: ${}^4I_{11/2} \rightarrow {}^4I_{13/2}$ emission spectrum for Er:YSGG (30%) at 300 K.

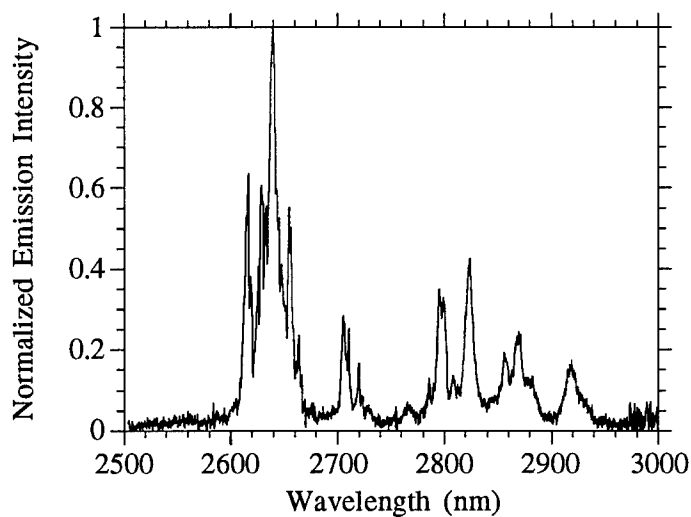


Figure 2-17: ${}^4I_{11/2} \rightarrow {}^4I_{13/2}$ emission spectrum for Er:GGG (30%) at 300 K.

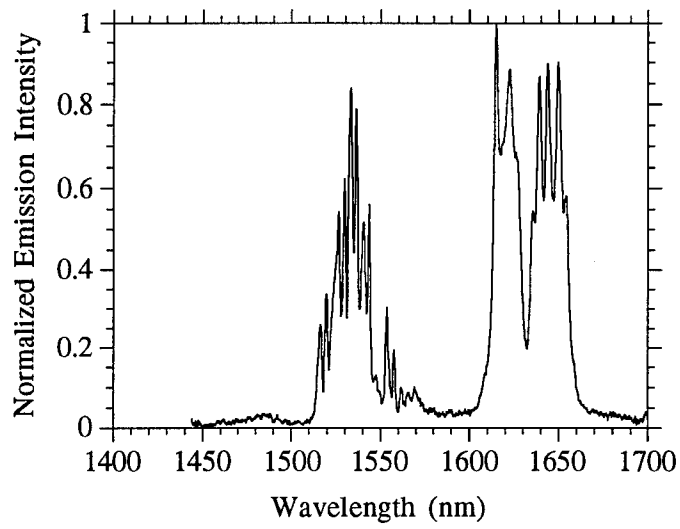


Figure 2-18: $4I_{13/2} \rightarrow 4I_{15/2}$ emission spectrum of Er:GGG (30%) at 77 K.

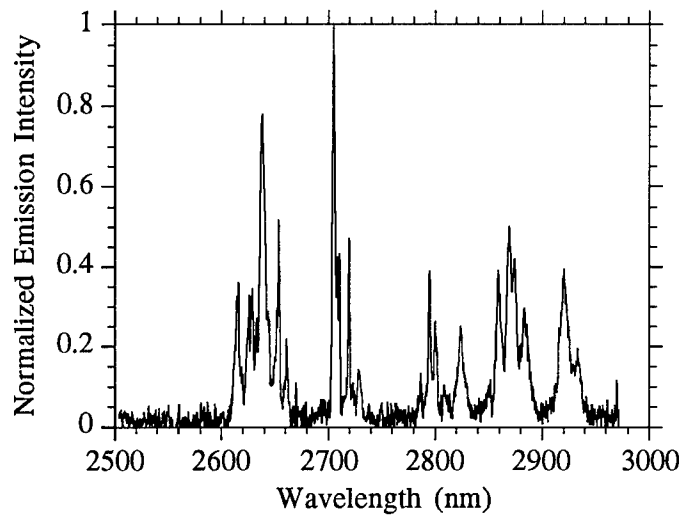


Figure 2-19: $4I_{11/2} \rightarrow 4I_{13/2}$ emission spectrum of Er:GGG (30%) at 77 K.

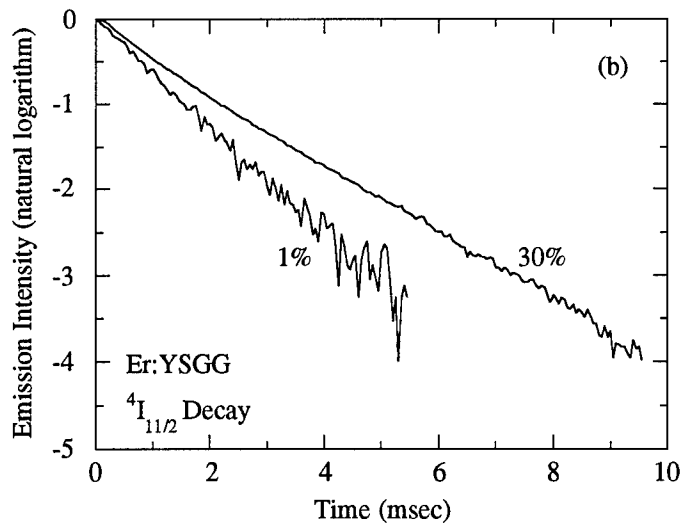
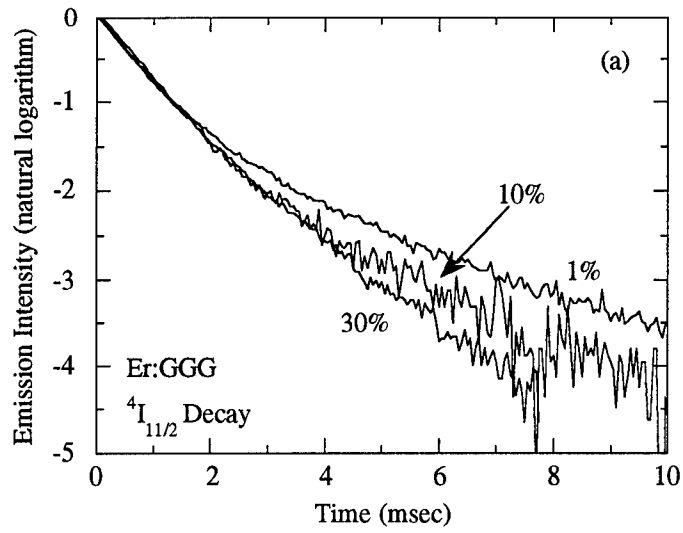


Figure 2-20: $^4I_{11/2}$ emission from (a) Er:GGG and (b) Er:YSGG for indicated concentrations at 300 K. The non-linear decay at early times for GGG is indicative of strong energy-transfer processes. The effect is less pronounced in YSGG.

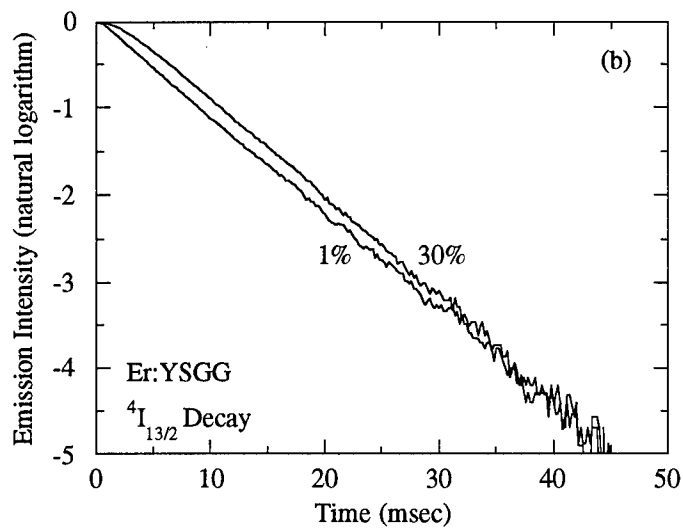
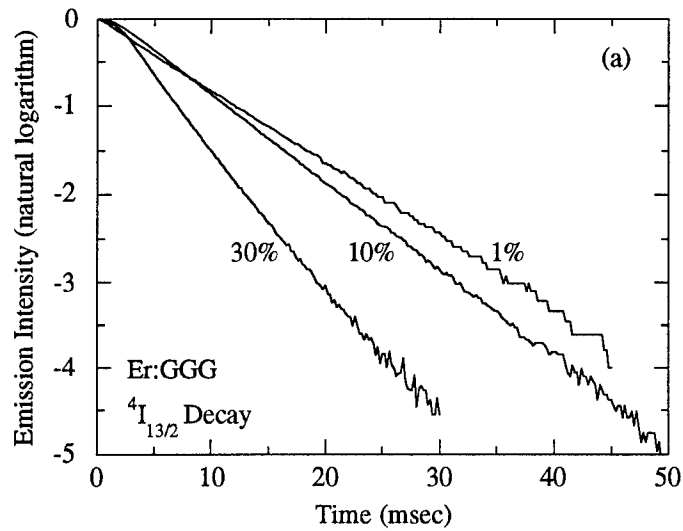


Figure 2-21: $^4I_{13/2}$ emission from (a) Er:GGG and (b) Er:YSGG for indicated concentrations at 300 K. The linear lineshape indicates that energy transfer affects this state much less than the $^4I_{11/2}$ state, as shown in Figure 2-20, at the pump densities encountered in the samples. Radiative trapping is probably responsible for the long lifetime of the 30%-doped sample relative to the 1%-doped sample.

2.6 Calculation of the Judd-Ofelt Parameters

The Judd-Ofelt Parameters for GGG and YSGG were calculated by considering the absorption spectra and parameters such as refractive index and dopant concentration in the host. The absorption spectra were analyzed to determine the maximum and minimum wavelength of each ground-state transition (or group of transitions whose spectra overlapped); and the mean wavelength of each transition (or group of transitions). The absorption coefficients in each region were summed to determine the integrated absorption intensity. Tables 2-7 and 2-8 present the data extracted from the absorption spectra of 30%-doped Er:GGG and Er:YSGG at room temperature.

${}^4I_{15/2} \rightarrow$	$\bar{\lambda}$ (nm)	Region of Integration	$\Sigma\alpha(\lambda)$ [cm ⁻¹]	$\Sigma\sigma(\lambda) \Delta\lambda$ [x 10 ⁻²⁰ nm-cm ²]
${}^4I_{13/2}$	1547.5	1430 nm-1665 nm	17129.0	45.1
${}^4I_{11/2}$	972.5	925 nm-1020 nm	3994.1	5.3
${}^4I_{9/2}$	802.0	784 nm-820 nm	595.8	1.57
${}^4F_{9/2}$	657.5	635 nm-680 nm	2814.3	7.41
${}^2H_{11/2}, {}^4S_{3/2}$	532.0	504 nm-	3730.3	9.82
${}^4F_{7/2}$	491.0	482 nm-500 nm	1157.0	3.04
${}^4F_{3/2}, {}^4F_{5/2}$	451.0	440 nm-462 nm	476.7	1.25
${}^2H_{9/2}$	410.0	402 nm-418 nm	322.5	0.85
${}^4G_{11/2}$	382.5	375 nm-390 nm	2632.8	6.93
${}^2G_{7/2}, {}^4G_{9/2}, {}^2K_{15/2}$	365.0	355 nm-375 nm	1495.4	3.94

Table 2-7: Data extracted from absorption spectra of Er:GGG (30%) used to calculate the Judd-Ofelt Parameters.

${}^4I_{15/2} \rightarrow$	$\bar{\lambda}$ (nm)	Region of Integration	$\Sigma\alpha(\lambda)$ [cm ⁻¹]	$\Sigma\sigma(\lambda) \Delta\lambda$ [x 10 ⁻²⁰ nm-cm ²]
${}^4I_{13/2}$	1547.5	1425 nm-1650 nm	13064	35.2
${}^4I_{11/2}$	972.5	930 nm-1025 nm	2746.39	3.71
${}^4I_{9/2}$	802.0	784 nm-820 nm	437.68	1.18
${}^4F_{9/2}$	657.5	635 nm-680 nm	2629.07	7.10
${}^2H_{11/2}, {}^4S_{3/2}$	532.0	500 nm-560 nm	3456.4	9.33
${}^4F_{7/2}$	491.0	483 nm-500 nm	1037.55	0.28
${}^4F_{3/2}, {}^4F_{5/2}$	451.0	440 nm-461 nm	419.84	1.13
${}^2H_{9/2}$	410.0	403 nm-418 nm	332.72	0.90
${}^4G_{11/2}$	382.5	380 nm-390 nm	1347.04	3.64
${}^2G_{7/2}, {}^4G_{9/2}, {}^2K_{15/2}$	365.0	350 nm-380 nm	2452.81	6.62

Table 2-8: Data extracted from absorption spectra of Er:YSGG (30%) used to calculate the Judd-Ofelt Parameters.

The only other parameters necessary to calculate the Judd-Ofelt Parameters are the indices of refraction for the two hosts. It is not a reasonable approximation, however, to consider that the index is a constant for each material over the entire wavelength range used in the calculations. The Sellmeier Coefficients, however, can be used to determine the index at a particular wavelength. Sellmeier Coefficients are obtained by measuring dispersion of light through a prism of the material to be investigated as a function of wavelength. Dispersion angles are measured at a series of wavelengths, and the index is then calculated for that particular wavelength. The data is then fit to:

$$n^2 - 1 = \sum_{i=1}^3 \frac{A_i \lambda^2}{\lambda^2 - L_i^2}$$

which is the Sellmeier Equation³; and in which A_i (dimensionless) and L_i (microns) are known as the Sellmeier Coefficients, and λ is the wavelength of radiation (microns) at which the refractive index is being calculated.

The Sellmeier Coefficients used for GGG are $A_1=1.7727$, $A_2=0.9767$, $A_3=4.9668$, $L_1=0.1567$, $L_2=0.01375$, $L_3=22.715$. [10] The data for YSGG have not been as extensively reported in the literature, and location of the coefficients for this material was difficult. Studenikin, however, has reported measurements from which A_1 and L_1 can be deduced. [13] These values were determined by studying dispersion at only four discrete wavelengths in the visible spectrum. Any values of index calculated in the infrared must therefore be considered to be approximate, at best. The coefficients deduced for YSGG are $A_1= 2.6695$ and $L_1=0.13035$, valid near 300 K.

³ The Sellmeier Equation is a derivation of the classical Lorentz-Lorenz formula, which relates a medium's refractive index to its polarizability in terms of characteristic oscillator frequencies of the medium. Reference [23] details the derivation.

These values, together with the appropriate series of reduced matrix elements and the extracted data presented in Tables 2-7 and 2-8, were then input into a computer program which executed a least-squares fit to the series of Judd-Ofelt line strength equations (one equation per transition) to ultimately determine the Judd-Ofelt Parameters and associated radiative lifetimes. The calculated results for both materials are:

$$\text{GGG (30\%): } \quad \Omega_2=1.51 \times 10^{-20} \text{ cm}^2 \quad \Omega_4=0.79 \times 10^{-20} \text{ cm}^2 \quad \Omega_6=1.95 \times 10^{-20} \text{ cm}^2$$

$$\text{YSGG (30\%): } \quad \Omega_2=0.43 \times 10^{-20} \text{ cm}^2 \quad \Omega_4=1.14 \times 10^{-20} \text{ cm}^2 \quad \Omega_6=1.17 \times 10^{-20} \text{ cm}^2$$

The software made calculations for radiative lifetimes based solely on electric-dipole transitions. The ${}^4I_{11/2} \rightarrow {}^4I_{13/2}$ and ${}^4I_{13/2} \rightarrow {}^4I_{15/2}$ transitions also contribute a significant magnetic-dipole component, however. The contributions to the total radiative decay probability by the magnetic-dipole component that are used in these calculations were borrowed from calculations for LaF_3 done by Weber. [21] It is not unreasonable to assume that the magnetic-dipole contributions will be similar in each material since the contributions, though not entirely negligible, are small.

The final results of the Judd-Ofelt calculations for 30%-erbium-doped GGG and YSGG are presented in Tables 2-9 (a,b) and 2-10 (a,b). Calculated values are shown of branching ratios (β), electric-dipole transition probabilities (A_{e-d}), magnetic-dipole transition probabilities (A_{m-d} , calculated for LaF_3), and total radiative lifetimes (τ).

transition	λ (nm)	β	A_{e-d} (sec ⁻¹)	A_{m-d} (sec ⁻¹)	τ (msec)
$4G_{11/2} \rightarrow 4H_{9/2}$	5333.3	0	1.28		0.082
$4F_{3/2}$	2551.7	0	2.93		
$4F_{5/2}$	2350.2	0	3.59		
$4F_{7/2}$	1690.3	0.001	12.32		
$2H_{11/2}$	1371.0	0.002	21.26		
$4S_{3/2}$	1242.5	0.001	14.38		
$4F_{9/2}$	894.8	0.020	247.31		
$4I_{9/2}$	712.6	0.009	105.35		
$4I_{11/2}$	614.1	0.006	71.64		
$4I_{13/2}$	502.0	0.145	1765.88		
$4I_{15/2}$	378.6	0.816	9957.75		
$2H_{9/2} \rightarrow 4F_{3/2}$	4892.4	0	0.06		
$4F_{5/2}$	4201.7	0	0.17		
$4F_{7/2}$	2474.6	0.001	4.48		
$2H_{11/2}$	1845.4	0.004	13.97		
$4S_{3/2}$	1620.0	0	0.40		
$4F_{9/2}$	1075.2	0.008	30.12		
$4I_{9/2}$	822.4	0.004	17.71		
$4I_{11/2}$	694.0	0.074	294.36		
$4I_{13/2}$	554.2	0.394	1563.60		
$4I_{15/2}$	407.5	0.515	2047.68		
$4F_{3/2} \rightarrow 4F_{5/2}$	29761.9	0	0		0.242
$4F_{7/2}$	5007.5	0	0.29		
$2H_{11/2}$	2963.0	0	0.15		
$4S_{3/2}$	2421.9	0.001	2.12		
$4F_{9/2}$	1378.0	0.009	35.17		
$4I_{9/2}$	988.6	0.056	228.97		
$4I_{11/2}$	808.7	0.354	1461.34		
$4I_{13/2}$	625.0	0.052	212.83		
$4I_{15/2}$	444.5	0.529	2184.2		
$4F_{5/2} \rightarrow 4F_{7/2}$	6020.5	0	0.06		
$2H_{11/2}$	3290.6	0.001	4.86		
$4S_{3/2}$	2636.4	0	0.39		
$4F_{9/2}$	1444.9	0.033	144.69		
$4I_{9/2}$	1022.6	0.031	134.88		

Table 2-9.a : Values of branching ratios, electric- and magnetic-dipole transition probabilities, and lifetimes for excited-state transitions in Er:GGG (30%), as calculated from the Judd-Ofelt Theory.

transition	λ (nm)	β	A_{e-d} (sec ⁻¹)	A_{m-d} (sec ⁻¹)	τ (msec)
$^4F_{5/2} \rightarrow ^4I_{11/2}$	831.3	0.017	73.74		0.227
$^4I_{13/2}$	638.4	0.361	1590.20		
$^4I_{15/2}$	451.3	0.558	2459.90		
$^4F_{7/2} \rightarrow ^2H_{11/2}$	7256.9	0	0.87		0.193
$^4S_{3/2}$	4690.4	0	0.02		
$^4F_{9/2}$	1901.1	0.001	3.76		
$^4I_{9/2}$	1231.8	0.037	190.83		
$^4I_{11/2}$	964.4	0.042	218.50		
$^4I_{13/2}$	714.1	0.054	282.42		
$^4I_{15/2}$	487.9	0.866	4487.80		
$^2H_{11/2} \rightarrow ^4S_{3/2}$	13262.6	0	0.20		0.325
$^4F_{9/2}$	2576.0	0.003	8.66		
$^4I_{9/2}$	1483.7	0.022	69.31		
$^4I_{11/2}$	1112.2	0.012	36.97		
$^4I_{13/2}$	792.1	0.030	93.39		
$^4I_{15/2}$	523.0	0.932	2872.56		
$^4S_{3/2} \rightarrow ^4F_{9/2}$	3196.9	0	1.01		0.324
$^4I_{9/2}$	1670.6	0.029	90.75		
$^4I_{11/2}$	1214.0	0.021	65.27		
$^4I_{13/2}$	842.4	0.275	848.87		
$^4I_{15/2}$	544.5	0.674	2077.38		
$^4F_{9/2} \rightarrow ^4I_{9/2}$	3499.0	0.001	1.58		0.655
$^4I_{11/2}$	1957.3	0.008	12.48		
$^4I_{13/2}$	1143.8	0.040	60.61		
$^4I_{15/2}$	656.3	0.951	1451.33		
$^4I_{9/2} \rightarrow ^4I_{11/2}$	4442.5	0.007	1.18		5.969
$^4I_{13/2}$	1699.2	0.510	85.49		
$^4I_{15/2}$	807.8	0.483	80.85		
$^4I_{11/2} \rightarrow ^4I_{13/2}$	2751.8	0.115	27.65	8.4	4.006
$^4I_{15/2}$	987.3	0.885	213.57		
$^4I_{13/2} \rightarrow ^4I_{15/2}$	1539.6	1.000	160.67	37.6	5.044

Table 2-9.b : Values of branching ratios, electric- and magnetic-dipole transition probabilities, and lifetimes for excited-state transitions in Er:GGG (30%), as calculated from the Judd-Ofelt Theory.

transition	λ (nm)	β	A_{e-d} (sec ⁻¹)	A_{m-d} (sec ⁻¹)	τ (msec)
$^4G_{11/2} \rightarrow ^4H_{9/2}$	5333.3	0	1.13		0.077
$^4F_{3/2}$	2551.7	0	3.30		
$^4F_{5/2}$	2350.2	0	4.36		
$^4F_{7/2}$	1690.3	0.001	16.70		
$^2H_{11/2}$	1371.0	0.003	37.48		
$^4S_{3/2}$	1242.5	0.003	33.01		
$^4F_{9/2}$	894.8	0.011	143.03		
$^4I_{9/2}$	712.6	0.006	81.01		
$^4I_{11/2}$	614.1	0.010	134.80		
$^4I_{13/2}$	502.0	0.178	2311.54		
$^4I_{15/2}$	378.6	0.787	10226.93		
$^2H_{9/2} \rightarrow ^4F_{3/2}$	4892.4	0	0.12		
$^4F_{5/2}$	4201.7	0	0.24		
$^4F_{7/2}$	2474.6	0.001	4.13		
$^2H_{11/2}$	1845.4	0.005	21.45		
$^4S_{3/2}$	1620.0	0	0.68		
$^4F_{9/2}$	1075.2	0.008	35.67		
$^4I_{9/2}$	822.4	0.004	15.89		
$^4I_{11/2}$	694.0	0.077	349.11		
$^4I_{13/2}$	554.2	0.387	1751.67		
$^4I_{15/2}$	407.5	0.519	2351.49		
$^4F_{3/2} \rightarrow ^4F_{5/2}$	29761.9	0	0		0.216
$^4F_{7/2}$	5007.5	0	0.66		
$^2H_{11/2}$	2963.0	0	0.16		
$^4S_{3/2}$	2421.9	0	1.01		
$^4F_{9/2}$	1378.0	0.008	35.59		
$^4I_{9/2}$	988.6	0.094	433.82		
$^4I_{11/2}$	808.7	0.349	1618.26		
$^4I_{13/2}$	625.0	0.047	217.59		
$^4I_{15/2}$	444.5	0.502	2324.82		
$^4F_{5/2} \rightarrow ^4F_{7/2}$	6020.5	0	0.05		
$^2H_{11/2}$	3290.6	0.001	4.79		
$^4S_{3/2}$	2636.4	0	0.34		
$^4F_{9/2}$	1444.9	0.036	186.80		
$^4I_{9/2}$	1022.6	0.032	163.99		

Table 2-10.a : Values of branching ratios, electric- and magnetic-dipole transition probabilities, and lifetimes for excited-state transitions in Er:YSGG (30%), as calculated from the Judd-Ofelt Theory.

transition	λ (nm)	β	A_{e-d} (sec ⁻¹)	A_{m-d} (sec ⁻¹)	τ (msec)
$^4F_{5/2} \rightarrow ^4I_{11/2}$	831.3	0.033	171.90		0.194
$^4I_{13/2}$	638.4	0.392	2026.01		
$^4I_{15/2}$	451.3	0.506	2611.87		
$^4F_{7/2} \rightarrow ^2H_{11/2}$	7256.9	0	0.87		0.153
$^4S_{3/2}$	4690.4	0	0.04		
$^4F_{9/2}$	1901.1	0.001	5.48		
$^4I_{9/2}$	1231.8	0.032	208.17		
$^4I_{11/2}$	964.4	0.052	342.83		
$^4I_{13/2}$	714.1	0.106	689.71		
$^4I_{15/2}$	487.9	0.809	5287.52		
$^2H_{11/2} \rightarrow ^4S_{3/2}$	13262.6	0	0.04		0.331
$^4F_{9/2}$	2576.0	0.002	4.66		
$^4I_{9/2}$	1483.7	0.021	62.50		
$^4I_{11/2}$	1112.2	0.011	32.97		
$^4I_{13/2}$	792.1	0.040	120.31		
$^4I_{15/2}$	523.0	0.927	2800.46		
$^4S_{3/2} \rightarrow ^4F_{9/2}$	3196.9	0	1.01		0.315
$^4I_{9/2}$	1670.6	0.033	103.60		
$^4I_{11/2}$	1214.0	0.021	67.02		
$^4I_{13/2}$	842.4	0.268	852.41		
$^4I_{15/2}$	544.5	0.678	2151.59		
$^4F_{9/2} \rightarrow ^4I_{9/2}$	3499.0	0	0.97		0.442
$^4I_{11/2}$	1957.3	0.005	10.57		
$^4I_{13/2}$	1143.8	0.041	93.12		
$^4I_{15/2}$	656.3	0.954	2159.89		
$^4I_{9/2} \rightarrow ^4I_{11/2}$	4442.5	0.005	1.45		3.684
$^4I_{13/2}$	1699.2	0.314	85.27		
$^4I_{15/2}$	807.8	0.680	184.69		
$^4I_{11/2} \rightarrow ^4I_{13/2}$	2751.8	0.124	29.44	8.4	4.074
$^4I_{15/2}$	987.3	0.876	207.60		
$^4I_{13/2} \rightarrow ^4I_{15/2}$	1539.6	1.000	165.54	37.6	4.923

Table 2-10.b : Values of branching ratios, electric- and magnetic-dipole transition probabilities, and lifetimes for excited-state transitions in Er:YSGG (30%), as calculated from the Judd-Ofelt Theory.

2.7 Discussion of the Judd-Ofelt Results

The radiative lifetimes shown in Tables 2-9 and 2-10 are derived from calculations of the Judd-Ofelt theory which are based only absorption measurements. As such, it is important to know how closely these values resemble the actual observed data, which are reported for the four lowest states in Table 2-5.

The results show agreement to within 4% for transitions from the ${}^4I_{13/2}$ state. Lifetimes of the ${}^4I_{11/2}$, ${}^4I_{9/2}$, and ${}^4S_{3/2}$ states, however, are significantly longer in the calculations than they are for the measured values. This variation occurs due to the influence of non-radiative decays from these states. Specifically, the thermal relaxation within the ${}^4I_{9/2} \rightarrow {}^4I_{11/2}$ and ${}^4I_{11/2} \rightarrow {}^4I_{13/2}$ states significantly shortens the overall lifetime of the respective upper states. The near-resonance of many states means that in addition to thermal relaxation, cross-relaxation processes will also assist to deplete the ${}^4S_{3/2}$ state (this process will be discussed further in Chapter 3), shortening its overall lifetime even further.

The numbers obtained through the Judd-Ofelt calculations, though only partially representative of reality, are similar to the results found in the literature based on other erbium-doped hosts. These calculations, as well as those reported for other rare-earth ions, indicate that the method is best suited to analyze ions under conditions of minimal energy transfer in order to reduce energy-transfer-related lifetime-quenching. The process may in these cases serve as an approximation of radiative lifetimes when experimental data are difficult to obtain.

The Judd-Ofelt Theory is better suited to accurately determine values for branching coefficients than it is for radiative lifetimes. The branching coefficients are relative terms, which can be expected to vary little in the presence of nonradiative energy transfer.

The results of the Judd-Ofelt theory may be additionally applied to determine the radiative quantum efficiency of the ${}^4I_{11/2} \rightarrow {}^4I_{13/2}$ laser transition. The radiative quantum

efficiency of a transition, η , may be qualitatively defined as the fraction of excitation which decays via spontaneous emission. Quantitatively:

$$\eta = \tau_{\text{observed}} \sum_m A_m = \tau_{11/2} (A_{11/2 \rightarrow 13/2} + A_{11/2 \rightarrow 15/2}). \quad [24]$$

The efficiency may be calculated by using the appropriate values: the observed lifetime for the ${}^4I_{11/2}$ state ($\tau_{11/2}$) at the concentration for which the Judd-Ofelt calculations were made (30%, in this case) and the Judd-Ofelt-calculated transition probabilities ($A_{i \rightarrow j}$). The resultant radiative quantum efficiencies are 0.24 for GGG and 0.32 for YSGG.

References for Chapter 2

- [1] B.J. Dinerman and P. F. Moulton, "CW Laser Operation from Er:YAG, Er:GGG, and Er:YSGG". Proceedings of the Advanced Solid State Lasers Conference, Santa Fe, New Mexico. February, 1992.
- [2] R.C. Stoneman and L. Esterowitz "Efficient Resonantly Pumped 2.8- μm Er³⁺:GSGG Laser". Optics Letters. **17**, 11. (1992).
- [3] B.J. Dinerman and P.F. Moulton. "CW Laser Operation from Er:YAG, Er:GGG, Er:YSGG, and Er:BYF". Proceedings of the IEEE Lasers and Electro-Optics Society Annual Meeting, Boston, MA. November, 1992.
- [4] G.J. Kintz, R. Allen, and L. Esterowitz. "CW and Pulsed 2.8 μm Laser Emission From Diode-Pumped Er³⁺:LiYF₄ at Room Temperature". Applied Physics Letters. **50**, 22. (1987).
- [5] E.V. Zharikov, "Features of Rare-Earth Scandium Garnets Influencing Crystal Growth for Solid-State Lasers". Proceedings of the Tunable Solid State Lasers Conference, Salt Lake City, Utah. March, 1990.
- [6] from the Materials Progress Corporation specification sheet for Gadolinium Gallium Garnet. Materials Progress Corporation, Santa Rosa, California.
- [7] P.F. Moulton, in the CRC Laser Handbook. CRC Press, Florida. 1982.
- [8] J. Ahn. "Thermal and Optical Properties of Gadolinium Gallium Garnet". Materials Research Bulletin. **17**, 1393. 1982.
- [9] A. A. Kaminskii, Laser Crystals (Second Edition). Springer-Verlag. 1990.
- [10] D.L. Wood and K. Nassau. "Optical Properties of Gadolinium Gallium Garnet". Applied Optics. **29**, 25. 1990.
- [11] E.V. Zharikov and I.A. Shcherbakov, "New Scandium Garnet Mixtures for Solid State Lasers".
- [12] M. Randles, at Airtron-Synoptics Group, Charlotte, North Carolina. Personal Communication.
- [13] P.A. Studenikin, at the Russian Academy of Sciences, General Physics Institute, Moscow, Russia. Personal Communication.
- [14] C. Morrison, et al, "Theoretical Temperature-Dependent Branching Ratios and Laser Thresholds of the ⁵I₇ → ⁵I₈ Levels of Ho³⁺ in Ten Garnets". Harry Diamond Laboratories Report HDL-TR-2185. 1990.
- [15] B. Di Bartolo. Optical Interactions in Solids. Wiley Press. 1968.

- [16] J.A. Koningstein and J.E. Geusic. "Energy Levels and Crystal-Field Calculations of Er in YAG". *Physical Review*. **136**, 3A. (1964).
- [17] B.R. Judd. "Optical Absorption Intensities of Rare-Earth Ions". *Physical Review*. **127**, 3. (1962).
- [18] G.S. Ofelt. "Intensities of Crystal Spectra of Rare-Earth Ions". *Journal of Chemical Physics*. **37**, 3. (1962).
- [19] W.T. Carnall, H. Crosswhite, and H.M. Crosswhite. "Energy Level Structure and Transition Probabilities in the Spectra of the Trivalent Lanthanides in LaF₃". Argonne National Laboratory Report ANL-78-XX-95.
- [20] D.L. Dexter, in Solid State Physics (Vol. 6). Academic Press, Inc. 1958.
- [21] M.J. Weber. "Decay of Er³⁺ in LaF₃". *Physical Review*. **157**, 262 (1967).
- [22] P.F. Moulton, J.G. Manni, and G.A. Rines. "Spectroscopic and Laser Characteristics of Er,Cr:YSGG". *IEEE Journal of Quantum Electronics*. **24**, 6. (1988).
- [23] B. Di Bartolo, Classical Theory of Electromagnetism. Prentice Hall, 1991.
- [24] M. Kh. Ashurov, et al. "Nonradiative Losses Due to the $^4I_{11/2} \rightarrow ^4I_{13/2}$ Transition of the Er³⁺ Ion in Y₃Al₅O₁₂, Gd₃Sc₂Al₃O₁₂, Y₃Ga₅O₁₂, Gd₃Ga₅O₁₂, and CaF₂ Crystals". *Soviet Journal of Quantum Electronics*. **8**, 5. (1978).

Chapter 3: Energy Transfer in Er:GGG and Er:YSGG

3.1 Introduction to Chapter 3

This chapter discusses the application of the results of an experiment to calculate the upconversion rate coefficients of the ${}^4I_{11/2}$ and ${}^4I_{13/2}$ states. Upconversion energy transfer plays a major role in the distribution of population amongst the electronic states. The results of Chapter 2 indicate the presence of quenching processes which significantly shorten the ${}^4I_{13/2}$ radiative lifetime as the concentration of erbium is increased. This effect indicates the potential of using these materials as hosts in cw lasers and is the motivation for quantifying the upconversion process.

A rate-equation analysis is used to model the system in order to determine the upconversion coefficients associated with the ${}^4I_{11/2}$ and ${}^4I_{13/2}$ states. The analysis studies the emission from ${}^4I_{9/2}$ and ${}^4S_{3/2}$ which results from upconversion processes after the system is excited directly into ${}^4S_{3/2}$. This emission is analyzed as a function of time and pump rate. Data may then be extracted which relate the quantity of upconversion-induced luminescence to pump-induced luminescence, from which the upconversion coefficients are derived.

3.2 Energy Transfer within Rare-Earth-Doped Solids

Many channels exist in rare-earth-doped solids through which the energy deposited by the excitation source can flow. These channels include radiative and nonradiative decay, excited-state absorption, cross-relaxation, upconversion, and energy migration.¹ It is necessary to understand these mechanisms and their interaction in the solid in order to properly model the rare-earth-doped system.

Radiative decay, or luminescence, occurs when an excited state decays to a lower state via emission of a photon. (Figure 3-1.a) In most trivalent rare-earth-doped systems, the emitted photons have energies falling within the visible to near-infrared regions of the electromagnetic spectrum due to the energy state structure within the 4f electronic shell.

Nonradiative decay, while in reality defining de-excitation via any means other than luminescence, more commonly refers to the decay of an excited state via emission of one or more quanta of vibration, or phonon. (Figure 3-1.b) Nonradiative relaxation most frequently occurs within manifolds or between manifolds not greatly separated in energy, and by definition results in the heating of the crystal. The probability for nonradiative decay is greatest in materials such as the garnets, which have high phonon energies. This contrasts with the fluorides, which are softer, have lower phonon energies, and therefore show a reduced probability for phonon decay.

Excited-state absorption occurs when an ion in an excited state absorbs one or more photons, promoting the ion to a yet higher state. (Figure 3-1.c) The absorbed photon may be produced by the excitation source or it may be internally generated through the decay

¹ Energy transfer is generally thought of as a process involving the non-radiative exchange of energy between two or more ions in the lattice. Strictly speaking, luminescence and phonon relaxation are therefore not considered to be energy transfer mechanisms. None-the-less, their description here clarifies the description of the mechanisms to follow.

from another transition. In either case, the photon must be resonant with the energy difference of the two excited states.

Cross-relaxation is a nonradiative interaction that occurs between two neighboring ions. One ion in an excited state transfers some of its excitation to a nearby ion in a much lower state, resulting in two ions in an 'intermediate' excited state. (Figure 3-1.d) In this situation, resonance or near-resonance is required. (The process may be phonon-assisted.) Cross-relaxation is highly dependent upon the concentration of the ions under consideration and the excitation density of the ions.

Upconversion is essentially the opposite of cross-relaxation. One ion in an excited state interacts with another ion also in an excited state, de-exciting the former and promoting the latter to a higher state. (Figure 3-1.e) Again, near-resonance is required for this process to occur. Concentration and excitation density similarly influence the probability for upconversion.

Energy migration refers to the transfer of excitation between similar ions in the lattice. (Figure 3-1.f) The energy transfer is resonant, meaning that the first excited ion will promote the second ion to the same excited state. This process is highly dependent upon the inter-ionic distance. The migration may occur until the excitation is intercepted by an impurity ion, or any ion which may release the excitation as luminescence, phonon decay, etc.

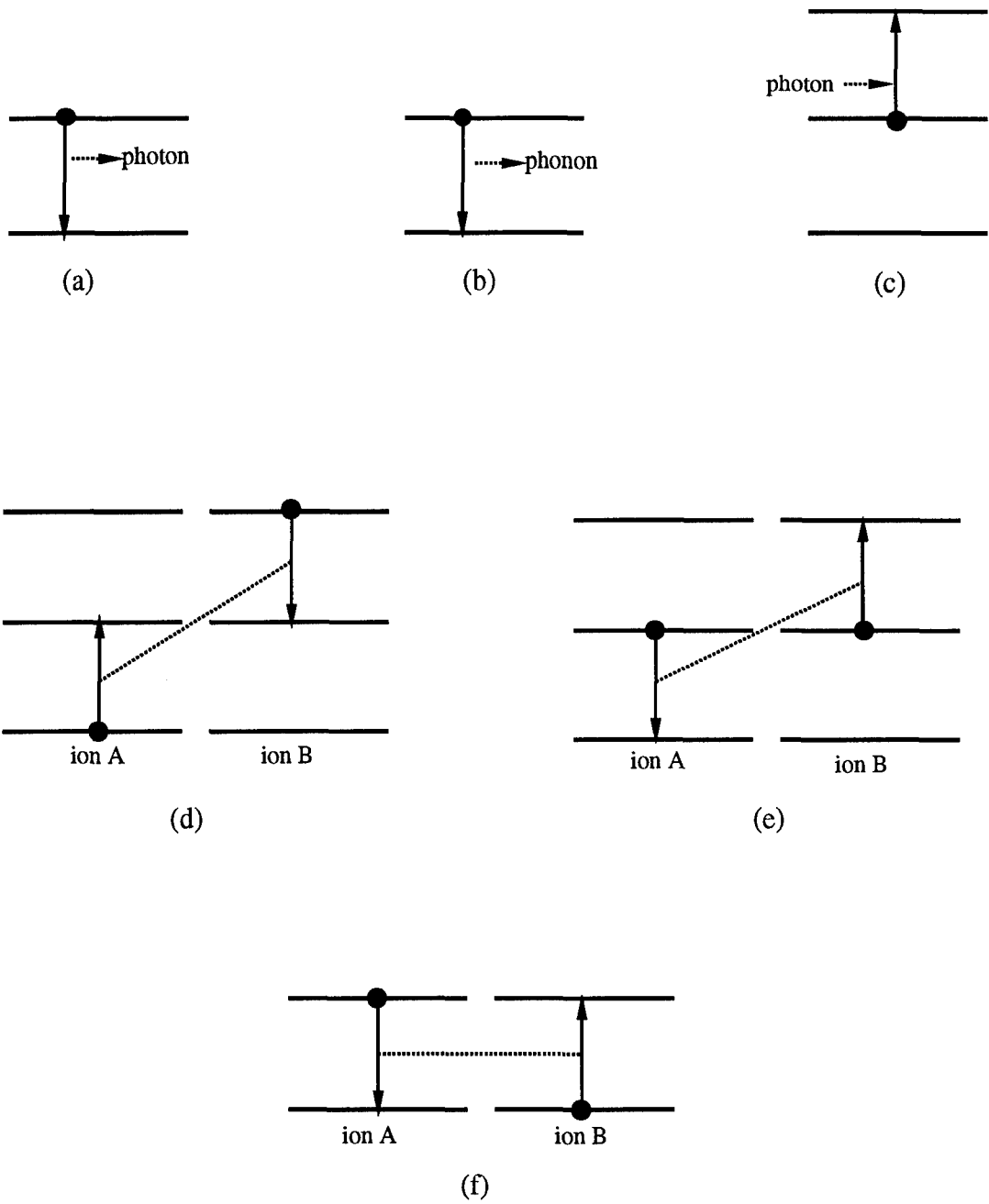


Figure 3-1: Basic Energy Transfer. (a) radiative decay (b) nonradiative decay (c) excited state absorption (d) cross-relaxation (e) upconversion (f) energy migration/diffusion. Dashed lines indicate nonradiative transfer. Dark circles indicate initial state(s) of ion(s).

The Förster-Dexter theory of energy transfer [1,2] quantifies energy transfer within rare-earth-doped solids. The model calculates the probability of energy transfer between two ions in a crystal by considering the overlap between the absorption and emission bands of two ionic states. It has been used with varying degrees of success to model systems such as Cr,Nd:GSGG and Cr,Tm,Ho:YAG. It has also been applied to model the Er:YAG system by Lacovara [3] and Er:BYF by Knowles. [4] Although the theory will not be applied to this analysis of erbium, a summary will be presented due to its relevance to such systems.

The Förster-Dexter theory models the probability of energy transfer between a donor (sensitizer) and an acceptor (activator) based on multipole-multipole interactions. The model, put into its most common form by Dexter, begins its calculation of the transfer probability between a sensitizer and activator using Fermi's Golden Rule as derived from time-dependent perturbation theory:

$$P_{SA} = \left(\frac{2\pi}{\hbar} \right) \left| \int \Psi_i H_1 \Psi_f d\tau \right|^2 \rho(E) \quad [3.3.1],$$

where Ψ_i and Ψ_f are the product wave functions of the sensitizer and activator, H_1 is the interaction Hamiltonian of the system, and $\rho(E)$ is the density of states. The Hamiltonian, expressed as the sum of the interactions of the electrons of the sensitizer with those of the activator,

$$H_{SA} = \frac{1}{\kappa} \sum_{i,j} \frac{e^2}{|\bar{r}_i - \bar{r}_j|} \quad [3.3.2],$$

is expanded in a Taylor series about the separation \mathbf{R} between the nuclei of the sensitizer and the nuclei of the activator, such that the interaction energy becomes

$$H_{SA}(\mathbf{R}) = \left(\frac{e^2}{\kappa R^3} \right) \left\{ \mathbf{r}_S \cdot \mathbf{r}_A - \frac{3(\mathbf{r}_S \cdot \mathbf{R})(\mathbf{r}_A \cdot \mathbf{R})}{R^2} \right\} + \dots \quad [3.3.3].$$

This term is the dipole-dipole interaction energy which is the basis for van der Waals interactions. Higher order terms such as dipole-quadrupole are typically neglected.

The probability for donor-acceptor energy transfer is derived by Dexter from the above consideration by combining [3.3.3] with expressions for the Einstein A Coefficient,

$$A(i, f) = \frac{4e^2 E^3}{3\hbar^4 c^3} \left| \langle \mathbf{r}_{if} \rangle \right|^2 \quad [3.3.4],$$

and with expressions for radiative lifetime and absorption cross section [4] as a function of the transition oscillator strength f ,

$$\frac{1}{\tau} = \frac{2e^2 \omega^2}{mc^3} f_d \quad [3.3.5]$$

$$\int \sigma(\omega) d\omega = \frac{2\pi^2 e^2}{mc} f \quad [3.3.6].$$

The final result is given by

$$P_{SA}(d-d) = \frac{3\hbar^4 c^4 Q_A}{4\pi R^6 n^4 \tau_S} \int \frac{f_S(E) F_A(E)}{E^4} dE \sim \frac{C^{(6)}}{R^6} \quad [3.3.7],$$

where $Q_A = \int \sigma(E) dE$; $f_S(E)$ and $F_A(E)$ are the normalized lineshapes of the sensitizer and activator absorption and emission bands; and $C^{(6)}$, known as the dipole-dipole microscopic interaction parameter, represents the probability per unit time of energy transfer when the donor and acceptor are separated by a distance of 1 cm. [5] The integral involving the

overlap of the sensitizer's emission with the absorption of the activator is the only unknown in this expression. This value may be calculated directly from spectroscopic measurements.

Equation [3.3.7] describes the probability for dipole-dipole energy transfer between sensitizer and activator. The more general expression which includes dipole-quadrupole, quadrupole-quadrupole, and higher order terms may be expressed as

$$P_{SA} = \frac{C^{(6)}}{R^6} + \frac{C^{(8)}}{R^8} + \frac{C^{(10)}}{R^{10}} + \dots = \sum_n \frac{C^{(n)}}{R^n} \quad [3.3.8].$$

The probability for a given energy transfer mechanism may also be expressed as

$$P_{SA} = \frac{C^{(n)}}{R^n} = \frac{1}{\tau_0} \left(\frac{R_0}{R} \right)^n \quad [3.3.9],$$

where τ_0 is the lifetime of an isolated sensitizer and R_0 is the ionic separation for which the sensitizer decay rate equals that of the sensitizer-activator energy transfer. Furthermore, R_0 may be expressed in terms of the same overlap integral used in [3.3.7] as

$$R_0^6 = \epsilon f_A \left[\frac{3\pi\epsilon^2 c^3 \hbar^5}{2m} \right] \int \frac{f_s(E) F_A(E)}{E^4} dE \quad [3.3.10],$$

where ϵ is the ratio of the sensitizer's overall lifetime to that of its radiative lifetime.

3.4 Energy Transfer in Er³⁺

Erbium possesses many energy transfer pathways due to the near-resonance of many of its lower 4f energy states. Upconversion, especially, plays an important role in erbium. Figure 3-2 shows schematically three upconversion channels which are present in erbium and relevant to this study. These include $(^4I_{13/2}, ^4I_{13/2}) \rightarrow (^4I_{15/2}, ^4I_{9/2})$; $(^4I_{11/2}, ^4I_{11/2}) \rightarrow (^4I_{15/2}, ^4F_{7/2})$; and $(^4I_{9/2}, ^4I_{9/2}) \rightarrow (^4I_{15/2}, ^2H_{9/2})$. The two latter processes are frequently followed, at room temperature, by a rapid nonradiative relaxation to the $^4S_{3/2}$ state, from which luminescence near 550 nm follows as a result of a transition to the $^4I_{15/2}$ ground state. The thermal relaxation is much less probable, however, at liquid-helium temperatures. Lasing under these conditions may also be seen in Er:BYF near 470 nm, 617 nm, 669 nm, and 703 nm. [6]

Cross-relaxation processes are also significant in erbium. Cross-relaxation, similar to upconversion, quenches the radiative lifetime of a given state at high concentrations. There are three significant processes which play a role in the spectroscopic characterization of erbium. These are $(^2H_{11/2}, ^4I_{15/2}) \rightarrow (^4I_{9/2}, ^4I_{13/2})$ and $(^2H_{11/2}, ^4I_{15/2}) \rightarrow (^4I_{13/2}, ^4I_{9/2})$ which may not be experimentally differentiated since both processes result in the same number of ions in initial and final states; and $(^4I_{9/2}, ^4I_{15/2}) \rightarrow (^4I_{13/2}, ^4I_{13/2})$. [7] Figure 3-3 shows these channels schematically.

The effects of energy transfer within erbium is crucial to the operation of the system as an efficient laser device. Low concentration hosts are required in the operation of a 1.5- μm laser in order to inhibit depopulation of the upper laser state due to the $(^4I_{13/2}, ^4I_{13/2}) \rightarrow (^4I_{15/2}, ^4I_{9/2})$ upconversion process; and also to minimize losses due to ground-state reabsorption. Higher concentrations are required for cw 2.8- μm -operation in order to promote the upconversion processes responsible for the reduction of the lifetime-induced

population bottleneck of the ${}^4I_{13/2}$ lower laser state. Although both the $({}^4I_{13/2}, {}^4I_{13/2}) \rightarrow ({}^4I_{15/2}, {}^4I_{9/2})$ and the $({}^4I_{11/2}, {}^4I_{11/2}) \rightarrow ({}^4I_{15/2}, {}^4F_{7/2})$ processes operate efficiently, it has been speculated that upconversion from the lower state (the former process) is greater than that from the upper laser state. This process 'recycles' the energy within the system and therefore makes cw laser action possible. Although the lifetime studies of erbium do not measure the absolute strengths of upconversion from the different states, they do hint that the lifetime of the ${}^4I_{11/2}$ upper laser state is much less sensitive to concentration (and therefore upconversion) than is the ${}^4I_{13/2}$ lower state. Quenching processes shortens the ${}^4I_{13/2}$ state lifetime in Er:GGG by a factor of 2.8 as a result of increasing the concentration from 1% to 30% erbium; the ${}^4I_{11/2}$ state lifetime, however, is reduced by only a factor of 1.2. The following sections will describe a procedure to measure the absolute strength of upconversion from the different states.

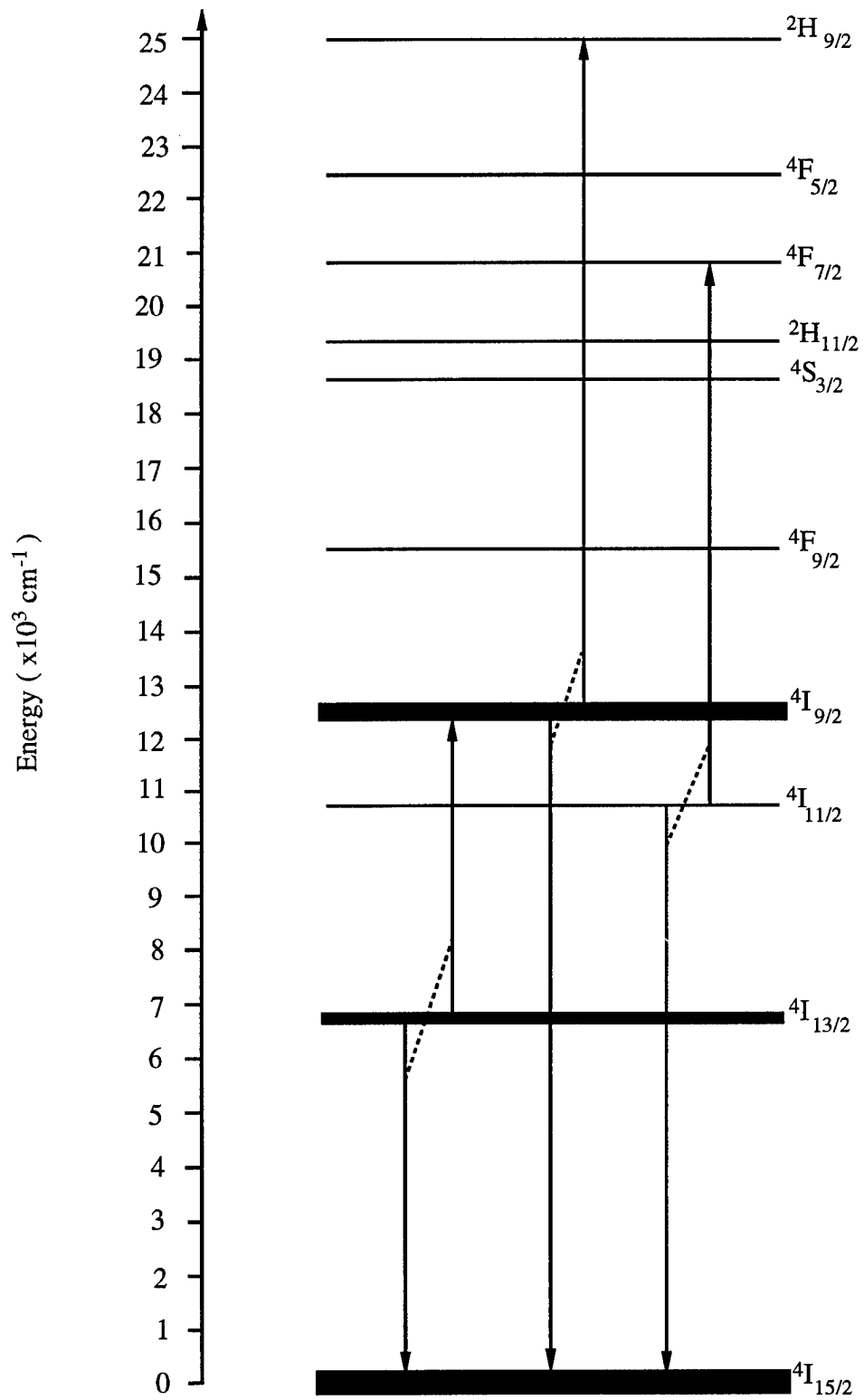


Figure 3-2: Upconversion pathways within the erbium-doped system.

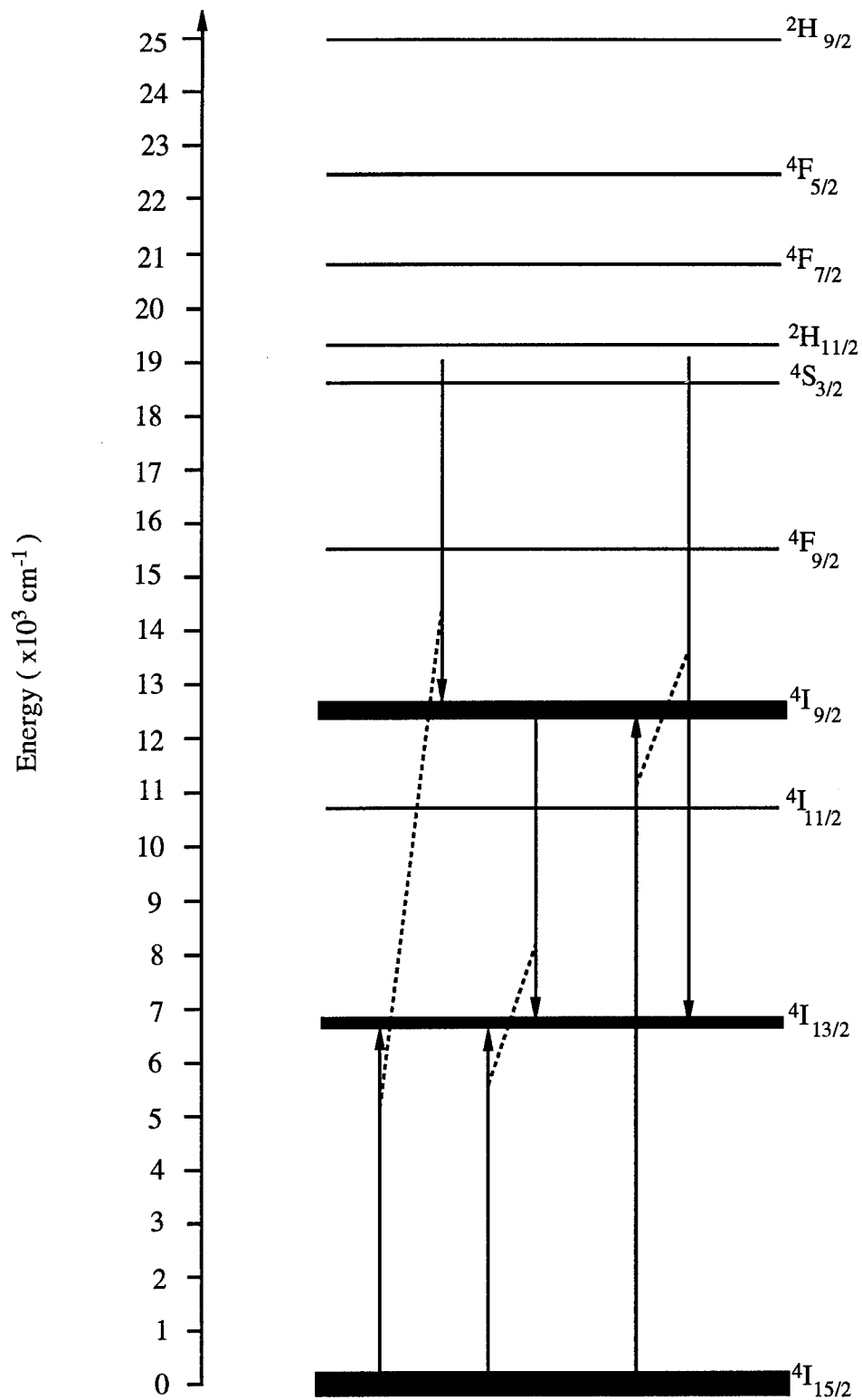


Figure 3-3: Cross-relaxation pathways within the erbium-doped system.

3.5 Rate Equations

The effect of the radiative, non-radiative, and energy transfer processes upon the system as a whole should be incorporated in the treatment to properly model the erbium-doped system. The Förster-Dexter theory does this by considering energy transfer from a microscopic point of view, where the roles of the different donor and acceptor atoms are considered. The system may also be viewed macroscopically, however, by considering the average effect of energy transfer upon the ensemble of atoms. This is done by modeling the dynamics of the erbium system through a series of coupled equations which describe the rate at which energy flows via the different processes to and from each level under consideration.

The rate equations most frequently used to model erbium were recently modified by Chou [7] to also incorporate the effects of cross-relaxation processes upon the overall population dynamics of the four lowest states. The rate equations which describe the erbium system relate the rate of population change of these states as functions of measurable spectroscopic parameters. These equations are summarized in Equations [3.5.1]-[3.5.4].

$$\frac{dn_1}{dt} = \beta_{21}A_2n_2 + 2(1 - \beta_{32})A_3n_3 - A_1n_1 - 2\alpha_1n_1^2 \quad [3.5.1]$$

$$\frac{dn_2}{dt} = \beta_{32}A_3n_3 - A_2n_2 - 2\alpha_2n_2^2 \quad [3.5.2]$$

$$\frac{dn_3}{dt} = A_4n_4 + \alpha_1n_1^2 - A_3n_3 \quad [3.5.3]$$

$$\frac{dn_4}{dt} = W + \alpha_2n_2^2 - A_4n_4 \quad [3.5.4],$$

where the subscripts 1, 2, 3, and 4 designate the states ${}^4I_{13/2}$, ${}^4I_{11/2}$, ${}^4I_{9/2}$, and $({}^4S_{3/2}, {}^2H_{11/2})^2$, respectively; n_i the population in excited-state i normalized to the concentration N_0 of erbium in the sample (i.e., $n_i = N_i / N_0$); A_i the probability for radiative decay from state i ; β_{ij} the branching coefficient between states i and j ; W the excitation, or pump rate (for convenience, excitation will occur from the ${}^4I_{15/2}$ ground state into the ${}^4F_{7/2}$ state using an Argon laser at 488 nm); and α_i the upconversion coefficient of state i averaged over the entire system.

Cross-relaxation, which varies as a function of the population of the acceptor state, affects the radiative decay rates A_3 and A_4 of the ${}^4I_{9/2}$ and $({}^4S_{3/2}, {}^2H_{11/2})$ states, respectively. Cross-relaxation terms are implicit to the rates, which may be written as:

$$A_4 = \frac{1}{\tau_4} + \alpha_4 n_0 \quad \text{and} \quad A_3 = \frac{1}{\tau_3} + \alpha_3 n_0,$$

where $\alpha_i n_0$ is the cross-relaxation rate which is proportional to the number of acceptors n_0 . n_0 is the ground-state population, which is assumed to be constant (undepleted).

Population growth of the ${}^4I_{13/2}$ state due to cross-relaxation from the ${}^4I_{9/2}$ state is incorporated into the model through the term $(1-\beta_{32})$, which is related to the feeding efficiency and which was calculated in Section 2.4. The two decays from ${}^4I_{9/2}$ are the radiative ${}^4I_{9/2} \rightarrow {}^4I_{11/2}$ and the cross-relaxation ${}^4I_{9/2} \rightarrow {}^4I_{13/2}$, whose rates can now be defined as $\beta_{32}A_3$ and $2(1-\beta_{32})A_3$, respectively. The factor of two in the cross-relaxation term represents the fact that two ions are promoted to the ${}^4I_{13/2}$ state via this process.

² The ${}^4I_{13/2}$, ${}^4I_{11/2}$, ${}^4I_{9/2}$, ${}^4S_{3/2}$, and ${}^2H_{11/2}$ states are the most relevant in this study of erbium. The proximity of ${}^4S_{3/2}$ to ${}^2H_{11/2}$, which results in a thermal equilibrium between the two, allows the consideration of these two states as one "effective" state. The ${}^4F_{9/2}$ state may be neglected since upconversion and other processes essentially bypass this state under current conditions.

The upconversion constants α_i and the state populations n_i are the only variables in these equations. The terms containing the upconversion coefficients are quadratic with respect to excited-state population, and represent the average rate of upconversion through all possible pathways to or from the states under consideration. All other parameters are measured directly from the spectroscopic data.

3.6 Determination of the Upconversion Coefficients

The method to be used to determine the upconversion coefficients α_1 and α_2 of the ${}^4I_{13/2}$ and ${}^4I_{11/2}$ states is a modified version of that put forth by Chou. [7] It involves the measurement and comparison of upconversion-induced luminescence to pump-induced luminescence in the excited system. Emission that occurs due to upconversion from the ${}^4I_{11/2}$ and ${}^4I_{13/2}$ excited states occurs only after the population from a higher, pumped state (${}^4F_{7/2}$, in this case) has had a chance to decay and redistribute itself in such a way that upconversion may occur. If a chopped cw source is used to excite the system into the ${}^4F_{7/2}$ state, then the emission from the excited states populated by upconversion processes (${}^4S_{3/2}$ and ${}^4I_{9/2}$ for upconversion from the ${}^4I_{11/2}$ and ${}^4I_{13/2}$ states, respectively) will occur on two time scales. The first will be on a time scale approximate to the lifetimes of the ${}^4S_{3/2}$ and ${}^4I_{9/2}$ states. Luminescence occurring within this regime results from direct-feeding from the pumped state. This will then be followed by a slower increase of luminescence from the ${}^4S_{3/2}$ and ${}^4I_{9/2}$ states which occurs on a time scale comparable to the lifetimes of the ${}^4I_{11/2}$ and ${}^4I_{13/2}$ states. Luminescence occurring within this second regime results from a population buildup within the states due to upconversion processes. The goal of the experiment is to measure and compare the buildup of the different luminescence regimes as a means to measure the rate and efficiency of the upconversion process.

Inherent to the model are two assumptions and simplifications which make the experiment and calculations more manageable. These assumptions are:

- 1) The Gaussian profile of the pump source is ignored. The pump profile is treated instead as rectangular. A Gaussian excitation density results in different excited-state densities within the medium, which in turn results in different rates of upconversion across the cross-section of the medium. The model, which does not incorporate spatial variations

of the pump source, results instead in an 'average' rate of upconversion over the excited region.

2) A constant pump rate is assumed through the length of the sample. This assumption is made to account for the different rates of upconversion which result from a non-constant excitation density along the pump path. [The absorption of excitation energy within the sample along the pump path varies as $e^{-\alpha z}$, where α is the coefficient of absorption and z is the distance in the sample.] This was accomplished physically by using optically thin crystals; and mathematically by making calculations of pump rate W only at the crystal surface. This approximation also results in an 'average' rate of upconversion over the excited region.

The experimental arrangement used to excite luminescence from the samples is shown in Figure 3-4. The chopped emission from an argon laser at 488.0 nm was spatially filtered and then focused to a 129- μm -radius spot on crystals of Er:GGG or Er:YSGG using a 30-cm lens. [The spatial filter removed the 'wings' of the Gaussian cross-section pump to give some validity to the rectangular cross-section approximation.] Luminescence was collected with 0.25-m scanning monochromator (which also filtered emission from states other than those being studied) and detected with a photomultiplier tube. The variation of signal intensity through time was digitized and stored via a digital oscilloscope interfaced with a personal computer.

Measurements were made in this manner for each sample as a function of pump power for emission from the $^4I_{9/2}$ and $^4S_{3/2}$ states. A polarizing beamcube and half-wave-plate pair attenuated the pump power for the different measurements. This combination resulted in attenuation without a variation in beam size for consistent measurements. The pump rate was determined from:

$$W = \frac{I(r)\alpha e^{-\alpha z}}{h\nu} = \frac{P\alpha e^{-\alpha z}}{(\pi r^2)(h\nu)} \quad [3.6.1],$$

where I is the pump intensity (assumed to be constant along its cross-section), α is the coefficient of absorption of the material at the pump wavelength, P is the power of the pump light incident on the crystal, z is the distance in the sample at which the pump rate is being measured (set identically equal to zero since it is assumed that all absorption occurs at the surface), r is the radius of the focused pump spot, h is Planck's Constant, and ν is the frequency of the pump light.

Samples of the data are shown in Figure 3-5, which represent emission from Er:YSGG from the $^4I_{9/2}$ (835 nm) and $^4S_{3/2}$ (558 nm) states, respectively, as functions of time. The signal strength has been normalized to unity for convenience. This data may be reduced to a quantity called the upconversion ratio, which is the ratio of the population due to upconversion (the change of magnitude of the signal in the slow-rise regime), designated U , to that due to direct-feeding (the change of magnitude of the signal in the fast-rise regime), designated V . The ratios U/V corresponding to emission from the $^4I_{9/2}$ and $^4S_{3/2}$ states will hereafter be called Y and Z , respectively. Data for Er:YSGG and Er:GGG are summarized numerically in Tables 3-1 to 3-3. The upconversion ratios Y and Z corresponding to the weakest pump rates were difficult to extract due to a poor signal-to-noise ratio. Errors are typically $\pm 50\%$ in this region, whereas they are $\pm 10\%$ in the strong pump-rate region.

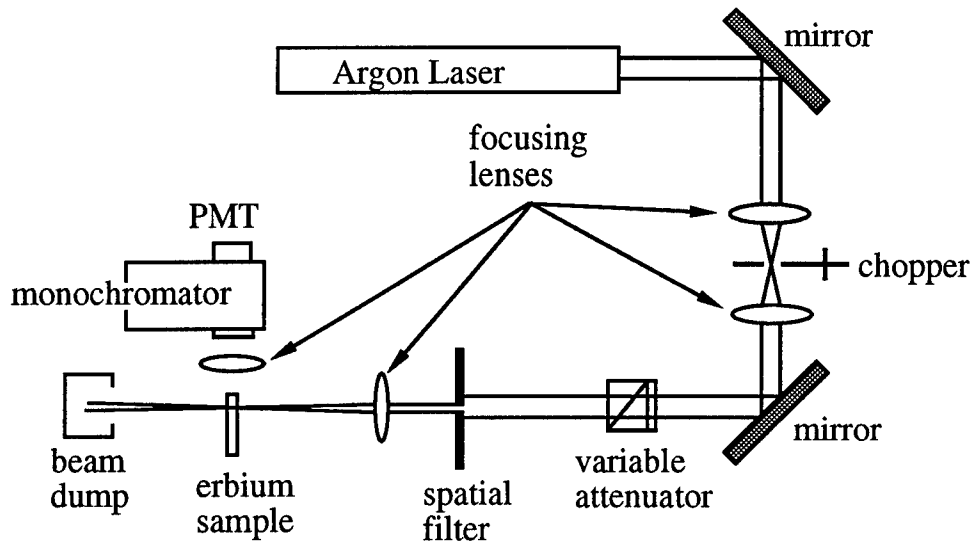


Figure 3-4: Experimental arrangement used to measure upconversion luminescence.

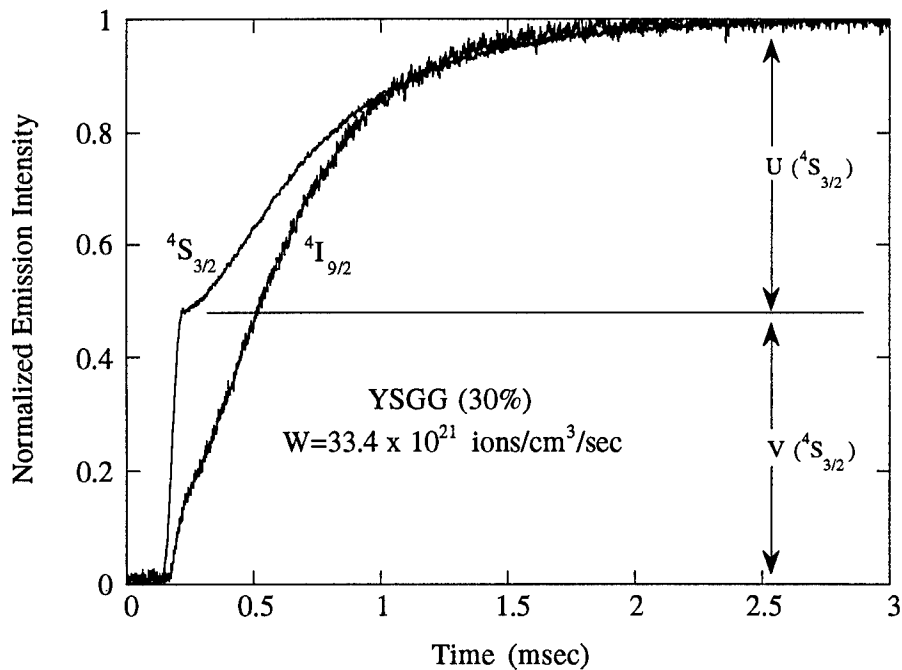


Figure 3-5: Typical luminescence waveform of erbium-doped solids. Data show emission from the indicated states. Direct- and upconversion-fed luminescence regimes (V and U) are shown only for the $4S_{3/2}$ state.

Er:YSGG (30%) [α @ 488.0 nm = 47.4 cm ⁻¹]			
Pump Power (mW)	Pump-Rate W (x 10 ²¹ ions/cm ³ /sec)	Y	Z
230	51.2	5.37	1.26
150	33.4	5.21	1.09
120	26.7	5.11	1.04
90	20.1	4.95	1.03
70	15.6	4.68	0.95
50	11.1	4.00	.86
30	6.7	3.17	.72
10	2.2	2.23	.43

Table 3-1: Upconversion data for Er:YSGG (30%).

Er:GGG (30%) [α @ 488.0 nm = 56.0 cm ⁻¹]			
Pump Power (mW)	Pump-Rate W (x 10 ²¹ ions/cm ³ /sec)	Y	Z
230	60.5	4.68	0.89
200	52.6	4.62	0.84
150	39.5	4.52	0.82
120	31.6	4.32	0.79
90	23.7	4.21	0.74
70	18.4	3.75	0.70
50	13.2	3.30	0.63
30	7.9	2.85	0.56
10	2.6	1.60	0.33

Table 3-2: Upconversion data for Er:GGG (30%).

Er:GGG (10%) [α @ 488.0 nm = 26.7 cm ⁻¹]			
Pump Power (mW)	Pump-Rate W (x 10 ²¹ ions/cm ³ /sec)	Y	Z
230	28.9	2.05	0.27
200	25.1	1.89	0.27
150	18.8	1.62	0.25
120	15.1	1.47	0.23
90	11.3	1.20	0.19
70	8.8	1.12	0.18
50	6.3	1.01	0.15
30	3.8	0.78	0.12
10	1.3	0.50	0.05

Table 3-3: Upconversion data for Er:GGG (10%).

To understand the physical significance of the upconversion ratios and how they may be applied to solve the rate equations for the upconversion coefficients, a method different from that used in [4] and [7] will be developed. Knowles and Chou solve the rate equations numerically by inserting the appropriate spectroscopic parameters into the equations, selecting arbitrary values (educated guesses) for the upconversion coefficients α_i , and after solving the differential equations, comparing the population growth predicted by the model with that seen in the experimental data. This method, however, is extremely

time-consuming when one considers the quantity of data to be analyzed and the possible sources of uncertainty that exist in the data and parameters used.

The rate equations may be simplified, however, by searching for solutions in the steady-state, as done in [4]. Equation [3.5.4] then reduces to

$$n_4 = \frac{W + \alpha_2 n_2^2}{A_4} \quad [3.6.2]$$

which reduces [3.5.3] to

$$n_3 = \frac{W + \alpha_2 n_2^2 + \alpha_1 n_1^2}{A_3} \quad [3.6.3].$$

Equation [3.6.3] may be substituted into [3.5.1] and [3.5.2] to reduce these equations to

$$A_1 n_1 + 2\beta_{32} \alpha_1 n_1^2 = W(3 - 2\beta_{32}) + \beta_{21} A_2 n_2 + (3 - 2\beta_{32}) \alpha_2 n_2^2 \quad [3.6.4]$$

and

$$\beta_{32} W + \beta_{32} \alpha_1 n_1^2 = A_2 n_2 + (2 - \beta_{32}) \alpha_2 n_2^2 \quad [3.6.5].$$

It is helpful at this point to consider a simplification which may be used to further reduce [3.6.4] and [3.6.5]. The populations of states n_3 and n_4 are the sums of the populations which result from direct- and upconversion-feeding. The first terms in [3.6.2] and [3.6.3] represent the populations from direct-feeding. The remaining terms must therefore be that which result from upconversion-feeding. The ratios of the populations of these two regimes are identically the upconversion ratios Y and Z:

$$Z = \frac{\frac{\alpha_2 n_2^2}{A_4}}{\frac{A_4}{W}} = \frac{\alpha_2 n_2^2}{W} \quad [3.6.6]$$

$$Y = \frac{\frac{\alpha_1 n_1^2 + \alpha_2 n_2^2}{A_3}}{\frac{A_3}{W}} = \frac{\alpha_1 n_1^2 + \alpha_2 n_2^2}{W} = \frac{\alpha_1 n_1^2}{W} + Z \quad [3.6.7]$$

Y and Z are quantities determined experimentally. These values may be inserted into the theoretical expressions [3.6.4] and [3.6.5], and, after some algebra, arrive at values for the upconversion coefficients α_1 and α_2 . The following are the major steps to solve for α_1 and α_2 :

1. Solve 3.6.5 for $\beta_{32}\alpha_1 n_1^2$, substitute this expression into [3.6.4], and solve for n_2 to obtain

$$n_2 = \frac{A_2(\beta_{21} - 2) \pm \sqrt{A_2^2(2 - \beta_{21})^2 + 4\alpha_2[3W - A_1 n_1]}}{2\alpha_2} \quad [3.6.8].$$

2. Substitute [3.6.6] and [3.6.7] into [3.6.5] to obtain an alternate expression for n_2 :

$$n_2 = \frac{\beta_{32} W(1 + Y) - 2WZ}{A_2} \quad [3.6.9].$$

3. Rewrite [3.6.6] in terms of α_2 , substitute n_2 from [3.6.9], and solve for α_2 :

$$\alpha_2 = \frac{WZ}{n_2^2} \quad [3.6.10].$$

4. Equate [3.6.8] with [3.6.9], solve for α_2 , and rewrite as:

$$\alpha_2 \pm \frac{A_2 \sqrt{A_2^2(2 - \beta_{21})^2 + 4\alpha_2(3W - A_1 n_1)}}{2\beta_{32}W(1 + Y) - 4WZ} = \frac{A_2^2(\beta_{21} - 2)}{2\beta_{32}W(1 + Y) - 4WZ}$$

or
$$\alpha_2 \pm \Gamma \sqrt{A_2^2(2 - \beta_{21})^2 + 4\alpha_2(3W - A_1 n_1)} = \Gamma A_2(\beta_{21} - 2) \quad [3.6.11]$$

where
$$\Gamma \equiv \frac{A_2}{2\beta_{32}W(1 + Y) - 4WZ}$$

5. Substitute [3.6.10] into [3.6.11] to solve for n_1 :

$$n_1 = \left[\left(\frac{\alpha_2}{\Gamma} \right)^2 - \frac{2A_2\beta_{21}\alpha_2 + 4A_2\alpha_2}{\Gamma} - 12W\alpha_2 \right] \cdot \left[\frac{-1}{4A_1\alpha_2} \right] \quad [3.6.12].$$

6. Substitute [3.6.12] into [3.6.7] to solve for α_1 :

$$\alpha_1 = \frac{W(Y - Z)}{n_1^2} \quad [3.6.13].$$

Equations [3.6.13] and [3.6.10] may now be used to calculate values for α_1 and α_2 , both which depend on spectroscopic parameters and experimental data. The rate equations may be solved using these values, the solutions to which may then be compared to the data.

This method is much quicker to use than the method by which values for α_1 and α_2 are arbitrarily selected and run through the rate equations. An example of the parameters used and the results obtained for Er:YSGG is shown below in Table 3-4:

Er:YSGG (30%)			
PARAMETERS		RESULTS	
α (cm ⁻¹ @ 488 nm)	47.4	n_1 (ions/cm ³)	4.63×10^{19}
P (mW @ 488 nm)	150	n_2 (ions/cm ³)	3.48×10^{19}
β_{32}	0.48	α_1 (cm ³ /sec)	6.42×10^{-17}
β_{21}	0.12	α_2 (cm ³ /sec)	3.01×10^{-17}
A_1 (sec ⁻¹)	294.1		
A_2 (sec ⁻¹)	769.2		
Y	5.21		
Z	1.09		
W (ions/cm ³ /sec)	33.4×10^{21}		
Γ (cm ³)	1.44×10^{-20}		

Table 3-4: Parameters used and results obtained for selected example of upconversion data.

The calculated values of α_1 and α_2 for each pump rate may now be analyzed to determine mean values ($\bar{\alpha}_1$ and $\bar{\alpha}_2$) and standard deviations (σ_1 and σ_2). [The three lowest pump rates resulted in values for Y and Z that possessed a large measure of uncertainty

due to a poor signal-to-noise ratio. These values, which could subsequently result in unrealistic results for α_1 and α_2 , were not used in the calculations.] The results are summarized below in Table 3-5. Results for Er:BYF (20%), Er:YLF (20%), and Er:YAG (30%) are also listed in this table. BYF and YLF were investigated in the experiment in order to make a comparison between the method derived in this work to that used by Chou and Knowles. The YAG results are shown for comparison.

	$\bar{\alpha}_1$	$\bar{\alpha}_2$	σ_1	σ_2
	(x10 ⁻¹⁷ cm ³ /sec)			
GGG (10%)	2.2	1.3	5.2	1.1
GGG (30%)	0.5	5.2	0.2	1.3
GGG (30%) [†]	2.5	2.0	n/a	n/a
YSGG (30%)	6.7	4.3	3.3	1.1
YAG (33%)	4.0	3.0	n/a	n/a
BYF (20%)	16.0	0.7	26.6	0.8
BYF (20%)*	3.5	0.8	n/a	n/a
BYF (20%)**	12.0	0.7	0.4	0.2
YLF (20%)	2.1	0.5	0.5	0.3
YLF (30%)***	3.0	1.8	n/a	n/a

Table 3-5: Values of upconversion coefficients and standard deviations calculated from the experiment. The GGG results indicated by the dagger (†) have been adjusted from the calculated results for a better fit to the data. The BYF results with a single asterisk (*) are those reported by [4]; those with a double asterisk (**) are results using the data of [4] with the calculations developed in this section. The YLF results with a triple asterisk are those reported by [7]. Results for YAG are from [8]. "n/a" indicates not available.

3.7 Discussion of Experimental Results

The results of the previous section indicate that values for upconversion coefficients may be determined directly from equations in 'closed-form' solutions. Two questions should be asked, however, at this point: 1) How accurately do the values of the calculated upconversion coefficients, if inserted back into the rate equations [3.5.1]-[3.5.4], reflect the luminescence data? In other words, do the calculations reflect reality? and 2) What are the possible sources of error for any differences in these values from the luminescence results and from other results found in the literature?

The first question may be answered by inserting the calculated coefficients back into the rate equations with the appropriate spectroscopic parameters to generate solutions for n_3 and n_4 . These solutions should match the luminescence data from the same states. This is a test that may be quickly run using differential-equation-solving software. The program *DiffEq* [9] was used to solve the equations [3.5.1]-[3.5.4] using a Euler technique with a step size equivalent to or less than the shortest lifetime of the states being analyzed, and was run until the populations reached steady-state. The equations were solved for pump rates corresponding to each measurement obtained in the experiment. The upconversion ratios U and V were then extracted from the fit and plotted against the pump rate. The results of this comparison are shown in Figures 3-8 through 3-10.

The comparison indicates that the calculated values $\bar{\alpha}_1$ and $\bar{\alpha}_2$ fit best to the experimental data for low to medium pump rates. A saturation of the experimental data for the 30%-doped samples appears in Y at high pump rates, however, which may be due to ground-state depletion. The rate-equations do not account for this effect, which is reflected in the fit. It would be expected that the upconversion ratios predicted by the model would continue to increase as the pump rate is increased. This difference could be resolved if the

rate equations were modified to account for the effect, and consideration of what the modifications should be will be given at a later time.

The calculated results of Y for Er:GGG (30%) do not match the data as closely as those of Er:YSGG (30%) at the low pump rates. Arbitrary values of $\bar{\alpha}_1$ and $\bar{\alpha}_2$ that were chosen in the vicinity of the calculated values were run through the rate equations to determine if a better fit could be established. An improved fit was obtained for the lower pump rates with a value of $\bar{\alpha}_1$ that was a factor of five times the calculated value, and an $\bar{\alpha}_2$ that was one-half the calculated value. The source of this discrepancy is not clear at this time. The adjusted values are shown in Table 3-5, and the adjusted fit is shown in Figure 3-9.

It is evident that error exists in the method due to the large standard deviations associated with the means. These errors may be attributed to the uncertainty that exists in the accuracy of the spectroscopic parameters used and in the accurate measurement of pump rates. An analysis of the equations used to solve for the upconversion coefficients shows a high sensitivity of the solutions to slight variations of either of the upconversion ratios Y and Z ; the pump rate W , which itself is derived from a measurement of the focused pump-spot size r ; and the branching ratio β_{32} , which is determined from the radiative lifetime of the ${}^4I_{9/2}$ state.

This sensitivity may be studied by fixing all parameters except the one of interest and observing the behavior of the solutions after running through the equations. This was done for each parameter mentioned above, for values greater than and less than those actually used, yet for values which were still within reasonable experimental error. The results are shown in Figures 3-10 to 3-13 for Er:YSGG (30%), in which the vertical lines represent the position of the data point actually used in the final solutions.

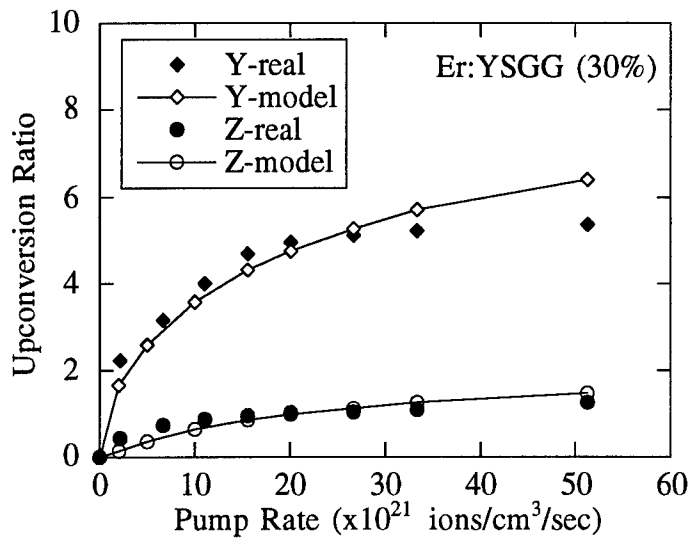


Figure 3-6: Comparison of upconversion ratios derived from data ('real') to values calculated from model for Er:YSGG (30%).

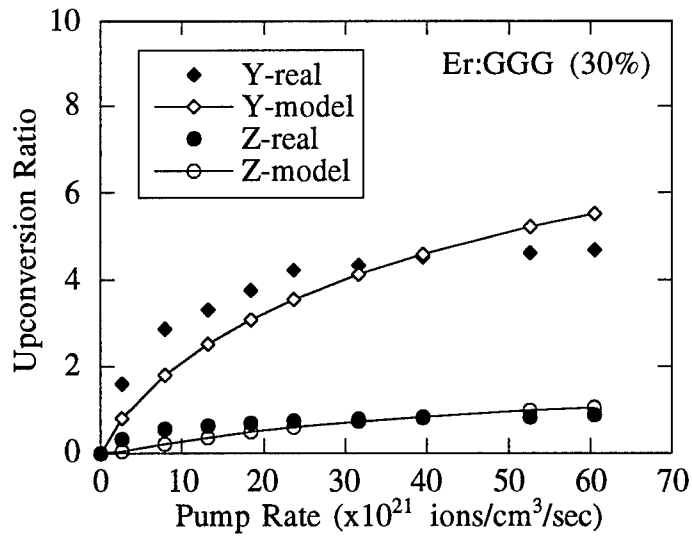


Figure 3-7: Comparison of upconversion ratios derived from data ('real') to values calculated from model for Er:GGG (30%).

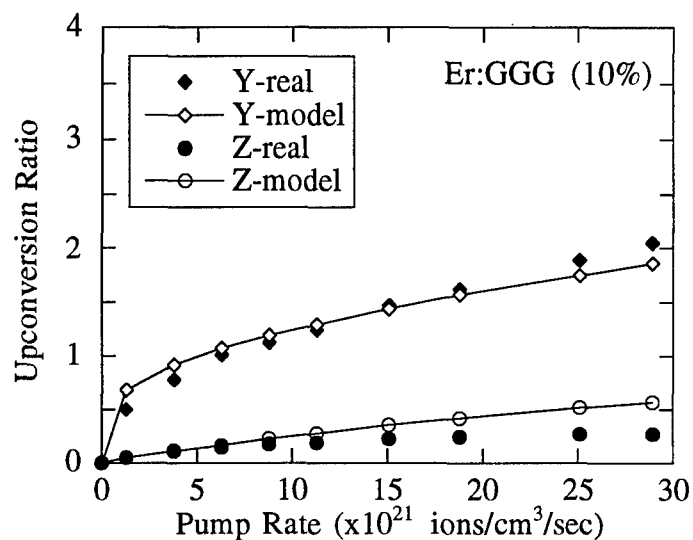


Figure 3-8: Comparison of upconversion ratios derived from data ('real') to values calculated from model for Er:GGG (10%).

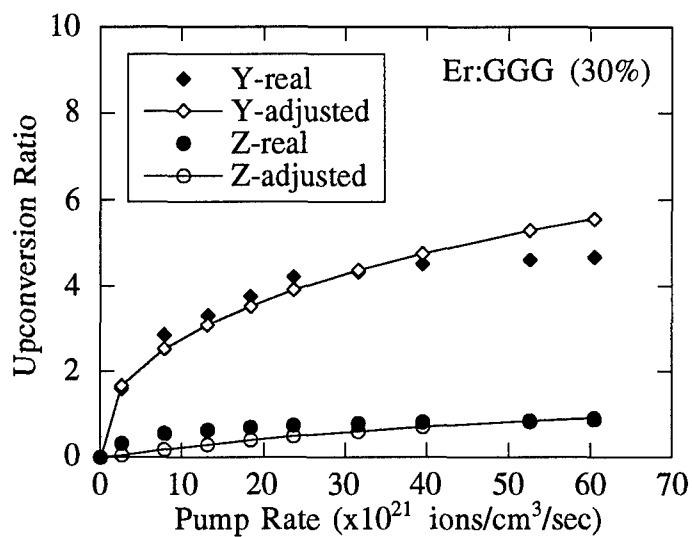


Figure 3-8: Comparison of upconversion ratios derived from data ('real') to those obtained from 'adjusted' $\bar{\alpha}_1$ and $\bar{\alpha}_2$ via the rate equations for Er:GGG (30%).

The upconversion ratios Y and Z appear to have the strongest influence on the calculated coefficients. The variation in Y shown in Figure 3-10 is $\pm 6\%$. This range of error, however, is much larger than that actually measured. Typical uncertainties observed are $\pm 3\%$, except at very low pump rates, in which range the signal-to-noise ratio is smaller due to the reduced sensitivity of the detector at these signal levels and in this spectral region (835 nm). The uncertainty in these cases is more typically $\pm 10\%$. The calculated value of α_1 in the range $Y \pm 3\%$ may double, yet $\bar{\alpha}_2$ remains relatively unchanged. The converse is true for variations of Z .

The radiative lifetime of the ${}^4I_{9/2}$ state, which manifests itself through the branching ratio β_{32} , has a similar influence to Y and Z on the solutions to the equations (Fig. 3-12). Variations associated with this measurement occur mainly due to quenching effects which result in a radiative lifetime that is highly nonlinear with respect to excitation density. Care must be taken when analyzing highly-doped samples ($>5\%$ dopant concentration) that large excitation densities do not reduce the lifetime so much as to give a deceptive measurement of the true radiative lifetime for that concentration. The solution is to keep the pump source defocused on the sample (low pump rate) to minimize cross-relaxation and upconversion processes, yet intense enough to maintain a measurable signal.

Variations of the radius r of the focused pump beam, which manifest themselves as changes in the pump rate W , result in linear variations of $\bar{\alpha}_1$ and $\bar{\alpha}_2$. Variations of $\pm 5\%$ in the accuracy of the spot radius result in shifts of $\pm 25\%$ for $\bar{\alpha}_1$ and $\bar{\alpha}_2$, according to the test performed in Figure 3-13. These large potential variations, in addition to the uncertainties inherent in the other measurements, indicate the need for highly accurate measurements of each parameter, and is probably one of the greatest drawbacks of this method.

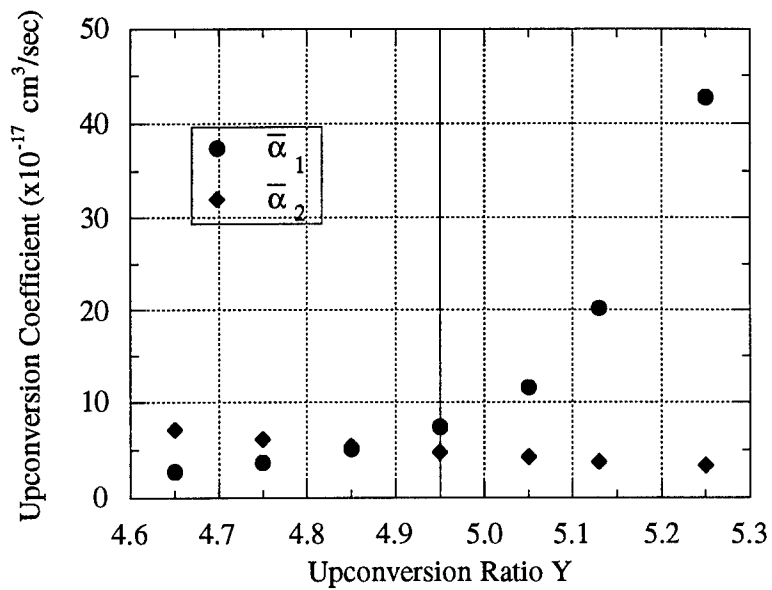


Figure 3-10: Dependence of upconversion coefficients on upconversion ratio Y.

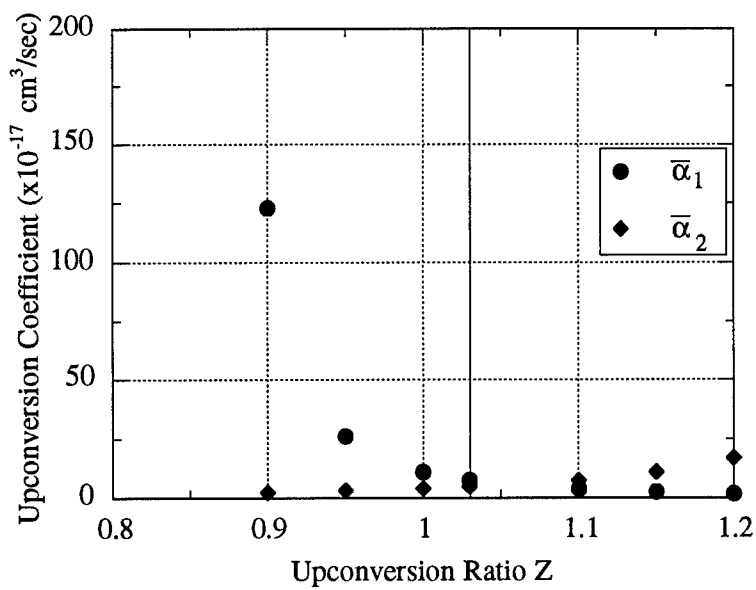


Figure 3-11: Dependence of upconversion coefficients on upconversion ratio Z.

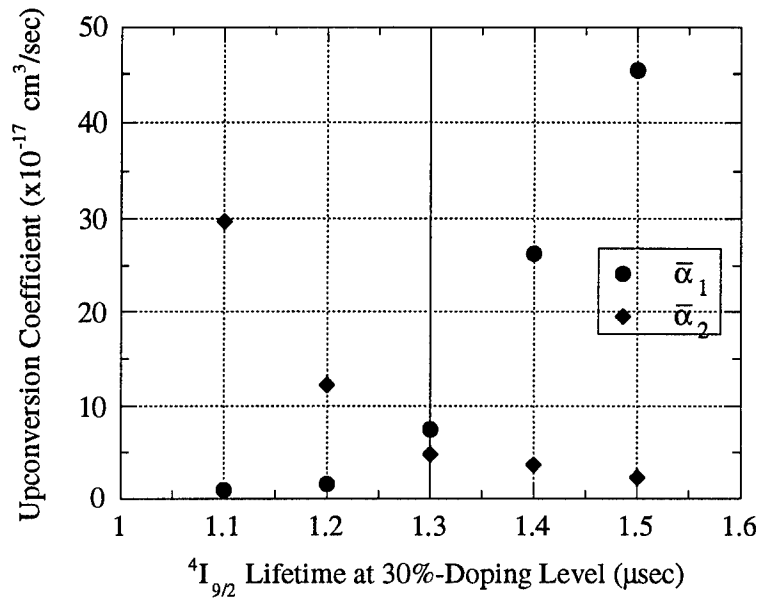


Figure 3-12: Dependence of upconversion coefficients on ${}^4I_{9/2}$ radiative lifetime τ_3 .

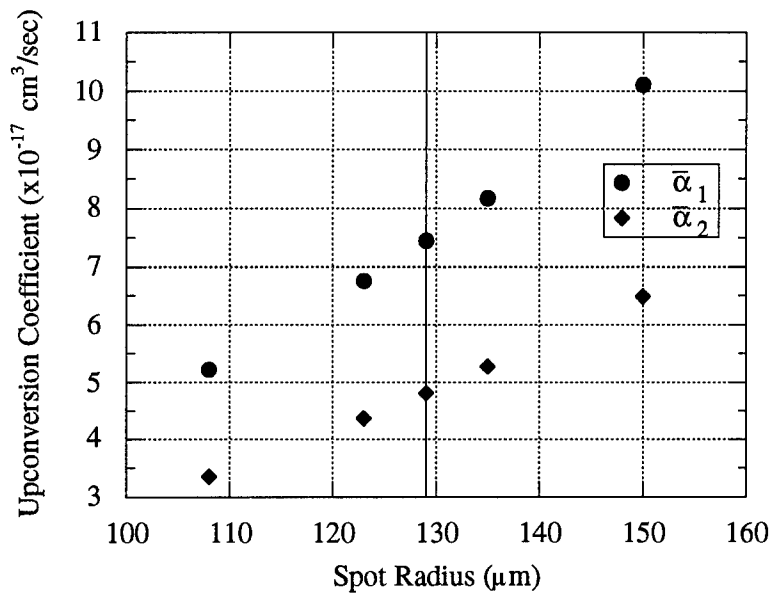


Figure 3-13: Dependence of upconversion coefficients on spot radius r .

References for Chapter 3

- [1] T. Förster. "Zwischenmolekulare Energiewanderung und Fluoreszenz". *Annalen der Physik.* **2**, 55 (1948).
- [2] D.L. Dexter. "A Theory of Sensitized Luminescence in Solids". *Journal of Chemical Physics.* **21**, 836 (1953).
- [3] P. Lacovara. Energy Transfer and Upconversion in Yb:YAG and Yb,Er:YAG. Doctoral Thesis. Boston College, Newton, Massachusetts. 1992.
- [4] D.S. Knowles. Energy Transfer Under Strong Pumping in High Concentration Rare Earth Doped Laser Crystals. Doctoral Thesis. Massachusetts Institute of Technology, Cambridge, Massachusetts. 1991.
- [5] G. Armagan, B. Di Bartolo, and A.M. Buoncristiani. "Kinetics and Microscopic Interaction Parameters of Cr to Tm Energy Transfer in Yttrium Aluminum Garnet Crystals". *Journal of Luminescence.* **44**, 141 (1989).
- [6] R. MacFarlane. "Spectroscopic Studies and Upconversion Laser Operation of BaY₂F₈:Er 5%". Proceedings of the OSA Advanced Solid State Lasers Conference, Santa Fe, New Mexico. February, 1992.
- [7] H. Chou. Upconversion Processes and Cr-Sensitization of Er- and Er,Ho-Activated Solid State Laser Materials. Doctoral Thesis. Massachusetts Institute of Technology, Cambridge, Massachusetts. 1989.
- [8] W.Q. Shi, M. Bass, and M. Birnbaum. "Effects of Energy Transfer Among Er³⁺ Ions on the Fluorescence Decay and Lasing Properties of Heavily Doped Er:Y₃Al₅O₁₂." *Journal of the Optical Society of America.* **7**, 8. 1990.
- [9] *DiffEq: Numerical Solution of Differential Equations.* Distributed by MicroMath Scientific Software, Salt Lake City, UT. 1991.

Chapter 4: Laser Operation of Er:GGG and Er:YSGG

4.1 Introduction to Chapter 4

This chapter presents the results of measurements of the laser properties of 30%-Er-doped GGG and YSGG. These hosts were originally chosen in anticipation that laser operation would be more efficient and practical than that using other hosts such as YAG or BYF. The aluminum-garnet hosts have short upper-state lifetimes and high laser thresholds due to efficient multi-phonon relaxation of the upper-state. Fluorides, on the other hand, have reduced multi-phonon decay rates and typically operate efficiently as laser hosts, but are inherently softer and easier to damage.

The spectroscopic measurements of Chapter 2 indicate the potential of these gallium-garnet materials as laser sources. The absorption peaks are strong and fall within spectral regions for which pump sources are currently available, though the radiative lifetime of the upper-state does not favor cw oscillation.

Two upconversion processes working concurrently in erbium redistribute the population of the upper and lower states. The measurements of the rates of these processes in Chapter 3 indicate that for these concentrations, upconversion from the lower state is greater than that from the upper state. This results in a partial depopulation of the lower state and repopulation of the upper state, which assists to maintain cw laser oscillation.

The following sections report the results of experiments on the operation of these materials as gain media for 3- μm cw lasers. The physical characteristics of the resonators are described as are measurements of the properties of the laser emission.

4.2 Three-, Four-, and Quasi-Three-Level Lasers

Laser media operate in three-, four-, or quasi-three-level manners, depending on the details of energy transfer within the gain medium. In a three-level laser (Figure 4-1a), the medium is excited to an energetic state from which there is a rapid decay to a metastable state. This metastable state has a relatively long lifetime and a population inversion may be established. The active ions will then decay from this state via stimulated emission to the ground state. Thus in a three-level laser, it is necessary for at least 50% of the ions to be excited into the upper-state in order to create the inversion necessary for oscillation to occur.

In a four-level laser (Figure 4-1b), the state on which the laser transition terminates is not the ground state, but rather a state from which a rapid depopulation occurs. Inversion threshold is easier to reach since the lower state remains essentially unpopulated. Four-level lasers are more favorable than three-level lasers since the pump rates required to reach and maintain oscillation are generally less than that of a three-level laser.

Occasionally, a laser ion will possess an energy level structure that possesses characteristics of both three- and four-level systems. The 2- μm laser transition of holmium (Ho^{3+}) terminates on one of the higher Stark levels of the $^5\text{I}_8$ ground state manifold. The rapid thermalization which immediately follows within the manifold allows consideration of this transition as quasi-three level, even though this is a ground state transition. [1]

The 3- μm laser transition in erbium terminates on an excited state, characteristic of a four-level laser. This terminal state, however, typically has a radiative lifetime longer than that of the upper state when doped into crystalline hosts. A population bottleneck rapidly forms which prevents the system from maintaining the required inversion levels necessary for oscillation. CW oscillation is possible, however, due to a rapid thermalization within

the lower manifold (the transition terminates on one of the upper Stark components of the lower state) and also due to upconversion from the lower state, quenching its lifetime and effectively repopulating the upper-state.

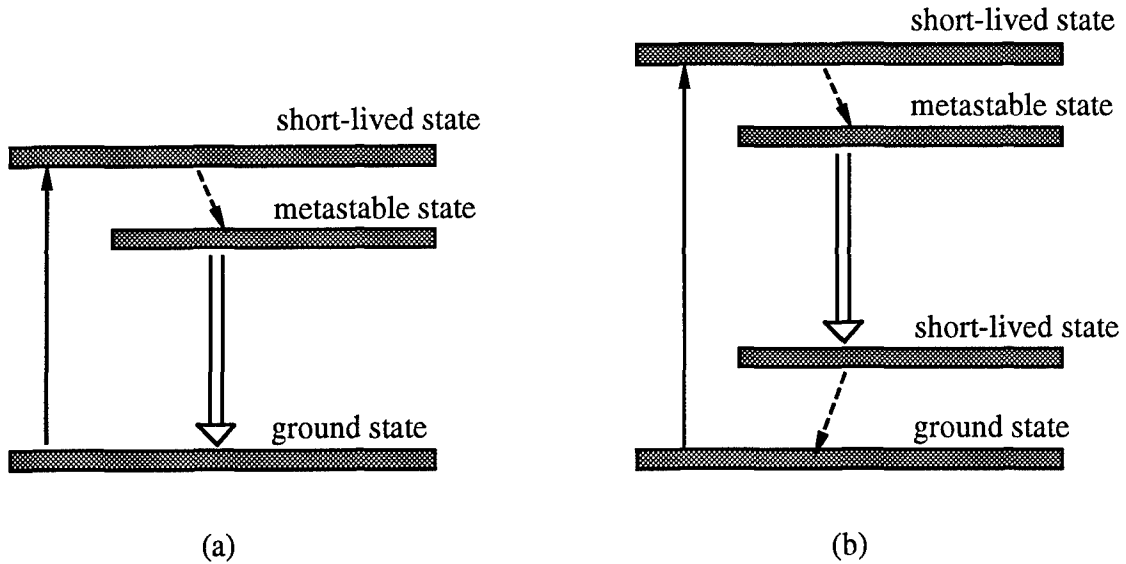


Figure 4-1: Partial energy-level diagram of typical three-level (a) and four-level (b) lasers.

4.3 The Laser Oscillator

The first true-cw 2.8- μm erbium laser was demonstrated in diode-pumped Er:YLF via excitation into the $^4\text{I}_{9/2}$ state near 0.79 μm . [2] The slope efficiency of this laser (defined as the rate of change of output power as a function of input power), however, was low ($\sim 10\%$) due to an unfavorable combination of upconversion and excited-state absorption losses from the $^4\text{I}_{9/2}$ state and due to losses in the form of thermal relaxation from the $^4\text{I}_{9/2} \rightarrow ^4\text{I}_{11/2}$ transition.

In this work, using a Ti:sapphire or InGaAs laser emitting near 0.97 μm , the erbium ions were pumped directly into the upper-state ($^4\text{I}_{11/2}$). Direct upper-state pumping of the erbium 3- μm transition was first demonstrated in Er:GSGG by Stoneman [3], and shows higher efficiencies relative to pumping into other states for which pump sources are also available. The $^4\text{S}_{3/2}$ state, for example, may be pumped with an argon laser operating at 512 nm; or more common, the $^4\text{I}_{9/2}$ state is pumped with an AlGaAs diode-laser at wavelengths near 0.79 μm . Higher efficiencies result from direct upper-state pumping, however, due to a combination of higher quantum-defect³, reduced upconversion losses relative to $^4\text{I}_{9/2}$ excitation, and a reduced thermal load resulting from $^4\text{I}_{9/2} \rightarrow ^4\text{I}_{11/2}$ and other thermal relaxation pathways. The quantum-defect of direct upper-state pumping is approximately 0.36, nearly 25% larger than the 0.28 characteristic to $^4\text{I}_{9/2}$ excitation.

Samples of Er:GGG and Er:YSGG were fabricated into laser crystals that were 3-mm in length and 3-mm in diameter. A monolithic laser resonator, shown schematically in Figure 4-2, was chosen over the more conventional open resonator configuration for two reasons: 1) The strong absorption of 3- μm radiation by atmospheric water vapor present in the resonator may increase resonator losses and therefore raise the laser threshold if the

³ The quantum defect of a laser is defined as the ratio of the pump (input) wavelength to that of the laser (output) wavelength. It is a measure of the maximum possible efficiency of a laser system in the absence of energy transfer.

laser transition falls on one of the water absorption bands. This could result in oscillation on a lower-gain transition whose threshold is now lower than that of the high-gain transition, or no oscillation at all. 2) The manufacture of high-quality, durable antireflection (AR) coatings at 3 μm has proven to be a difficult task. AR coatings are frequently applied to laser crystals to reduce Fresnel losses at the crystal surfaces. The use of a monolithic resonator will bypass the requirement for AR coatings on the laser crystal, and therefore reduce the laser threshold.

The flat, pump surface of the laser monolith was dichroically coated to be highly transmitting (HT) at 0.97 μm and highly reflecting (HR) at 3 μm . The output surface was polished with a convex 1-cm radius-of-curvature and coated for 99.7% reflection at the laser wavelength. This low output coupling was chosen to inhibit high laser thresholds, which could result due to the low-gain nature of the medium. The erbium-doping concentrations were 30% for both materials. The high erbium doping was chosen to ensure that upconversion processes effectively depleted the lower-state to prevent self-termination of laser oscillation.

The equations for an ideal plano-convex resonator define the TEM_{00} -mode diameters at the mirrors as:

$$2w_f = \left[\frac{16L\lambda}{\pi n} \sqrt{\frac{g}{1-g}} \right]^{\frac{1}{4}} \quad [4.3.1]$$

$$2w_c = \left[\frac{16L\lambda}{\pi n} \sqrt{\frac{1}{g(1-g)}} \right]^{\frac{1}{4}} \quad [4.3.2],$$

where $2w_f$ and $2w_c$ represent the diameters at the flat and curved mirrors, respectively; L is the length of the resonator; λ is the laser wavelength; n is the index of refraction of the gain medium at the laser wavelength; and g represents the stability parameter defined as

$$g = 1 - \frac{L}{R} \quad [4.2.3],$$

where R is the radius of the curved mirror.

A computer program was used to calculate mode sizes rather than running the calculations by hand. The program used a matrix formulation of ray optics, which accounts for effects for beam shaping and propagation at various points and on different surfaces within the resonator for which the standard equations above do not account. The resonator mode (the region in which laser oscillation occurs) inside the crystal was calculated to vary from a 98- μm diameter at the input face to 116- μm at the output face (Figure 4-2) for $L=0.003$ m, $\lambda=2.8$ μm , and $n=1.8$. The pump beam typically should overlap this region for the most efficient conversion of the pump energy into laser energy. If the pump diameter is too large, then its energy may be deposited in regions which excite higher-order spatial modes. If the pump is focused too tightly, on the other hand, then the high excitation densities may result in low efficiencies due to greater upconversion losses.

For the case of Ti:sapphire pumping, an AR-coated plano-convex glass lens of 10-cm focal length was used to focus the pump light in the crystal. The beam diameter at the focus was measured to be 80 μm at $1/e^2$ of the maximum intensity. For diode-laser-pumping, two four-element spherical lenses of 15-mm focal length (Special Optics 54-18-15) were used to first bring the laser emission to near-collimation and then to focus the beam by placing the lenses back-to-back. These lenses were AR-coated from 800 nm to 1000 nm. The emitting region of the InGaAs semiconductor diode laser was 100 μm wide. It is estimated that the focused emission of the InGaAs laser was ~ 100 μm diameter.

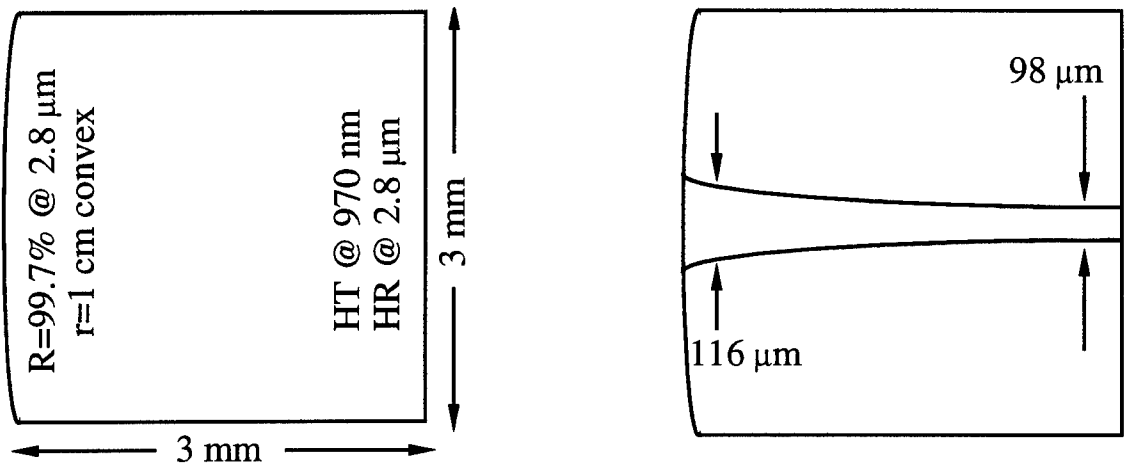


Figure 4-2: Dimensions and coatings of erbium laser monolith, and calculated TEM₀₀ resonator mode.

4.4 CW Laser Measurements

A. Excitation Data

A Ti:sapphire laser was tuned through the ${}^4I_{11/2}$ absorption band of erbium in order to determine the dependence of output power on pump wavelength (and ultimately efficiency). The relative erbium laser output, detected and recorded through a lock-in amplifier and normalized to the power of the pump source, was then displayed as a function of the pump wavelength. The experimental arrangement is shown schematically in Figure 4-3.

The results, shown in Figure 4-4, show that for pump powers near the laser threshold of that pump wavelength corresponding to the strongest laser emission, lasing occurs only for those pump wavelengths directly overlapping the ions' strongest absorption bands. Lasing occurs well into the wings of the absorption bands, where the absorption coefficients are very small relative to those of the peaks (Figures 4-4 and 4-5), when high pump powers are used. The fact that the laser emission remains strong at high pump densities at the peak of the absorption bands indicates that excited-state absorption (ESA) from the upper laser state is either wavelength-independent or not a source of depopulation at the pump-densities used in the experiment. (The probability for ESA increases quadratically with respect to excited-state population.)

In summary, the results of the laser excitation spectra indicate that the laser efficiency is fairly insensitive to the pump wavelength in the vicinity of the peak of the absorption bands. None-the-less, some pump wavelengths do result in a stronger emission than others. Specifically, an excitation wavelength of approximately 965 nm shows the highest output, and for this reason, was chosen to be the standard pump wavelength used.

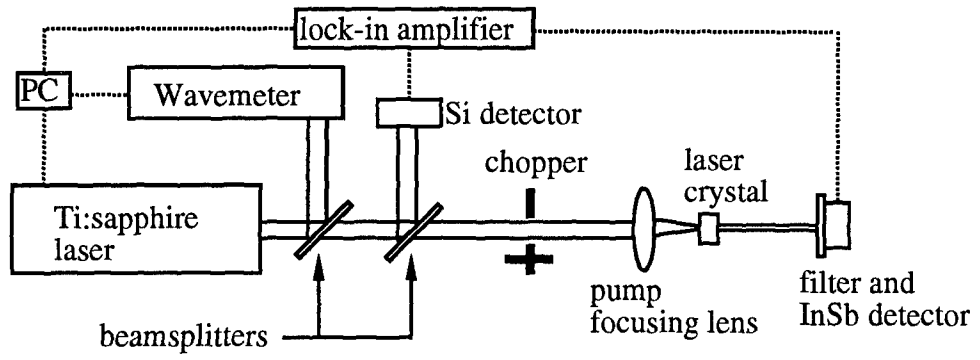


Figure 4-3: Experimental arrangement used for excitation measurements.

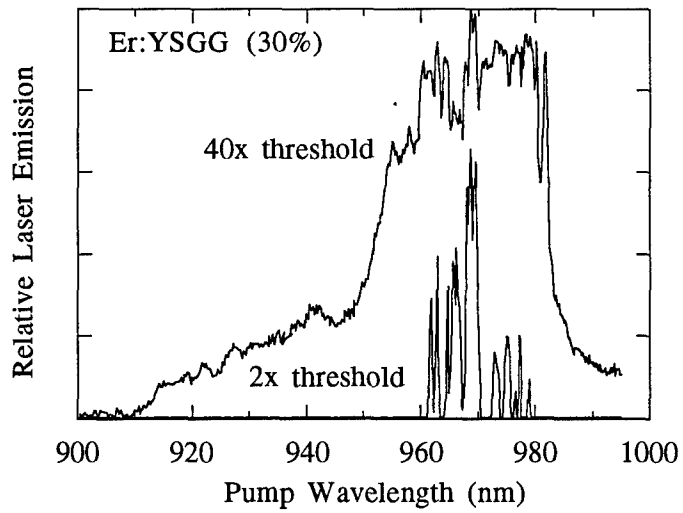
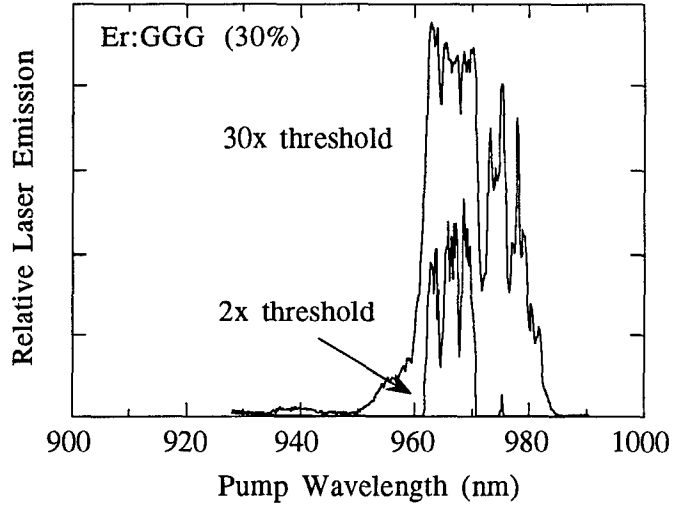


Figure 4-4: Laser excitation spectra for Er:GGG and Er:YSGG. The intensity units for each of the four spectra are arbitrary. The “x threshold” values are indicated for the pump wavelength corresponding to the highest intensity laser emission for that particular scan.

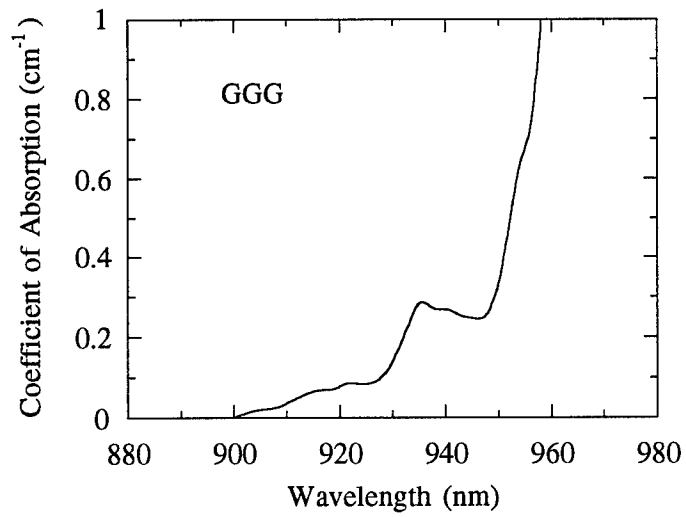
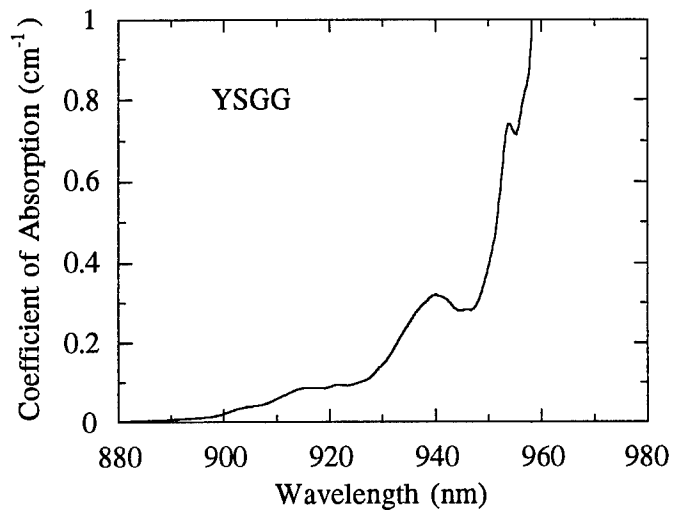


Figure 4-5: Absorption spectra of Er:YSGG (30%) and Er:GGG (30%).

B. Power, Temperature, Spectral, and Spatial Data

The lasers were aligned relative to the pump system to maximize the output power once the optimal excitation wavelength was determined. Proper alignment was established by mounting the laser crystal and the copper heatsink on which the crystal was permanently bonded, and all focusing optics, on three-dimensional translators.

Power data were obtained for both materials under Ti:sapphire- and diode-laser-pumped conditions. In addition, power measurements were made as functions of temperature by mounting the samples in a liquid-nitrogen-cooled, evacuated Dewar. Data are presented graphically in Figure 4-6. Slope efficiencies and laser thresholds were obtained from these data. These results are summarized numerically in Table 4-1.

The lasers, given the same ambient temperature and pump source, exhibit different slope efficiencies, even though GGG and YSGG share fairly similar physical properties. It is possible that these differences are fundamental to the materials, arising from factors such as different upper- and lower-state radiative lifetimes. It is also possible, however, that these differences are due to scattering centers within the material which may have formed either during boule growth or during crystal fabrication; or to minor variations of the output transmissions due to the optical coatings on the crystals. A series of output transmissions should be studied to properly characterize and optimize the laser efficiencies.

The slope efficiencies and pump thresholds also differ significantly when comparing the different pump sources used. The diode-laser-pumped lasers categorically exhibit higher thresholds and lower efficiencies than their Ti:sapphire-pumped counterparts. This difference arises from the spectral and spatial structure of the two sources. The diode lasers used in these experiments had spectral linewidths of 2.5 nm, which is generally greater than or equal to the width of the absorption lines of erbium; compared to ~0.1 nm for the Ti:sapphire laser, which is less than the width of the absorption lines. The spectrally narrower lines of the Ti:sapphire laser are absorbed through a shorter path length

of gain medium, resulting in higher excitation densities. In addition, the Ti:sapphire laser operates in the TEM₀₀ mode (Gaussian cross-section), in contrast to the multiple-transverse-mode diode laser. The TEM₀₀ pump mode is more efficiently coupled into the TEM₀₀ resonator mode of the laser crystal, conducive to a higher overall slope efficiency.

Laser spectra were obtained using an Acton Research 0.25-m Scanning Monochromator. Each material lased on one line at 300 K. The transitions shifted to longer wavelengths due to the different thermal populations within the Stark levels, however, when the materials were cooled to 77 K. Er:YSGG lased simultaneously on two lines at the low temperature. The temperature-wavelength results are shown in Table 4-2.

Material (Temp)	Pump Source	Laser Threshold (mW)	Slope Efficiency (%)
Er:GGG (300 K)	Ti:sapphire	7	27
Er:GGG (300 K)	InGaAs	250	19
Er:GGG (77 K)	Ti:sapphire	7	28
Er:YSGG (300 K)	Ti:sapphire	5	31
Er:YSGG (300 K)	InGaAs	175	26
Er:YSGG (77 K)	Ti:sapphire	5	35

Table 4-1: Laser thresholds and slope efficiencies for different erbium lasers as functions of crystal temperature and pump source.

Material	77 K	300 K
Er:GGG	2867.4 nm 2873.5 nm	2821.7 nm
Er:YSGG	2869.5 nm	2797.1 nm

Table 4-2: Erbium-laser wavelengths as functions of host and temperature.

The laser spectra were also analyzed and compared for each medium at 300 K. Resonators may support a number of standing waves, dependent upon the resonator's length. Laser resonators will therefore oscillate on a number of axial, or longitudinal modes. Only those modes which lie within the gain bandwidth of the active medium will oscillate. The mode separation is given by

$$\Delta\lambda = \frac{\lambda^2}{2nL},$$

where λ is the mean wavelength of the laser transition, n is the refractive index of the gain medium at the laser wavelength, and L is the length of the laser resonator. The mode separation is calculated to be $\Delta\lambda=0.69$ nm for GGG and $\Delta\lambda=0.68$ nm for YSGG.

Each laser oscillated on approximately four or five longitudinal modes for excitation well above threshold, as shown in Figure 4-8. The vertical lines along the x-axis of the graphs represent the calculated separation of the mode peaks based on use of the strongest line for each spectrum as the central wavelength. The measured wavelengths possess a degree of uncertainty due to the low resolution (0.4 nm) of the monochromator in this spectral region. The lines shown therefore represent the resolution limit of the instrument rather than the true transition linewidths.

Tunable, single-frequency operation of these materials is also possible. This has been demonstrated using YAG as the host medium. [4] The crystal used was doped with 50% erbium. The coatings on the crystal were optimized for performance at 2.94 μm , and the output coupler was polished with a convex 4-cm radius. The crystal length was 1.0 mm, and its diameter was 1.5 mm. These dimensions were chosen with the expectation that the axial modes would be spaced far enough apart that only one mode would fall within

the laser gain-bandwidth. It is expected that GGG and YSGG would operate in a similar manner, since the laser gain-bandwidths of each ion-host combination vary little.

The tuning-rate of the single-frequency YAG laser was determined by measuring the wavelength with an interferometric wavemeter (Burleigh Wavemeter Sr.) as a function of pump power and crystal temperature. The results indicate a wavelength tuning rate of +0.042 nm/°C in the temperature interval 15°C to 27°C for 300 mW of pump power.

The spatial structure of the laser emission was analyzed for both the Ti:sapphire-pumped and diode-pumped lasers (the 3-mm length lasers), using a linear-array detector (Spiricon LaserProbe). The beam diameter (@1/e²) was measured with the array at a series of distances along the axis of the emission. These measured values were then converted to divergence values, from which values of M² were also obtained. [The M² value is a measure of beam quality, or more specifically, it is a representation of the number of times the emission diverges from its diffraction-limited value. The intensity profile of a true diffraction-limited beam is Gaussian through its diameter. M²=1 represents the diffraction-limited case, and obviously, M² is always greater than unity.]

The 1/e² beam diameter for the Ti:sapphire-pumped crystals, at 76.2 mm from the crystal aperture, was 2.75 mm. This expanded to 7.75 mm at a distance of 228.6 mm from the aperture, which corresponds to a full-angle beam divergence of 32.7 mrad. This converts to M²=1.03, which for all practical considerations, is diffraction-limited.

The emission from the one-diode-pumped lasers was analyzed in two planes which correspond to the planes parallel and perpendicular to the diode laser emitter. The measured 1/e² beam diameters were 4.75 mm x 9.5 mm at a distance of 110 mm from the crystal, and 9.4 mm x 19.0 mm at a distance of 240 mm from the aperture. This corresponds to divergences of 42.1 mrad x 84.2 mrad, or M² = 1.3 x 2.6, respectively. The elliptical beam profile is a result of the asymmetric diode-laser emission, which was focused into the laser crystal such that only one plane (corresponding to the near-diffrac-

tion-limited plane) was fully coupled into the TEM_{00} resonator mode. The other dimension probably overfilled this mode, resulting in multi-mode operation in that plane. Profiles were not measured for the two-diode-pumped system.

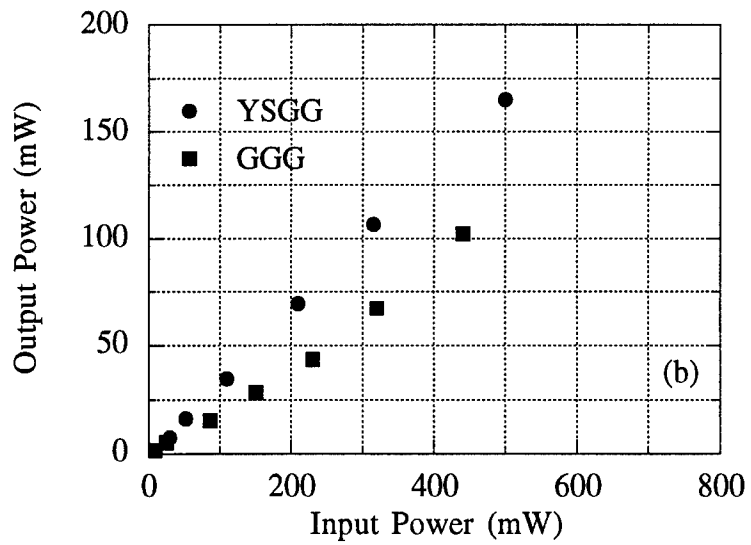
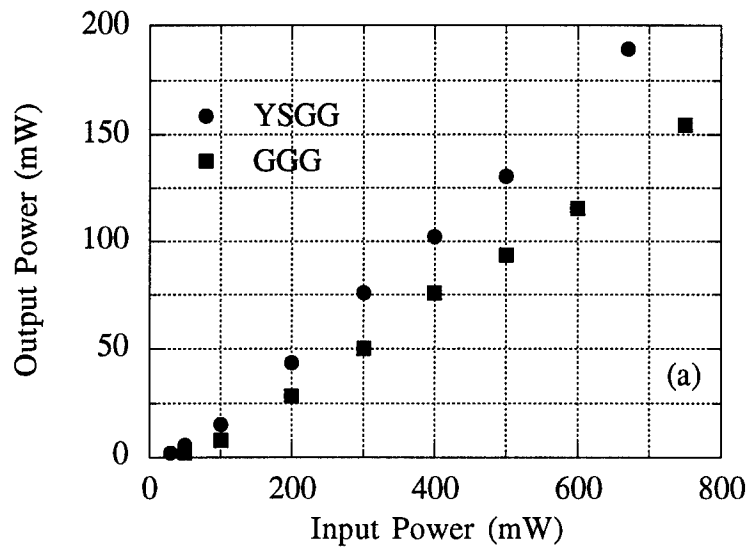


Figure 4-6: Ti:sapphire-pumped erbium-laser power data for (a) 300 K and (b) 77 K.

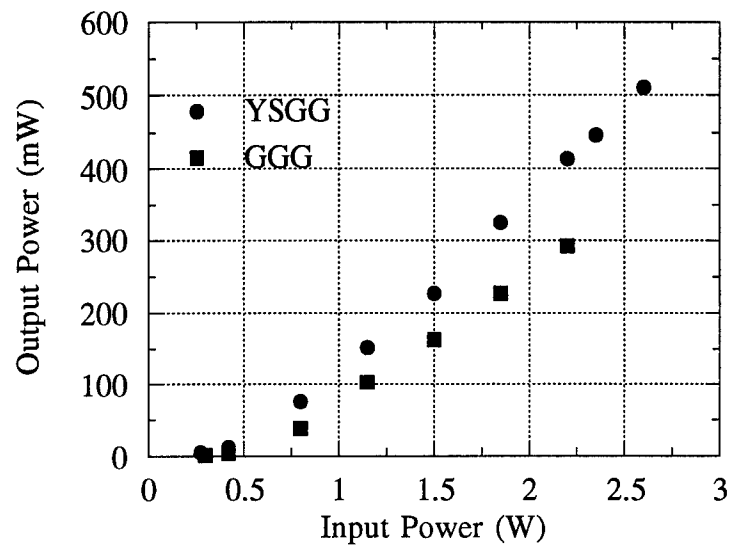


Figure 4-7: Diode-pumped erbium-laser power data for 300 K.

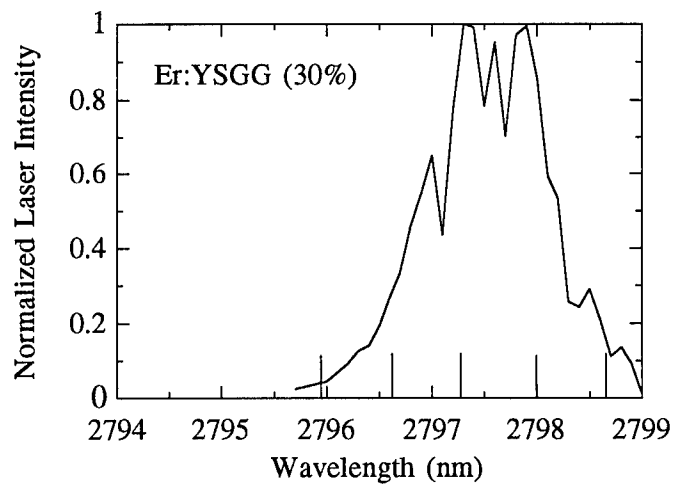
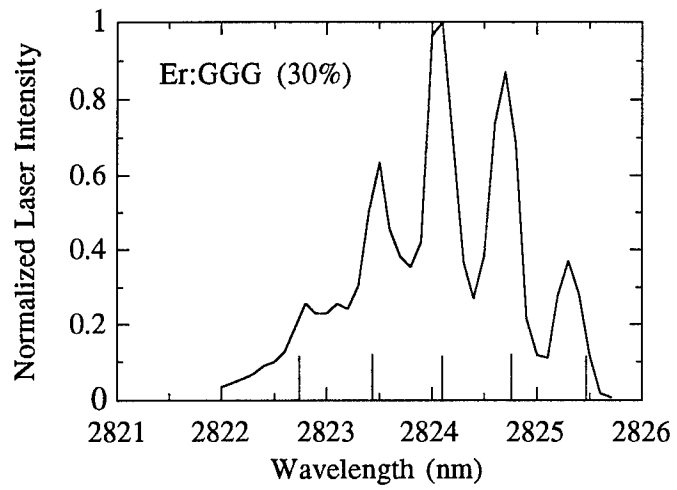


Figure 4-8: Laser spectra of Ti:sapphire-pumped Er:GGG and Er:YSGG.

References for Chapter 4

- [1] B. Dinerman. Loss Mechanisms in a Cr, Tm, Ho:YAG Laser Crystal Under High Power Diode Pumping. Master's Thesis. Boston College, Newton, MA. 1991.
- [2] G.J. Kintz, R. Allen, and L. Esterowitz. "CW and Pulsed 2.8 μm Laser Emission From Diode-Pumped $\text{Er}^{3+}:\text{LiYF}_4$ at Room Temperature". *Applied Physics Letters*. **50**, 22. (1987).
- [3] R.C. Stoneman and L. Esterowitz. "Efficient Resonantly Pumped 2.8- μm $\text{Er}^{3+}:\text{GSGG}$ Laser". *Optics Letters*. **17**, 11. (1992).
- [4] B.J. Dinerman and P.F. Moulton. "3- μm CW Laser Operation in Erbium-Doped YSGG, GGG, and YAG". Submitted to *Optics Letters*, October, 1993.

Chapter 5: Summary and Conclusions

5.1 Introduction to Chapter 5

This chapter will attempt to summarize and put into perspective the results of the spectroscopic and laser investigations of the past three chapters. Potential directions for future work will be suggested, and the results of a preliminary investigation toward more advanced laser designs will be presented.

5.2 Summary of the Results

Spectroscopic and laser investigations were conducted on Er:GGG and Er:YSGG in three parts (chapters): 1) basic spectroscopy, 2) upconversion measurements, and 3) 2.8 μm laser properties. The spectroscopic properties, which include absorption, emission, and radiative lifetime obtained with standard experimental techniques, were presented in Chapter 2. Transitions involving the absorption of visible or infrared radiation characteristically show strong and narrow lines. The number of electronic states is conducive to many possible laser transitions within the configuration, as has been demonstrated in BYF and YLF. The ${}^4\text{I}_{15/2} \rightarrow {}^4\text{I}_{11/2}$ absorption transition is of particular significance to this study since it allows direct pumping of the 2.8 μm upper-state.

The emission spectra reveal Stark transitions which are not visible in the absorption spectra. Emission spectra typically result from low-energy transitions between two manifolds (lowest Stark levels of the upper state), whereas the absorption spectra result from higher-energy transitions (lowest Stark levels of the lower state). The spectral lines of the emission spectra were compared to those of the absorption spectra, and from this, the details of the Stark splittings were identified, as shown in Table 2-4.

Radiative lifetimes were measured for transitions from the ${}^4\text{S}_{3/2}$, ${}^4\text{I}_{9/2}$, ${}^4\text{I}_{11/2}$, and ${}^4\text{I}_{13/2}$ states. These measurements were used to deduce feeding efficiencies of the ${}^4\text{I}_{9/2} \rightarrow {}^4\text{I}_{11/2}$ transition and cross-relaxation efficiencies of the ${}^4\text{I}_{13/2} \rightarrow {}^4\text{I}_{15/2}$ transition.

The absorption spectra were used in a Judd-Ofelt analysis, which calculates theoretical values for electric-dipole transition probabilities, radiative lifetimes, branching ratios, and radiative quantum efficiencies. The predicted lifetimes were, in many instances, significantly longer than those actually observed due to the influence of thermal relaxation and concentration quenching processes. These results, however, are not unique to GGG and YSGG. Similar results are reported in the literature for other erbium-doped hosts.

The procedure may be used with greater reliability to determine branching coefficients and radiative quantum efficiencies. The radiative quantum efficiency of the ${}^4I_{11/2}$ state was determined using the Judd-Ofelt-predicted radiative lifetime and the actual observed lifetime. The results of this measurement (24% for GGG and 32% for YSGG) are indicative of the potential of these materials as laser gain media. These are favorable efficiencies, greater than those observed in aluminum-garnet materials such as YAG, yet less than those observed in fluorides, which have lower phonon energies.

Chapter 3 was concerned with measurement of the upconversion coefficients of the ${}^4I_{11/2}$ and ${}^4I_{13/2}$ states. These coefficients represent the average rate of upconversion from the respective states. The magnitude of the coefficients is another indicator of the potential of the materials as laser gain media. Previous investigations using similar systems employed a rate-equation technique in which arbitrary values for the coefficients were put into the equations, the solutions to which were then compared to actual luminescence data.

A quantitative solution to the rate equations was derived which used spectroscopic parameters in conjunction with the so-called 'upconversion ratios' (representatives of the luminescence data) to solve numerically for the upconversion coefficients. The solutions were then run back through the rate equations to compare the method with the observed data. A good fit was in most instances observed. This method is much easier to use than the previous method since it reduces much of the 'guesswork' involved to solve the equations.

The upconversion coefficients which result from the calculations indicate that upconversion from the lower state (${}^4I_{13/2}$) is greater than that from the upper state (${}^4I_{11/2}$) for the 30% sample of YSGG and for both the 10% and 30% samples of GGG. The ratio of the coefficients (α_1/α_2 , not the upconversion ratios Y and Z) is slightly higher for 30% YSGG than it is for 30% GGG, which may explain the slightly better YSGG laser performance typically observed in Chapter 4. The ratios are not as favorable, however, com-

pared to YLF, which is a factor of three larger, and BYF, which may be larger by three to ten times. [These numbers are, of course, not a true comparison, since the doping levels for the different materials are not identical. The fluorides were doped with 20% erbium, and the garnets with 30% erbium, due to availability of materials.]

This has been the first application of this procedure, and therefore the number of data points (materials and concentrations) is limited. A greater range of doping levels should be studied to model dependence of the coefficients upon the concentration. The dependence can not be properly derived from only two data points (10% and 30%), especially with the large error bars associated with method. The model does, however, give results which appear to be within reasonable limits, and may, with care, be used to further study these materials.

The 2.8- μm laser properties of these materials were investigated in Chapter 4. Monolithic laser resonators were chosen over the more conventional open resonators to inhibit losses from atmospheric water vapor. The lasers, pumped with either a Ti:sapphire laser or InGaAs diode laser, exhibited efficient operation (typically greater than 25% slope efficiency), low thresholds, and high output powers. The output power dependence on pump wavelength was studied to determine the optimal pump wavelength with which to excite the system. The results of this experiment further indicate that the upper laser-state is either not significantly affected by ESA, or that the ESA is wavelength-insensitive at the peaks of the absorption bands.

The spectral and spatial structure of the emission was also analyzed. The results indicate that the lasers typically operate in four or five axial modes. [Tunable, single-frequency operation was demonstrated using Er:YAG.] The emission from the Ti:sapphire-pumped lasers was diffraction-limited with a full-angle beam divergence of 32.7 mrad ($M^2=1.03$). That from the diode-pumped lasers was elliptical with full-angle divergences of 42.1 mrad x 84.2 mrad ($M^2=1.3$ x 2.6, respectively), with the smaller

divergence corresponding to the near-diffraction-limited plane of emission from the diode laser.

5.3 Suggestions for Future Work

The basic spectroscopy of the materials studied and other similar erbium-doped hosts is fairly well-known, and at this point, the host-to-host differences of the systems are minor. The rate-equation model, however, needs significant improvement to properly and confidently model the system.

Ground-state depletion is typically neglected in the rate equations, yet the use of high-power excitation sources may, in fact, deplete the ground state of the ion. The saturation of the observed luminescence (as reflected in the upconversion ratios) may indicate the onset of the depletion process. It is not possible, at this point, to conclude that this is in fact the case, and depletion should therefore not be entirely disregarded. The rate-equations should be modified to account for the finite ground-state population, and a comparison made between the solutions to the modified and unmodified equations. If no difference is observed, then it may be possible to conclude that depletion is not a factor.

The rate-equation model is also limited by the accuracy of the measurements of the spectroscopic parameters and pump rate. The calculations of the upconversion coefficients indicate that small variations in the measured parameter may result in dramatically different results. This high sensitivity is characteristic to the method derived, and accurate results may only be guaranteed with highly accurate measurements.

The upconversion coefficients for the materials Er:GGG and Er:YSGG have only been determined for one or two doping levels. It is not possible, based on just two measurements, to accurately predict what the rate of upconversion will be for an arbitrary sample. Results of another study (reference 4 of Chapter 4) indicate that the rate of upconversion from the ${}^4I_{11/2}$ state may be greater than that from the ${}^4I_{13/2}$ state at higher concentrations, at least for BYF. This is just the reverse of that observed here, and would imply that cw 3- μ m laser operation at the highly-doped level may not be possible, or would at

best be much less efficient. A knowledge of the upconversion coefficients at different doping levels would at least allow the observation of a trend, if not a modelling, of the behavior of the system. Future work in these and similar materials should therefore also include the analysis of the rate of upconversion as a function of erbium concentration.

The cw 3- μm erbium laser should be further investigated by considering new pump sources and resonator configurations. Previous efforts have focused on monolithic laser resonators in order to avoid high laser thresholds which result from intra-cavity losses due to the absorption of 3- μm radiation by atmospheric water vapor and poor anti-reflection coatings. Resonators employing external mirrors, however, are required when the use of intracavity elements such as Q-switches or étalons is anticipated.

A first-step has been taken to advance the resonator design in an experiment whose resonator includes a gain element (one surface flat and coated for high-reflectivity at the laser wavelength, the other surface cut at Brewster's angle to eliminate the need for an anti-reflection coating) and a concave high reflector. Output coupling is achieved using a CaF_2 window set near Brewster's angle within the cavity. This element can be rotated for different angles to adjust for different levels of output coupling. The setup is shown schematically in Figure 5-1.

The pump source for this resonator was a 971 nm, quasi-cw InGaAs diode-laser array (SDL-3230-TS) which was driven by a variable pulsewidth (100 μsec to 1 msec) and variable repetition rate current source (Analog Modules 770-34). The single emitting layer was 1 cm x 1 μm . The focusing optics are based on a similar experiment by Shannon and Wallace which used Nd:YAG as the gain medium⁴. A rod lens ($f=1.2$ mm), placed in near-contact with the pump laser, brought the divergent emission in the vertical plane to near collimation (the emission in the horizontal plane was significantly less divergent). An

⁴ D.C. Shannon and R.W. Wallace, "High-Power Nd:YAG Laser End-Pumped by a CW, 10 mm x 1 μm Aperture, 10-W Laser-Diode Bar". *Optics Letters*, **16**, 5. 1991.

aspheric lens ($f=8.5$ mm), placed 9 mm from the rod lens and 5 mm from the erbium crystal, focused the emission in both planes to a spot $\sim 150 \mu\text{m} \times 1.1$ mm on the surface of the crystal. A cylinder lens ($f=12.7$ mm) was additionally placed between the rod lens and the asphere to reduce aberration.

Data were obtained for Er:GGG (30%) and Er:YSGG (30%) as a function of pump pulsewidth and pump power at a repetition rate of 10 Hz (higher repetition rates risked damage to the pump laser), and are shown graphically in Figures 5-2 and 5-3. YSGG performed slightly better than GGG, consistent with the results obtained using the monolithic lasers. One data point was obtained for each material at a 20-Hz pump repetition rate, with observed outputs of 3.8 mJ from YSGG and 2 mJ from GGG.

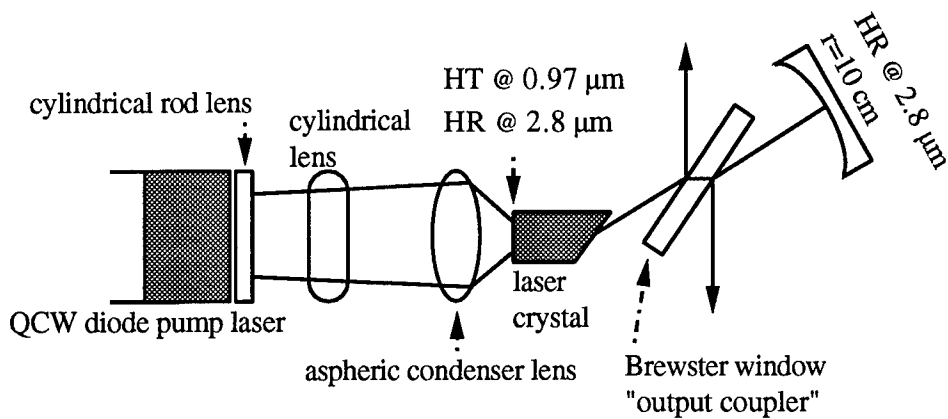


Fig. 5-1: Experimental arrangement of diode-pumped erbium laser using external-mirror resonator (view from above).

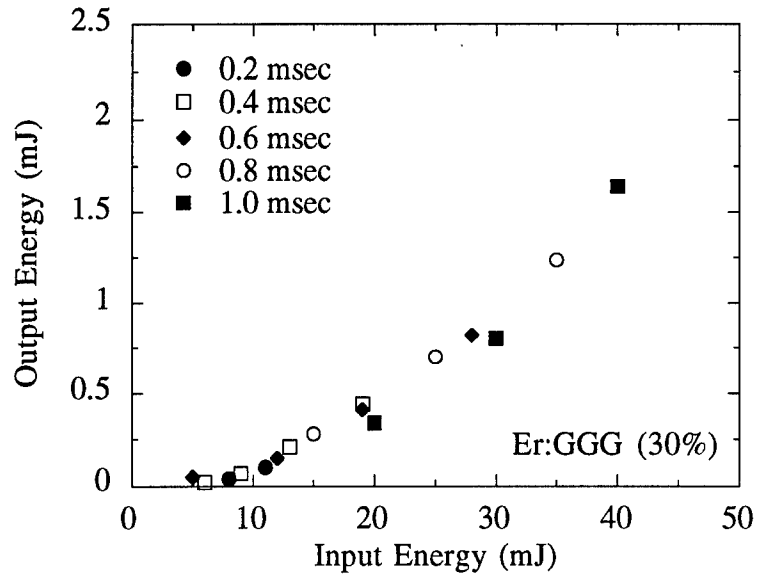


Figure 5-2: Energy data as a function of pulsewidth at 10 Hz for pulsed-pumped Er:GGG.

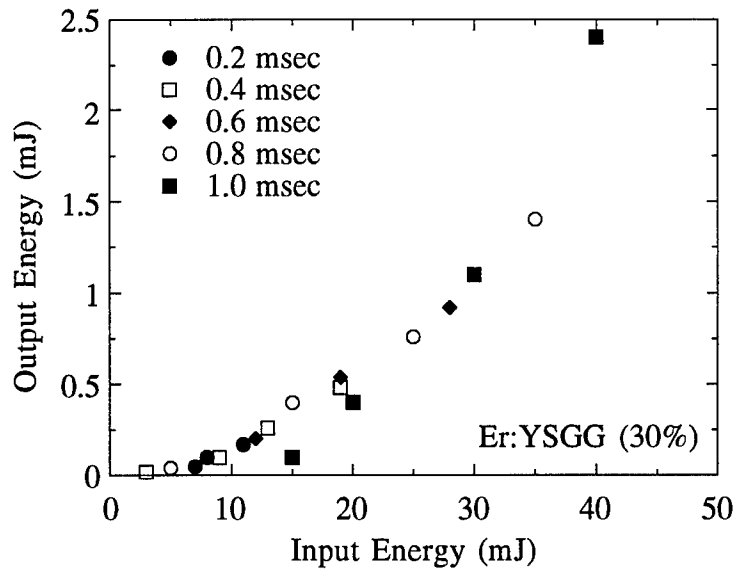


Figure 5-3: Energy data as a function of pulsewidth at 10 Hz for pulsed-pumped Er:YSGG.

This experiment is only the first step toward advanced resonator designs. Future experiments should also consider fiber-coupled pump sources and intra-cavity devices for Q-switching or frequency conversion. A more detailed model of the system, which could include determinations of laser thresholds as functions of erbium concentration and pump wavelength, coupled with advanced resonator designs, should result in a reasonable evaluation of which systems will optimize laser operation.

Appendix: Relevant Publications

The following is a list of the publications which have resulted from this research:

- B.J. Dinerman, J. Harrison, and P.F. Moulton. "CW and Pulsed Laser Operation at 3- μ m in Er³⁺-Doped Crystals". Accepted for presentation at the OSA Advanced Solid-State Lasers Conference, Salt Lake City, UT. February, 1994.
- B. J. Dinerman and P. F. Moulton. "Efficient 3- μ m CW Laser Operation in Erbium-Doped YSGG, GGG, and YAG". To be submitted for publication to Optics Letters. January, 1994.
- B. J. Dinerman, P. F. Moulton, and D. M. Rines. "Pulsed Gain Measurements and 3- μ m CW Laser Operation in Er³⁺-Doped Crystals". Proceedings of the OSA Advanced Solid-State Lasers Conference, New Orleans, LA. February, 1993.
- B.J. Dinerman and P. F. Moulton. "CW Laser Operation from Er:YAG, Er:GGG, Er:YSGG, and Er:BYF". Proceedings of the IEEE Lasers and Electro-Optics Society Annual Meeting, Boston, MA. November, 1992.
- B.J. Dinerman and P. F. Moulton. "CW Laser Operation from Er:YAG, Er:GGG, and Er:YSGG". Proceedings of the OSA Advanced Solid-State Lasers Conference, Santa Fe, New Mexico. February, 1992.

7.2 Appendix B - Optics Letters Paper

3- μm cw laser operation in erbium-doped YSGG, GGG and YAG

Reprint from Optics Letters, Vol. 19., August 1, 1994

3- μm cw laser operations in erbium-doped YSGG, GGG, and YAG

Bradley J. Dinerman and Peter F. Moulton

Research Division, Schwartz Electro-Optics, 45 Winthrop Street, Concord, Massachusetts 01742-2052

Received March 29, 1994

We have demonstrated cw laser operation at wavelengths near 3 μm from monolithic, Er-doped YSGG, GGG, and YAG lasers by direct upper-state pumping in the 0.97- μm wavelength region with either a Ti:sapphire laser or InGaAs diode lasers. We have obtained slope efficiencies as high as 31% and, with diode-laser pumping, output powers of 0.5 W. In addition, we have demonstrated tunable single-frequency operations from Er:YAG.

Laser transitions of trivalent Er at wavelengths near 3 μm operate between the $^4I_{11/2}$ (upper) and the $^4I_{13/2}$ (lower) states. The long lifetime of the lower state impedes cw operation but is mitigated by a rapid thermalization among the lower-state Stark-split levels. Thermalization favors laser action from transitions terminating in the highest-lying Stark levels. In Er:LiYF₄ (YLF), cw operation should be possible solely because of thermalization.¹ Upconversion from the lower state, identified as an important factor in early studies of long-pulse, flash-lamp-pumped lasers,²⁻⁴ also aids in establishing net cw gain for crystals with high Er concentrations.

The first true cw, 3- μm Er laser,⁵ operating with the host crystal YLF, was pumped by excitation of the $^4I_{9/2}$ state at a 0.79- μm wavelength with an AlGaAs laser and produced an output power of $\sim 180 \mu\text{W}$, which was later improved to nearly 10 mW.⁶ Direct excitation of the upper state by pumping near 0.97 μm leads to higher efficiencies than does excitation at 0.79 μm , because of reduced energy losses resulting from other deexcitation processes. Recent experiments with 0.97- μm , Ti:sapphire-pumped Er:GSGG lasers⁷ have shown power outputs approaching 130 mW, with slope efficiencies of 36%, greater than the ratio of pump to laser wavelength. The high slope efficiency is attributed in part to re-pumping of the upper laser state by upconversion.

In the experiments discussed here we extend operation of direct-pumped 3- μm Er lasers to three new crystals and report on efficient operation with 0.97- μm , InGaAs diode pump lasers at 3- μm output power levels as high as 0.5 W. In addition, we demonstrate the first, to our knowledge, single-frequency, tunable output from a cw Er:YAG laser.

As in previous studies,^{1,5-7} the laser configuration that we used was a longitudinally pumped monolithic resonator. The laser crystals were 3 mm long and 3 mm in diameter, except for the single-frequency monolith, which was 1 mm long and 1.5 mm in diameter. The flat, pump surfaces of the monoliths were coated to be highly transmitting at 0.97 μm and highly reflecting at the laser wavelength. The output surfaces were coated for nominal 99.7% reflection at the laser wavelength and were polished with convex 1- and 4-cm radii of curvature for the 3- and 1-mm

lengths, respectively. Materials used for the 3-mm monoliths were 30%-doped Er:YSGG, 30%-doped Er:GGG, and 33%-doped Er:YAG. We fabricated the 1-mm monolith from 50%-doped Er:YAG in order to maintain a high level of pump absorption. Unless indicated, all data apply to the 3-mm-long monoliths.

We conducted our initial experiments using a cw Ti:sapphire laser as the pump source, focused to a 40- μm spot ($1/e^2$ radius) on the flat surface of the crystals by a 10-cm focal-length lens. We obtained power, threshold, slope efficiency and laser wavelength data for each material at 300 K. Our results are presented in Table 1, along with our measured lifetimes for the upper and lower laser states. To our knowledge, these data represent the first cw operation from Er:GGG and the first cw operation in the other hosts by direct pumping of the Er³⁺ ion. Er:YSGG typically showed the best performance of the three materials, with a slope efficiency of 31% well over threshold.

We observed laser action from the YSGG and GGG hosts at Ti:sapphire pump wavelengths ranging from 0.91 to 0.99 μm . Figure 1 shows, for the Er:YSGG laser, plots of the ratio of output power to pump power as a function of pump wavelength for pump powers near threshold (15 mW at 0.97 μm) and far over threshold (400 mW at 0.97 μm). Also shown in the figure is the absorption coefficient for the laser material; laser action occurred for absorption coefficients as low as 0.2 cm⁻¹. We find good agreement between the shapes of the laser excitation spectra and the absorption spectra, indicating that pump excited-state absorption either is wavelength independent or has a minimal effect on laser performance at the excited-state densities encountered in the monoliths.

We used two different types of strained-layer, quantum-well InGaAs diode lasers to pump the Er-doped monoliths. The first was a 50-mW, single-transverse-mode device (SDL-6302-H1); we were able to pump the GGG and YSGG crystals over threshold, using a 10-cm single-element spherical focusing lens. With 48 mW of 965-nm diode-laser power incident upon the crystals, we observed 6.1 and 8.3 mW of output power from the GGG and YSGG lasers, respectively.

Table 1. Performance Summary of 3- μm Er Lasers at 300 K^a

	Er:YSGG	Er:GGG	Er:YAG
Wavelength (nm)	2797	2821	2937
Output power (mW)	190 (511)	155 (293)	143 (171)
Threshold (mW)	5 (70)	7 (250)	40 (410)
Slope efficiency (%)	31 (26)	27 (19)	26 (12)
⁴ I _{11/2} Lifetime (ms)	1.3	0.96	0.12
⁴ I _{13/2} Lifetime (ms)	3.4	4.86	7.25
α (cm ⁻¹)	15	18	12

^aEfficiency and power measurements in parentheses indicate results of diode-laser pumping; other values refer to Ti:sapphire pumping.

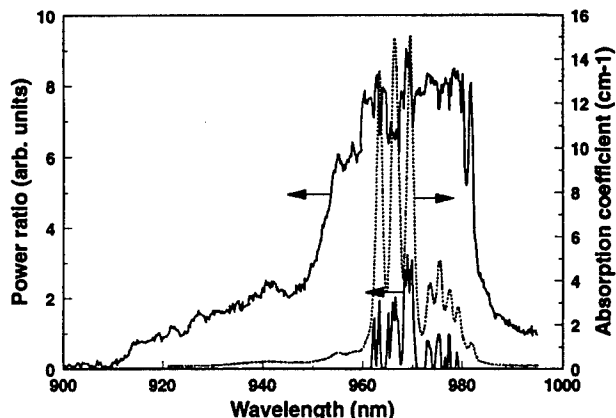


Fig. 1. Er:GGG laser excitation spectra (solid curves) for two pump levels, along with the absorption spectrum of the crystal (dashed curve).

The second diode laser was a 1-W, multimode device (SDL-6562-P1) with a 100- μm stripe width. To obtain high pump powers, we used two of the devices, oriented for orthogonal polarization and combined into a single beam with a polarizing beam cube. The individual diode laser outputs were collimated with a four-element lens ($f = 15$ mm, 18-mm aperture). An identical lens focused the combined beams onto the monoliths. Figure 2 shows the input-output curves for the three materials. Power, threshold, and efficiency data for the double-diode pumping scheme are summarized in Table 1.

We used a 0.25-m grating spectrometer to measure the emission spectrum of the Er lasers. Longitudinal modes of the 3-mm-long-crystals were spaced approximately 0.7 nm apart and were resolved by the spectrometer. The 3-mm monoliths generally operated on 3–5 longitudinal modes, with a resultant overall width of ~ 2.5 nm FWHM. The 1-mm-long crystal of Er:YAG, when pumped by the Ti:sapphire laser, operated on a single axial mode based on the observed spectrometer output and on the fact that a stable reading of wavelength was evident when the laser output was analyzed by a high-resolution wavemeter (Burleigh wavemeter). For the 1-mm crystal, we obtained a 40-mW threshold, a 16% slope efficiency, and 70 mW of output power for 540 mW of pump power.

We placed the 1-mm Er:YAG crystal mount on a thermoelectric cooler to determine the temperature

and pump-power tuning rate of the laser wavelength, which we measured with the wavemeter to a resolution of 0.01 nm and an absolute accuracy of 0.1 nm. We observed that the monolith switched between the 2.94- and 2.83- μm laser transitions, depending on the crystal temperature and pump power. By changing both pump power and crystal temperature, we were able to tune the 2.83- μm line over a 1.9-nm range. The 2.83- μm line demonstrated a constant-pump-power wavelength tuning versus temperature relation, plotted as points in Fig. 3. The solid line in the figure is the slope predicted if tuning results entirely from the shift in the cavity mode wavelength with temperature. We calculated the slope, 0.033 nm/ $^{\circ}\text{C}$, using dn/dt and a thermal expansion coefficient of 7.3 and 7.5×10^{-6} , respectively, for the YAG host crystal. The agreement between the data and the predicted tuning rate is excellent, and the deviation from a straight line at the extremes of the temperature range may result from a shift with temperature of the transition peak wavelength. The pump-power tuning rate, for a fixed heat-sink temperature of 25 $^{\circ}\text{C}$, was 0.004 nm/mW in the pump-power range of 300–500 mW. The two rates combined imply that the monolith temperature, in the volume occupied by the laser mode, rises at a rate of 0.10 $^{\circ}\text{C}/\text{mW}$ of incident pump power.

In analyzing our results, we estimated the expected threshold pumping level for the lasers by setting up

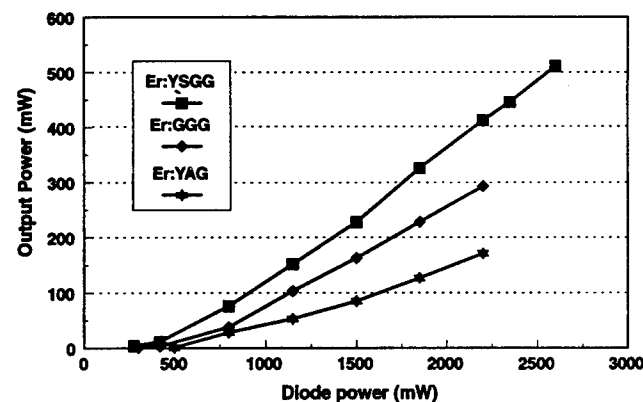


Fig. 2. Input-output curves for Er-doped monolithic lasers pumped by two 1-W diode lasers.

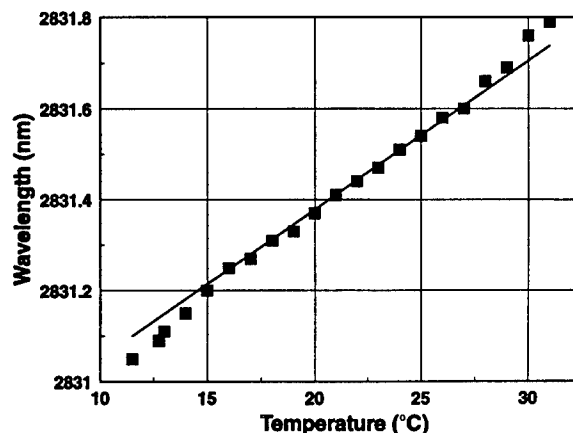


Fig. 3. Observed temperature tuning of single-frequency Er:YAG laser wavelength.

the rate equations for populations of the upper and lower laser states and finding the steady-state solutions as a function of pump rate. We included terms for upconversion from each state and, in addition, terms accounting for the finite probability that excitation arriving in the $^4I_{9/2}$ state from upconversion may cross relax and generate two excitations in the lower laser state, rather than excite the upper state after nonradiative relaxation, as discussed by Chou and Jenssen.⁸ We measured the upconversion coefficients and the $^4I_{9/2}$ branching term for YSGG and employed the upconversion data of Shi *et al.*⁹ for Er:YAG. After calculating the cw population densities in the upper and lower states, we determined the pumping rate needed to obtain a net gain in the laser crystal, accounting for the thermalized fraction of excitation in the appropriate upper- and lower-state Stark-split levels.

We find that pumping rates of 4×10^{21} and 2.5×10^{22} cm⁻³ are predicted to obtain net cw gain in Er:YSGG and Er:YAG at the doping levels we used in our 3-mm monoliths. We calculated the actual threshold pumping rates, W_{th} , at the crystal surface for Ti:sapphire pumping, using the formula (for a Gaussian pump)

$$W_{th} = \alpha P_{th} / (\pi w_0^2 E_p),$$

where α is the pump absorption coefficient, P_{th} is the threshold pump power, w_0 is the pump beam radius, and E_p is the energy of the (965-nm) pump photon. The values for α and P_{th} for the lasers appear in Table 1, and w_0 is 40 μ m. We find that W_{th} is 7.3×10^{21} and 4.7×10^{22} cm⁻³ for Er:YAG and Er:YSGG, respectively, which in both cases is slightly less than twice the theoretical value needed to yield net gain. A more involved threshold calculation requires full accounting for the overlap between the spatial variation in gain in the laser crystal and the laser mode.

The issue of enhanced efficiency from lower-state upconversion has been discussed before.⁷ The highest Er:YSGG laser slope efficiency that we observed is 88% of the quantum limit, for a system with a nominal 0.3% output coupling. We estimate the enhancement factor for both Er:YSGG and Er:YAG to be 1.6, based on the formulas in Ref. 7. This may account for the high efficiency despite the low level of output coupling.

As higher-power, higher-brightness, 0.97- μ m diode-laser sources become available, we expect that higher levels of 3- μ m, cw power output can be generated by Er-doped materials.

The authors gratefully acknowledge the support of the Advanced Research Projects Agency.

References

1. R. C. Stoneman, J. G. Lynn, and L. Esterowitz, *IEEE J. Quantum Electron.* **28**, 1041 (1992).
2. M. A. Andriasyan, N. V. Vardanyan, and R. B. Kostanyan, *Sov. J. Quantum Electron.* **12**, 366 (1982).
3. Kh. S. Bagdasarov, V. I. Zhekov, V. A. Lobachev, T. M. Murina, and A. M. Prokhorov, *Sov. J. Quantum Electron.* **13**, 262 (1983).
4. V. I. Zhekov, V. A. Lobachev, T. M. Murina, and A. M. Prokhorov, *Sov. J. Quantum Electron.* **13**, 1235 (1983).
5. G. J. Kintz, R. Allen, and L. Esterowitz, *Appl. Phys. Lett.* **50**, 22 (1987).
6. G. J. Kintz and L. Esterowitz, in *LEOS '88 Annual Meeting* (Institute of Electrical and Electronics Engineers, New York, 1988), paper EL1.6.
7. R. C. Stoneman and L. Esterowitz, *Opt. Lett.* **17**, 816 (1992).
8. H. Chou and H. P. Jenssen, in *Tunable Solid State Lasers*, M. L. Shand and H. P. Jenssen, eds., Vol. 5 of OSA Proceeding Series (Optical Society of America, Washington, D.C., 1989), pp. 167-174.
9. W. Q. Shi, M. Bass, and M. Birnbaum, *J. Opt. Soc. Am. B* **7**, 1456 (1990).

7.3 Appendix C - ASSL '92 Summary

CW Laser Operation from Er:YAG, Er:GGG and Er:YSGG

**Summary of paper presented at
OSA Advanced Solid State Lasers Conference
Santa Fe, NM, February, 1992**

CW Laser Operation from Er:YAG, Er:GGG and Er:YSGG

B.J. Dinerman* and P.F. Moulton

Schwartz Electro-Optics, Inc.

45 Winthrop Street, Concord, Massachusetts 01742

(508) 371-2299

Abstract

We report the first cw operation of monolithic Er:YAG, Er:GGG and Er:YSGG lasers at wavelengths near 3 μm . Pumping with a 960-970-nm Ti:sapphire or InGaAs diode laser, we have observed thresholds as low as 5 mW and power outputs as high as 190 mW, with absolute efficiencies approaching 30%.

* Corresponding author

CW Laser Operation from Er:YAG, Er:GGG and Er:YSGG

B.J. Dinerman and P.F. Moulton

Schwartz Electro-Optics, Inc.

45 Winthrop Street, Concord, Massachusetts 01742

(508) 371-2299

Summary

Er-doped lasers operate at wavelengths near 3 μm on transitions from energy levels in the $^4I_{11/2}$ manifold to those in the $^4I_{13/2}$ manifold. For practically all host crystals the lifetime of the upper manifold is shorter than that of the lower. CW laser action from these so-called "self-terminating" transitions is nevertheless possible, for two reasons. First, for some specific transitions the lower level lies high in the $^4I_{13/2}$ manifold and thermalization within the manifold effectively reduces the lower-level population. Second, upconversion from the $^4I_{13/2}$ manifold increases the lower-level decay rate at high excitation densities and at the same time provides an additional pumping channel for the upper level. The first true-cw, 3- μm laser operation was observed in Er:YLF under diode-pumped conditions by Kintz [1,2] and, recently, Stoneman has obtained more efficient and higher-power operation from Ti:sapphire-pumped Er:GSGG [3].

As part of a general study of diode-pumped Er-doped laser systems, we have been investigating cw laser operation from a variety of host crystals. Our studies of cw lasers have been motivated by their application as gain-probe sources in the characterization of pulsed-pumped, Er-doped, 3- μm -wavelength amplifiers. In spectroscopic studies of Er-doped GGG and YSGG we have confirmed the conclusion [3] that diode pumping directly into the upper laser level, with pump wavelengths around 970 nm, should be more efficient than 790-nm pumping into the higher-lying $^4I_{9/2}$ level, not only because of a reduced quantum defect but also because of reduced pump excited-state absorption. Fortunately, 970-nm, strained-quantum-well InGaAs diode lasers with performance characteristics comparable to conventional GaAlAs lasers are now becoming commercially available.

To date, we have fabricated monolithic lasers from 30%-Er-doped YAG, GGG and YSGG. The laser crystals were 3-mm in length and polished to form a plano-concave resonator. The crystal flat surface was coated for HR at 2800-2900 nm and HT at 970 nm while the 1-cm-radius curved surface was coated for a nominal 99.7-% reflectivity at 2800-2900 nm.

Input-output data for the three materials are plotted in Figure 1, where the pump source is a TEM₀₀-mode cw Ti:sapphire laser; Table 1 summarizes the laser performance data. All pump power levels are those incident on the single, uncoated lens used to focus the pump beam on the laser crystals. To our knowledge, this data represents the first cw operation from all the different crystals and shows, for YSGG, the highest cw output power yet obtained from a room-temperature 3- μ m Er laser. The relatively high threshold from Er:YAG is expected because the material has a much shorter upper-state lifetime (0.1 msec) than either GGG (0.9 msec) or YSGG (1.4 msec), while having about the same gain cross section. Further studies will be needed to determine whether the differences in pump-conversion efficiencies are truly representative of the materials and not just the result of variations in monolith-crystal losses and coatings. The slope efficiency of the Er:YSGG laser well over threshold is 30.5%, or 88% of the ultimate quantum limit. We suspect that some of the pump energy is being recycled as a result of lower-level upconversion.

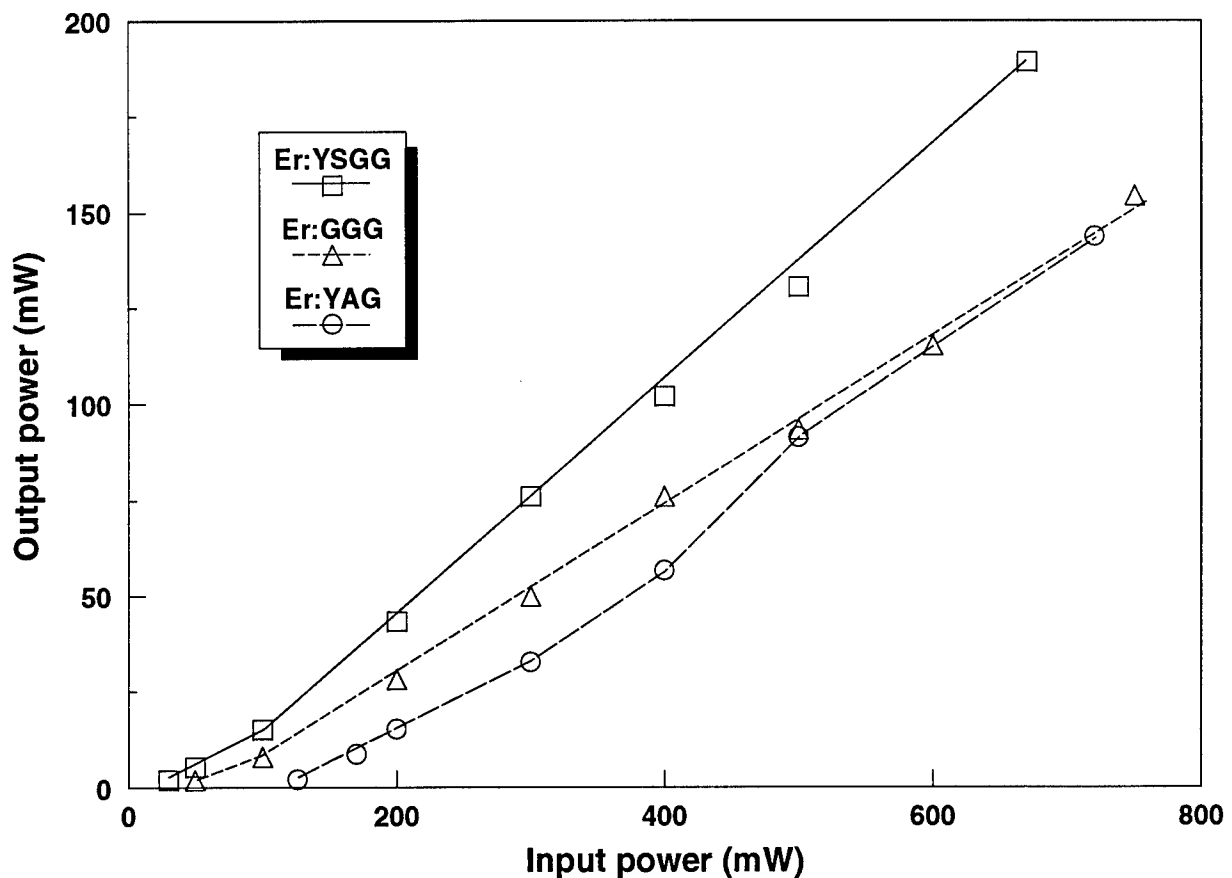


Figure 1. Input-output curves for Er-doped monolithic lasers pumped by a Ti:sapphire laser.

We have conducted a number of parametric studies of the Ti:sapphire-pumped monolithic lasers, including the variation in threshold and slope efficiency with pump spot size and wavelength. Over the range of spot sizes examined, we found that the threshold power increased with spot size, while the slope efficiency remained essentially constant. Figure 2 shows a plot of the output power of the Er:GGG laser as a function of pump wavelength, for pumping near and well over threshold. In carrying out the measurements, the Ti:sapphire wavelength was scanned by driving the birefringent tuner with a computer-controlled stepper motor. The computer also took simultaneous data on 1) the pump-laser wavelength from the output of a wavemeter 2) the Er:GGG-laser power output and 3) the power output of the Ti:sapphire laser. In Fig. 2 the laser output has been normalized to the incident pump power. We find a good agreement between the laser excitation spectra and the absorption spectra, indicating that pump excited-state absorption has a minimal effect on laser performance at the excited-state densities encountered in the monoliths.

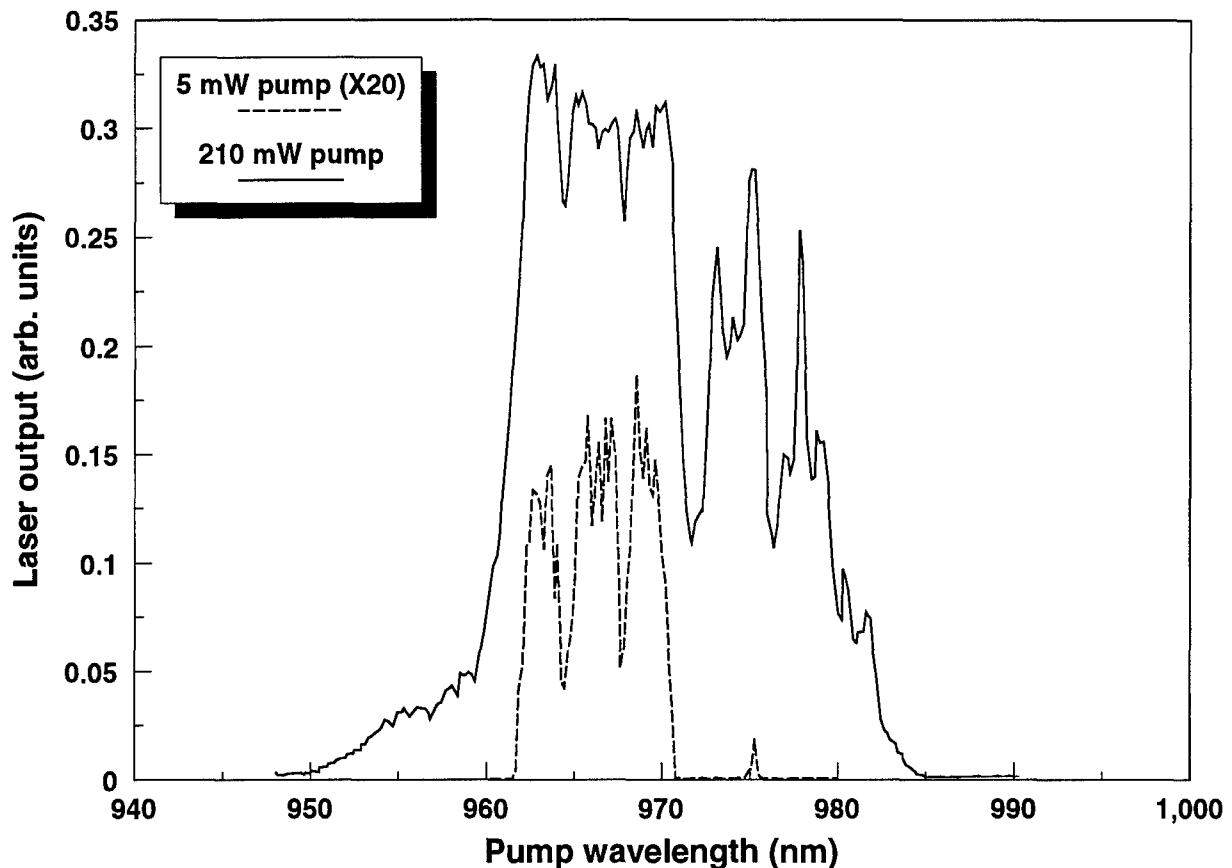


Figure 2. Er:GGG laser excitation spectrum for two pump levels.

The low observed thresholds for the Er:YSGG and Er:GGG lasers permit pumping by low-power, single-transverse-mode diode lasers. In preliminary experiments, we were able to obtain laser action from both materials by using a cw InGaAs diode laser as the pump. As an example, with 19 mW of 965-nm diode power incident on the Er:GGG monolith we observed 4.4 mW of output power, for an overall conversion efficiency of 22%. Our results compare favorably with those for previous diode-pumped cw Er-doped lasers, where slope efficiencies of 10% were measured for GaAlAs-diode pumping of Er:YLF [2]. Current efforts are directed towards improving the diode coupling optics and the use of multimode diodes with higher output powers.

Table 1. Performance Summary

Material	YSGG	GGG	YAG
Pump wavelength (nm)	965	968	960
Laser wavelength (nm)	2797	2821	2937
Pump threshold (mW)	5	7	78
Conversion efficiency (%)	28.2	20.5	19.9
Max. output power (mW)	190	155	143

References:

1. G.J. Kintz, R. Allen, and L. Esterowitz, "CW and pulsed 2.8 μm laser emission from diode-pumped $\text{Er}^{3+}:\text{LiYF}_4$ at room temperature," *Appl. Phys. Lett.* **50**, 22 (1987).
2. G.J. Kintz and L. Esterowitz, "Diode pumped CW 2.8 μm Er:LiYF₄ laser with high slope efficiency," Paper EL1.6, LEOS '88 Annual Meeting (IEEE/LEOS, Piscataway, NJ, 1988).
3. R.C. Stoneman, J.G. Lynn, and L. Esterowitz. "Laser-pumped 2.8 μm $\text{Er}^{3+}:\text{GSGG}$ laser," in Conference on Lasers and Electro-Optics, 1991 (Optical Society of America, Washington, D.C., 1991) p. 134. We wish to thank R. Stoneman for his information on the fabrication of monolithic crystals.

7.4 Appendix D - LEOS '92 Abstract and Summary

CW Laser Operation from Er:YAG, Er:GGG, Er:YSGG and Er:BYF

**Abstract and Summary of paper presented at
IEEE Lasers and Electro-Optics Society Annual Meeting
Boston, MA, November, 1992**

CW Laser Operation from Er:YAG, Er:GGG, Er:YSGG and Er:BYF

B.J. Dinerman* and P.F. Moulton

Schwartz Electro-Optics, Inc.

45 Winthrop Street, Concord, Massachusetts 01742

(508) 371-2299

Abstract

We report the first cw operation of monolithic Er:YAG, Er:GGG, Er:YSGG and Er:BYF lasers at wavelengths near 3 μm . Pumping with a 960-970-nm Ti:sapphire or InGaAs diode laser, we have observed thresholds as low as 5 mW and power outputs as high as 190 mW, with absolute efficiencies approaching 30%.

* Corresponding author

CW Laser Operation from Er:YAG, Er:GGG, Er:YSGG and Er:BYF

B.J. Dinerman and P.F. Moulton

Schwartz Electro-Optics, Inc.

45 Winthrop Street, Concord, Massachusetts 01742

(508) 371-2299

Er-doped lasers operate at wavelengths near 3 μm on transitions from energy levels in the $^4I_{11/2}$ manifold to those in the $^4I_{13/2}$ manifold. For practically all host crystals the lifetime of the upper manifold is shorter than that of the lower. CW laser action from these so-called "self-terminating" transitions is nevertheless possible because of thermalization within and upconversion from the $^4I_{13/2}$ manifold. The first true-cw, 3- μm laser operation was observed in Er:YLF under diode-pumped conditions by Kintz [1,2] and, recently, Stoneman has obtained more efficient and higher-power operation from Ti:sapphire-pumped Er:YLF [3] and Er:GSGG [4]. In other work, Huber *et al* obtained cw 3- μm operation from Cr,Er:YSGG, Cr,Er:YAG and Cr,Er:YSAG by using a 647.1 nm Kr-ion laser to excite Cr^{3+} ions, which in turn excited the Er^{3+} ions [5].

As part of a general study of diode-pumped Er-doped laser systems, we have been investigating cw laser operation from a variety of host crystals. To date, we have fabricated monolithic lasers from 30-%-Er-doped YAG, GGG, YSGG and BYF (BaY_2F_8). The laser crystals were 3-mm in length and polished to form a plano-concave resonator. The crystal flat surface was coated for HR at 2800-2900 nm and HT at 970 nm while the 1-cm-radius curved surface was coated for a nominal 99.7-% reflectivity at 2800-2900 nm.

Input-output data for the four materials are plotted in Figure 1, where the pump source is a TEM_{00} -mode cw Ti:sapphire laser; Table 1 summarizes the laser performance data. To our knowledge, this data represents the first cw operation from Er:GGG and the first cw operation in the other garnet hosts via direct pumping of the Er^{3+} ion. For YSGG, the cw output power is the highest yet obtained from a room-temperature 3- μm Er laser. The relatively high threshold from Er:YAG is expected because the material has a much shorter upper-state lifetime (0.1 msec) than either GGG (0.9 msec), YSGG (1.4 msec) or BYF (9.6 msec), while having about the same gain cross section. The slope efficiency of the Er:YSGG laser well over threshold is 30.5%, or 88% of the ultimate quantum limit. We suspect that some of the pump energy is being recycled as a result of lower-level upconversion. We have conducted a number of parametric studies of the Ti:sapphire-pumped monolithic lasers, including the variation in threshold and slope efficiency with pump spot size and wavelength. We were able to observe laser action with Er:YSGG at pump wavelengths ranging from 910-1000 nm. The lasers operated on 3-5 longitudinal modes well over threshold, for an overall linewidth of approximately 1.5 nm.

The low thresholds for Er in the YSGG, GGG and BYF hosts permit pumping by low-power, single-transverse-mode diode lasers. We were able to obtain laser action from these materials by using a 50-mW cw InGaAs diode laser as the pump. As an example, with 48 mW of 965-nm diode power incident on the Er:YSGG monolith we observed 8.3 mW of output power, for an overall conversion efficiency of 17%. Our results compare favorably with those of previous low-power diode-pumped cw Er-doped lasers, where slope efficiencies of 10% were measured for GaAlAs-diode pumping of Er:YLF [2].

We have also performed experiments with a 1-W multimode InGaAs diode pump, and have observed 120, 92 and 13 mW of output from the YSGG, GGG and YAG crystals for approximately 750 mW of incident pump power. We expect somewhat better performance with more optimal pumping optics.

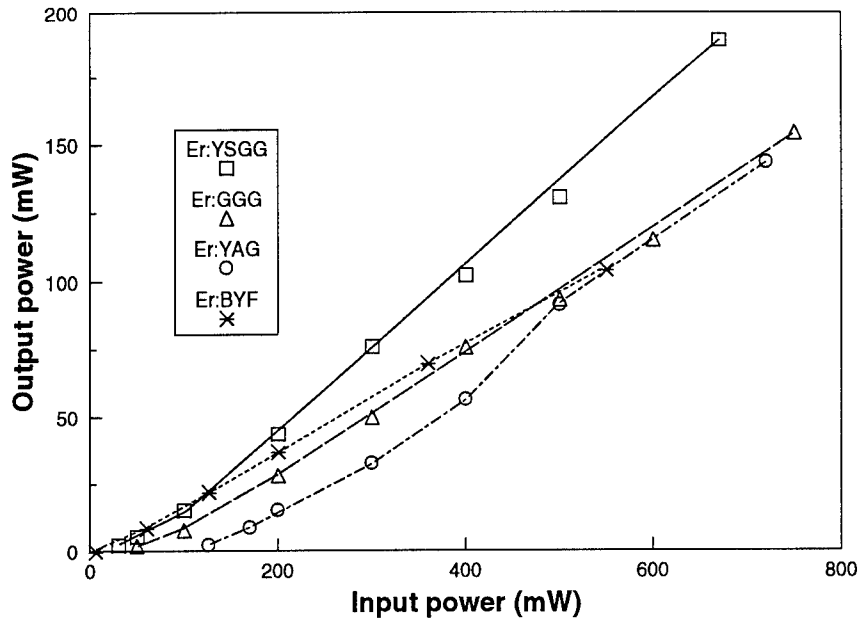


Figure 1. Input-output curves for Er-doped monolithic lasers pumped by a Ti:sapphire laser.

Table 1. Performance Summary

Material	YSGG	GGG	YAG	BYF
Pump wavelength (nm)	965	968	960	970
Laser wavelength (nm)	2797	2821	2937	2800
Pump threshold (mW)	5	7	78	6
Conversion efficiency (%)	28.2	20.5	19.9	18.9
Max. output power (mW)	190	155	143	104

References:

1. G.J. Kintz, R. Allen, and L. Esterowitz, "CW and pulsed 2.8 μm laser emission from diode-pumped $\text{Er}^{3+}:\text{LiYF}_4$ at room temperature," *Appl. Phys. Lett.* **50**, 22 (1987).
2. G.J. Kintz and L. Esterowitz, "Diode pumped CW 2.8 μm $\text{Er}:\text{LiYF}_4$ laser with high slope efficiency," Paper EL1.6, *LEOS '88 Annual Meeting* (IEEE/LEOS, Piscataway, NJ, 1988).
3. R.C. Stoneman, J.G. Lynn and L. Esterowitz, "Direct upper-state pumping of the 2.8 μm $\text{Er}^{3+}:\text{YLF}$ laser," *IEEE J. Quantum Electron.* **28**, 1041 (1992). We wish to thank R. Stoneman for his information on the fabrication of monolithic crystals.
4. R.C. Stoneman and L. Esterowitz, "Efficient resonantly pumped 2.8- μm $\text{Er}^{3+}:\text{GSGG}$ laser," *Opt. Lett.* **17**, 816 (1992).
5. G. Huber, E.W. Duczynski and K. Peterman, "Laser pumping of Ho-, Tm-, Er-doped garnet lasers at room temperature," *IEEE J. Quantum Electron.* **24**, 920 (1988).

7.5 Appendix E - ASSL '93 Summary

**Pulsed Gain Measurements and 3- μm CW Laser Operation in
Er³⁺-Doped Crystals**

**Summary of paper presented at
OSA Advanced Solid State Lasers Conference
New Orleans, LA, February, 1993**

Pulsed Gain Measurements and 3- μm CW Laser Operation in Er³⁺-Doped Crystals

B.J. Dinerman, P.F. Moulton, and D.M. Rines*

*Schwartz Electro-Optics
45 Winthrop Street, Concord, Massachusetts 01742-2052
(508) 371-2299*

Summary

Recent research into 3- μm -wavelength erbium lasers has shown that efficient operation can be achieved in both the pulsed and cw modes of operation, despite the population bottleneck that arises due to a long lower laser state lifetime. This, we believe, is due in part to the upconversion acting within the system that effectively removes ions from the lower laser state and repopulates the upper state. In a past paper, we reported the first cw operation in monolithic Er³⁺-doped YAG, GGG, and YSGG via resonant excitation into the ⁴I_{11/2} upper laser state (Figure 1). [1] We now report further investigations into these materials, with the addition of BYF and YLF, which include studies of the 3- μm gain properties under conditions of pulsed pumping.

Using a cw Ti:sapphire laser for preliminary laser investigations, we obtained laser thresholds as low as 5 mW, slope efficiencies greater than 30%, and outputs approaching 200 mW. We also achieved CW laser action using one or two 1-W, 964-nm strained-quantum-well diode lasers, where the diode laser outputs were coupled into the erbium-laser crystal using identical lenses to collimate and focus the light. Higher thresholds and lower efficiencies resulted from the multimode and asymmetrical nature of the pump beam. Table 1 presents the results from Ti:sapphire-pumped and diode-pumped erbium.

Using a 0.25-m monochromator with a 300-groove/mm grating blazed at 2 μm , we investigated the spectral nature of the laser output. In operation well above threshold, the spectral widths were typically ~ 1.5 nm,

including 2-5 longitudinal modes. Er:BYF was the only material which appeared to operate on a single longitudinal mode for operation as high as six times threshold.

The spectral nature of the output is also affected by operating temperature. We chose Er:YAG as a representative material to study this dependence. We mounted the monolithic laser crystal in a variable-temperature, liquid-nitrogen-cooled, evacuated Dewar. The 2.937- μm line steadily increased in intensity as we cooled the system from room temperature, but near 180 K, this line decreased and two new lines, one at 2.858 μm and one at 2.899 μm , appeared. At 77 K, these two lines gained strength and laser action ceased entirely at 2.937 μm .

More recently, we have begun investigating the 3- μm wavelength laser gain of these erbium-doped materials using a "pump-probe" method. We side-pumped sample crystals with a pulsed, 970-nm Cr:LiSAF laser, and probed gain using our cw, diode-pumped monolithic lasers. The flashlamp-pumped Cr:LiSAF laser was excited by a transistor-switched variable-pulsewidth lamp driver in order to observe the effect of pump pulsewidth on gain.

To date, we have conducted gain measurements for Er-doped YSGG, GGG, BYF, and YLF. We conducted the measurements for each sample as a function of pump pulse duration and pump energy. We studied the temporal dependence on a digital oscilloscope, and the values we used to calculate gain were recorded directly from this measurement. Figure 2 shows gain measurements for Er:YSGG for two different pump energies.

Results of the measurements show that the gain signal remains fairly linear

throughout the range of energies, indicating that gain saturation has not yet occurred. We anticipate that at higher energies, saturation will occur due to upconversion processes affecting the upper laser level at high excitation densities. [2] Upconversion adds a term quadratic in upper-state population to the system rate equations, and has the effect of reducing the apparent storage time as pump levels increase. Results of gain measurements for 30%-doped YSGG are shown in Figure 3. We plan to determine the upconversion coefficients for all the materials to be studied by fitting our gain data to a rate-equation model. We expect the garnet crystals to have similar properties, but the coefficients for the fluoride crystals may be substantially lower.

In summary, we have studied the cw laser properties of Er-doped YSGG, GGG, YAG, BYF, and YLF. Low thresholds and high efficiencies have been demonstrated. In addition, we have conducted gain measurements near 3 μm for each material. Large gains have been observed under high-power, short-pulse pumping.

References:

- [1] B. J. Dinerman and P. F. Moulton. "CW Laser Operation from Er:YAG, Er:GGG and Er:YSGG." OSA Proceedings on Advanced Solid-State Lasers. (Santa Fe, New Mexico, 1992).
- [2] V. A. Smirnov and I. A. Scherbakov. "Nonlinear Interactions in Scandium Garnets Doped by Chromium and Erbium Ions." OSA Proceedings on Tunable Solid State Lasers. (North Falmouth, Massachusetts. May, 1989).

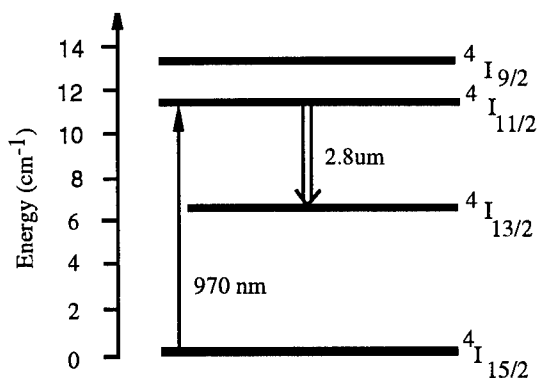


Figure 1. Relevant energy states of Er³⁺.

	Er:YSGG	Er:GGG	Er:YAG	Er:BYF	Er:YLF
laser wavelength (nm)	2797	2821	2937	2800	~2800
laser threshold (mW)	5 (70)	7 (250)	40 (410)	6 (10)	4
slope efficiency (%)	31 (26)	27 (19)	26 (12)	20 (13)	28
laser output (mW)	190 (511)	155 (293)	143 (171)	104 (163)	95

Table 1. Performance summary of 3- μ m erbium lasers. Values in parentheses indicate results from double 1-W-diode pumping. All other values from Ti:sapphire pumping.

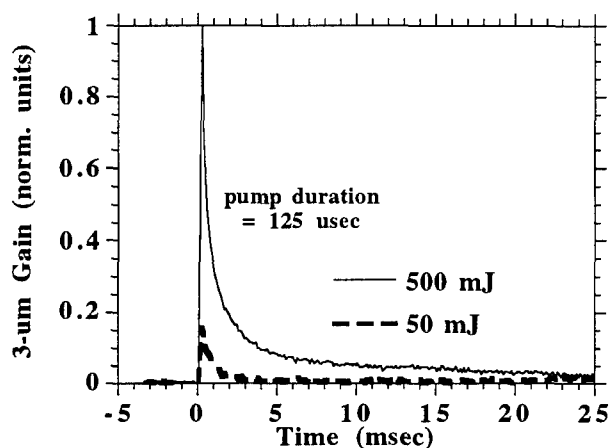


Figure 2. Gain measurements for Er:YSGG using a 125- μ sec pump pulse. (The DC baseline has been subtracted for purpose of presentation.)

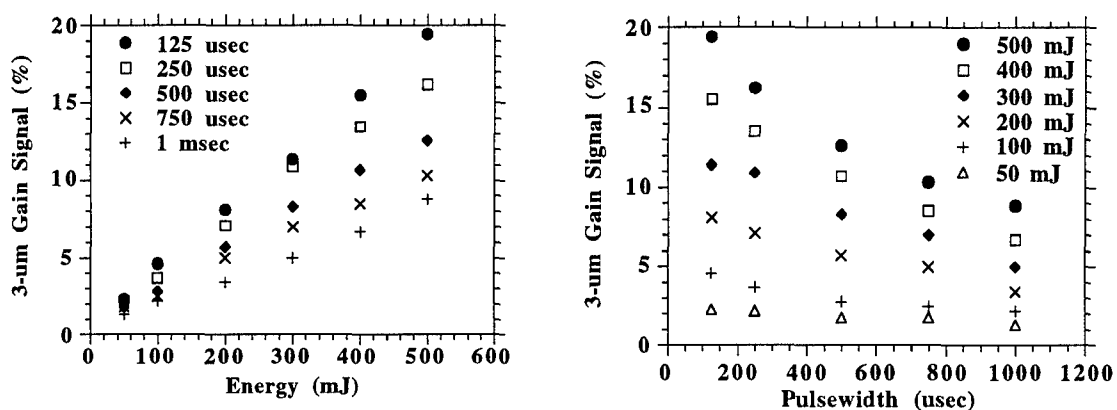


Figure 3a,b. Results of gain measurements for Er:YSGG as functions of pump energy and pulsewidth.

7.6 Appendix F - ASSL '94 Abstract and Summary

CW and Pulsed Laser Operation at 3- μm in Er³⁺-Doped Crystals

**Abstract and Summary of paper presented at
OSA Advanced Solid State Lasers Conference
Salt Lake City, UT, February, 1994**

CW and Pulsed Laser Operation at 3- μm in Er^{3+} -Doped Crystals

B.J. Dinerman*, J. Harrison, and P.F. Moulton

Schwartz Electro-Optics, Research Division
45 Winthrop Street, Concord, Massachusetts 01742-2052
(508) 371-2299

Abstract

We report the results of ongoing investigations of 3- μm -wavelength, erbium-doped lasers. Tunable, single-frequency operation of Er:YAG is demonstrated from a monolithic resonator. Efficient, quasi-cw-diode-pumped operation is reported for Er:YSGG, Er:GGG, and Er:BYF using a conventional, open resonator.

Summary

Recent research into 3- μm erbium-doped lasers has shown that efficient operation is possible despite a lower-state radiative lifetime that is longer than that of the upper-state. This is due to upconversion processes and thermalization acting within the $^4\text{I}_{11/2}$ (upper) and $^4\text{I}_{13/2}$ (lower) laser states (Fig. 1). We have previously reported the results of cw laser investigations using direct upper-state-pumped, monolithic, erbium-doped YSGG, GGG, YAG, BYF, and YLF. [1,2]

We report here on the results of cw, single-frequency, temperature-tuned operation of a monolithic Er:YAG laser near wavelengths of 2.94 μm or 2.83 μm , with a demonstrated continuous tuning range of ~ 2 nm in the temperature interval 15 $^{\circ}\text{C}$ to 35 $^{\circ}\text{C}$ (Fig. 2). The crystal length was reduced from 3 mm to 1 mm to allow operation on only one axial mode. Pump power was supplied by a Ti:sapphire laser tuned to the 0.97 μm region.

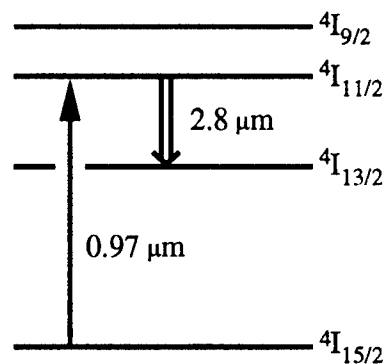


Figure 1. Partial energy-level diagram of Er.

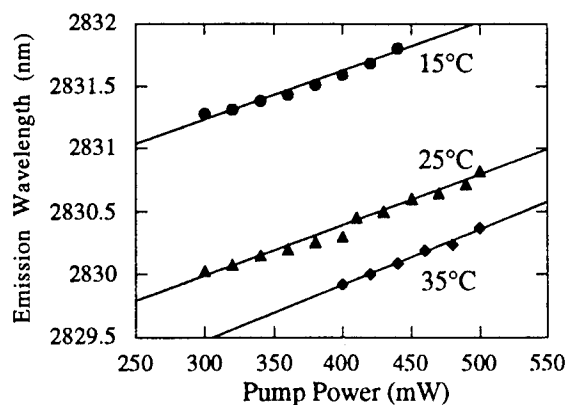


Figure 2. Tuning data for Ti:sapphire-pumped, monolithic Er:YAG laser near 2.83 μm . Tunability near 2.94 μm was also observed.

In addition, we report the results of further studies of Er-doped materials that include efficient operation from conventional external-resonator lasers pumped by a quasi-cw, diode-laser bar. Our previous efforts have focused on monolithic laser resonators in order to avoid high laser thresholds resulting from intra-cavity losses due to the absorption of 3- μm radiation by atmospheric water vapor and poor anti-reflection coatings. Resonators employing external mirrors, however, are required when the use of intracavity elements such as Q-switches or étalons is anticipated. We have studied the properties of a system with a resonator that includes a flat-Brewster gain element (coated for high-reflectivity on the flat surface) and a concave high reflector. Output coupling is achieved using a CaF_2 window set near Brewster's angle within the cavity. This element can be rotated for different levels of output coupling. (Fig. 3)

The properties of Er:YSGG (30%), Er:GGG (30%), and Er:BYF (20%) were studied and compared in this configuration. The pump source was a variable-pulsewidth, 80-W peak-power, 0.97 μm , quasi-cw diode-laser bar, whose emitting region was 1 μm x 1 cm. The emission was focused to a region ~1.1 mm x 150 μm using a rod and aspheric lens combination, described in [3]. Er:YSGG typically showed the best performance of the three materials. 2.4 mJ of 2.79- μm emission were extracted in a 1-msec pulse at 10 Hz, corresponding to a 9.1% slope efficiency. (Fig. 4). The efficiencies of Er:GGG and Er:BYF at 1.0 msec and 10 Hz were 6.5% and 6.8%, respectively. The maximum observed output was 3.8 mJ from Er:YSGG for 80 mJ of input in a 1.0 msec pump-pulse at 20 Hz repetition rate.

We have also investigated the characteristics of Er-doped lasers pumped by a 15-W, 0.97 μm , cw diode-laser bar. The emission from the pump source, which occurred in two distinct lobes due to coherent-coupling effects, was focused using a monolithic cylindrical-lens array to two adjacent 0.6-mm-radius spots. This source was used to pump a

plane-parallel, monolithic resonator of Er:YSGG, 1-mm in thickness. Difficulties in matching the pump and resonator modes (due to the dual pump spots) limited the efficiency of the system. Greater than 500 mW of 2.79- μm emission from Er:YSGG was observed for pump powers of 9.2 W. We anticipate that Watt-level output powers will be attainable with bar lasers combined with improved pump optics.

Acknowledgements

The authors gratefully acknowledge the support of the Advanced Research Projects Agency. The authors also thank SDL, Inc. of San Jose, California; and CECOM Night Vision and Electronic Sensors Directorate of Fort Belvoir, Virginia, for the use of the diode lasers.

References

1. B.J. Dinerman and P.F. Moulton. "CW Laser Operation from Er:YAG, Er:GGG, Er:YSGG, and Er:BYF." Proceedings of the 1992 LEOS Annual Meeting, Boston, MA. Paper SSLT2.5.
2. B.J. Dinerman and P. F. Moulton. "Pulsed Gain Measurements and 3- μm CW Laser Operation in Er³⁺-Doped Crystals." Proceedings of the OSA Advanced Solid-State Lasers Conference, New Orleans, LA. February, 1993.
3. D.C. Shannon and R.W. Wallace. "High-Power Nd:YAG Laser End-Pumped by a CW, 10 μm x 1 mm Aperture, 10-W Laser-Diode Bar." Opt. Lett. 16, 5 (1991).

*corresponding author

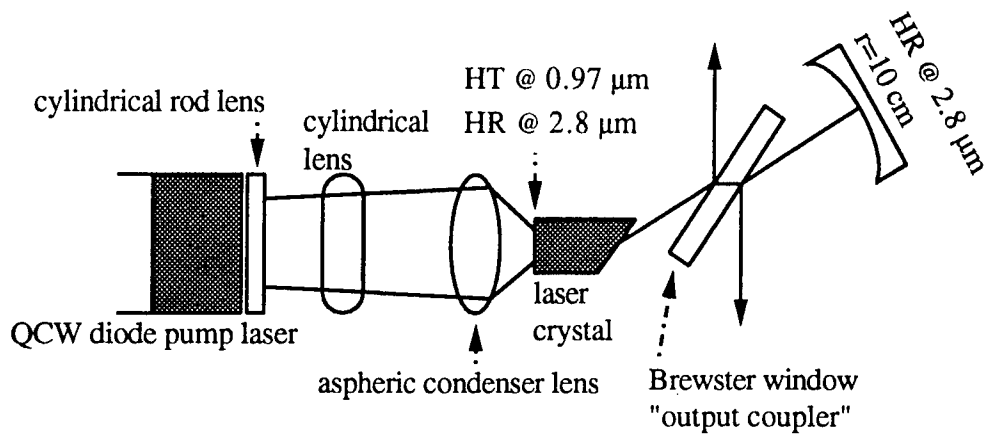


Figure 3. Experimental setup for QCW-diode-pumped erbium lasers.

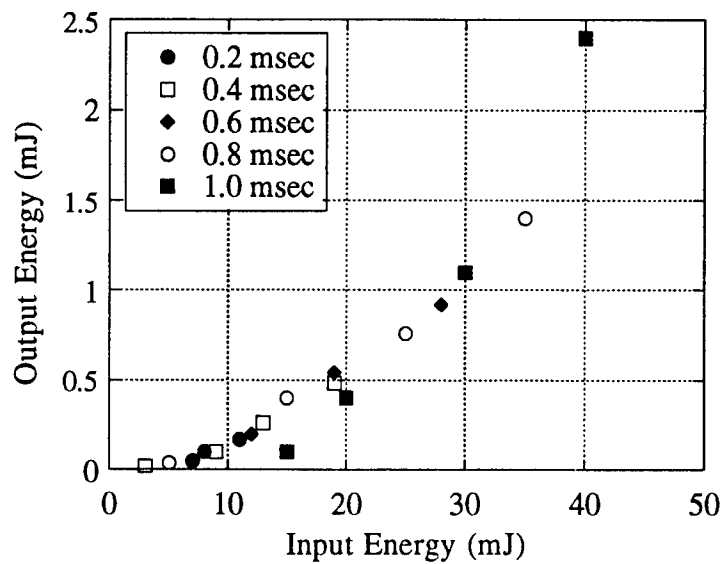


Figure 4. Energy data for variable pulsewidth, diode-pumped Er:YSGG (emission @ 2.79 μm). Data shown is for operation at 10 Hz.